Red-shifted Spectrum in Multi-frequency Raman Generation

by

Zujun Xu

A thesis
presented to the University of Waterloo
in fulfillment of the
thesis requirement for the degree of
Doctor of Philosophy
in
Physics

Waterloo, Ontario, Canada, 2021

Examining Committee Membership

The following served on the Examining Committee for this thesis. The decision of the Examining Committee is by majority vote.

External Examiner	NAME: **Alexei Sokolov** Title: **Professor**
Supervisor	NAME:**Donna Strickland** Title: **Professor**
Internal Member	NAME:**Melanie Campbell** Title: **Professor**
Internal-external Member	NAME: **Marcel Nooijen** Title: **Professor**
Other Member	NAME: **Joseph Sanderson** Title: **Associate Professor**

AUTHOR'S DECLARATION

This thesis consists of material all of which I authored or co-authored: see Statement of Contributions included in the thesis. This is a true copy of the thesis, including any required final revisions, as accepted by my examiners.

I understand that my thesis may be made electronically available to the public.

Statement of Contributions

Zujun Xu was the sole author for this whole thesis which were written under the supervision of Professor Donna Strickland. Dr. Kisor Kumar Sahu's group provided the simulation results in Chapter 7, section 7.5, *Gradient descent method for finding the best matching traces*.

Abstract

Multi-frequency Raman Generation (**MRG**) is a promising technique to generate few-femtosecond to sub-femtosecond pulses with high energy conversion efficiency. During the transient MRG experiments coupled with two chirped pulses in Donna Strickland's lab, phenomenon of red-shifted spectrum occurring and disappearing as the change of the instantaneous frequency separation between the pump pulse and the Stokes pulse was observed. The red-shifted spectrum may help us to get higher power pulses. We are interested in what the red-shifted spectrum is, where it comes from and how it behaves. The pulse measuring method Frequency Resolved Optical Gating (**FROG**) is applied to study the red-shifting effect, and a single shot FROG setup is built in the lab for pulse measurement.

Different sets of experiment were carried out to study the red-shifted MRG, such as MRG with different instantaneous frequency separation of the pumping pulses, the effects from the intensity of the pump, and the chirp sign of the pump pulses. To begin with, the first anti-Stokes Raman order is measured with different instantaneous frequency separations. The reconstructed results from the FROG program give similar results as what we observed from the auto-correlator and spectrometer, but with much more details and higher resolution. As the instantaneous frequency separation decreases, the spectrum of the first anti-Stokes Raman order transforms from a single peak to a head-shoulder pattern, and then reaches a spectrum with two discrete peaks. For the intensity effects, the higher the pulse intensity goes, the larger the separation of the two spectral peaks becomes. When the pump pulses are negatively chirped, the red-shifting of the Raman order is not obvious.

After investigating the cases with the spectrum of Raman order with two separated peaks, we think that the Raman order is a mixing of two pulses. Then, a double-pulse model, where the total pulse is made up of the Raman pulse and the red-shifted pulse, was introduced to describe the phenomenon. Simulation with the double-pulse model achieved lower errors as compared to the results from the FROG program. The results show that the Raman pulse stays similar to the pump pulses, while there is extra higher order phase for the red-shifted pulse. The experimental results along with the double-pulse model simulation suggest that the Raman pulse comes from the regular Raman scattering of MRG, while the red-shifted part is generated from the Raman scattering with the intensity dependent two-photon Stark shift.

Acknowledgements

It has been a long and arduous journey for this PhD study, but also a meaningful chapter of my life. I would not be able to complete it without the help and support from all the wonderful people along the way. It is full of pleasure and a great honor to learn, to discuss, and to share with everyone.

First of all, I would like to say thanks to my supervisor, Professor Donna Strickland, for giving me this great opportunity to work in the MRG project, supporting and encouraging me during the whole PhD period. Every conservation with her is constructive and beneficial. Her perception of the problems and innovative ideas have been an encouragement all the time. I am deeply indebted to everything that she has done for me.

I also want to thank the committee members, Professor Melanie Campbell, Professor Marcel Nooijen, and Professor Joseph Sanderson. They have always been helpful in all the committee meetings, pointing out all the challenges I faced and giving excellent suggestions to move forward. Their kindness, knowledge, and vision are truly inspirational.

I would like to thank all my colleagues in the group that I have come across along the journey. Hao Yan, the ever first graduate student that I met in Donna's lab, showed me the rainbow colorful spectrum from MRG, which became the first motivation for me to work in the MRG project. Years later, Abdullah Rahnama joined Donna's team, and worked with me for his master's degree. He is energetic and full of passion all the time. Working with him had brought me a lot of new things, and new ideas were being formed during discussions. I would also like to say thanks to Siyuan Bian, Tuyen Hoang, and Xingyang Su for their accompany in the lab, especially during the experiments in the quiet and endless nights.

Last but not least, I do want to thank to the colleagues from Professor Sanderson's team. Reza, a super nice and knowledgeable friend, has helped me in a lot of ways including fixing the devices in lab, giving doable suggestions when there were troubles, and has been a truly helpful mentor both in daily life and academic study. Thanks to Benj, a handsome and talented colleague, for always being there ready to help.

Dedication

Dedicated to my wife, Yanyun Hu, as she never stopped believing in and supporting me to get the PhD. Laughs and tears, she has always been there. And to my two kids, Eirika Xu and Robert Xu, their faces are like sunshine that brighten up my days.

Table of Contents

List of Figures

List of Tables

List of Abbreviations

AC Alternating Current

AI Artificial Intelligent

ASE Amplified Spontaneous Emission

auto-FROG auto-correlation Frequency-Resolved Optical Gating

BBO β-Barium borate (BaB_2O_4)

CARS Coherent Anti-stokes Raman Spectroscopy

CCD Charge-coupled Device

COS Carbonyl sufide

CPA Chirped Pulse Amplification

cross-FROG cross-correlation Frequency-Resolved Optical Gating

DC Direct current

FROG Frequency-Resolved Optical Gating

FWHM Full Width at Half Maximum

GDD Group Delay Dispersion

GGG Great Grand Goal

GRENOUILLE Grating-eliminated no-nonsense observation of ultrafast incident laser light e-fields

HHG High Harmonic Generation

KGW Potassium gadolinium tungstate (KGd(WO4)2)

MRG Multi-frequency Raman Generation

PCF Photonic crystal fiber

PG Polarization-gate

PSRS Parametric Stimulated Raman Scattering

rf Radio-frequency

RL Rayleigh scattering

SD Self-diffraction

SF_6	Sulfur Hexafluouride
SHG	Second Harmonic Generation
SPM	Self Phase Modulation
SPIDER	Spectral Phase Interferometry for Direct Electric-field Reconstruction
SRS	Stimulated Raman Scattering
TG	Transient-grating
THG	Third Harmonic Generation
TOD	Third Order Dispersion
TP	three photon resonance

List of Units

fps frame per second

ns nano-second (10^{-9} s)

ps picco-second (10^{-12} s)

fs femeto-second (10^{-15} s)

as atto-second (10^{-18} s)

THz terahertz (10^{12} Hz)

µm micrometer (10^{-6} m)

nm nano-meter (10^{-9} m)

MW megawatt (10^{6} w)

Nomenclature

ϵ_0	Vacuum permittivity
ϵ	Relative permittivity
λ	Wavelength
n	Refractive index
f	Frequency
Δt	Pulse duration
$\Delta \upsilon$	Bandwidth
ω	Angular frequency
ω_0	Center-frequency
ω_R	Raman frequency
$\phi(\omega)$	Spectral phase
χ	Susceptibility
$\chi^{(2)}$	Second order nonlinear susceptibility
$\chi^{(3)}$	Third order nonlinear susceptibility
$\chi^{(n)}$	n-th order nonlinear susceptibility
Ω	Rabi frequency
Ω'	Generalized Rabi frequency
c	Speed of light
δ_{ij}	Dirac delta function
ρ	Volume density
α	Amplitude ratio
τ	Time delay
G	Raman gain
γ	Damping constant

$\boldsymbol{\psi(r,t)}$	wave function
$\boldsymbol{\Delta}$	Detuning
$\boldsymbol{\delta}$	Pump-probe detuning

横看成岭侧成峰，远近高低各不同；

不识庐山真面目，只缘身在此山中。

----陆游《题西林壁》

Front, it is a ridge; side, it turns into a single peak. It has different shapes as you see it from different perspectives – far or near, high or low.

Could not tell the true shape of Lushan*, as you are within the mountain.

----Lu, You† "Writing on 'Xilin' wall"

* Lushan: a famous mountain in Jiangxi, China. My hometown is also in Jiangxi Province, but a different city.

† Lu, You: a prominent poet of China in Southern Song Dynasty, 1125–1209

Chapter 1

Introduction

As an analogy, we will start this chapter from the photographing of how we can take clear images of fast moving objects or things in darkness. With the same idea and by pushing the limits, we will see how the ultra-short pulses can benefit us in ultra-short event recording. To date, the ultra high power of the pulses has found applications in a wide range of fields, such as nonlinear study, high resolution manufacturing, and ignition of nuclear reaction. We will then describe the main techniques that are used to generate short pulses and introduce the Multi-frequency Raman Generation (MRG) as an excellent technique for the generation of high power ultra-short pulses. In the end, we will introduce the main research of this study, the red-shifted spectrum that occurs during our MRG experiments.

It starts from the very beginning of life, driven by the curiosity of exploration, we want to learn about the surroundings, know what is going on, and use the rules of the nature to make our own benefits. So, we feel things as hard or soft, rough or smooth, and cold or hot; we taste things for sweet, bitter, sour, spicy, and salty; we see things in different colours and shapes. We are excited about the new findings, but could also be frustrated as we might not able to see things clearly, for example, when the object is moving too fast or it is too dark to see.

1.1 Shorter the better

We get most of the information by eyes, and also have a saying goes, seeing is believing. However, it might not be true all the time, as we might not able to see clearly in some situations. There was a famous debate in 1870s, Leland Standford set a claim that at some point of the gallop, all of the horse's four feet are in the air, while other colleagues went with the common sense that the horse should always have at least one foot on the ground[1]. The galloping horse is moving so fast that human's eyes can not capture all the steps of the process. It became a bet, and the photographer, Eadweard Muybridge, developed a method of using 12 connected cameras with triggers to settle down the bet and proved that Standford was right. We can have a similar experiment to show that how the shutter speed affects the clearness of an image of a fast moving object.

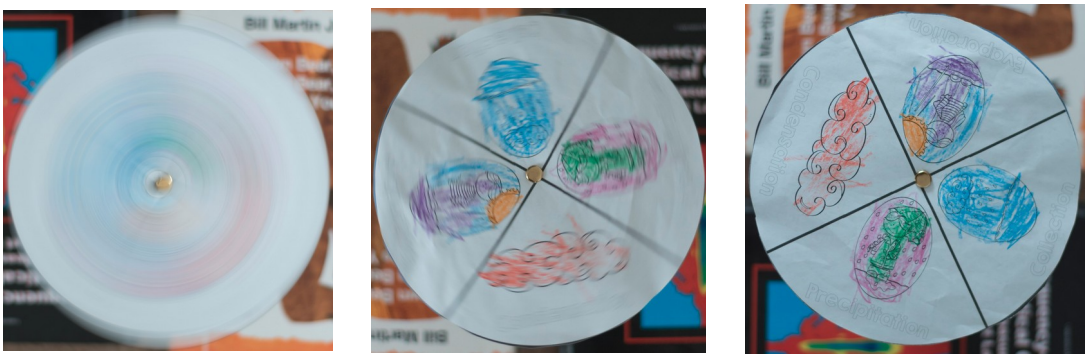

Figure 1.1: Photos of a rotating plate[i] taken with different shutter speed, from left to right the shutter speeds are 200 fps, 1000 fps, and 4000 fps, respectively.

As shown in figure 1.1, with low shutter speed, the fast rotating plate is a stirred image as the details are mixed up. To get a clear image of the rotating plate, we can simply increase the shutter speed. The stirred image becomes much clearer as we increase the shutter speed from 200 fps to 1000 fps. When the shutter speed gets to 4000 fps, the image is as clear as it is not rotating. The images of a rotating

i A water circulation plate coloured by my daughter, Eirika Xu, 2019.

plate with different shutter speeds show that with shorter reaction time, we can get better image of a fast moving object.

Muybridge's self-built high-speed cameras showed that in order to see a short event clearly, an even faster responding "eye" is needed. After that, new techniques were developed to make it possible to capture images of the high-speed objects, such as bullet. Using the rotating mirror technique, the frame speed can get up to 25 million frame per second[2]. However, as we get down to the microscopic level, shorter event with the duration of picco-second(10^{-12}s), femeto-second(10^{-15}s), or atto-second(10^{-18}s) will make the high speed camera useless. The ultra short time of duration makes it impossible for the mechanic shutter to catch up and thus a new technique is required. By changing their point of view, researchers have found that we can use short light pulses as both illumination source and shutter. With the help of ultra-short pulses to freeze the action, researchers are able to capture images of the molecular dynamics at the scale of atto-second(10^{-18} s)[3]. The *LASER* pulse used here works not only as the flashing light, but also as the shutter. Hence, the duration of the *LASER* pulse determines the quality of the captured image. As the shorter the pulse goes, the faster the event that we can freeze and record.

1.2 Brighter the better

In some cases, we might not be able to see things clearly due to the lack of light. As illustrated in figure 1.2, the low illumination makes it impossible to see the plate, and then a supporting light can be added to get a clear view of the plate.

Figure 1.2: Images with different light conditions. Left- image taken with low light;

Right- image taken with flashing light

A bright light source is required not only when it is too dark to see, but also in other situations such as studying the non-linear effects. With scientists' continued efforts and exploration, intense beams with high power are generated and applied in a variety of fields. Ever since the first ruby *LASER* created by Maiman in 1960[4], gigantic progress has been made in shortening the *LASER* pulse and increasing the power. Thanks to the advanced techniques such as Q-switching[5], mode locking[6], chirped pulse amplification[7], and Kerr-lens mode locking[8], *LASER* pulses with peak power at the level of $10^{21} W/cm^{-2}$ are achieved[9]. As a comparison, the average power of the sunlight we are receiving on Earth is about $0.1 W/cm^{-2}$. With the high power pulses, researchers are able to carry out experiments to study the non-linear effects. The intense beam has also found applications in different fields such as surgery and high resolution manufacturing. One of the well-known projects is the National Ignition Facility, which is going to use 192 beam lines at all circular directions to create a single 500 terawatts peak pulse that can heat and compress a small amount of hydrogen fuel to start the nuclear fusion reaction[10].

1.3 Ultra-short *LASER* pulse

A *LASER* is different from other sources of light for its coherence, i.e., spatial coherence and temporal coherence, and high intensity. As a few examples shown above, the shortness and brightness of *LASERs* can make some work possible. However, generating a short and intense *LASER* beam takes effort. As shown in figure 1.3, the pulse duration and bandwidth have an inverse relationship with each other, where a short pulse requires wide bandwidth and a long pulse leads to narrow bandwidth.

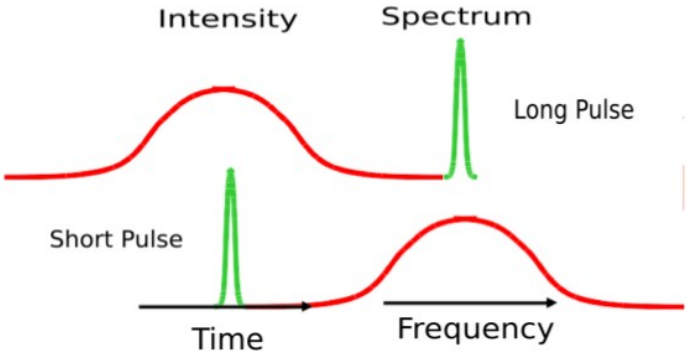

Figure 1.3: Relationship between pulse in the time domain and the frequency domain

As limited by the Fourier Transform theory, the pulse duration Δt and the bandwidth Δv have a relation that goes as

$$\Delta t * \Delta v \geqslant K \quad (1.3\text{-}1)$$

where K is a constant number depending on the profile of the pulse, and as an example, a Gaussian pulse has K = 0.441. Therefore, to generate a 1fs Gaussian pulse with perfect phase, a super wide spectrum of 441THz bandwidth is required. Besides the generation of wide spectrum, we also need to optimize the pulse forming process. Techniques such as Q-switching and mode locking were developed to generate short pulses.

Q-switching is a method for generating short pulses by changing the quality factor of the *LASER* cavity.[11] As shown in figure 1.4, at time zero, after the reduction of the loss triggered by an external signal, the gain is higher than the loss, the *LASER* seed pulse builds up, and a Q-switched pulse is produced. The pulses generated by Q-switching are typically in the nanosecond range, which is longer than the cavity round trip time. The repetition rate is usually less than Megahertz. The output energy of the pulse depends on the pump power and the pulse repetition rate, commonly around tens of mJ.[12] Depending on how the switch of loss works, the Q-switching is divided into two types, active Q-switching and passive Q-switching. In active Q-switching, devices such as acousto-optic[13], electro-optic modulator, and Pockels cell are used, while saturable absorber is used in passive Q-switching[14,15].

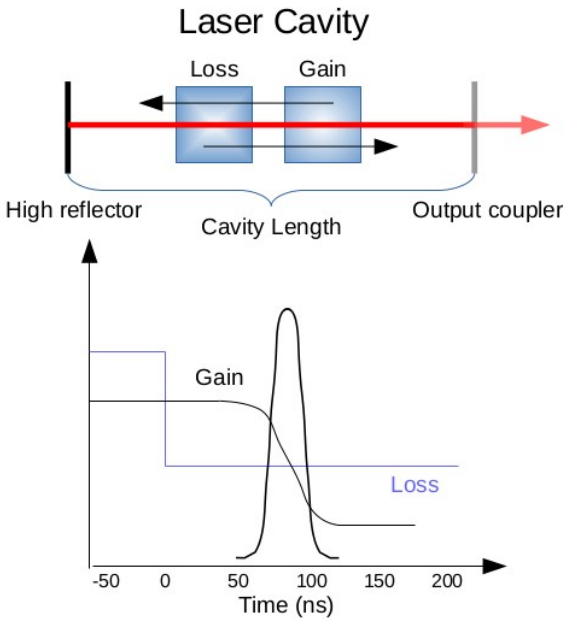

Figure 1.4: Scheme for *LASER* pulse generated with Q-switching technique

Mode locking is another widely used technique in generating ultra-short pulses. It is a technique that deals with the modes in a *LASER* cavity. The most common ways are using an externally excited modulator such as acousto-optic modulator, or a saturable absorber, or pumping the gain medium by a second short pulse *LASER* beam. As in a cavity with optical length of L, the modes are given by

$$\lambda_n = \frac{2L}{n} \quad (1.3\text{-}2)$$

where n is an integer. In practice, the cavity length is much larger than the optical wavelength. Thus, there will be a large number of modes in the cavity, usually more than 10^5. In a free run *LASER*, each of the modes goes randomly, with no fixed relationship among them. Figure 1.5 gives an intuitive look of how the mode locking affects the output pulses. As the left plot shows the situation where all the modes go randomly, the total pulse (green) seems more like a fluctuation of noise with average low power. However, once the modes are locked, the output (blue) turns into single pulses with much higher power. Similar to the Q-switching, mode locking also works in active or passive way depending on the device that is used.

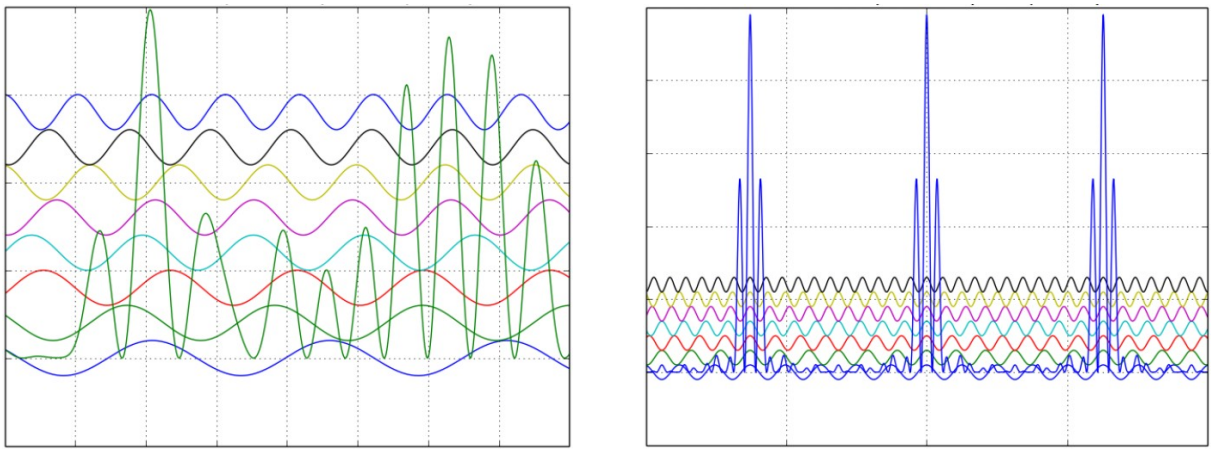

Figure 1.5: Example of Mode locking with 8 modes. Left- random phases; Right- mode locked

There are also other techniques such as Kerr-lens effect and control of dispersion that can help get shorter pulses. R. Ell and his colleagues have generated 5-fs pulses directly from a Ti:sapphire *LASER* oscillator.[16] However, due to the limitation of the bandwidth of the gain medium in the cavity, the spectrum can not go wider, and thus can not get shorter pulses. Luckily, techniques such as High Harmonic Generation(**HHG**)[17], Super-continuum Generation[18], and Multi-frequency Raman Generation(**MRG**) have the ability to generate the wider spectrum.

HHG is a non-linear process where an intense $\mathcal{LASER}$ beam is focused into a target. The output contains high order of harmonics of the insert beam. A good review paper about HHG and its application in electron and nuclear dynamics in atomic, molecular, and condensed matter is written by Jie Li and his colleagues.[19] The HHG process is explained in the strong field dynamics of the Coulombic systems. In the early 1990s, P. B. Corkum and his colleagues, and K. J. Schafer and the co-authors developed a classical three-step model for the HHG.[20,21] The three steps are: tunnel ionization of the atom/molecule, free propagation of the ions within the field, and recollision and recombination of the ions by releasing HHG photons.[22] The HHG process has a relatively low efficiency with only a very small part of the $\mathcal{LASER}$ power converted into the high harmonics due to the $\chi^{(n)}$ process. As illustrated in figure 1.6, to get the n-th harmonic order, n photons will be absorbed. Though the HHG has a very low efficiency, to date, the HHG has the ability to generate the shortest pulse of 43 atto-second(as) in the extreme ultraviolet and soft-X-ray region[23]. Currently, the energy of the atto-second pulses generated with HHG technique is too weak to be used in non-linear related studies of atom or molecule.

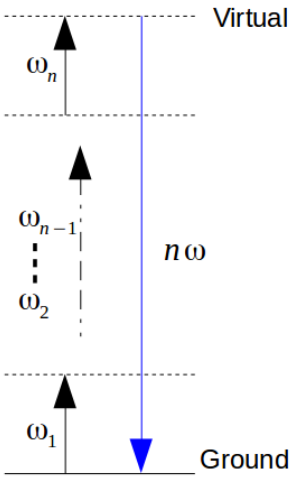

Figure 1.6: $\chi^{(n)}$ process in the view of energy levels

MRG is a cascaded Raman scattering process, where two $\mathcal{LASER}$ beams, the pump and the Stokes as shown in figure 1.7, are sent into Raman material to couple the Ground and Raman levels. The atom on the Raman level can be pumped to a higher virtual level by using a pump beam, then come down to the Ground level releasing a new photon with higher energy as the first anti-Stokes Raman order. Then, the first anti-Stokes will work as the pump and generate the second anti-Stokes Raman order. This process will cascaded which ends up with lots of discrete spectrum orders separated by the Raman frequency of the material used. Different from the HHG, the Raman orders in MRG are always generated by a

$\chi^{(3)}$ process, and thus it is much more efficient. MRG is a promising method for the generation of ultra-short pulses with high energy, as the efficiency of the process can be close to 100%[24,25]. A much more detailed introduction for MRG will be given in chapter 2.

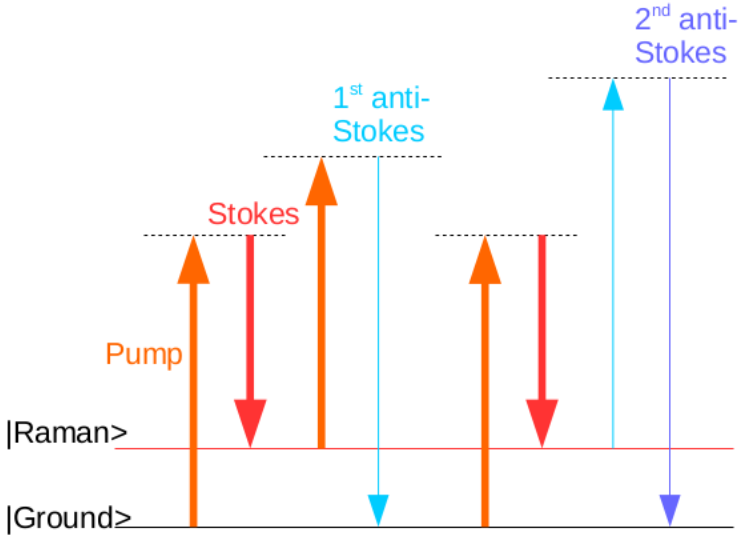

Figure 1.7: Energy level diagram of MRG with the generations of 1st and 2nd anti-Stokes Raman orders

Super-continuum Generation is a complicated non-linear process with many non-linear effects acting together. The spectral broadening mechanism is caused by self-phase modulation, Raman scattering, four-wave mixing, etc. The Super-continuum Generation commonly happens within optical fibres, and that is because in the fibres, the energy threshold of the insert beam is much lower and that the fibre can be particularly designed to enhance certain non-linear effects. The super-continuum spectrum is a good resource for the generation of ultra-short single pulse.

HHG, super-continuum Generation, and MRG techniques have their own advantages and disadvantages in the generation of a wide spectrum. In this thesis, we are studying the generation of the super wide spectrum by using MRG. After generating the wide spectrum, for a Fourier transform limited pulse, we also need to make sure that the phase of the spectrum stays constant. However, as the pulse travels through materials, the added dispersion will modify the phase of the spectrum and therefore will change the profile of the pulse. Researchers have worked hard on maintaining the phases and compressing pulses to generate short pulses. Setups such as prism-pair, grating-pair, and dispersion mirror are applied and developed.

It is worth noting that, the ultra high intensity of the beam can also cause big problems in the lasing process. It can damage optical devices along the path and also introduce other unwanted non-linear

effects, for instance, self-focusing. To increase the pulse power while not causing these problems, a technique named chirped pulse amplification(CPA) was developed by Donna Strickland and Gerard Mourou in the 1980s[26]. The state-of-the-art CPA technique can increase the *LASER* power by orders of magnitude. Nowadays, almost all the high-peak-power *LASER*s around the world are using the CPA technique, the Vulcan *LASER* at the Rutherford Appleton Laboratory's Central *LASER* Facility, the OMEGA EP *LASER* at university of Rochester, and GEKKO XII *LASER* at the GEKKO XII facility, to name a few.

1.4 Red-shifted spectrum in MRG

In our lab, we can generate a wide spectrum with discrete Raman orders separated by the Raman frequency of the material with MRG technique. Factors such as the gas pressure, pump power, and frequency separation between pump and Stokes have been studied to maximize the Raman orders. In the process of generating high orders of Raman spectra, a novel phenomenon occurs with a second spectral peak appearing on the red side of each of the Raman orders[27]. The extra spectrum turns each of the Raman orders into a double-peak pattern, and the double-peak becomes more separated as the higher the order goes. This phenomenon can also be seen in other groups' experiments[28,29,30], but no further discussion was made. During the study of Raman gas self-organizing into a deep nano-trap lattice done in 2015, M. Alharbi and his colleagues observed both red and blue shifted spectra occurring on each side of the Raman peaks.[31]

As we mainly focus on the study of the red-shifted spectrum, let's take a look at how the extra spectrum will change our final pulses. To make it simple, as shown in figure 1.8, we take the Raman orders from MRG to have a Gaussian profile, and 11 Raman orders are used. The total bandwidth is V=102.4 THz, with the Raman orders separated by 20.0 THz and each of them have a bandwidth of u=4.0 THz with constant phases. By synthesizing all the Raman orders, the Fourier transform limited pulses will become the one on the right side of figure 1.8. For this transform limited case, we have $\Delta t * \Delta v = 441$ by using fs as unit for time duration and THz for bandwidth, such that the pulse duration for each of the single pulses is t=4.3 fs, and the Gaussian envelope of the pulses has a full wave half maximum (FWHM) of T=110 fs. With the appearance of the red-shifted spectrum, shown as in figure 1.8-S2, each of the Raman orders is shown with a double peaked pattern, and the bandwidth

can be more than doubled. As a result, the Fourier transform limited pulses train will have a Gaussian envelope with the FWHM reduced to around 50 fs, as shown in figure 1.8-E2. Comparing the pulse-train of the two, fewer pulses are achieved under the Gaussian envelope for the spectrum with red-shifted spectrum. Therefore the energy is stored within the central pulse and leading to higher pulse power for the pulse.

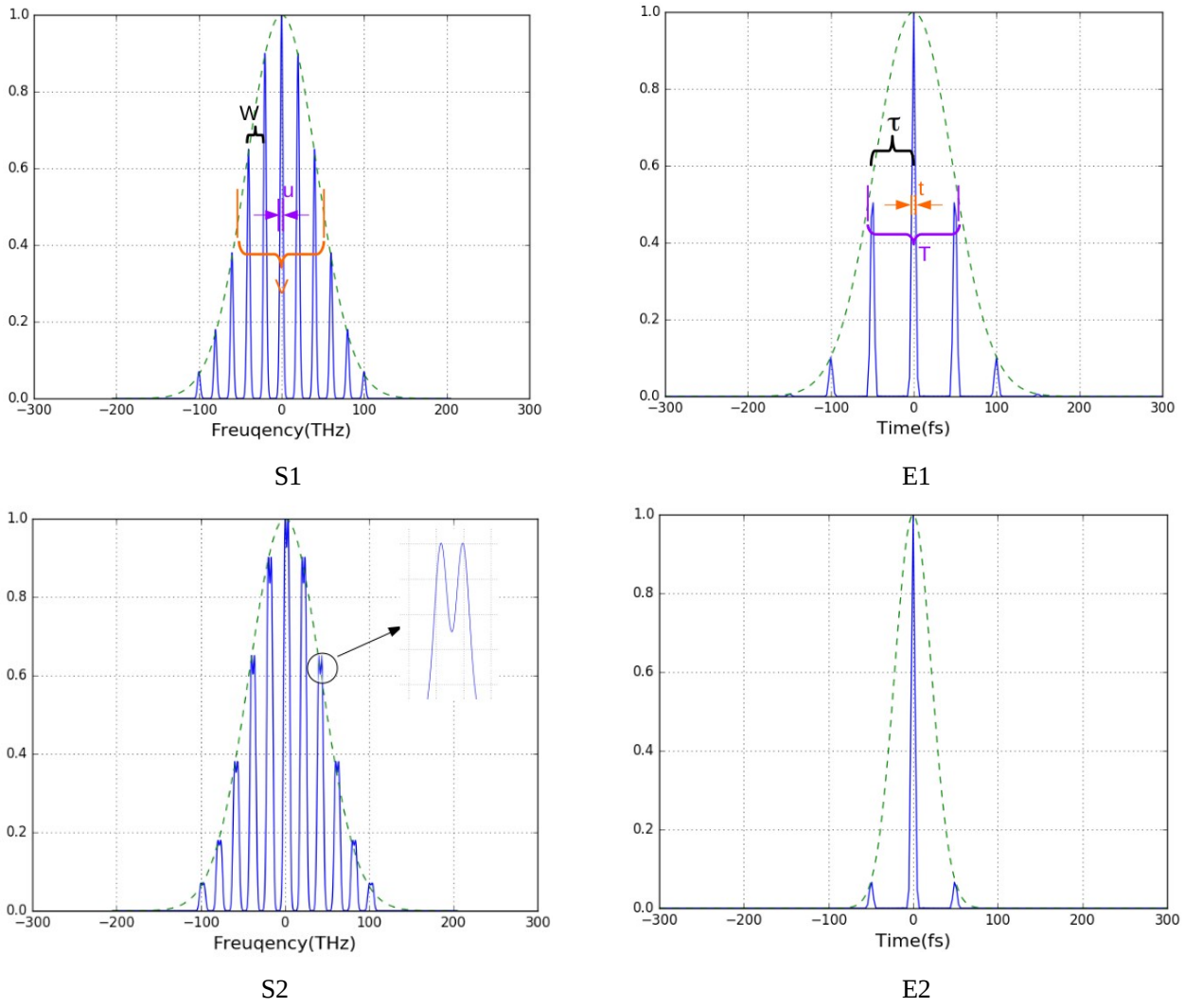

Figure 1.8: Fourier transform limited pulses with spectrum from 11 Raman orders. S1- Frequency domain of the Raman orders; E1- Pulses train in Time domain with spectrum in S1; S2- Frequency domain of the Raman orders with red-shift spectrum; E2- Pulses train in Time domain with spectrum in S2. In plot S1, each of the Raman orders has a bandwidth of ‘u’, the frequency separation between the Raman orders is ‘w’, and the total bandwidth is ‘v’; in plot E1, each pulse has a pulse duration of ‘t’, and the pulses are separated by ‘ τ ’, and the overall Gaussian envelope has a duration of ‘T’.

The potential of obtaining higher peak power with the red-shifted spectrum is of great interest to us. On the other hand, if the red-shifted spectrum has a negative effect on our final pulses, we should try to get rid of it. In addition, we are also curious about the mechanism of the appearance of the red-shifted spectrum. The main project of my PhD study is trying to figure out what is the red-shifted spectrum and how it is produced.

Before this MRG study, previous students in the group used spectrometer to measure the Raman orders, and they found that the red-shifted spectrum appears with red-tuned pumps and disappears as the pumps are blue-tuned.[32,33,34] The results indicated that the red-shifted spectrum may come from Stark shifting rather than four-wave mixing. Also, the amount of red-shifting is intensity dependent. H. Yao also set up a measurement device called SPIDER to further investigate the pulses, but it turned out that the noise is too big for the SPIDER to get a good measurement[35].

1.5 Pulse measurement with FROG and double-pulse model

The information we can get from the spectrometer is very limited, to further understand the phenomenon and inspired by Rick Trebino's pulse measurement idea, Frequency-Resolved Optical Gating(FROG) is applied. We built up the FROG setup based on the auto-correlator in our lab, and tested the device with our pump pulse. The FROG gives more details, not only the pulse shapes, but also the phases. Besides, the FROG device has much higher resolution. For the spectrum, the FROG device can get down to 0.1 nm, while the Ocean Optics spectrometer we are using is more than 1 nm. At the beginning, we were using auto-FROG such that the pulse auto-correlates with itself. However, as we carried out the measurement, it is hard to get a well-separated Raman order from the output beam. We then moved to the cross-FROG, where the output beam is sent to cross-correlate with the Stokes pulse. There are a few advantages by switching to cross-FROG. Firstly, we can get rid of the Raman order separation problem. Secondly, we can easily measure different Raman orders by only rotating the grating. Last but not least, the relatively high power of the Stokes pulse makes it possible to measure weak orders.

The cross-FROG works and it gives all the information for a chosen Raman order. However, with the appearance of the red-shifted spectrum, the Raman order is no longer a single pulse, it looks more like a mixing of pulses. Investigating the situation where the two spectral peaks are widely separated, we have a strong intuition that the Raman order is a mixing of two pulses, while the FROG algorithm only

provides a single total pulse (Detailed discussion in section 7.1, Chapter 7). In order further describe the red-shifted Raman orders, we then came up with a double-pulse model with the total Raman pulse E described as

$$E = E_1(\omega_1, \phi_1, t) + \alpha E_2(\omega_2, \phi_2, t+\tau) \quad (1.5\text{-}1)$$

where E_1 and E_2 are normalized Gaussian pulses for the Raman part and the Red-shifted part, respectively. In addition, an amplitude ratio factor " α " and time delay " τ " between the two pulses are introduced in the model to match the original data. To start with, we assumed that E_1 and E_2 are Gaussian pulses with second and third order phases. The double-pulse model simulation has shown a great success with smaller errors compared to the results from FROG algorithm. Later, we refined our model by taking the pump pulse and Stokes pulse into consideration, such as using the shape of the pump instead of a Gaussian shape and using the phases from the pump and Stokes rather than a defined second and/or third order phase. We have good matching in some cases, but it turned out that the iteration program for the simulation is very sensitive to the initial conditions (Detailed discussion in section 7.2, Chapter 7). Work has been done to improve the program, and also we worked with an AI group to figure out a good strategy, and the task is still under the way.

Meanwhile, we realized that the model of two pulses with a time delay between them may not be appropriate as it is hard to have a physical explanation for the hundreds of fs time delay between the two pulses. Then, similar to equation 1.5-1, but adding an extra phase ψ to the red-shifted pulse E_2. The total pulse is given as

$$E = E_1(\omega_1, \phi_1, t) + \alpha E_2(\omega_2, \phi_2 + \psi, t) \quad (1.5\text{-}2)$$

Better simulation results were obtained with the phase shifting double-pulse model.

We then realized that the red-shifted spectrum may come from the intensity dependent Rabi frequency. Thus, the double-pulse model has a simplified form that goes as

$$E = E_1(\omega, \phi, t) + \alpha E_2(\omega, \phi + \Phi(t), t) \quad (1.5\text{-}3)$$

where now the two pulses share the same , and an extra phase $\Phi(t)$ caused by the time varying Rabi frequency is added to the red-shifted pulse. Simulations show high degree of match with the experiment results. Inspired by the transient MRG theory done by A. P. Hickman and the co-authors,

we think the time varying Rabi frequency could probably explain the occurrence of the red-shifted spectrum, and the Raman orders can be described with our double-pulse model.

1.6 Outline

In Chapter 2, starting from the Raman scattering, we will provide an overview of MRG, covering the development of MRG, and the theory of MRG. In Chapter 3, a brief introduction of the FROG will be given as it is the main pulse measurement that we have been using in this study. We will focus on the single-shot FROG setup that we built and used in our lab. In Chapter 4, we will describe our experimental apparatus, including the front end *LASER* source, the pulse stretcher, the regenerative amplifier, the multipass amplifier, the grating pulse compressor, the hollow fibre chamber, and the pulse measurement setups. In Chapter 5, a single run of the whole experiment process with key checking points for each steps is provided. In addition, the calibration for the self-built measurement devices is shown. Then, we have the experimental results and data analysis in Chapter 6 by using the FROG algorithm. In Chapter 7, a double-pulse model is introduced to describe and explain the red-shifting phenomenon, and an iteration program is developed and several simulations are done to support our double-pulse idea. Conclusions and future possible work will be included in chapter 8 as a closure of this thesis.

Chapter 2

Multi-frequency Raman Generation and Stark Shift

Starting in this chapter, we will go along the route for the generation of short pulses, from the initial *LASER* pulse to picosecond, femtosecond, sub-fs, and even attosecond pulses. We will have a detailed introduction of MRG as it is the technique we are using in our lab for the generation of ultra wide spectrum. MRG study has three regimes depending on the duration of pulses used, adiabatic regime, transient regime, and impulsive regime. We will go though some remarkable studies in each of the regimes, together with the very recent researches. A transient MRG theory from Hickman and his colleagues is described, and it will be the main theory that we use in this study. Then, descriptions of Rabi oscillation and Stark shift of two-photon dressed states are provided as they may explain the phenomena that we have seen for the red-shifted spectrum in MRG. A brief walkthrough of the red-shifted MRG work done in Donna Strickland's group is provided at the end of this chapter.

Ultra-short pulses with high-power have promising applications in measuring ultra-fast phenomena, for example, recording microscopic chemical reactions, super-high-resolution manufacturing, surgery, etc. Discovered in 1960 by Maiman, the first *LASER* pulse had a pulse duration in the microsecond scale and peak power of 5 kW. The unprecedented intensity of the *LASER* pulse quickly found applications in non-linear research, for instance, second harmonic generation(SHG)[36]. Since the intensity plays an important role in the study of non-linear phenomena, a lot of work has been done to achieve higher power pulses. The method we are using in this thesis is by making the pulse shorter. Key pulse shortening techniques such as Q-switching in 1963 by McClung[37] and mode-locking in 1964 by Hargrove were developed, bringing the pulse duration to picoseconds scale[38]. In 1981, by inserting two synchronized counter-propagating pulses in a saturable absorber, R. L. Fork and his colleagues obtained a continuous stable train of pulses shorter than 100 fs.[39] Later on, with the use of self-phase modulation, Kerr-lens effect, and pulse compression methods, ultrashort pulses shorter than 10 fs were achieved.[40] However, as we learnt from the relationship between the pulse duration and bandwidth that goes as $\Delta t * \Delta v \geqslant K$, a shorter pulse would require a wider bandwidth. Taking the Ti:sapphire as an example, the gain bandwidth is around 100 THz, thus the shortest pulse a Ti:sapphire *LASER* can generate is about 4.4 fs.

2.1 Single-cycle and sub-femotosecond pulse

To obtain even shorter pulses, for example pulses with duration of 1 fs, there are two main challenges . Firstly, it is impossible to get a wider bandwidth over 440 THz with only the Ti:Sapphire *LASER* gain medium. Secondly, a pulse duration of 2.7 fs cap will be reached as the limit of a single-cycle pulse duration at the center-wavelength of 800nm. For the single-cycle pulse limitation, switching to a wavelength smaller than 300 nm would work. Thus, the short wavelength makes the x-ray a promising region to get ultra-short pulses below 1 fs. With sub-fs pulses applied in the X-ray pump-probe spectroscopy, scientists would be able to trace the inner shell relaxation processes. By using tens of attoseconds pulses, we would be able to study the Bohr orbit[ii] of electrons and promisingly to open a whole new world in atomic physics.

The first promising method for the generation of sub-fs pulse is the HHG. In 1988, M. Ferray, et al., obtained up to 33rd harmonics ranging from 350 nm to 32.2 nm in the XUV generated by the rare gas

ii Bohr orbit time for hydrogen: ~150 attoseconds

argon.[41] In theory, this bandwidth is good enough to generate pulses below 100 attoseconds. HHG meets all the requirements for the generation of attosecond pulses. The centre-frequency is in the XUV region that can easily get rid of the single-cycle pulse limit. The bandwidth of the generated spectrum is super wide, which makes it possible to produce pulses less then 10 attoseconds. Besides, studies have shown that very little phase control is required to synthesize the spectrum to get attosecond pulses, and even trains of attosecond pulses are automatically produced right after the HHG process[42]. In some theoretical studies, I. P. Christov and his colleagues showed that with pump pulses shorter than 10 fs, the harmonic orders' bandwidth becomes broader and the coherence increases, and that attosecond pulses can be generated[43]. Works has been done to generate sub-fs pulses, and researchers have pushed the shortest pulse to 43 attosecond by using a passively carrier-envelope phase stable mid-infrared driver[44]. HHG is able to generate sub-fs pulses, and holds the record to produce the shortest pulse. However, a big drawback is the low energy conversion efficiency at a level of 10^{-5}.

The second promising method is MRG. Almost right after the invention of the $\mathcal{LASER}$, large number of Stokes and anti-Stokes Raman orders have been seen in labs.[45] Later, researchers found that the $\chi^{(3)}$ process becomes more effective with a second beam coupling the Raman transition, and more Stokes and anti-Stokes orders are showing up. In 1989, by focusing two beams into hydrogen, T. Imasaka, et al., obtained an intense output consisting of more than 40 Raman orders.[46] With the rainbow colourful spectrum ranging from infrared to deep ultraviolet, S. Yoshikawa et al., proposed a new technique to generate short pulses in 1993, and their simulation showed that pulses with duration of 1.4 fs could be generated.[47] A. E. Kaplan proposed that the Raman orders from MRG can form a 2π soliton, and the coherent interference of the mode-locked Raman orders can lead to sb-fs pulses with high intensity.[48] In 1999, during MRG experiment with SF_6, A. Nazarkin and his colleagues found that the energy transformation is very effective, and up to 100% of the injected pulse energy will transform into Stokes and anti-Stokes Raman order.[49] The width and the coherence of the spectrum, together with its high energy efficiency gradually attract researchers' attention for the potential of generating ultra-short pulses. By using 7 Raman orders, M. Y. Shverdiin and his colleagues achieved single-cycle pulses with pulse duration of 1.6 fs.[50] Later, a numerical experiment carried out by K. Yoshii et al., showed that they can generate 728 attosecond pulses with the Raman spectrum from MRG.[51]

As techniques for the generation of single-cycle and sub-fs pulses, the HHG and MRG have their own advantages in certain situations. Besides, method of synthesizing separated phase-locked laser oscillators was proposed by T. W. Hansch to generate sub-fs pulses, where they can use oscillators with

different frequencies, and get phase-locked spectra with the harmonics and sum-frequencies.[52] In this thesis, we will focus on MRG technique. MRG process is based on the Stimulated Raman Scattering(**SRS**), which was seen and developed after the initial discovery of Raman scattering in 1928. Let us start with Raman Scattering.

2.2 Raman scattering

The Raman scattering was discovered by C. V. Raman and his student K. S. Krishnan in 1928. It is an inelastic scattering process in which a photon is scattered by a molecule, with the molecule in a changed energy level and releasing a photon with different energy[53]. As photons propagate through materials, they are scattered by atoms or molecules, and mostly the scattering is elastic scattering called Rayleigh scattering. During Rayleigh scattering, the molecule keeps in the same energy level with the scattered photon holding the same frequency as the incident photon. However, a small amount of scattering processes are inelastic, leaving the molecule with a changed energy state. Thus, the scattered photon has a different frequency and energy from the incident photon. The scattering with higher energy scattered photon is called anti-Stokes Raman scattering while the lower energy photon one is named as Stokes Raman scattering.

The Raman scattering process described above is the spontaneous Raman scattering which happens randomly and very weakly, approximately 1 in a million of the incident photons[54]. With the incident light getting stronger, a much enhanced Raman scattering occurs. This much stronger process is called the SRS.

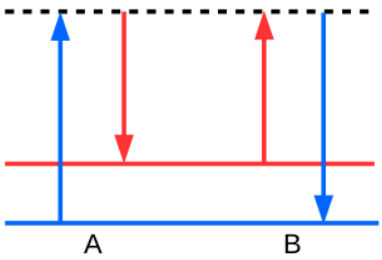

Figure 2.1: Diagram of Raman scattering, A: Stokes scattering; B: Anti-Stokes scattering

The Raman scattering process can be easily understood by using energy levels. As shown in Figure 2.1, for the Stokes Raman scattering, the molecule is excited from its ground energy level to a virtual level. Then, instead of coming all the way down to the ground level, it reaches the Raman energy level,

releasing a photon with less energy. On the other hand, there is also the anti-Stokes scattering, where the molecule is pumped from its Raman energy level and then comes all the way down to the ground level, releasing a photon with higher energy. In general, the Stokes scattering is way stronger than the anti-Stokes scattering, as shown by the Boltzmann distribution $e^{-\hbar\omega/kT}$ that most of the molecules stay in their ground energy level in room temperature.

The spontaneous Raman scattering is a very weak process, the scattering cross section factor is about $10^{-6}cm^{-1}$, while the SRS process has a higher efficiency up to unity of energy transition. The spontaneous Raman scattering and SRS can be written in terms of an intuitive argument introduced by Hellwarth in 1963[55], which is given as

$$m_S(z)=\begin{Bmatrix} m_S(0)+G\,z\cdots\cdots(a) \\ m_S(0)e^{Gz}\cdots\cdots\cdots(b) \end{Bmatrix} \quad (2.2\text{-}1)$$

where (a) for spontaneous Raman scattering and (b) for SRS. The G is defined as Raman gain coefficient, m_S is the number of photons in Stokes mode, and z as the distance measured along the beam propagation direction, which starts from the front surface of the Raman medium. As can be seen from the equations, for spontaneous Raman scattering the number of photons in Stokes mode increases linearly with propagation distance, whereas the number grows exponentially for the SRS. Another big difference between the two is that the radiation from the spontaneous Raman scattering comes with random directions and phases; for the SRS, the radiation is mainly kept in the forward and backward directions and in coherent phases. Also, due to the directions of the radiation, the SRS is categorized into two areas, the forward SRS and backward SRS. They show different behaviours mainly because of the pump pulse they are going through. The biggest difference is that the backward SRS can be amplified to a much higher intensity than the pump pulse.[56] Also, the backward SRS will disappear if the pump pulse is too short.

The discovery of SRS came much later than the Raman Scattering, mainly due to the shortage of intense light beams. Soon after the invention of the ruby $\mathcal{LASER}$, in 1962, during a study of ruby $\mathcal{LASER}$ Q-switching with a nitrobenzene Kerr cell, Woodbury and Ng detected a strong infrared radiation with an unknown source.[57] Later, several other experiments with different materials have confirmed this phenomenon[58], and Woodbury and Eckhardt proposed that the signal comes from SRS[59]. Soon after the discovery, SRS was observed in experiments with other liquids such as Benzene,

Acetone[60], and CS_2[61], gases like H_2, D_2, and CH_4[62], and solids of diamond, and calcite[63]. Thereafter, lots of work has been done to study SRS, and several theories have been developed to explain it. Bloembergen and Shen have written good review articles about the SRS[64,65]. One of the widely used classical theories for SRS is the coupled-wave model. The coupled-wave model uses a semi-classical treatment, where the waves are defined as classical. In this model, two sets of equations coming from two assumptions are used to describe the SRS process. Here we go with the derivation from Boyd's Nonlinear Optics book.[66] The fist assumption says that the optical polarizability $\tilde{\alpha}$ of molecule depends on the internuclear separation, which can be described as

$$\tilde{\alpha}(t)=\alpha_0+\left(\frac{\partial\tilde{\alpha}}{\partial q}\right)_0\tilde{q}(t)+O(\tilde{q}(t)^2) \quad (2.2\text{-}2)$$

where α_0 is the polarizability at equilibrium, and $\tilde{q}(t)$ is the internuclear separation, as shown in Figure 2.2. Since the internuclear separation is a very small change, we only consider the first order dependence.

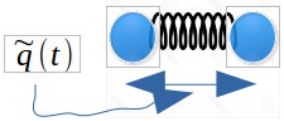

Figure 2.2: Simple harmonic molecular model for Stimulated Raman Scattering

The second assumption is that the molecule vibrates like a simple harmonic oscillator with frequency ω_v, damping constant γ, and reduced nuclear mass m. Therefore the equation of motion for the molecule vibration becomes

$$\frac{d^2\tilde{q}}{dt^2}+2\gamma\frac{d\tilde{q}}{dt}+\omega_v^2\tilde{q}=\frac{\tilde{F}(t)}{m} \quad (2.2\text{-}3)$$

where the force $\tilde{F}(t)$ comes from the external field that is applied on the molecule.

The induced dipole moment of a molecule is given by

$$\tilde{P}(z,t)=\epsilon_0\tilde{\alpha}\tilde{E}(z,t) \quad (2.2\text{-}4)$$

where $\tilde{E}(z,t)$ is the applied electric field. With the slowly varying amplitude approximation, the wave propagating equation goes as

$$-\nabla^2\tilde{E}+\frac{\partial^2\tilde{E}}{c^2\partial t^2}=-\frac{1}{\epsilon_0 c^2}\frac{\partial^2\tilde{P}}{\partial t^2} \quad (2.2\text{-}5)$$

By applying the polarization from equation 2.2-4 to the wave equation, a two coupled equations between Stokes and anti-Stokes Raman gain are reached as

$$\frac{dA_S}{dz} = -\alpha_S A_S + \kappa_S A_A^* e^{i\Delta k z} \quad (2.2\text{-}6A)$$

$$\frac{dA_A}{dz} = -\alpha_A A_A + \kappa_A A_S^* e^{i\Delta k z} \quad (2.2\text{-}6B)$$

where A_S and A_A are the amplitudes of the electric fields of Stokes and anti-Stokes, repectively, A_S^* and A_A^* are the corresponding complex-conjugate; α_S and α_A are the nonlinear absorption and κ_S and κ_A as the coupling coefficients; Δk is defined as the wave-vector mismatch, and z as the distance measured along the beam propagation direction. Please refer to Boyd's book for more detailed definitions and derivation.

The model has been adopted to explain several experiments, which shows a good match between the theory and experimental results[67,68,69,70,71]. However, there is a limitation to explain the efficient Raman effect with a large number of anti-Stokes orders generated in H_2[72], and other experiments with reported anti-Stokes up to 8 orders[73].

2.3 Rabi oscillation and Stark shift

For the Raman scattering, and in fact, for all the resonant optical driving molecular transition processes, there are some interesting side effects on the molecular energy levels from the applied field, such as the Stark effect and Zeeman effect. We will talk about the effect from the electric field, the Stark effect.

Let us start with a two-level molecule system. We will follow R. W. Boyd's description in his Nonlinear Optics book[74]. We can describe the system in terms of the wave function $\Psi(\boldsymbol{r},t)$, which follows the Schrodinger equation

$$i\hbar\frac{\partial\Psi}{\partial t} = \hat{H}\Psi \quad (2.3\text{-}1)$$

with applied external electric field $\widetilde{E}(t)$, the Hamiltonian can be written as

$$\hat{H} = \hat{H}_0 + \hat{\mu}\widetilde{E}(t) \quad (2.3\text{-}2)$$

Solving the equation 2.3-1 with the new Hamiltonian, the wave function can be expressed as a superposition of the two states, thus

$$|\Psi(\boldsymbol{r},t)\rangle = C_1(t)e^{-i\omega_1 t}|1\rangle + C_2(t)e^{-i\omega_2 t}|2\rangle \quad (2.3\text{-}3)$$

the $C_1(t)$, and $C_2(t)$ are the probability amplitudes that the atom is in state 1 and state 2. Written in the form of interaction Hamiltonian with matrix elements, we have

$$\dot{C}_1 = -\frac{\mu_{12}}{i\hbar}C_2\left(E^* e^{-i(\omega_{21}-\omega)t} + E\, e^{-i(\omega_{21}+\omega)t}\right) \quad (2.3\text{-}3A)$$

$$\dot{C}_2 = -\frac{\mu_{21}}{i\hbar}C_1\left(E^* e^{i(\omega_{21}-\omega)t} + E\, e^{i(\omega_{21}+\omega)t}\right) \quad (2.3\text{-}3B)$$

using the rotating wave approximation, and by introducing the detuning factor $\Delta = \omega - \omega_{21}$ with ω_{21} as the transition frequency between the two levels, Rabi frequency $\Omega = 2\mu_{21}E/\hbar$ equation 2.3-3 is simplified to be

$$\dot{C}_1(t) = i\frac{\Omega^*}{2}C_2(t)e^{i\Delta t} \quad (2.3\text{-}4A)$$

$$\dot{C}_1(t) = i\frac{\Omega}{2}C_1(t)e^{-i\Delta t} \quad (2.3\text{-}4B)$$

the general solution for equation 2.3-4 is given as

$$C_1(t) = \left(A_+ e^{-\frac{1}{2}i\Omega' t} + A_- e^{\frac{1}{2}i\Omega' t}\right)e^{\frac{1}{2}i\Delta t} \quad (2.3\text{-}5A)$$

$$C_2(t) = \left(\frac{\Delta-\Omega'}{\Omega^*}A_+ e^{-\frac{1}{2}i\Omega' t} + \frac{\Delta+\Omega'}{\Omega^*}A_- e^{\frac{1}{2}i\Omega' t}\right)e^{-\frac{1}{2}i\Delta t} \quad (2.3\text{-}5B)$$

where, $A_\pm$ are constants depend on the initial conditions, and $\Omega' = \sqrt{|\Omega|^2+\Delta^2}$. To examine the solution of the probability amplitudes, C_1 and C_2, we can look at the solution with extreme cases. For off resonance case, where $\Delta \to \infty$, we will get $C_1(t) = 1$, and $C_2(2) = 0$, meaning no transition occurs. For the case of perfectly resonance, $\Delta = 0$, the solutions become

$$C_1(t) = \frac{1}{2}\left[e^{i\frac{\Omega}{2}t} + e^{-i\frac{\Omega}{2}t}\right] \quad (2.3\text{-}6A)$$

$$C_2(t) = \frac{1}{2}\left[e^{i\frac{\Omega}{2}t} - e^{-i\frac{\Omega}{2}t}\right] \quad (2.3\text{-}6B)$$

the probability for the molecule to be in state 1 and state 2 are

$$P_1(t)=\cos^2(\frac{\Omega}{2}t) \quad (2.3\text{-}7A)$$

$$P_2(t)=\sin^2(\frac{\Omega}{2}t) \quad (2.3\text{-}7B)$$

From the results in equations 2.3-7, we can see that the molecule is oscillating back and forth within the 2 states at the frequency of half the Rabi frequency, $\Omega/2$.

Substitute C_1 and C_2 from equation 2.3-5 into equation 2.3-3, we can get the wave function of the molecule as

$$|\Psi(\boldsymbol{r},t)\rangle=\frac{1}{2}[e^{-i(\omega_1+\frac{\Omega}{2})t}|1\rangle+e^{-i(\omega_1-\frac{\Omega}{2})t}|1\rangle+e^{-i(\omega_2+\frac{\Omega}{2})t}|2\rangle-e^{-i(\omega_2-\frac{\Omega}{2})t}|2\rangle] \quad (2.3\text{-}8)$$

As shown from the wave function, now the two level molecule system turns into new system with states of $\omega_1\pm\frac{\Omega}{2}$, and $\omega_2\pm\frac{\Omega}{2}$. The splitting of the energy levels by the applied electric field is called the Stark shift, and as we are using rapidly varying electric field, the specific name is dynamic Stark shift or AC Stark shift.

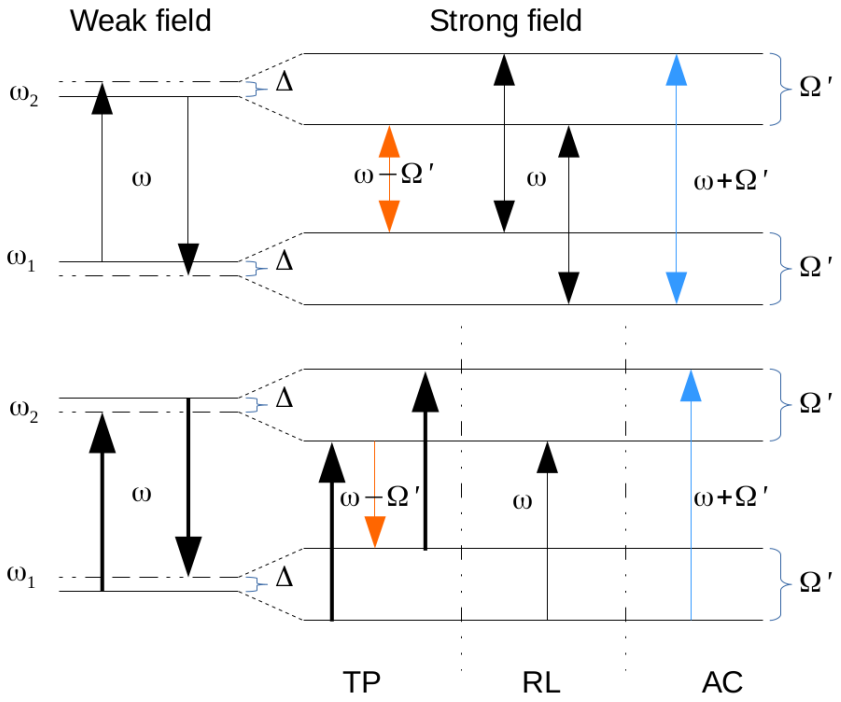

Figure 2.3: One-photon two-level system with external electric fields: Left-weak field; Right-strong field.

The Stark shift effect is named after J. Stark, who discovered it in 1913.[75] Originally, the Stark shift was found with DC electric field applied. In 1955, S. Autler and C. Townes found a new Stark effect in their experiment with two electromagnetic fields on gas carbonyl sulfide(COS), when the frequency of the radio-frequency(rf) electric field is near the transition frequency of the energy levels, the single absorption line becomes two separated lines, and the separation of the two lines is rf wave intensity dependent.

With the energy levels split into two sub-levels separated by the Rabi frequency, photons with new frequencies will be produced. In figure 2.3, when the applied field is weak, the two-level system is not changed but with a small detuning of Δ, here we used positive detuning with $\Delta>0$ for the upper plot, and negative detuning for the lower part. However, once the applied field becomes stronger, each of the energy levels is split into two sub-levels. After the splitting, two extra transition frequencies with the new components that each of them has a Rabi frequency shift, $\omega\pm\Omega'$, occur. By changing the pump-probe detuning δ, the phenomena of frequency absorption and emission are observed.[76,77] These phenomena can be explained with the Rabi frequency shift. As shown in the lower part of figure 2.3, the emission of a Stokes photon can be achieved by the transition of the state through the three photon resonance, marked as TP in the graph. The absorption of an anti-Stokes photon is caused by the AC Stark effect. The middle one labeled as RL is the regular Rayleigh scattering.

2.4 Description of the multi-frequency Raman generation

At the beginning, Raman scattering found major applications in Raman spectroscopy as a spectroscopic technique used to observe vibrational, rotational, and other low-frequency modes in a system[78]. It plays an important role in the spectroscopic applications as it can bypass the one-photon forbidden transitions. The technique has its limitation as the spontaneous Raman scattering is very weak. Such that, an intense *LASER* is needed, although this may introduce other problems, for example, damage to the materials. Then came Coherent anti-Stokes Raman spectroscopy(CARS) and Coherent Stokes Raman spectroscopy(CSRS), which used a second seed beam to enhance the signal output[79].

MRG is frequently observed in SRS experiments. Under the phase-matching condition, the Raman orders are usually produced with different angles. However, in 1981, F. R. Aussenegg et al., showed in

both theory and experiment that MRG can occur in a collinear way with a small phase mismatch.[80] A.Z Grasyuk and the co-workers studied the parametric generation of anti-Stokes Raman orders in both theory and experiment, with an external Stokes beam crossing the pump beam at an angle to meet the phase-matching condition, and achieving an efficiency of 11%[81]. Later, L. L. Losev et al., obtained 7 anti-Stokes and 6 Stokes in their parametric generation with hydrogen. Energy conversion efficiency up to 20% is reached for the first four Stokes, and $2^{-n}\times 20\%$ for the nth anti-Stokes.[82] In 1989, T. Imasaka saw more than 40 vibrational and rotational Raman orders by focusing a two-colour laser beam into pressurized hydrogen.[46] The two-colour laser beam was first accidentally achieved by an amplified ASE signal. Later, they realized that the rotational and vibrational Raman orders were generated simultaneously. By optimizing the gas pressure, beam polarization, and focusing condition, they were able to generate either vibrational or rotational Raman orders.[83] With the generated Raman spectrum consisting coherent equildistant frequencies, S. Yoshikawa and T. Imasaka proposed a new method to generate ultra-short pulses. Their simulation showed that pulses with duration of 1.4 fs can be produced.[84] To put it into practice, they suggested four requirements to be met, ie. a high-power transform-limited pulse, a two-colour laser beam with linear polarization, phase-locked multi-frequency laser beam, and no phase change from other nonlinear effects. From then on, MRG became a potential technique for the generation of ultra-short pulses.

The term “Multi-frequency Raman Generation” was first used in 1994 by McDonald as referring to the multiple high Stokes and anti-Stokes orders generated in the two $\mathcal{LASER}$ beams coupled SRS process, as more than 40 Raman orders are predicted in their Raman scattering experiment with H_2 gas[85]. MRG can be seen as a cascaded SRS process. As shown in Figure 2.4, molecules are activated from the ground energy level to a virtual energy level by the pump beam. Coupled by the Stokes beam, the molecular energy will come down to the Raman energy level instead of the ground level. The molecules in the Raman level can be pumped again by the pump beam to a new virtual energy level. Thereafter, the molecule goes all the way down to the ground energy level by releasing a new photon with higher frequency, the first anti-Stokes Raman order. As the first anti-Stokes photons accumulate, they will act as a new pump beam, and takes the molecule to higher virtual energy level. The returning of the molecule to the ground energy level will generate the second anti-Stokes Raman order. This process will continue and cascade, resulting in a wide discrete spectrum separated by the Raman frequency of the material used. As a cascaded SRS, each of the generation of the Raman orders is a third order nonlinear process ($\chi^{(3)}(\omega_i+\omega_R;\omega_i,\omega_i-\omega_R,\omega_i)$, where ω_i is the i-th anti-Stokes order).

Generally, like Raman scattering, MRG can happen in gas, liquid, and solid Raman materials. As the dispersion of the Raman material plays a critical role in MRG process, small dispersion materials like gases are the most widely used Raman medium. Thus, we will mainly focus on MRG in gases. We will also talk about the studies with solid Raman materials, since the use of angle crossed pump-probe beam together the significant higher Raman gain can help to produce large numbers of Raman orders even with high dispersion.

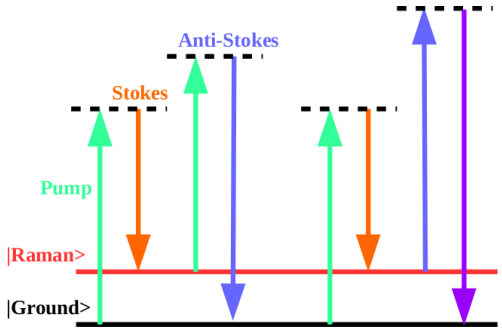

Figure 2.4: Diagram of Multi-frequency Raman Generation

Depending on the pump pulse duration, MRG works in three regimes, adiabatic regime, transient regime, and impulsive regime. In the adiabatic regime, the pulse duration is longer than the dephasing time of the molecules, which, for most of the cases, is around 1 ns. In the transient regime, the pulse duration is less than dephasing time but longer than the molecule's vibrational period, which is at the scale of 10 fs. If the pulse duration keeps decreasing and becomes comparable or even less than the vibrational period, then we have the impulsive regime. Good review articles on the works done in MRG in the three regimes can be found in F.C. Turner's thesis[86] and D. Strickland's review paper on MRG[87].

2.4.1 MRG in the adiabatic regime

During the early days, researchers worked mainly in the adiabatic regime as it was more theoretically studied in that regime. Nanosecond pulses are applied in this regime. The bandwidth of the pump is much smaller than the Raman line width.

Due to the small magnitude of the $\chi^{(3)}$ process and the difficulty of the phase matching condition, the nonlinear conversion rate stays low. In the later 1990s, Harris' group studied the SRS and found a good way to increase the energy conversion efficiency by creating a large nonlinear polarization. They used the electromagnetically induced transparency(EIT) to prepare a near-maximal atomic coherence for the

Raman transition, and the phase matching is achieved with a small detuning between the two pumps.[88] It turned out that the EIT method can be easily done by applying two beams with frequency separation slightly bigger than the Raman transition, and the intensity is high enough such that the Rabi frequency can over weight the inhomogeneous linewidth of the transition. The coherence of the transition can reach up to the maximum value of $|\rho_{ab}|=0.5$.[89] With the phase-locked wide Raman spectrum, A. V. Sokolov et al., suggested that sub-fs pulses can be formed with the spectrum generated from MRG process. Their simulation shows that a pulse train with pulse duration of 0.21 fs and separated by 11.1 fs can be achieved with the Raman spectrum from D_2[90], and within couple of months they suggested another way of using the rotational spectrum of H_2 which can led to pulses with 0.5 fs duration at a separation of 94 fs[91]. Later, they investigated the effects of phased($\delta=\omega_R-\omega>0$, where ω_R is the Raman frequency, and ω is the frequency separation of the two coupling pulses) and anti-phased($\delta<0$) of the Raman transition in D_2. The results showed that the Raman orders are maximized at the phased situation, and they addressed it as a result of the AC Stack shift. Yavuz, et al., studied the off-resonant Raman generation with rotational transitions. A spectrum of 37 coherent Raman orders spanning from 1.37 μm to 353 nm was observed and they also saw the number of Raman orders reaches the maximum with phased pumping.[92] Walker and co-workers studied a type of Raman self-focusing and defocusing in MRG process, and showed that the focusing occurs when the pumps are phased, and defocusing appears when they are antiphased.[93] To put it into practice, A. V. Sokolov and coworkers obtained a pulse train with duration of 3.7 fs separated by 11.1 fs by using only 3 sidebands of the Raman spectrum from D_2.[94] They also showed that the phase of the generated Raman sidebands has a π phase change when the input frequencies are switched between the phased and anti-phased cases. In 2004, M. Y. Shverdin, et al., synthesized seven Raman orders ranging from 1.56 μm to 410 nm and generated pulses with duration of 1.6 fs and peak power of 1 MW[50]. The large number of the pulses under one pulse train makes the peak power for each of the pulses at a relatively low level. S. E. Harris and coworkers then proposed a Raman technique for single-cycle pulses generation. They combined the rotational transition of D_2 and H_2, and with around 40 Raman orders for each of them, the total Raman orders are synthesized to single-cycle pulses with average peak power enhanced to 1600 times and pulse separation of 1.74 ps.[95] In 2006, S. Sensarn and coworkers then extended MRG experiments to a gas-filled hollow fibre.[96] With pump pulse energy of 2.8 mJ, and by optimizing the gas pressure, they obtained 12 Raman orders from 1.56 μm to 254 nm. S. W. Huang and his colleagues took the Doppler broadening effect into consideration in their MRG study with room temperature H_2,

and showed that Dicke narrowing helps to minimize the destructive effect from Doppler broadening.[97] In 2008, W. J. Chen and the co-authors used near Fourier transform limited lasers centered at 602 nm and 802 nm to do MRG experiment. The generated spectrum can be synthesized into ultra-short pulses with constant carrier-envelope phase. They were able to generate pulses with duration of 0.44 fs with 7 Raman sidebands.[98] Then, Z. M. Hsieh et al., demonstrated a method for controlling the carrier envelope phase of the synthesized pulses by using the fundamental frequency and its SHG to couple the Raman level of the H_2.[99] H. S. Chang and coworkers showed that they are able to synthesize arbitrary shape of attosecond optical waveforms with the Raman sidebands from MRG in H_2 that have a controlled carrier envelope phase.[100]

In 1999, F. L. Kien et al., studied the generation of sub-fs pulses with molecular coherence control of MRG. Their studies found that the anti-phased and phased MRG have different behaviours toward dispersion, and showed that the coherence is higher for the negative side of the detuning. A negative detuning that is about equal to the two-photon Rabi frequency will produce a broadband Raman spectrum with good pulse compression. They carried out a simulation with solid hydrogen, and showed trains of pulses down to 0.3 fs duration can be generated.[101] In 2002, L. L. Losev and coworkers showed a multipass design to increase MRG efficiency.[102] In their experiment, simple devices such as prisms and lens were used to set up a four-pass cell for an MRG experiment with hydrogen. With one pump beam at 532 nm, 80 mJ, and 3 ns, they were able to generate Raman lines from 450 nm to 830 nm. K. Yoshii and the colleagues reported a novel way to generate attoseconds pulses by placing a few thin dispersive materials with different thicknesses.[103] Their simulation shows that 728 attoseconds pulse can be generated with MRG spectrum from parahydrogen. The technique is based on the pulse compressing method proposed by N. K. Berger et al., where no propagating through a dispersive delay line for the compression of periodic optical pulses is needed. Instead, a superposition of replicated and time-delayed original pulse trains is required.[104] Later, they experimentally demonstrated the method by tilting the fused silica glass plates, and obtained Fourier Transform limited pulses train with duration of 1.78 fs.[105]

2.4.2 MRG in the impulsive regime

In the impulsive regime, femtosecond pulse is applied in MRG experiment. The pulse bandwidth is sufficient to cover the Raman frequency separation. Hence one pump pulse is good enough to couple to

the Raman scattering transition. Early theoretical and numerical work has shown that this regime is promising for the generation of half-cycle pulses[106]. In 1998, G. Korn et al., demonstrated the first MRG experiment in the impulsive regime. Their experiment with SF_6 showed that the generated spectrum appears as a continuous self-conversion of the pulse spectrum towards lower frequencies, and leads to the generation of a single-cycle pulse.[107] A hollow fibre of 250 micrometer in diameter and 72 cm long is used to enhance MRG process. The results showed that the continuity of the spectrum is pump-pulse-duration sensitive, and it disappears when the pump pulse becomes longer. A big drawback of working in this regime is that many other nonlinear effects caused by the high intensity beams, such as self-phase modulation and self-steepening are completing each other. These effects will reduce the efficiency of the Raman scattering and will also broaden the spectrum[108,109]. During MRG experiment with a 30 fs pump pulse pumping the SF_6 gas, A. Nazarkin and the co-workers sent another weak probe pulse along with the pump with some time delay(typically, a few 100 fs) to reduce the other nonlinear effects. By optimizing the gas pressure, they obtained MRG with efficiency up to 100%, and they showed that the mutually coherent Raman orders can be synthesized into sub-fs pulses.[110] Later, with positive GVD compensation, M. Wittmann et al., demonstrated a method for the generation of fs pulses with the spectrum generated in the impulsive region.[111] They carried out the experiments with SF_6, H_2, and N_2, and pulses down to 5.8 fs have been produced. Having the idea that the hollow fiber can not only enlarge the interaction length, but also match the group velocity, A. Nazarkin et al., did a study on MRG orders corresponding to the hollow fibre wave guide specifications. By changing the diameter and the pressure, they were able to optimize MRG process to increase the number of the high order Raman generation. The broader MRG spectrum can be synthesized into attosecond pulses. It has been shown that in the impulsive regime, sub-4 fs pulses can be generated with SF_6 as the Raman material[112].

Compared to MRG in the adiabatic regime, the stimulated Raman scattering efficiency in the impulsive regime is much lower as the pump energy is not fully used in coupling the transition of the Raman levels.

2.4.3 MRG in the transient regime

Between the adiabatic and impulsive regimes, we have the transient regime, where the pump duration is shorter than the dephasing time but longer than the molecular vibrational time. Typically, the pump duration is about 1 ps. Working in the transient regime might be a good choice for high-energy pulses,

as in this regime, the unwanted nonlinear effects can be highly reduced, while the resonant process of Raman scattering can still have high efficiency. Besides, the compressed pulse train is shorter as compared to that in the adiabatic regime. With fewer pulses within one pules train, each of the pulses will have higher energy. The steady-state SRS theory cannot explain effects such as the asymmetry of the forward and backward Raman scattering, and the sharp decrease of the SRS efficiency in liquids. The transient theory of SRS takes into account the dispersion of the media and the relaxation time.

G. S. McDonald, et al., used a transient model for the Raman scattering in H_2 gas with identical shape of the pump and the Stokes pulse, and predicted the generation of more than 40 Raman orders, spanning a bandwidth greater than the pump frequency[113]. He then discovered that in MRG process, a large number of long-lived solitons are generated spontaneously.[114] E. Sali, et al., demonstrated an experimental scheme and increased the efficiency of the generation of high-order Raman sidebands and the excitation of coherent molecular vibrations in a highly transient regime with two-colour pumping[115]. They carried out the experiments in both hydrogen and methane with pump pulse duration at 250 fs and 400 fs. The results confirmed that two pump pulses can significantly increase the number of Raman orders. Also, with lower air pressure, they can significantly decrease the SPM effect. The generated spectrum was sufficient to support the generation of sub-fs pulses. With higher air pressure and shorter pump pulse applied in their experiment, the Raman spectrum may form an isolated single-cycle pulse. F. Tani et al. generated Raman spectrum ranging from 180nm to 2400 nm, by sending 300 fs pump pulse into hydrogen-filled hollow fibre. The spectrum is broadened by both Kerr and Raman related self-phase modulation[116].

L. Losev collaborated with D. Strickland to do MRG experiments in both solid and gas. The experiment with a high gain Raman media of $KGd(WO_4)_2$ was the first MRG experiment in the transient regime. The experimental results show that in the solid medium the dispersion and Self Phase Modulation(SPM) greatly decrease MRG process such that the number of Raman orders generated collinear to the pump is way fewer than what is predicted by the steady-state theory of MRG[117]. Later, a collaboration of performing MRG experiment with Sulphur Hexafluorine gas in hollow fibre was carried out. With two beams coupling the A_{1g} vibrational Raman energy levels, up to 25 Raman orders with spectrum ranging from 1.37 micrometer to 425 nm were generated in their experiment[118]. Also, the experiment showed that the Raman scattering is much more efficient on the anti-Stokes side than the Stokes side, with about 4 times more anti-Stokes orders. Besides, the higher anti-Stokes Raman order starts to form a plateau structure, which may benefit the generation of ultra-short pulses. Later, F. C.

Turner and D. Strickland continued MRG experiment in a low dispersion region, where a 1.0 m long hollow fibre with inner diameter of 0.129 mm was used to increase the interaction length, and also to compensate the positive dispersion introduced by the gas. D. Strickland's group predicted that the generated spectrum from MRG with SF_6 has the potential to produce a train of pulses with duration of 2.8 fs and pulse energy of hundreds of micro joules[119].

2.4.4 MRG in the solid-state materials

Phase matching is essential for MRG process. In gases, the dispersion is small and hollow fibres can be used to confine the beam and to compensate the material dispersion. Thus, MRG in gases will result in a long interaction length. For solid-state medium, the high dispersion makes it impossible to propagate in a collinear fashion. However, the orders higher Raman gain is encouraging. The first solid medium that came to mind is solid hydrogen as it has the advantages of high molecular density, short medium length, small dephasing rate, and small dispersion. N. H. Shon et al., presented a numerical model for MRG in solid hydrogen pumped by two nanosecond-duration pulses. By optimizing the tilt angle between the pumps, their simulation showed that they can either obtain a broadband Raman spectrum that can be used to synthesize sub-fs pulses, or have the pump pulse converted into a single high Raman order to implement an efficient frequency up conversion.[120]

In 2003, A. S. Grabtchikov et al., studied SRS in $KGd(WO_4)_2$(KGW) in the impulsive regime with a pump pulse of 70 fs duration[121]. Inserting the pump at an angle of 15 degrees into a 4 mm long KGW, they observed 2 anti-Stokes and 1 Stokes orders. Later, broadband spectra were generated in various solid-state Raman active media, such as $YFeO_3$, $SrTiO_3$, $KNbO_3$, and TiO_2. In 2006, M. Zhi and A. V. Sokolov inserted two 50 fs pump into $PbWO_4$ with different cross angles.[122] Up to 20 anti-Stokes and 2 Stokes Raman orders are obtained. The most effective conversion of MRG occurs when the cross angle is 4 degrees. They observed that the change of the cross angle can not only affect the efficiency of the process, but also the separation between the Raman orders. With fixed cross angle, they changed the frequency separation of the pumps. At very large detuning, the anti-Stokes beam splits into two separated beams with one coming from the Four Wave Mixing and the other from Raman scattering. The overall efficiency of MRG in $PbWO_4$ can be up to 31%. They also showed the generated Raman orders are mutually coherent.[123] However, the applied pulses were short and intense, and some other unwanted nonlinear effects occurred along with MRG process that will decrease the efficiency of

MRG, such as SPM and self-focusing. M. Zhi and A. V. Sokolov continued the investigation of MRG in crystal $PbWO_4$ with two time delayed linearly chirped pulses with pulse duration ranging from 100 fs to 2 ps. The frequency difference between the two pulses is the instantaneous frequency difference and can be changed as the change of the time delay between the two pump pulses. By changing the insertion angle between the two pumps and optimizing the time delay, they were able to excite MRG with different Raman modes. Up to 40 anti-Stokes and 5 Stokes Raman orders have been achieved with MRG working in the Raman mode of frequency 191 cm^{-1}. The measured energy conversion efficiency goes up to 41% of the pump energy and 21% of the Stokes.[124] M. Zhi et al., then carried out a similar experiment with the Raman medium switched to diamond, since diamond has a few advantages for the generation of broadband spectrum. Diamond has a single strong narrow Raman line with high frequency shift at 1332 cm^{-1}, and it is isotropic with index of refraction well studied. Besides, diamond is able to transmit a wide range of spectrum, and has extremely high thermal conductivity. By applying two 50 fs pulses with frequency difference of 1250 cm^{-1}, they observed up to 16 anti-Stokes and 2 Stokes Raman orders. With a third probe beam, they observed multiple new orders that come from four wave mixing between the probe and the pump, the probe and the Stokes, and even six wave mixing from the pump and the probe. Their experimental results showed that the phase matching angle has a much larger effect on the frequency difference between the Raman orders than from the Raman resonance. The large dispersion of the solid medium and the phase matching technique of cross angled pumps led to the output of the Raman orders propagating at different angles, although the frequencies of the Raman orders are not having the same frequency difference, they are linear as a function of the output angle. Hence, they used a prism and a spherical mirror to combine the output Raman orders in both space and time. By combining 5 Raman orders from MRG in diamond, and using an acousto-optic pulse shaper to optimize the phases, they obtained pulses with duration down to 5 fs.[125] By focusing an 8fs pulse into diamond, C. Lu and the co-authors found that the Raman assisted four-wave mixing process can generate a coherent continuum spectrum that can be used to synthesize an isolated single-cycle pulse[126]. K. Wang and coworkers introduced a novel design to enhance MRG process by reflecting both the pump beam and the Raman sideband beams back to the Raman material. With the double-path configuration, they were able to generate a wider Raman spectrum[127]. A. Zhdanova and the co-authors demonstrated a scheme of combining six coherent Raman spectrum orders, and succeeded in synthesizing an isolated 5 fs pulse in the visible range[128,129]. Instead of using a spherical mirror, each of the Raman orders is aligned to an individual path, where phase control and time delay of each Raman order are manipulable. Dichroic mirrors are used in the combination of the Raman orders. An

interferometric cross FROG that combined the cross FROG and interferometric FROG is applied in the pulse measurement. With the adaptive optics to optimize the wavefront, M. Shutova et al., has shown that the technique is capable to improve the overall efficiency and can increase the power of the high-order sidebands[130].

2.4.5 MRG in the Photonic Crystal Fiber(PCF)

MRG experiments have been carried out in different forms of materials, gases like H_2, CH_4, and SF_6; liquids such as water, liquid helium, and liquid hydrogen; solids of diamond, solid hydrogen, and $KGd(WO_4)_2$. It has been a long journey for the research community to get the nonlinear effect of MRG maximized while the other unwanted effects are suppressed. Some of the main aspects are high Raman gain factor (solid), good optical quality with low dispersion (gas), and long interaction length and low pump power (hollow fibre). To increase the efficiency, researchers have combined some techniques together. A few of the widely used methods are inserting the pump beams at an angle to fulfil the phase matching condition in solid and using gas filled hollow fibre or a gas filled high finesse Fabry-Perot cavity[131] to guide and confine the pump beams for better interaction.

The hollow core photonic crystal fibre is introduced and developed to increase MRG efficiency. Compared with light travelling in a conventional hollow fibre, light in the hollow core PCF is trapped by a two-dimensional photonic band gap.[132] In theory, the light can be guided in a single transverse mode without any loss. The hollow core PCF has big advantages over the hollow fibre, especially when the hollow core is small, over 10000 times more effective. F. Benabid and coworkers carried out MRG in hollow core PCF. They found that the thresholds of the Stokes and anti-Stokes are sharply reduced to 800 nJ and 3.4 mJ, respectively. A pump to Stokes conversion efficiency of 30% is achieved.[133] Later, they tried a similar experiment with a narrower bandwidth and much lower transmission loss. In addition, they used a circularly polarized *LASER* pump beam to enhance the generation of the rotational SRS, and a 92% quantum conversion efficiency was reached with the threshold of energy sharply decreased to 40 nJ for 2.9 m of fibre.[134] The decreasing of efficiency of MRG is also due to the phase mismatching of the beams. B. M. Trabold and the colleagues used a mix of fundamental and high-order modes to compensate the dispersion and achieved a conversion efficiency of 5.3% to the first anti-Stokes[135].

F. Couny et al., demonstrated the generation of a Raman spectrum with wavelength spanning from 325 nm to 2300 nm in PCF filled with H_2.[136] Instead of the photonic band gap, the PCF in their experiment is designed according to a new photonic guidance, the Von Neumann-Wigner bound states[137]. With only a single *LASER* of pulse duration of 12 ns at 1064 nm and with peak power less then 40 kW, a spectrum of 45 Raman orders can be observed. The use of PCF would enable the generation of sub-fs pulses with significantly lower power pumps. With similar setup, but a much lower loss, A. Benoit and the colleagues achieved a generation of wide spectrum ranging from 321 nm to 12.5 micrometer by using a shorter *LASER* pump at 27 ps centred at 1030 nm with average power of 22.7 W.[138]

2.5 Theory of MRG

MRG can be seen as a cascaded SRS. Thus the theory of the SRS can be directly applied to understand MRG process. The coupled-equation of 2.2-6 still holds, but needs to be modified. In 1978, a Raman effect with high efficiency of Stokes and anti-Stokes from hydrogen gas was observed. The phenomenon can not be explained by the existing theories. A few years later, in 1981, early theoretical treatments based on multi-wave approach were developed. In these works, MRG process is treated with small molecular excitation. Instead of using only the pumps, Eimerl et al., suggested that in the process, all the Raman orders are mutually coupled together.[139] They treated the Raman orders as a group of parallel monochromatic plane waves travelling through a dispersionless Raman medium together. However, the calculated conversion rate is still orders less than that was observed in experiment. Hickman et al. generalized the theory described by Eimerl et al., by taking the fully molecular excitation into consideration[140]. They depicted the propagation of the process with a set of frequency components $\omega_j = \omega_0 + j\,\omega_R$, and described the interaction of the fields with the two-photon Bloch equation. The electric field is given as

$$\epsilon(z,t) = \sum_j E_j(z,t)\, e^{i(\omega_j(t - z/c) + \phi_j)} \quad (2.4\text{-}1)$$

With the multi-wave electric field above, and using $V_j = E_j e^{i\phi_j}$ they solved the two-photon Bloch equation, and obtained a set of coupled equations for the field amplitudes written as

$$\frac{\partial V_j}{\partial z} = \frac{\pi \rho \alpha_{12} \omega_j}{c} [q^* V_{j+1} - q V_{j-1}] \quad (2.4\text{-}2)$$

here ρ is the number density of the molecules in the ground state, α_{12} is the transition coefficient, and q is defined as in equation

$$\frac{\partial q}{\partial t}=\frac{\alpha_{12}}{2\hbar}\sum_j V_j V_{j-1}^* e^{i\theta} \quad (2.4\text{-}3)$$

Then, they obtained the coupled-equation for the electric field that given as

$$\frac{\partial E_j}{\partial z}=\frac{\omega_j}{2\omega_R}\frac{\partial \Omega}{\partial z}\sqrt{(\Omega^2+B^2)}(E_{j-1}-E_{j+1}) \quad (2.4\text{-}4)$$

where Ω is the Rabi frequency and B represents the initial condition. The Rabi frequency is given by

$$\Omega e^{i\theta}=\frac{\alpha_{12}}{2\hbar}\sum_j V_j V_{j-1}^* \quad (2.4\text{-}5)$$

With generalized Rabi frequency, detuning, and intensity given by

$$\Omega'^2=\Omega^2+\Delta^2 \quad (2.4\text{-}6)$$

$$\Delta=\frac{\partial\theta}{\partial t}+\frac{2\pi(\alpha_{22}-\alpha_{11})I}{\hbar c}+\delta\omega \quad (2.4\text{-}7)$$

$$I=\frac{c}{8\pi}\sum_j V_j V_j^* \quad (2.4\text{-}8)$$

the V_j is the amplitudes of the jth Raman order, α_{ij} is the transition moments, and $\delta\omega$ is the detuning between the frequency separation of the pumps and the Raman frequency. As can be seen from equation 2.4-5, the Rabi frequency Ω is related to the generation of the adjacent amplitudes. The equation 2.4-8 shows that the intensity "I" is related to the total intensity of the beam, including all the Stokes, anti-Stokes, and the pump pulses. From equation 2.4-6, the detuning Δ is determined by three terms, Raman frequency detuning $\delta\omega$, overall rate of change of phase θ , and the intensity. The overall phase is determined by the phases of the pump, the coupling Stokes order, and also the time delay between the two. The coupled equations 2.4-4 are used to describe MRG, but so far it seems impossible to get an analytical solution. Instead, A. P. Hickman and the colleagues ran a numerical simulation, and the results show a significant energy conversion to high anti-Stokes Raman orders with up to 40% energy is converted to the anti-Stokes Raman orders.

Hickman continued MRG theory study by taking consideration of the phase mismatching, Δk .[141] With the momentum mismatch, the new electric amplitude becomes

$$F_j(z,t)=e^{i\Delta k_j}V_j(z,t) \quad (2.4\text{-}9)$$

similar to equation 2.4-2, the new field amplitudes coupled-equation is then written as

$$\frac{\partial F_j}{\partial z}=\frac{\pi\rho\,\alpha_{12}\,\omega_j}{c}\left[e^{-i\Delta_{j+1}z}q^*F_{j+1}-e^{i\Delta_j z}qF_{j-1}\right] \quad (2.4\text{-}10)$$

where q can be calculated from

$$\frac{\partial q}{\partial t}=\frac{\alpha_{12}}{2\hbar}\sum_j F_j F_{j-1}^* e^{-i\Delta_j} \quad (2.4\text{-}11)$$

and the composite momentum mismatch term is given as

$$\Delta_j=\Delta k_j-\Delta k_{j-1}-(\Delta k_0-\Delta k_{-1}) \quad (2.4\text{-}12)$$

They calculated and discussed the situations with two limits, out of phase matching, $\Delta k\to\infty$, and perfectly phase matching, $\Delta k=0$. In the perfect phase matching case, the seed Stokes Raman pulse is amplified at the beginning but suppressed once the anti-Stokes Raman pulse becomes stronger. When the phase mismatching is large, the Stokes Raman pulse is amplified all along the process, and the effects from anti-Stokes Raman pulse is reduced and becomes ignorable.

Following Hickman's work, in 1993, L. L. Losev et al. presented a theory in the steady-state Parametric Stimulated Raman Scattering(PSRS), where they also considered an interaction of an infinite number of plane collinear light waves. Their numerical calculations showed that the total width of the region occupied by the components of the SRS with intensities comparable in order of magnitude is equal to the pump frequency when using bi-harmonic pump with equal intensity[142]. Later, G. S. McDonald and his colleagues presented a model calculation of MRG in H_2 in the transient regime. The results showed the output bandwidth is wider than the pump frequency.[143] In 1996, L. L. Losev and A. P. Lutsenko presented a PSRS in a highly transient regime(transient regime but close to the impulsive regime) with the absence of dispersion. The simulation showed that the maximum bandwidth generated by PSRS is approximately 1.4 times higher than the carrier frequency[144].

Syed and the co-authors generalized the theory of MRG by taking into account of the beam-propagation effects from intensity, phase quality and width of the input beams and the length of the Raman medium[145]. Similar to equation 2.4-10, but a transverse term is added, thus

$$\frac{\partial F_j}{\partial z}-\frac{i}{2k_j^0}\nabla_t'^2 F_j=\frac{\pi\rho\alpha_{12}\omega_j}{c}\left[e^{-i\Delta_{j+1}z}q^* F_{j+1}-e^{i\Delta_j z}q F_{j-1}\right] \quad (2.4\text{-}13)$$

where $\nabla_t'^2$ is the transverse Laplacian, and $k_j^0=k-\Delta k_j$. The q is defined by

$$\frac{\partial q}{\partial t}=-\frac{q}{T_2}+\frac{\alpha_{12}}{2\hbar}\sum_j F_j F_{j-1}^* e^{-i\Delta_j} \quad (2.4\text{-}14)$$

here T_2 is the dephasing time of the Raman medium. Simulation with both 1D and 2D transverse beams has been conducted and the results showed that the beam diffraction decreases MRG efficiency, while the focusing character or the phase quality of the pump beam has little effects on MRG.

Sali et al. carried out experiments and obtained high conversion efficiency of the pump energy to Raman orders with a very broad spectrum, and their numerical simulation based on a semi-classical model can reproduce with good accuracy matching with the experimental results as far as the efficient generation of high order MRG Raman orders is concerned[146]. A Cauchy dispersion model was applied in their simulation, while they did not take the $\chi^{(3)}$ effects such as four-wave mixing and self-phase modulation into consideration.

Based on the multi-wave propagating idea, the coupled equations of 2.4-2, 2.4-10, 2.4-13 and their corresponding models have been developed to explain MRG process. However, since the infinite number of plane waves were used, the coupled-equations are too complicated to get analytical results. Even in experiments, tens or even hundreds of Raman orders have been observed. Most of the theoretical treatments went with numerical simulations for the calculation of the results.

2.6 The red-shifted spectrum of Raman orders

As the great grand goal(GGG) of making high-energy few-fs pulses leads the way, a series of MRG experiments have been carried out in the transient regime in D. Strickland's lab. In the studies of improving MRG process, a novel phenomenon occurs with red-shifted spectrum showing up on each of the anti-Stokes Raman orders[147]. The red-shifted spectrum in Raman orders are also seen in other

groups' experiments, but no further discussion was given. We are interested in what the red-shifted spectrum is, where it comes from, how it is produced, and whether it will benefit our final ultra-short pulse generation. As the interest leads the way, from then on, MRG project in D. Strickland's group focuses on the study of the red-shifted spectrum. Before diving into the experimental results, let's get familiar with how the experiments are carried out.

In the experiments, two beams of pulses are generated with our dual-wavelength amplification system. Two pulses, the pump and the Stokes, are stretched and imperfectly compressed to leave a linear chirp with chirp rate around 1.5 THz/ps. As in Figure 2.5, in the frequency vs time diagram, when timed together, the pump pulse(deep red) and the Stokes pulse(orange) has an instantaneous frequency separation of 23.25 THz. The frequency separation is chosen to match the Raman frequency of SF_6. During experiments, we can easily change the time delay between the two pulses, and that will change the instantaneous frequency separation. When the pump pulse is 1/3 ps in advance of the Stokes pulse, the two pulses are blue-tuned and the instantaneous frequency separation becomes 23.75 THz.. For the red-tuned cases, the two Stokes pulse is 1/3 ps ahead of the pump pulse, and the instantaneous frequency separation is reduced to 22.25 THz.

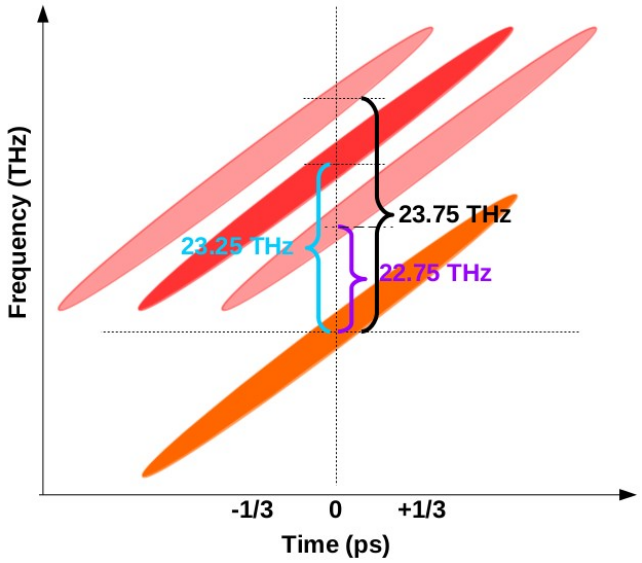

Figure 2.5: Instantaneous frequency separation of the pump(red and pink) and Stokes(orange) vs time delay, both of them have a linear chirp rate of 1.5 THz/ps.

Z. Cui, et al., studied MRG with tunable instantaneous frequency separations, in which both positively and negatively chirped pulses have been applied.[33] The red-shifted spectrum appears with red-tuned pumps and disappears as the pumps are blue-tuned. Blue-shifted spectrum that may come from four-wave mixing is observed only when the centre-frequency separation of the two pumps is much larger

than the Raman frequency. The results indicate that the red-shifted spectrum may come from Stark shifting rather than four-wave mixing. Thereafter, H. Yan and D. Strickland continued the study of red-shifted spectrum by carrying out the experiment with different pump energies. Longer pulse durations for the pump and Stokes around 1ps are used to further reduce the SPM effect. The results showed that the amount of red-shifting is intensity dependent, and they suggested that a two-photon dressed states Stark shift may explain the red-shifting process[148].

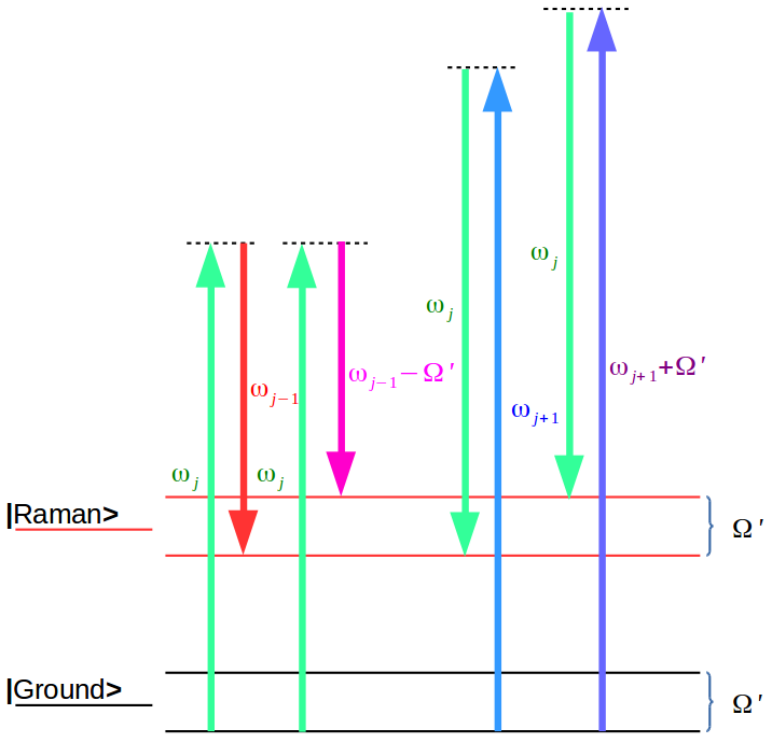

Figure 2.6: Linear Raman scattering in a two-photon dressed states for MRG, showing generations of Raman spectrum(red) and red-shifted spectrum(pink), and absorption of blue-shifted spectrum(purple).

The two-photon optical Bloch equations with multi-frequency have been applied to understand several experiments, and has shown the ability in determining the number of Raman orders.[149,150] However, as seen from the coupled equations 2.3-1, the Raman order frequency components are already set at the beginning of the simulation, and no extra spectrum peaks are allowed to be generated. Thus, it will not answer the question of what our red-shifted spectrum is. Recalling from section 2.3, by extending the one-photon, two-level system in figure 2.3, we have a diagram with two photon dressed system in figure 2.6. As shown in figure 2.6, since most of the molecules are in the ground state, there will be emission of photons with frequencies at Raman peak of ω_j and its red-shifted sideband at frequency of $\omega_j - \Omega'$. The blue-shifted sideband of frequency at $\omega_j + \Omega'$, however, experiences absorption. This two-photon Stark shift may explain that we only see the red shifted spectrum in MRG experiment.

The reason why M. Alharbi and his colleagues observed both red and blue shifted spectrum in each side of the Raman peak[151] is probably that they do not have a lot of Raman orders, and thus a strong absorption for blue-shifted frequency does not occur. However, the reason why we have constant blue shift of all the Raman orders with blue detuned pump and Stokes remains unknown.

To further understand MRG process and the red-shifting mechanism, we need to obtain detailed information about the Raman orders. Thus, the well developed pulse measurement technique, Frequency Resolved Optical Gating (FROG), is applied to measure the pulses generated from MRG experiments.

Chapter 3

Frequency-Resolved Optical Gating

The Frequency-Resolved Optical Gating is the main pulse measurement tool we used in this study. In this Chapter, we will give a simple introduction to the FROG tool. We will start from the description of the auto-correlator as the foundation of the FROG. Some variants of the FROG setup is discussed, and we will use the SHG FROG and cross-FROG in our pulse measurement. A basic FROG algorithm is provided so that we can get the idea of how the FROG works. As we are using a single-shot FROG setup in the lab, a detailed introduction of single-shot FROG setup is provided. Last but not least, we will talk about the data validation for the FROG data. It is essential to have the data checked before any further calculation or analysis.

As shown from the famous horse galloping bet, to clearly see a short event, an even shorter reference timer is required. This raises a problem in the measurement of the shortest ultra-short pulses, as we do not have any shorter pulse with which to measure it. Then, if we can not measure it directly, how can we make sure that it is the shortest pulse? With a second thought, since the pulse is already the shortest, why not just use this generated pulse to measure itself. With this idea, techniques based on self measurement have been invented, auto-correlation, for example. However, the self measurement techniques alone are not able to give a clear image of the pulses, as the measurement will blur the pulses by smoothing out the dips and jumps. In 1991, introduced by Rick Trebino and Daniel J. Kane, the Frequency-Resolved Optical Gating(FROG), which can measure the full information of the ultrashort pulses, including the amplitude of the electric field and the phase[152]. The FROG has been proved to be rigorous and robust, and to work with a wide range of wavelengths, and therefore has become a widely used technique for ultra-short pulse measurement. A well written book by Rick Trebino, et al., describes in detail of the FROG technique. I will follow Trebino's book and talk about the concepts that are used in our experiment setup building, data recording, and data analysis.

As we know, the pulses can be equally described in both time and frequency domain, and the Fourier transform is the connection between them. To make it simple, we will assume that the pulse has Gaussian shape that goes as

$$E(t)=A\sqrt{e^{-4\ln 2\left(\frac{t}{T}\right)^2}}\,e^{-i\phi(t)}e^{i\omega t}+c.c. \quad (3\text{-}1)$$

where A is the amplitude factor of the electric field, T is the pulse duration, $\phi(t)$ is the phase, and ω is the centre-frequency. The c.c. is the complex conjugate term, such that the E(t) is real.

To fully understand a Gaussian shape pulse, we need to know its amplitude, pulse duration, phase, and centre-frequency. However, in a lot of cases, people just interested in the pulse duration. In the following description, we will ignore the rapidly varying term $e^{i\omega t}$ and the c.c. part, such that

$$E(t)=A\sqrt{e^{-4\ln 2\left(\frac{t}{T}\right)^2}}\,e^{-i\phi(t)} \quad (3.2)$$

the intensity is then given as

$$I(t)=E(t)E^*(t)=A^2e^{-4\ln 2\left(\frac{t}{T}\right)^2} \quad (3.3)$$

Figure 3.1 shows a typical ultra short pulse with its intensity, electric field, and amplitude.

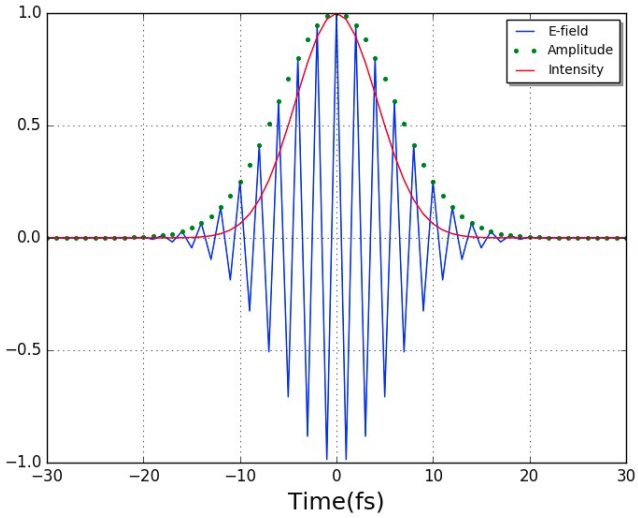

Figure 3.1: Plot for a 10fs pulse with e-field, amplitude, and intensity

3.1 Intensity auto-correlation

As in lots of cases, the pulse duration is what matters and of the greatest interest. Thus the intensity correlation has become a widely used technique to measure the pulse duration. Also, to understand the FROG, the intensity correlation is a good place to start, as they share the same temporal measurement scheme, in which pulses are combined within a nonlinear crystal. Let us begin with a basic auto-correlation optical technique

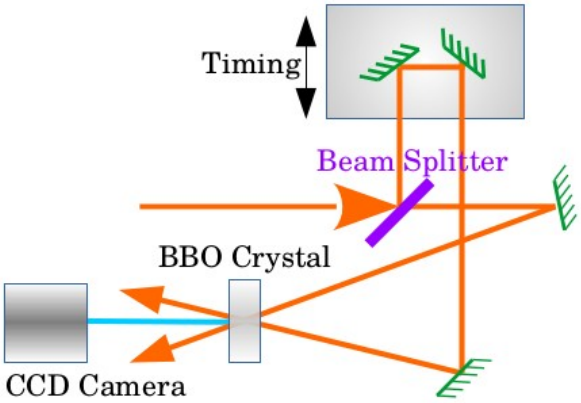

Figure 3.2: Diagram of an auto-correlator with BBO crystal

As shown in figure 3.2, in an auto-correlator, the pulse beam is divided into two parts by a beam splitter, with one beam delay-time changeable, and then both are sent into a nonlinear crystal at a specific angle. The crystal will generate a signal based on nonlinear effect. For simplicity, we will use

the Second Harmonic Generation(SHG), where the electric field of the second harmonic E_{sig}^{SHG} is proportional to the product of the two pump fields as:

$$E_{sig}^{SHG}(t,\tau) \propto E(t)E(t-\tau) \quad (3.1\text{-}1)$$

where τ is the time delay between the two pulses. However, detectors are too slow to catch this rapidly changing signal, instead, it will measure the time integral

$$I_{sig}^{SHG}(\tau) = \int_{-\infty}^{\infty} I(t)I(t-\tau)dt \quad (3.1\text{-}2)$$

Figure 3.3 shows how equation 3.1-2 works with a 10 fs pulse's auto-correlation. Once have the I_{sig}^{SHG}, it becomes an one-dimensional phase-retrieval problem to be solved in equation 3.1-2 for the I(t), which unfortunately is unsolvable. Despite that, some useful information still can be obtained, for example, the Full Width at Half Maximum(FWHM) of the signal. Further more, with an assumption of the pulse shape, most of the time a Gaussian or $sech^2$ shape, we can then calculate the pulse duration. For a Gaussian shape pulse that we use in our calculation, the pulse duration T_{pulse} can be easily calculated as, $T_{pulse} = T_{sig} / \sqrt{2}$, where T_{sig} is the FWHM of the signal.

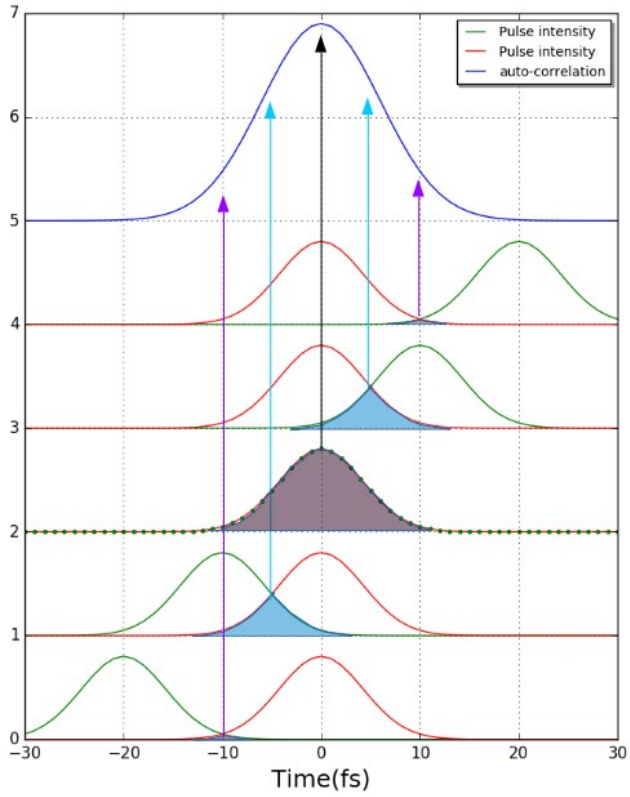

Figure 3.3: Graphical showing of intensity auto-correlation

The auto-correlation of pulses cannot give us the full information of the pulses, neither does the spectrum measurement with a spectrometer. This is because in both cases, a similar unsolvable one-dimensional phase-retrieval problem will occur. A combination of auto-correlation and spectrum have been used to get a better understanding of the pulses, with methods such as Temporal Information Via Intensity[153], Fringe-Resolved auto-correlation[154], and FROG having been introduced and developed.

3.2 Frequency Resolved Optical Gating(FROG)

FROG is a technique that records the information from both the time domain and the frequency domain into a 2D trace, and uses an algorithm to retrieve the electric field from the trace. Rick Trebino analogizes the trace to the musical score, where along the horizontal line is the time and the musical notes are in the vertical position with different frequencies. The FROG measurement is done by spectrally resolving the time-dependent signal output from a correlator. Instead of measuring the energy verses time delay in correlation, a FROG measures the signal's spectrum versus time delay, or the spectrogram of the pulse. Taking the SHG FROG as an example, the signal field is $E_{sig}(t,\tau)=E(t)E(t-\tau)$. By spectrally resolving each temporal measurement of the E_{sig} we are performing an optical Fourier transform of E_{sig}. Because we are measuring the spectral intensity the FROG trace yields the two-dimensional intensity trace $I_{FROG}(w,t)$ given by:

$$I_{FROG}(\omega,\tau)=\left|\int_{-\infty}^{\infty} E(t)E(t-\tau)e^{-i\omega t}\,dt\right|^2 \quad (3.2\text{-}1)$$

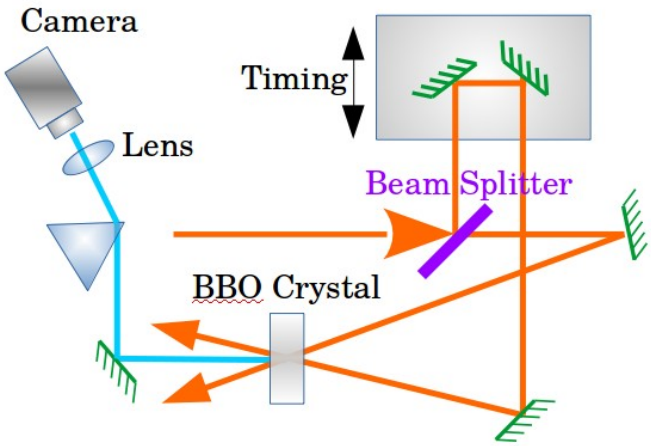

Figure 3.4: Schematic of a FROG setup

The trace $I_{FROG}(\omega,\tau)$ includes both temporal and spectral information of the measured pulse. Figure 3.4 shows a simple FROG setup. Different from the auto-correlator in figure 3.2, the output signal is sent into a device, a prism or a grating, to extract the spectral information. Then, an imaging system is used to record the 2D trace of the signal.

So, with the measured $I_{FROG}(\omega,\tau)$, how to obtain the pulse E(t)? We consider the $E_{sig}(t,\tau)$ as a Fourier transform with respect to τ , that is

$$E_{sig}(t,\tau)=\int_{-\infty}^{\infty}\hat{E}_{sig}(t,\xi)e^{-i\xi\tau}d\xi \quad (3.2\text{-}2)$$

where the $\hat{E}_{sig}(t,\xi)$ is a new defined function, applying equation 3.2-2 to replace the $E_{sig}(t,\tau)=E(t)E(t-\tau)$ term in equation 3.2-1, we can rewrite the $I_{FROG}(\omega,\tau)$ as

$$I_{FROG}(\omega,\tau)=\left|\int_{-\infty}^{\infty}\int_{-\infty}^{\infty}\hat{E}_{sig}(t,\xi)e^{-i\xi\tau}e^{-i\omega t}dt\,d\xi\right|^2 \quad (3.2\text{-}3)$$

Comparing equation 3.2-3 with equation 3.1-2, it is easy to recognize that it is a two-dimensional phase-retrieval problem to be solve, i.e. getting $\hat{E}_{sig}(t,\xi)$ from $I_{FROG}(\omega,\tau)$. At first sight, it can be frustrating, as the one-dimensional phase-retrieval problem is already not solvable, and adding another dimension! However, it has already been proven that the two-dimensional phase-retrieval problem does yield an essentially unique solution with certain additional information provided, such as nonlinear optical constraint[155].

3.2.1 Variants of FROG

Depending on the nonlinear optical effect that is used in the process, the FROG can have different variants, Polarization-gate(PG) FROG[156], Self-diffraction(SD) FROG[157], Transient-grating(TG) FROG[158], SHG FROG[159], Third Harmonic Generation(THG) FROG[160] etc. Each of them have their own geometries and advantages. As illustrated in Figure 3.5, PG FROG is the conceptually simplest FROG variant, where the pulse is split into two, with one pulse, the probe pulse, going through crossed polarizers, while the other(the gate pulse) through a half wave plate or any device to gain a 45 degrees linear polarization rotation. Then, the two pulses are sent through and overlapped in a nonlinear crystal. In the crystal, the gate pulse induces a birefringence through a third order effect, the electronic Kerr effect. The crystal plate then works as a wave-plate and changes the probe pulse's polarization, which

will allow the probe pulse to propagate through the second analyzer. With devices such as prism to resolve the spectrum, the imaging system will record the trace, $I_{FROG}^{PG}(\omega,\tau)$. PG FROG has a few advantages, including easy for the alignment, supporting infinite bandwidth, and free of ambiguities. However, a very high extinction ratio of polarizer is required.

SD FROG is similar to PG FROG but without any polarizer and wave-plate. The beams on the crystal will generate a sinusoidal intensity pattern, and the pattern acts as a grating that diffracts the signal beam to a new direction as shown in the figure 3.5. The SD FROG can be applied in the deep UV region as no polarizer is required. However, the SD is not a self phase-matched process. In order to minimize the phase mismatch, the nonlinear crystal must be kept thin(< $200\mu m$) and the angle between the beams should be small(< 2 degree).

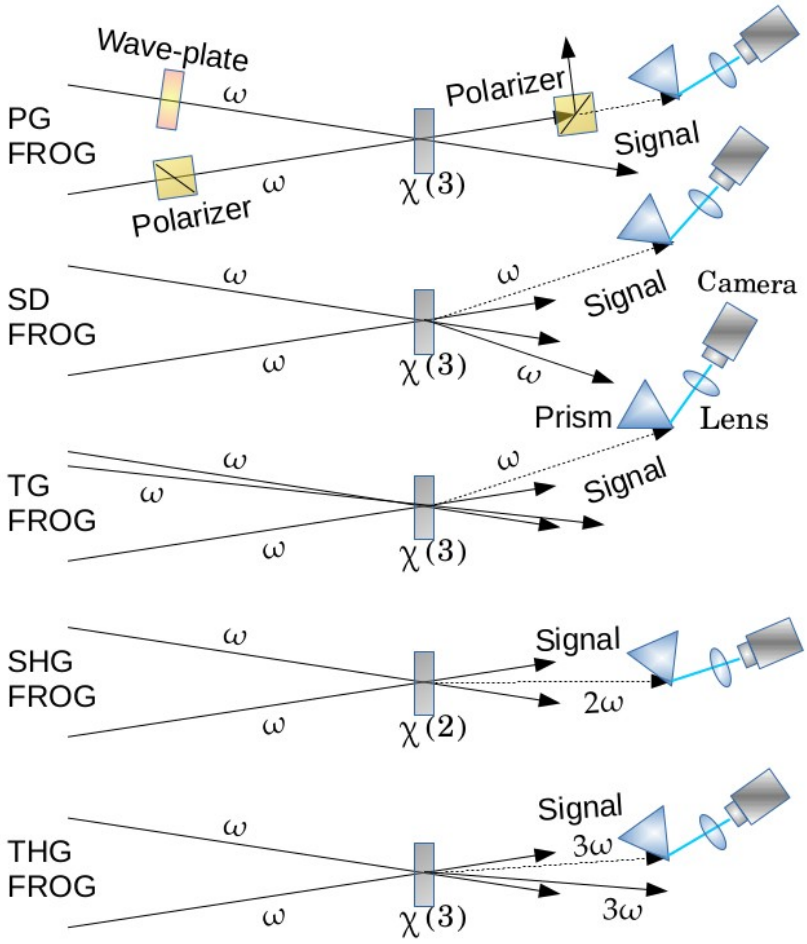

Figure 3.5: Schematic of FROG variants

TG FROG, is a variant that is aimed to be simple but at the same time maintains the phase-matching condition. However, it is a 3-beam geometry such that the original pulse needs to be split into three

parts. Two of the pulses are overlapped in time and space on the optical Kerr medium, similar as the SD FROG, inducing a refractive-index grating. The third pulse is variably delayed and is diffracted by the induced grating to generate the signal for measurement.

SHG FROG uses a $\chi^{(2)}$ process instead of $\chi^{(3)}$. The much higher sensitivity makes it the most widely used FROG variant. There is an ambiguity of the direction of time, but can be removed with extra information. For example, in our measurement of the chirped pump pulse, we already know the chirp of the pulse as positive or negative, and this piece of information can be used to get rid of the ambiguity. THG FROG uses a $\chi^{(3)}$ nonlinear optical effect, and thus it is less sensitive than SHG FROG. In the THG FROG, no extra information is needed to remove the direction of time ambiguity. In addition, a cross-FROG can be used if there is a short pulse that is already known to act as the reference pulse. The setup is similar to the SHG FROG, just replace one arm with the reference pulse. In our measurement, we built a FROG setup that can be easily switched between the SHG FROG and the cross-FROG. We use the SHG FROG to measure our pump pulse, and then use the pump pulse as a reference pulse in the cross-FROG to measure other pulses.

All the variants of FROG give a trace that has both temporal and spectral information, in mathematics it is given as

$$I_{FROG}(\omega,\tau)=\left|\int_{-\infty}^{\infty} E_{sig}(t,\tau)e^{-i\omega t}dt\right|^2 \quad (3.2\text{-}4)$$

where $E_{sig}(t,\tau)$ is different for each of the variants of FROG which are described as

$$E_{sig}(t,\tau)=\begin{pmatrix} E(t)|E(t-\tau)|^2\cdots\cdots\cdots PG \\ E^2(t)E^*(t-\tau)\cdots\cdots\cdots SD \\ E_1(t)E_2^*(t-\tau)E_3(t)\cdots TG \\ E(t)E(t-\tau)\cdots\cdots\cdots SHG \\ E^2(t)E(t-\tau)\cdots\cdots\cdots THG \end{pmatrix} \quad (3.2\text{-}5)$$

3.2.2 The FROG algorithm

The FROG algorithm for solving $\hat{E}_{sig}(t,\xi)$ from $I_{FROG}(\omega,\tau)$ is based on the iterative-Fourier-transform algorithm that is used in solving phase-retrieval problems[161]. Depending on their constraints

on signal field $\hat{E}_{sig}(t,\xi)$, different FROG algorithms have been developed to retrieve the pulses. Figure 3.6 shows the general steps in each iteration. Let us go with the standard FROG algorithm on SHG FROG to see how the pulse retrieval algorithm works.

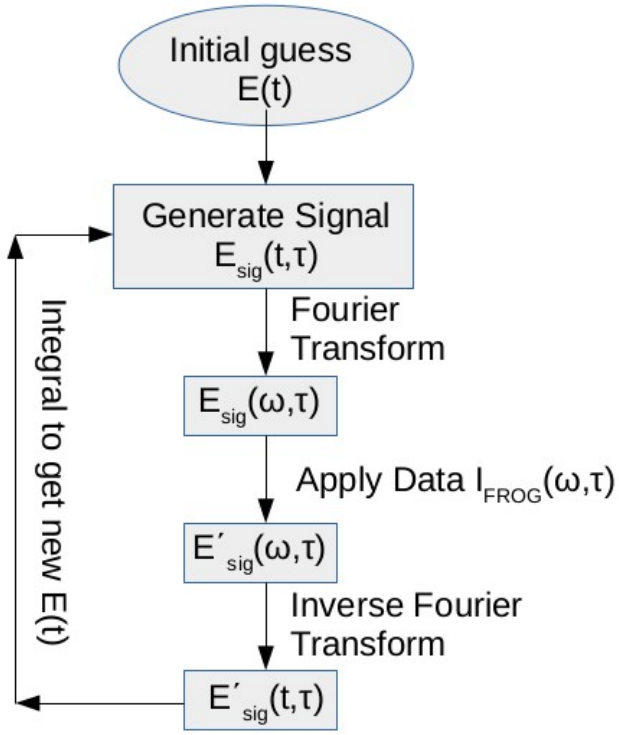

Figure 3.6: Steps of the FROG algorithm

To start with, an initial guess of E(t) is used. Basically, it can be anything, such as a random noise pulse. The signal is calculated as $E_{sig}(t,\tau)=E(t)E(t-\tau)$, and then a Fourier Transform is applied on $E_{sig}(t,\tau)$ to get $E_{sig}(\omega,\tau)$. In vanilla FROG, the data is applied in the frequency domain by simply replacing the magnitude of $E_{sig}(\omega,\tau)$ with the square root of $I_{FROG}(\omega,\tau)$, while keeping the phase the same

$$E'_{sig}(\omega,\tau)=\frac{E_{sig}(\omega,\tau)}{|E_{sig}(\omega,\tau)|}\sqrt{I_{FROG}(\omega,\tau)} \quad (3.2\text{-}6)$$

An inverse Fourier Transform is applied on $E'_{sig}(\omega,\tau)$ to get $E'_{sig}(t,\tau)$, and then integration is done to obtain $E_{new}(t)$ as

$$E_{new}(t)=\int_{-\infty}^{\infty} E'_{sig}(t,\tau)\,d\tau \quad (3.2\text{-}7)$$

Thereafter, $E_{new}(t)$ is set as the new field and carries on a new iteration. These iterative processes keep going until a certain condition(converge of calculation) is reached. Most of the cases, an error G is defined and used to monitor the process

$$G=\sqrt{\frac{1}{N^2}\sum_{i,j=1}^{N}\left|I_{FROG}(\omega,\tau)-\mu I_{FROG}^{(k)}(\omega,\tau)\right|^2} \quad (3.2\text{-}8)$$

where $I_{FROG}^{(k)}(\omega,\tau)$ is the retrieved FROG trace in k-th iteration, and μ is a normalization factor. The G factor is a quantitative measurement of how well the reconstructed trace matches the original trace. Several factors affect the G factor, including the size of the trace grid and the noise of the experimental data. Typically, an error of 0.005 or less can be achieved with accurate retrieval of low-noise data for a 128*128 pixels FROG trace.

The basic FROG is fast and works quite well in a lot of situations, but it can be unstable due to too much noises and may not converge for pulses with complicated pulse structure.[162,163] A more advanced method called Generalized Projections has been developed, and other improvements to the basic FROG can be found in details in Rick Trebino's book.

3.3 Single-shot FROG

Depending on the pulse energy and the repetition rate, the FROG works in multi-shot or single-shot. The main difference between the multi-shot FROG and single-shot FROG is their ways to achieve the time delay between the pulses. In multi-shot FROG, it is by changing the mirror positions, while the single-shot is using the relative positions along the narrow beam line that is focused by a cylindrical lens. In our experiment, the pulses used in MRG experiment is a 10 Hz pulse train, and according to our previous study, the pump pulses are different from pulse to pulse. Thus, a single-shot FROG is more suitable for our case.

As illustrated in Figure 3.7, the two pulses are sent through a cylindrical lens before crossing each other on the β-Barium borate(BaB_2O_4)(BBO) crystal. The beams are focused in the vertical direction while the horizontal direction is kept unchanged. The BBO crystal is placed right at the focal point of the cylindrical lens, such that the two beams cross each other within the crystal as a horizontal thin line.

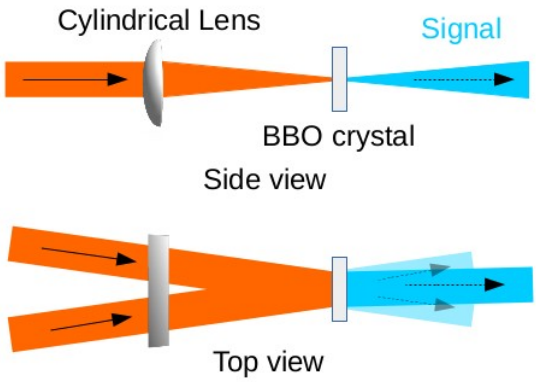

Figure 3.7: Side view and Top view of a single-shot auto-correlator

Figure 3.8 shows the correlation of the two pulses within the BBO crystal. As the two pulses are overlapped in the crystal, the middle point is the place where the two pulses are timed together. The upper part, as shown in the figure, pulse 1 arrives in advance of the pulse 2. The lower part, however, the pulse 2 takes the lead.

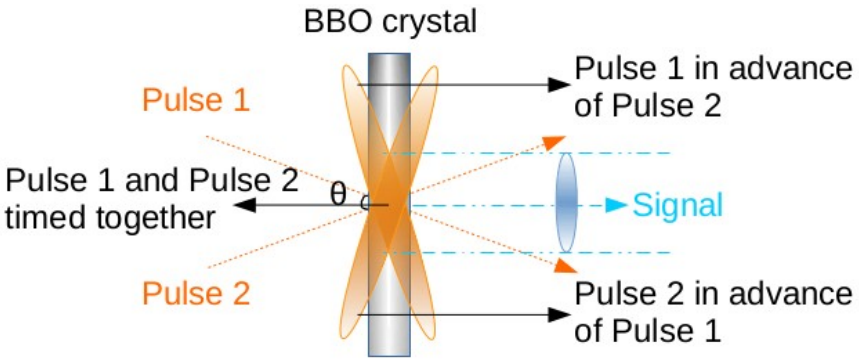

Figure 3.8: Two pulses correlating in a single-shot FROG with time-delay achieved by crossing two thin lines at an angle θ .

With a quick calculation, we can see the amount of time delay that it can be introduced by crossing the two beams with an angle of θ , and L as the length of the line. The time delay will be

$$\Delta t = \frac{2L}{c}\sin\left(\frac{\theta}{2}\right) \quad (3.3\text{-}1)$$

The length of the line is the diameter of the beam size, and in our experiment, it is about 0.8 cm. The crossing angle is about 20 degrees. Thus, the maximum time delay it can support is $\Delta t \simeq 9\ ps$, which is good enough for our experiment since most of the time the pulses are about 1 ps.

With the single-shot setup, the horizontal direction of the output signal contains the time delay information of the correlation. As shown in Figure 3.9, after the crystal, a lens in placed to collimate the

beam. A grating is applied after the collimation lens to disperse the signal in the vertical direction, in order to extract the spectral information. Then, an imaging system is used to record the FROG traces.

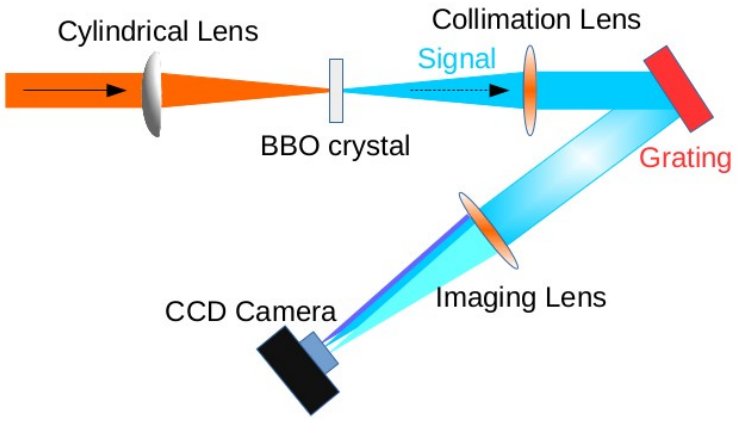

Figure 3.9: Single-shot FROG recording system(side view)

3.4 FROG trace data check

Before using the results, we want to be sure that the calculation of the FROG is reliable, especially when a lot of data processing is needed to get the final results. As we run the FROG algorithm, there are cases where the calculation does not converge. It could be caused by systematic errors, too many noises, incorrect calibration, bad alignment, etc. Luckily, methods have been developed to detect these types of errors. The most efficient one is the self-consistency check: The marginals.

As we know, for an electric field sample with N points, it has 2N degrees of freedom, as N degrees for magnitude and N degrees for the phase. Therefore, 2N points of data should be able to give us a full understanding of the electric field. In FROG, however, a N*N points of data is collected. With more than the needed data points, the marginal check can be used to ensure that the recorded data is valid. The marginal check is an approach that transforms the 2D data into a 1D curve by integrating the FROG trace over one of the coordinates, time or frequency. The mathematical form for the marginal in the frequency domain or the time domain goes as

$$M_{\omega}=\int_{-\infty}^{\infty} I_{FROG}(\omega,\tau)\,d\tau \quad \text{or} \quad M_{\tau}=\int_{-\infty}^{\infty} I_{FROG}(\omega,\tau)\,d\omega \quad (3.4\text{-}1)$$

The marginals of the FROG trace can be used to compare with the auto-convolution of pulse spectrum or the auto-correlation in time domain. A good match between them would indicate that the FROG

setup is working in good condition. Otherwise, it is certain that systematic errors exist in the setup, and further adjustment is needed. Some typical errors would be: incorrect calibration for the FROG setup, spatial chirp of the pulse, distortion of the beam, etc.

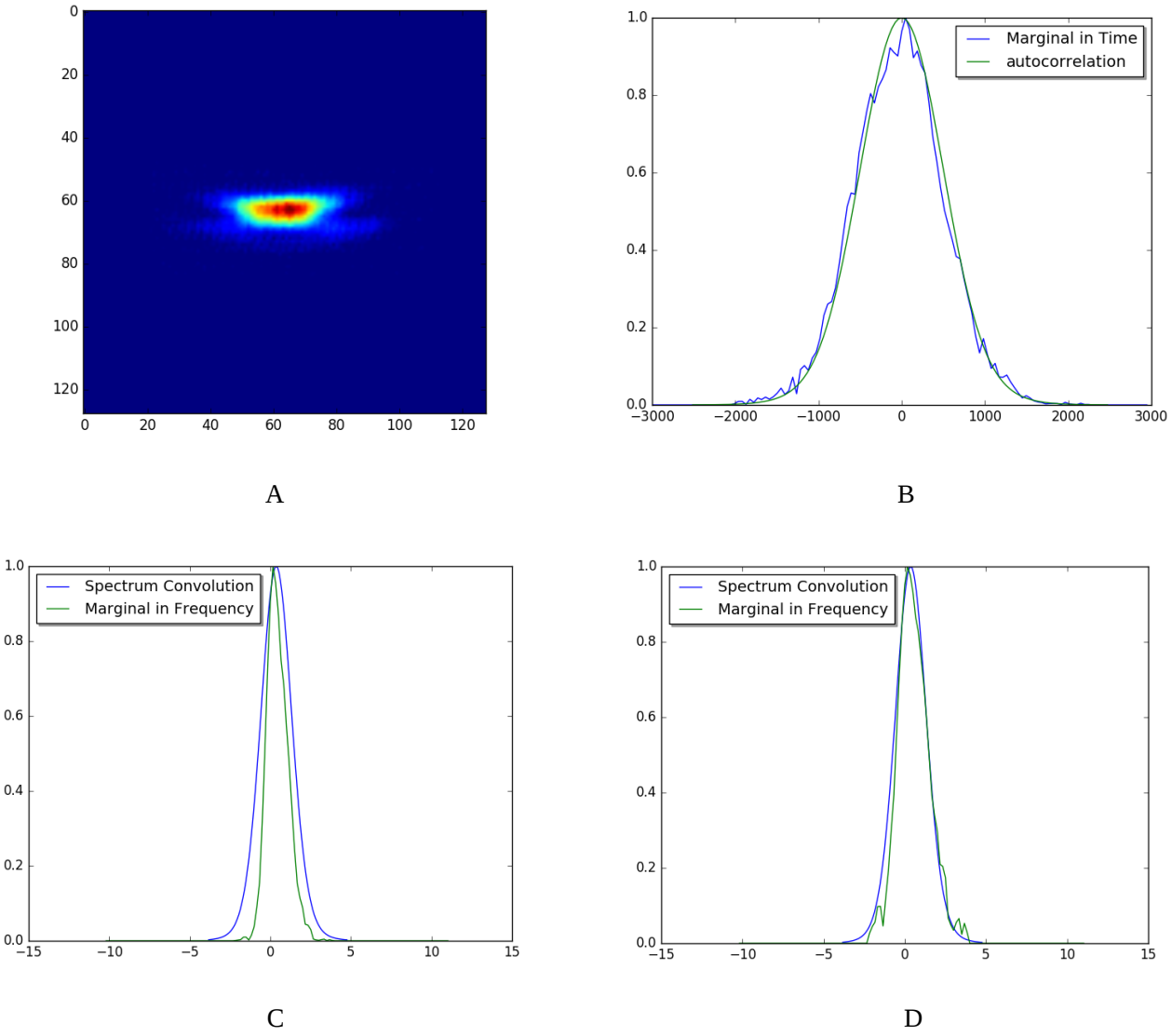

Figure 3.10: The marginal check for the pump, the numbers on the axises are unitless. A- The experimental FROG trace of the pump; B- Comparison between the marginal of the FROG and the intensity autocorrelation; C- Marginal check for the frequency domain with the spectrum convolution; D- Modified spectrum convolution with the effect of spectrometer resolution limit.

The marginal check is a rigorous and strong method to quickly check the data. So we run the marginal check with the pump pulse right after we set up of the FROG.

As shown in figure 3.10-A, the FROG trace is a 2D image with the horizontal containing the temporal information and the vertical frequency related. We are using a 128*128 pixel trace for the FROG calculation, and will use this number of pixels for all the FROG calculation in this thesis. Using equation 3.4-1 we can calculate the marginals for both time and frequency domain. On the other hand, we can easily get the intensity auto-correlation and spectrum from our auto-correlator and spectrometer, respectively. From figure 3.10-B, we can see that the marginal and the intensity auto-correlation have a high degree of matching. However, from figure 3.10-C, the frequency marginal does not agree with the auto-convolution of the spectrum. As what we learn from the marginal check, the mismatch can lead to some systematic errors in the setup. After checking all the possible errors and carefully re-aligning the devices in the FROG setup, the mismatch is still there. At last, we believe the mismatch comes from the resolution of the spectrometer we are using in the lab. The resolution is about 1.5 nm for the spectrometer we are using, while the FROG has a resolution up to 0.1 nm. Taking consideration of the effect from the resolution, we can have a modified frequency marginal as shown in figure 3.10-D, and that shows a good match.

It is important to get the setup in good condition before doing any further measurement. If the setup is not in excellent condition, the marginal can be very useful in correcting the errors in the FROG traces. For example, the systematic error in SHG FROG trace can be corrected simply by multiplying the trace by the ratio of the spectrum auto-convolution and the frequency marginal. More details can be found in Chapter 10 of Trebino's book where it shows the limitation of the FROG technique, and talks about how to choose sampling rate of FROG trace and the FROG algorithm errors.[164]

Chapter 4

Experimental Apparatus

In this Chapter, we will go through the details of the experimental apparatus used in our lab. In general, there are seven parts in our MRG setup. They are front end *LASER* source, dual-wavelength pulse stretcher, dual-wavelength pulse regenerative amplifier, multipass amplifier, grating compressor, hollow fiber chamber, and pulse measurement. The first five parts are used to prepare pulses for MRG experiment by using the state-of-art technique, CPA. As an essential part of the CPA technique, we will talk about how the dispersion changes the profile of pulse, and how we can use it for our own benefits. We will present the prism-pair and grating-pair as the tools to introduce positive and negative dispersion in the setup and also show how they work. In the following, we will use the light propagating path as the time line to do the description. For the final measurement, three devices are used including the spectrometer, auto-correlator, and the FROG. At the end, we will show the calibration of the auto-correlator and the FROG.

The experimental setup follows our group's previous MRG system that uses dual-wavelength LASER amplification system[165]. As shown in Figure 4.1, it has four stages, including a front end LASER source, chirped pulse amplification(CPA) system, hollow fiber chamber, and pulse measurement devices. The CPA system includes the dual-wavelength pulse stretcher, dual-wavelength pulse regenerative amplifier, multipass amplifier, and grating compressor.

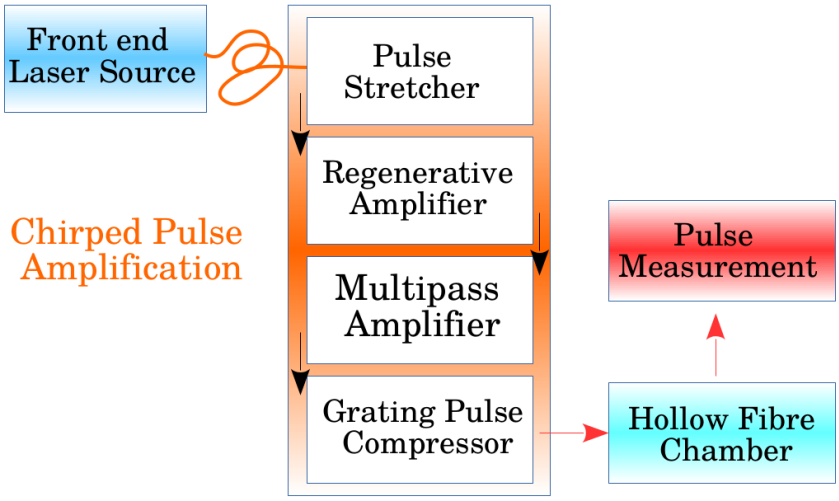

Figure 4.1: Experimental Setup block diagram of the whole MRG

The front end LASER source is a commercial 10 fs Ti-Sapphire LASER . It is shared with Professor Sanderson's group and placed in his lab. A 50% beam splitter is placed in the output beam to divide it into two beams. One of the beams is focused into a single mode fiber and directed to our lab as the LASER source. After the fiber, the beam goes through a Faraday isolator (FI) to prevent damage to the fiber end from the returning amplified LASER beam. Then the beam is sent into our dual-wavelength stretcher to choose two different spectral components and stretch the pulse to about 200 ps in duration. The stretched beam is sent through a second FI for further system protection. Following the second FI, the beam goes into the dual-wavelength regenerative amplifier and is amplified to an energy of about 1.8 mJ. A multipass amplifier is used to get higher pulse energy for MRG experiment. The beam energy is pumped up to 10 times within the multipass amplifier. After the multipass amplifier, the beam is sent towards a grating-pair pulse compressor, where the pulse is compressed to hundreds of femtoseconds. After compression, the beam is then focused into hollow fiber chamber filled with Raman material Sulfur Hexafluouride(SF_6), where MRG process takes place. Large number of Raman orders are generated with constant frequency separation. In our case, the frequency separation is 23.25 THz, given by the frequency separation of a vibrational level, A_{1g}, of SF_6.[166]

The output beam including all the Raman spectra is then sent to the measurement devices such as spectrometer, autocorrelator, Spectral Phase Interferometry for Direct Electric-field Reconstruction (SPIDER), and the FROG for further analysis.

4.1 Front end *LASER* source: the oscillator

The front-end *LASER* source is a 10 fs commercial Ti-Sapphire *LASER* with central wavelength at 800 nm. It generates pulses at a rate of 75 MHz with an average power of 400 mW. Half of the beam is sent through a 5 cm glass block before focusing into a 30m long single mode fiber. The glass block is used to stretch the pulse to minimize the self-phase modulation effect. Once well aligned, up to 100 mW of the pulse power will get through the fiber and reach to our system as a seed beam. A daily maintenance procedure can be found in the appendix B.

4.2 Chirped pulse amplification

CPA is a technique used to amplify ultrashort pulses. The main purpose of the technique is to avoid optical damage while amplifying a short *LASER* pulse to higher energy. The materials used in an amplifier system have their damage thresholds, which limit the peak power of the pulse. The idea of the CPA is to stretch the ultrashort pulse to a much longer pulse, then amplify it, and at the final stage compress the pulse back to ultrashort pulse. As we know, the shortest pulse for a certain bandwidth of spectrum is reached when the phase is constant, which is called a Fourier transform limited pulse. However, the pulse is dispersed as it propagates through materials, resulting in different frequencies travelling at different speeds. The added dispersion, positive or negative, will change the duration of the pulse. The dispersion that the pulse gains when passing through an optical device is frequency dependent, $D(\omega)$. Such that, the amount of phase-change for the pulse is given as

$$\phi(\omega)=\frac{2\pi c\, D(\omega)}{\lambda(\omega)} \quad (4.2\text{-}1)$$

where c is the speed of light, and $\lambda(\omega)$ is the wavelength. The phase-change is also commonly written in the form of Taylor expansion with centre-frequency of ω_0 ,

$$\phi(\omega)=\phi_0+\frac{d\phi}{d\omega}(\omega-\omega_0)+\frac{1}{2!}\frac{d^2\phi}{d\omega^2}(\omega-\omega_0)^2+\frac{1}{3!}\frac{d^3\phi}{d\omega^3}(\omega-\omega_0)^3+O(\omega^4) \quad (4.2\text{-}2)$$

where the ϕ_0 is the absolute phase, and it is commonly not measurable in the experiment, but it does not affect the shape of the pulse. The second term, $\frac{d\phi}{d\omega}$, is the group delay, or called the linear phase. As the blue line illustrated in figure 4.2, the linear phase affects the time delay of the pulse. The following term, $\frac{d^2\phi}{d\omega^2}$, is the group delay dispersion(GDD) or second order phase. The next term, $\frac{d^3\phi}{d\omega^3}$, is the third order dispersion(TOD).

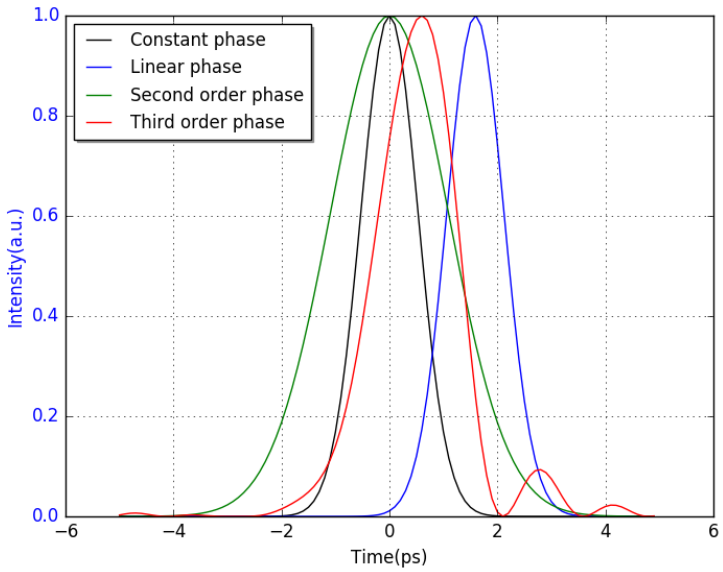

Figure 4.2: Pulses with the same spectrum but different phases. Constant phase, linear phase, second order phase, and third order phase are plotted

GDD and TOD are the main terms that change the profile of the pulses, as illustrated in the green and red lines in the plot. The GDD stretches the pulse, while the TOD turns the pulse into an oscillation pattern. The higher order term $O(\omega^4)$ also changes the profile of the pulses, but it is not a main factor and we will not study it in details. There are several ways to introduce a certain amount of dispersion to a pulse, such as prism-pair, grating-pair, prism&grating-pair, optical fibers, and chirped Bragg Gratings. We will focus on the mechanism of how the prism-pair and grating-pair introduce dispersions to pulses, as they are commonly used devices in labs.

4.2.1 Prism-pair

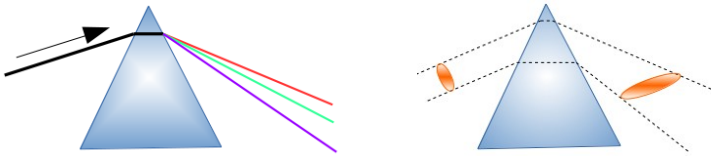

Figure 4.3: Prism works as a dispersive element

A prism is a device that can be used to introduce dispersion, as shown in Figure 4.3-left, the beam is spectrally dispersed as it travels through the prism.[163] However, since the upper part of the beam goes through less material than the lower part, as illustrated in Figure 4.3-right, the pulse spatial profile becomes front tilted and the beam-size changed after a prism. To get rid of these effects, a four-prism system is used. The symmetry of the double prism-pair, as can be seen from Figure 4.4-Left, can keep the beam spatially unchanged while adding a certain amount of dispersion. In many cases, a variant that uses 2 prisms and a back mirror to reflect back the beam is shown in Figure 4.4-Right.

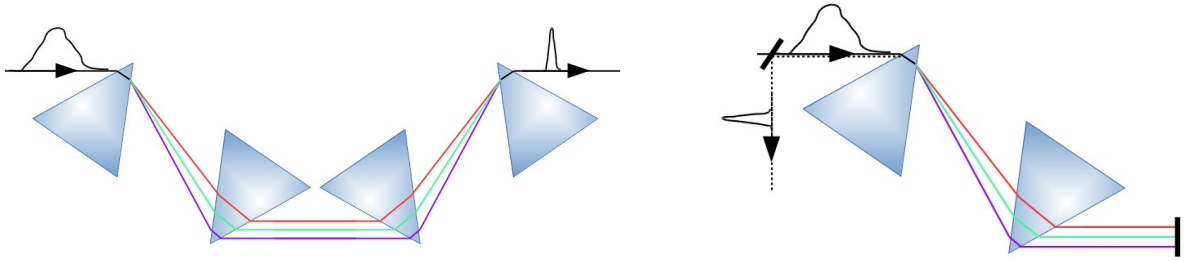

Figure 4.4: Prism-pair that works as a compressor, Left- 4-prism pair configuration; Right- 2-prism pair and a mirror configuration

The dispersion that introduced by the prism-pair comes from two parts, with the positive one from the prism's materials that the pulse propagates through and the negative dispersion from the angular dispersion that makes the longer wavelength travel less. The total amount of dispersion is given by[167]

$$\frac{d^2\phi}{d^2\omega}=\frac{\lambda^3}{2\pi c^2}\left[4L\left(\frac{dn}{d\lambda}\right)^2-2D\left(\frac{d^2n}{d\lambda^2}+2n-\frac{1}{n^3}\right)\right] \quad (4.2\text{-}3A)$$

$$\frac{d^3\phi}{d^3\omega}=\frac{\lambda^4}{\pi^2 c^3}\left[6L\left(\frac{dn}{d\lambda}\right)^2-\frac{1}{2}D\left(\frac{d^2n}{d\lambda^2}\right)\right] \quad (4.2\text{-}3B)$$

where L is the distance between the prims, and the D is the length that the pulse travels through the prisms.

4.2.2 Grating-pair

Compared to the prism, the grating is a device that can introduce much larger dispersion. However, similar problems would occur if only one grating is used. Hence, four gratings are used, and similar to the prism-pair, a more commonly used configuration has two gratings and a back mirror, as shown in Figure 4.5. There are also variants with lenses placed inside the grating-pair that can switch the device between positive dispersion and negative dispersion by simply changing the distance.

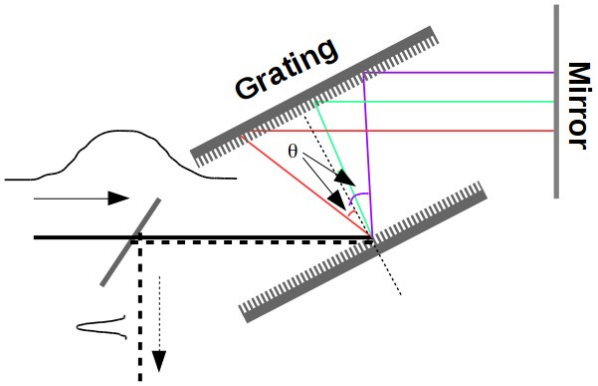

Figure 4.5: Compressor configuration with two gratings and a back mirror

The second order and third order dispersion introduced by the grating-pair is given by[168]

$$\frac{d^2\phi}{d\omega^2}=\frac{\lambda^3 L\,sec\theta}{\pi c^2 D^2\cos^2\theta} \quad (4.2\text{-}4A)$$

$$\frac{d^3\phi}{d\omega^3}=\frac{-3\lambda^4 L\,sec\theta}{2\pi^2 c^3 D^2\cos^2\theta}\left[1+\frac{\lambda\sin\theta}{Dcos^2\theta}\right] \quad (4.2\text{-}4B)$$

where L is the distance between the gratings, D is the grating period, and θ is the reflection angle.

The prism-pair and grating-pair have their own advantages and disadvantages. Grating-pairs can introduce much larger dispersion, which is the biggest advantage. However, the energy loss is relatively high, as quite a big part of energy goes to the other orders of grating reflection. On the other hand, as can be seen from the equations 4.2-4, the second order is purely negative while the third order is purely positive, which means a lack of tuning ability. The prism-pair has a good energy efficiency, and therefore is commonly used and placed inside of a *LASER* cavity for beam control.

From the dispersion equation 4.2-3, the second order and third order dispersions are tunable to be positive or negative, which makes it possible to get rid of the unwanted dispersions, such as the third order dispersion. In many cases a combination of the grating-pair and prism-pair is used in order to get a large amount of dispersion while also eliminating the unwanted third order dispersion introduced by the grating-pair.

4.2.3 Pulse stretcher

Since we need to stretch the pulse before amplifying it, the first stage of a CPA system is the pulse stretcher. In our lab, the dual-wavelength stretcher is set up as shown in figure 4.6. Two pairs of prisms, P1-P2 and P1-P3, are used to separate and select two parts of spectrum with separation of about 23.25 THz. Then, both of the beams are sent onto a grating to gain dispersion for pulse stretching. For instance, one of the beams goes from prism P1 to prism P2, and is re-directed by mirrors M1 and M2. Thereafter, it is dispersed by the grating for the first time. Then it travels to mirror M3 via the concave mirror. Reflected by mirror M3 and then focused by the concave mirror, the beam reaches the grating for the second time. The output beam from the grating propagates to the right-angle mirror M4 and comes back to the grating for the third time. Thereafter, the beam gets to the concave mirror the fourth time and then reflected back to the grating for the final fourth time. Afterward, the beam goes all the way back to prism P1 via mirror M2, mirror M1, and prism P2. With the dispersion introduced by the grating, the pulses are stretched to around 200 ps. The outward beam (dashed line) differs from the input beam by being slightly lower in height, and thus, a lower placed mirror M5 sends the beam through a half-wave plate, a FI, and then all the way into the next stage, the Regenerative amplifier.

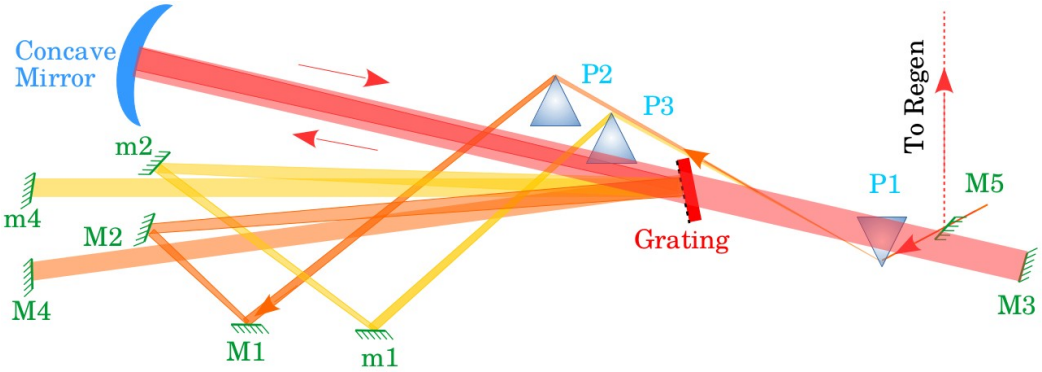

Figure 4.6: Diagram for Dual wavelength stretcher

4.2.4 Regenerative amplifier

For MRG experiment, two beams of different center-wavelengths are required. Similar to the pulse stretcher, as shown in Figure 4.7, three prisms are placed inside a *LASER* cavity to provide amplification for the two pulses of different center-wavelengths. For each of the paths, it has front and end mirrors (M1-M2, and M1-M3) forming a *LASER* cavity. A Ti-sapphire crystal optically pumped by a Nd:YAG *LASER* is used as the gain medium. The crystal is placed about 8 cm away from the focus point of the pumping *LASER* to prevent optical damage. Two concave mirrors are used to focus the LASing beam while being transparent to the pump beam, such that the pump beam can be sent into the crystal to pump the LASing process. Two slits are applied to select the center-wavelengths that we are going to use in MRG experiment. Also, a back mirror M3 is locked down on a translation platform so that we can time the two pulses.

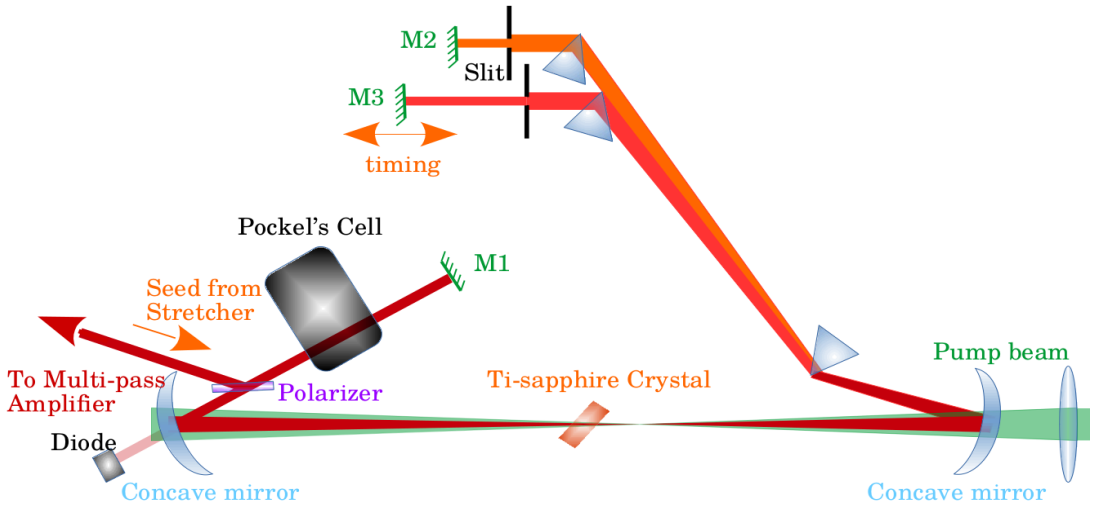

Figure 4.7: Diagram for the Regenerative Amplifier with dual-wavelength

In order to switch in the seed pulse from the stretcher and switch out the amplified pulse, a polarizer and Pockel's Cell are placed inside the cavity. The thin-film polarizer is set at the Brewster angle so that it reflects S-polarized light and transmits P-polarized light. The Pockel's Cell is a polarization changing device, and the birefringence effect of its crystal depends on the voltage applied. When the voltage is off, it is aligned to work as a quarter-wavelength plate. When the voltage is switched on, the Pockel's Cell is turned into a half-wave plate or a three-quarter-wavelength plate, depending on the magnitude of the applied voltage. The seed from the stretcher is S-polarized, thus the polarizer will reflect the seed toward the Pockel's Cell side.

At the first stage, the voltage is off, such that the S-polarized seed becomes circularly polarized as it goes through the Pockel's Cell. The seed is then reflected back by the front mirror M1 and sent back to the Pockel's Cell again. This time, the seed gains another quarter-wavelength plate effect and is turned into a P-polarized beam. Once the seed beam becomes P-polarized, it will propagate through the polarizer and stay inside the cavity for amplification. To prevent other seed pulses from getting into the cavity while keeping the pulses inside the regenerative amplifier, the Pockel's Cell is then switched to the half-wave plate mode. All the S-polarized pulses will be sent out of the cavity by the polarizer. The trapped seed pulse travels back and forth inside the cavity and gets amplified at each time it goes through the crystal. Once the seed is amplified to a maximum energy, which can be detected by the photo-diode placed behind the first concave mirror, the Pockel's Cell will be switched to the three-quarter-wavelength plate mode. The new mode will turn the amplified P-polarized pulse into S-polarized. Thereafter, the amplified S-polarized beam will be reflected by the polarizer and sent out of the *LASER* cavity. The system repeats the above process to amplify the pulses.

4.2.5 Multipass amplifier

After the Regenerative amplifier, the average power of the pulses is about 2 mW. However., it is still too low to carry out our MRG experiment. Therefore, a second amplifier is built to get higher power. As shown in Figure 4.8, the biggest difference between the multipass amplifier and the Regenerative amplifier is that the multipass amplifier is not in a cavity. A pair of lenses is applied to increase the size of the beam from the previous stages and to maintain a collimated beam. Pairs of mirrors are used to send the beam back through the Ti:Sapphire crystal with different paths. That is why, I would refer it as multipath amplifier instead of multipass amplifier.

In this setup, the number of times the beam goes through the crystal can be changed by adding or reducing mirror pairs. Currently, in our lab, 5 passes are used. The pump beam comes from our Nd:YAG *LASER*. 10% of the beam goes into our Regenerative amplifier and the remaining 90% is used in the multipass amplifier. The pump beam is split into two beams and sent into the Ti:Sapphire crystal from opposite directions. Going through this multipass amplifier, the output beam gains an energy up to 10 times that of the input beam. The amplified beam is then sent toward the compressor for final pulse configuration.

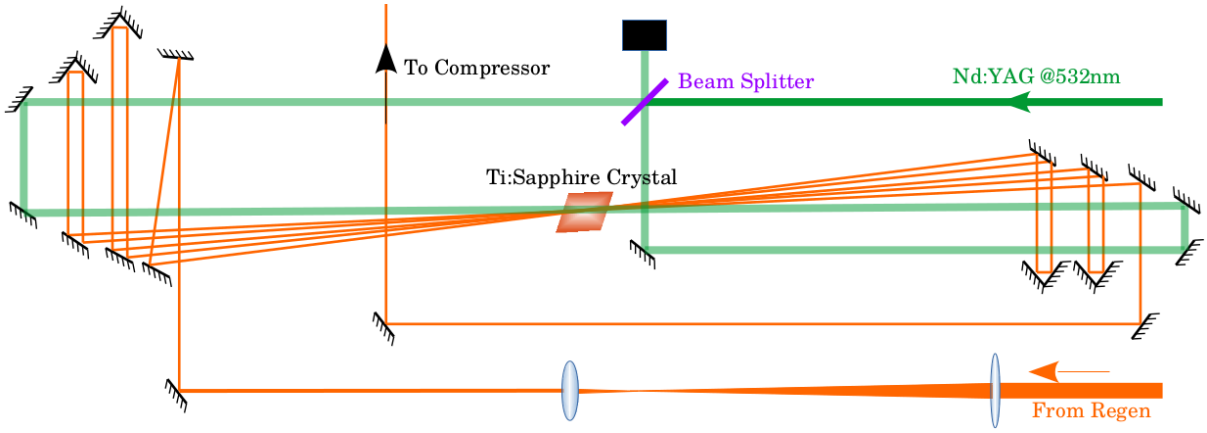

Figure 4.8: Diagram of the multipass amplifier

4.2.6 Grating compressor

After the previous stages, the pulses have gained high energy. One more step before MRG experiment is to compress the pulses. The output pulse from the multipass amplifier has a pulse duration of around 200 ps. We need to compress it to around 1 ps as we are working in the transient regime. To achieve this goal, a grating pair compressor is introduced. As illustrated in Figure 4.9, the beam is sent into grating G1-G2 and G1-G3 pairs as we have two pulses with separate center-wavelengths. The grating pair will introduce negative dispersion to the pulses. By changing the distance between the gratings, we can have positively chirped, unchirped, and negatively chirped pulses. Back mirrors M2 and M3 will reflect the beam back and slightly aiming downward. Mirror M2 is placed on a translation platform such that we can change the timing between the two pulses. The lowered returning beam (dashed line) will be re-directed by mirror M4 to our final experiment part, the hollow fiber chamber.

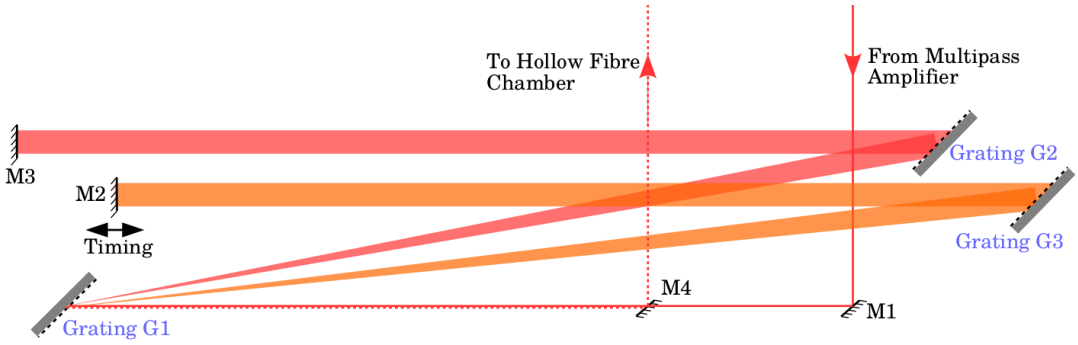

Figure 4.9: Diagram of the Grating compressor for the pump and the Stokes

4.3 Hollow fiber chamber

With the two pulses having sufficient energy and being compressed down to hundreds of femtoseconds, we are ready to carry out MRG experiment. A fused silica hollow fiber is used to confine the beam to enhance MRG process. The hollow fiber waveguide will keep the beam within the fiber and increase the interaction length. Also, the hollow fiber's negative dispersion can compensate the positive dispersion that the beam gains from the gas. In our group's previous study, hollow fibers of different diameters have been used in experiments. The results showed that the size of the fiber changes the negative dispersion and affects the amount of transmission energy. For the experiment reported in this thesis, we are working with hollow fiber at 0.5 meter long and 150 micrometer in the diameter.

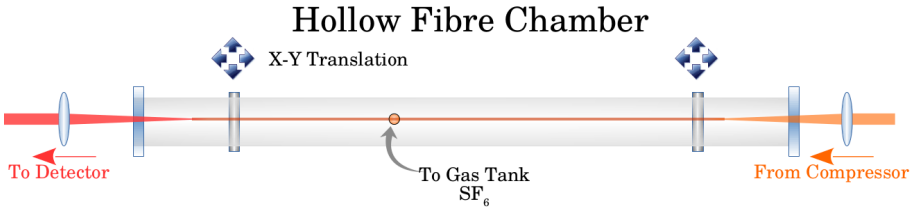

Figure 4.10: Diagram of the Hollow Fiber Chamber(top view)

As seen from Figure 4.10, the hollow fiber chamber is a glass built high-pressure chamber, and is connected to a gas tank and vacuum system. The pressure in the chamber goes from 1 atm - 30 inch Hg to 1 atm + 30 PSI. A V-shape Aluminum bar is used to hold the position of the hollow fiber. The chamber itself is free to move in both horizontal and vertical direction at each end. In this setup, we are using a 30 cm lens to focus the beam into the gas filled hollow fiber. As the beam propagates through the fiber, MRG takes place and generates a wide spectrum with separated Raman orders. The output beam, which contains all the different spectra is then collimated by another lens and sent towards the measurement part.

The dephasing time of SF_6 fits the transient regime that we are working in, and the symmetry of the SF_6 molecule makes it simple for the Raman levels as only vibrational Raman level occurs. Furthermore, compared to gases such as H_2 and CH_4, SF_6 is much more stable and safer to handle in daily experiments. In addition, the dual-wavelength system in our lab can be tuned to couple this particular Raman transition.

4.4 Pulse measurements setup

As we have the output signal from MRG process, a study of the signal might tell us what is going on inside the hollow fiber chamber. To measure a pulse, a general approach is to detect its time domain pulse duration, and/or frequency domain pulse spectrum.

4.4.1 Spectrometer

For the spectrum, we use an Ocean Optics spectrometer to do the measurement. The result from the spectrometer is straightforward and tells us what spectra are contained in the output beam. As can be seen from Figure 4.11, the spectrometer shows that the output beam contains a spectrum with equally separated orders. However, since the phase of the spectrum is unknown, we do not have enough information to fully understand the pulses.

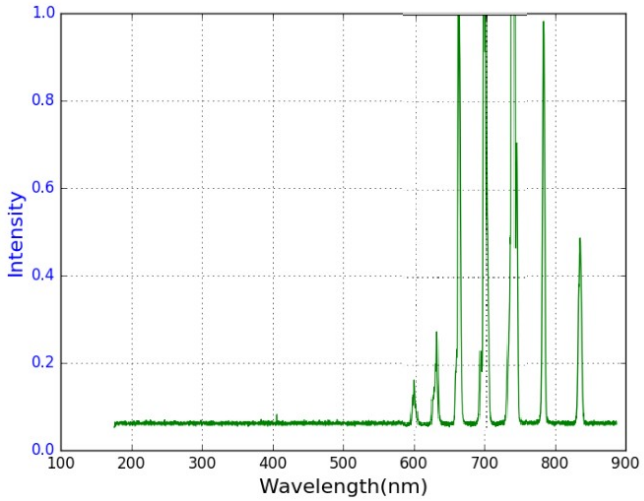

Figure 4.11: A sample of MRG spectrum measured by the Ocean Optics Spectrometer

Another way of examining a pulse is to measure it in the time domain, and the most commonly used method is by sending the beam into an auto-correlator.

4.4.2 Auto-correlator

Auto-correlator is widely used in measuring the duration of pulses. Figure 4.12 shows the setup in our

lab. For the auto-correlation, the beam is divided into two parts, one of them is re-directed by a mirror and sent into a BBO crystal, and the other part is sent to a translation platform before going into the crystal. This scheme allows us to change the timing between the two parts, and to perform the calibration. The two beams overlap in the BBO crystal and by turning the crystal to a certain angle, a sum frequency of the two parts can be obtained. The direction of the output sum frequency signal follows the phase matching condition. After the crystal, a charge-coupled device(**CCD**) camera is placed to record the signal.

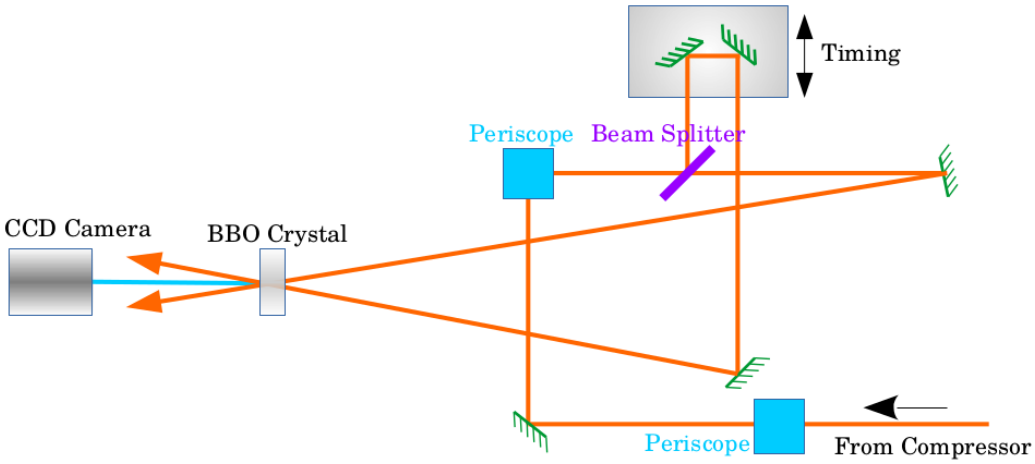

Figure 4.12: Diagram of auto-correlator, two periscopes are used to adjust the height of the inserting beam while maintaining the polarization. A diagram of periscope can be found in figure 4.13

In the setup, two periscopes are used to change the height of the beam while maintaining its input polarization. Figure 4.13 shows how the periscope works: a S-polarized beam propagates horizontally, and it is reflected up by a 45 degree(to the X-axis) placed mirror. After a short distance up, the beam is then reflected horizontally out by a 45 degree(to Y-axis) placed mirror. The output beam changes its height and also becomes P-polarized. By using another periscope, the polarization will be switched back to S-polarized with the beam's height being changed.

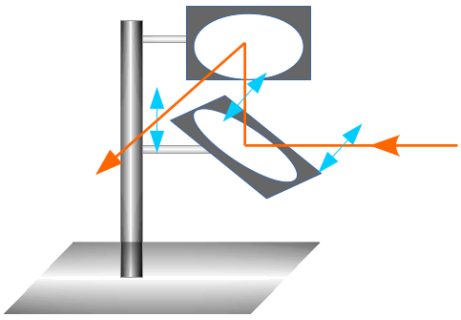

Figure 4.13: Diagram of Periscope, the orange line is the inserted beam and the blue arrows are the polarization directions of the beam. In the plot, the polarization of the beam is switched from a horizontal linear polarization to a vertical linear polarization

The calibration of the auto-correlator can be achieved by changing the timing of one arm and recording the corresponding peak intensity pixels with the CCD camera. As illustrated in Figure 4.14, the calibration factor of the auto-correlator that we are using is 10.1 fs/pixel, and of course, this factor depends on the configuration.

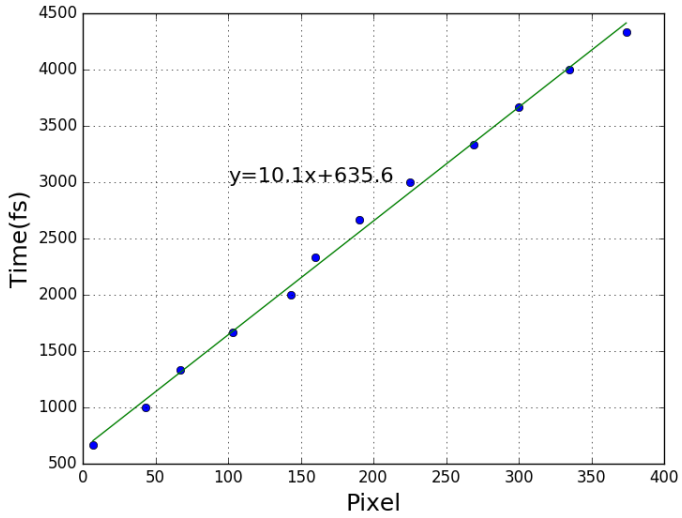

Figure 4.14: Calibration measurement of the auto-correlator. It is obtained by changing the timing of one arm in the auto-correlator and recording the maximum intensity position of the image

The CCD camera records the intensity auto-correlation that goes as

$$A(\tau)=\int_{-\infty}^{\infty} I(t)\,I(t-\tau) \quad (4.1)$$

Therefore, the calculated FWHM from the recorded trace will not be the pulse duration of our pulse. Since we are assuming that our pulse has a Gaussian shape, then by dividing a factor of $\sqrt{2}$ will give us the pulse duration. Alternatively and in fact what we do in our recording program is to use a modified calibration factor divided by $\sqrt{(2)}$, which ends up with 7.14 fs/pixel.

4.4.3 Frequency resolved optical gating setup

The spectrometer and the auto-correlator measure the pulse in their own domains, frequency and time, respectively. Each of them gets part of the information out of the pulse, like each side of a coin. However, we want to know not only the two sides, but also the relation between them. We have the spectrum and amplitude of the electric field, and also know that they are related by the Fourier transformation, though phase information is still required to fully describe the pulse. Hence, if we use

both the frequency and time domain information, we should be able to get all the details of the pulse. In fact, that is a phase retrieval problem and a few techniques have already been developed including Grating-eliminated no-nonsense observation of ultrafast incident *LASER* light e-fields (**GRENOUILLE**)[169], and FROG.

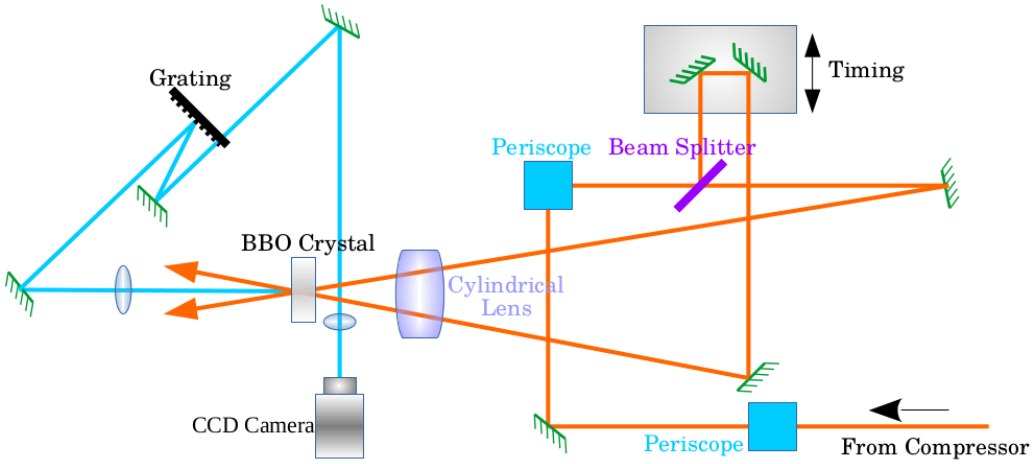

Figure 4.15: Diagram of the FROG setup. The right half is similar to the auto-correlator but adding a cylindrical lens. The cylindrical lens is added to obtained time-delay between the beams. On the left side, a grating and imaging system is added to fulfil the FROG setup

In this study, most of the measurements of MRG process are done by using the FROG setup. As shown from Figure 4.15, the FROG setup can be built based on the auto-correlator. Given that our final signals are pulses with 10 Hz repetition rate, the single pulse FROG setup is adopted in our lab.

A data recording program written in Python can be found in the Appendix A. With the recorded FROG trace, we can run the FROG algorithm to retrieve the phases and figure out the pulses. Also, a data processing program written in Python can be found in the Appendix A, which shows in detail how to prepares the raw data for the FROG program.

Similar to the auto-correlator, we need to do the calibration before using the setup, and this time both temporal and spectral calibrations are needed. The temporal calibration is that in the calibration of auto-correlator. The calibration factor for frequency is done by changing the center-wavelength of the pump pulse, and then record the maximum pixel in the vertical axis. As shown in Figure 4.16, the calibration factor are 21.6 fs/pixel and 0.0191nm/pixel.

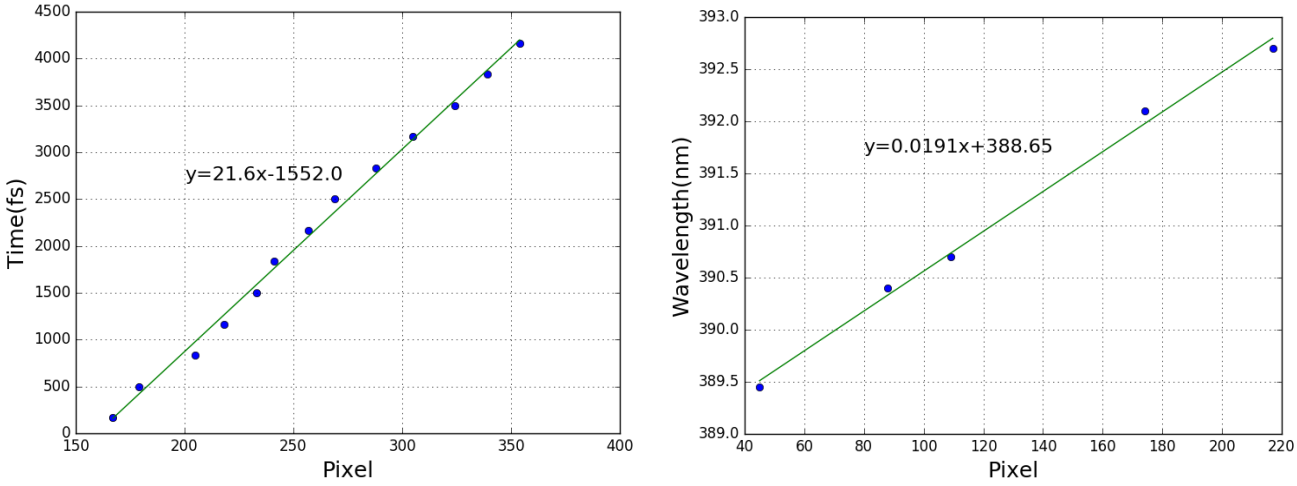

Figure 4.16: FROG calibration: Left-temporal; Right-spectral. These calibrations were done similar to that for the calibration of auto-correlator in figure 4.14.

The FROG setup can be seen as a spectrometer in addition to an auto-correlator. However, the measurement is better than the auto-correlator and spectrometer that we are using. The cylindrical lens focuses the beam, which increases the beam intensity and makes it far more sensitive. The grating and imaging system in the FROG system also gives higher resolution, as the dispersion for the FROG setup goes down to 0.005 nm/pixel, and from figure 4.17, the optical slit covers around 20 pixels on the screen. Thus the optical resolution would be about 0.1 nm, while the Ocean Optics spectrometer in our lab has a resolution of 1.5 nm.

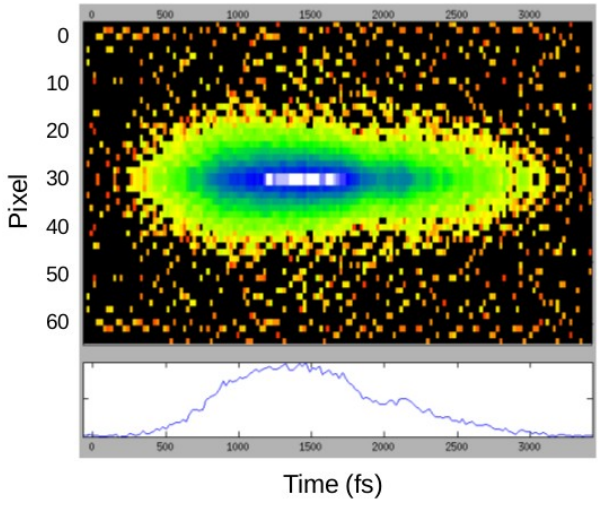

Figure 4.17: Optical slit showing on screen as used for the calibration of spectral resolution

4.5 FROG data preparation

After the time and the frequency calibrations, we need to prepare the recorded data to get it ready for the FROG program provided by Rick Trebino.

As shown in the image below, the original FROG trace is just a 2D array with 720 columns and 576 rows, and with background noises embedded in the data as shown in figure 4.18-A. To feed the data into the FROG program, a header line with information of the trace, including data dimensions, the calibration factors, and centre-frequency, should be included. A program that can add the header line to the data file is written in Python and is presented in Appendix A.

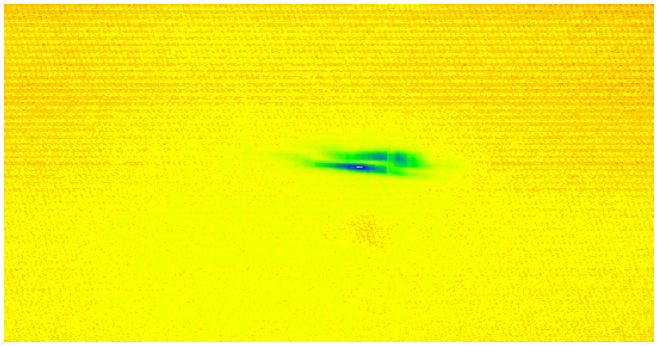

A

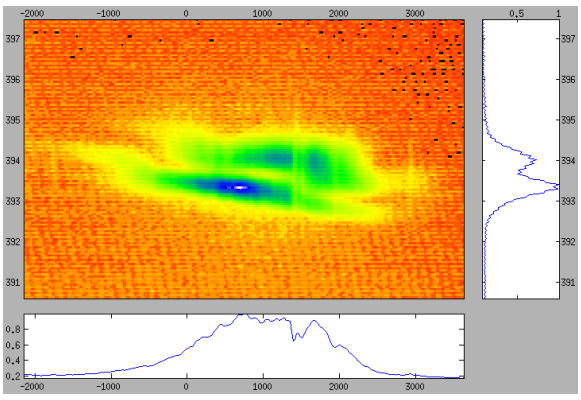

B

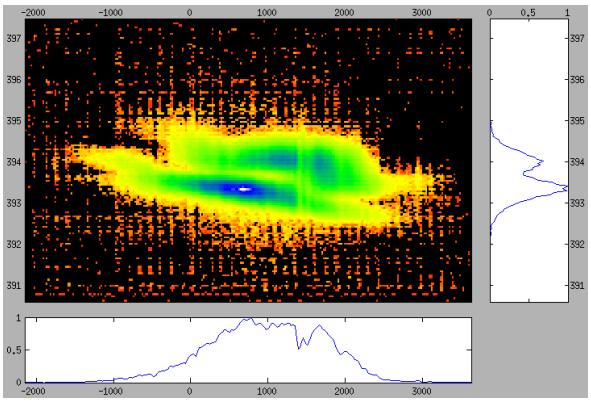

C

Figure 4.18: FROG trace data preparation: A-the original FROG trace; B-extract the part of data that is useful; C-reduce the background noise of the trace.

With the header line added to the data file, we can now load the data file using the “binner” program, since the trace is just the centre part of the image, we can extract the useful part of the data from the original trace, as shown in figure 4.18-B. In the plot, the horizontal axis is the time and the vertical axis

is the frequency. Two blue curves are provided that give the view of the trace in either the time domain or the frequency domain. There is a function in the “binner” program that can reduce the background noise, and a much cleaner trace can be obtained as shown in figure 4.18-C. Thereafter, we can send the prepared data into the FROG algorithm program to get the reconstructed pulses.

Chapter 5

MRG Experimental Process

The experiment of MRG in our lab includes a series of processes. Before the MRG experiment, we need to prepare the pump and the Stokes pulses, including seeding, pulse regeneration, pulse amplification, pulse compression, and hollow fibre alignment. After the pulses are well prepared, the multipass amplifier is activated to get up to 10 times higher energy for MRG. The output beam containing all the Raman orders is then sent into pulse measurement devices. Each of the steps is essential for the success of the experiment. Therefore, in this Chapter, I will describe an end-to-end single run of the experiment process along with critical checking points. At the end of this Chapter, we will give a check of the quality of our pump pulse.

Before sending the final beam to the hollow fibre chamber for MRG, the main processes are stretching the seeding pulse, seeding the Regen for a well amplified single pulse output, using a second stage of multi-pass amplifier for a higher pulse power, and applying a compressor to compress the pulse to around 800 fs. In F. Turner's thesis, a very detailed instruction of how to do all the setups and alignment is provided[32].

5.1 Preparing the pump pulses for MRG experiment

The seeding source that we are using has a spectrum as shown below. It is a spectrum of a 10 fs ultrashort pulse centred at 800 nm. For our MRG experiment, the dual-wavelength amplifier system works with the two centre-wavelength separated by about 50 nm. The frequency separation is chosen to match the 23.25 THz Raman frequency of the Raman material SF_6. The prism pair and grating in the stretcher can choose two parts of spectra from the original spectrum, as shown in Figure 4.1-B. Rotating the grating will shift the whole spectrum to either side. In this thesis, two spectra centred at 786 nm and 837 nm are used.

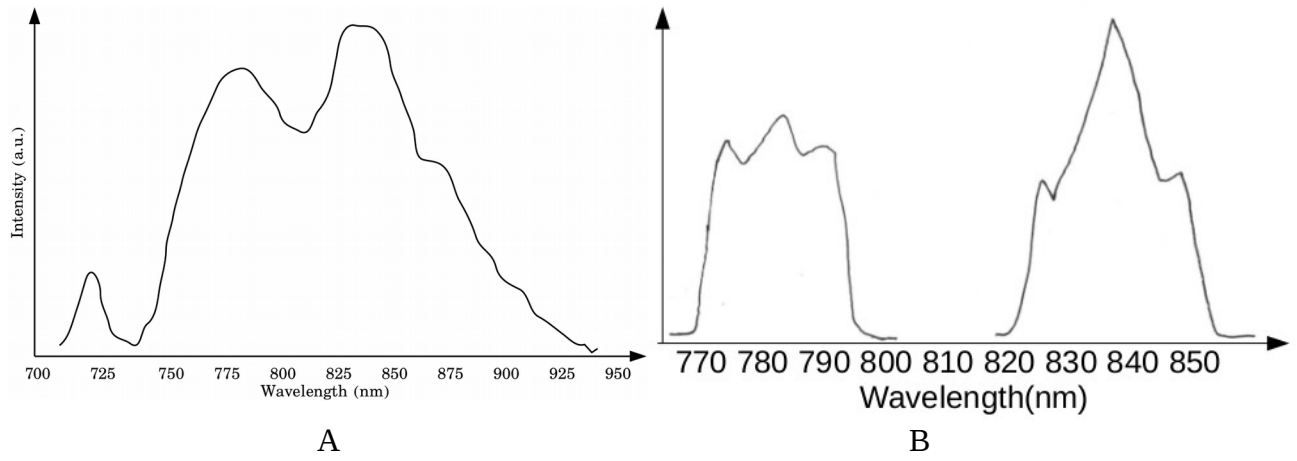

Figure 5.1: Spectrum of the seeding, A-original spectrum of the seeding beam from Joe's lab; B-the chosen seeding spectra that we use in the dual-wavelength amplifier system

During the alignment of seed beam, a fast diode is used to monitor the output beam. The beam in the *LASER* cavity will have a competition between the amplified spontaneous emission(ASE) and the amplified seed. As we can see from figure 5.2-A, if it is not working in a good status, the ASE will be very strong, and that is what we need to get rid of or at least be minimized. Once well aligned, the ASE will be reduced, and the ratio of the amplitude of ASE and seeded pulse will reach more than 1:50 in

the lab, as shown in Figure 5.2-B. However, since we are using a dual-wavelength Regen with a center-wavelength difference of 50 nm, it is not doable to have both seeding to work all in the best. Most of time, a ratio of 1:40 is the compromised working condition for both of them. Practice should be made to get familiar with the ways that leads to better seeding.

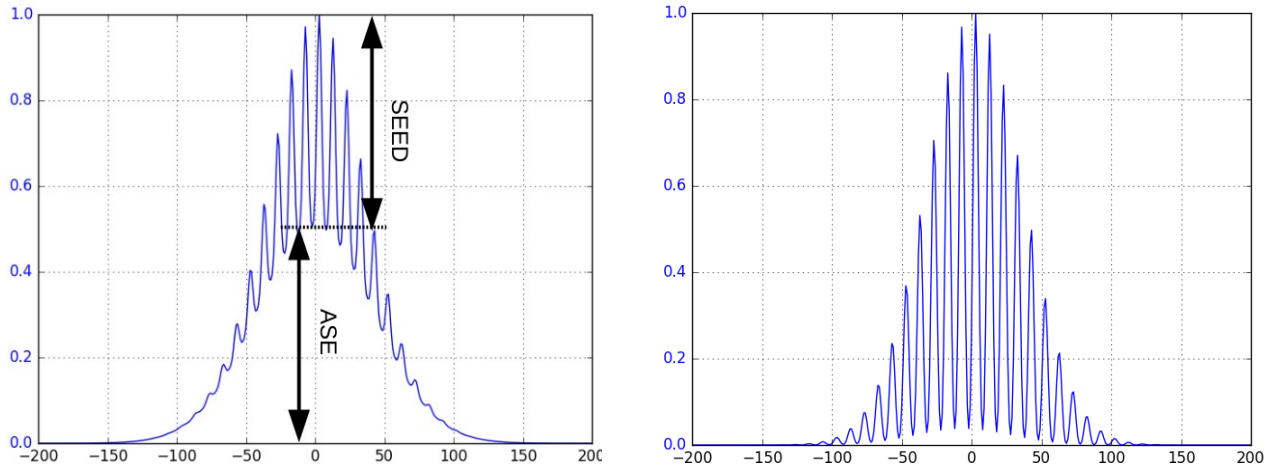

Figure 5.2: Seeding of the Regenerative amplifier: A-partially seeded, B-well seeded

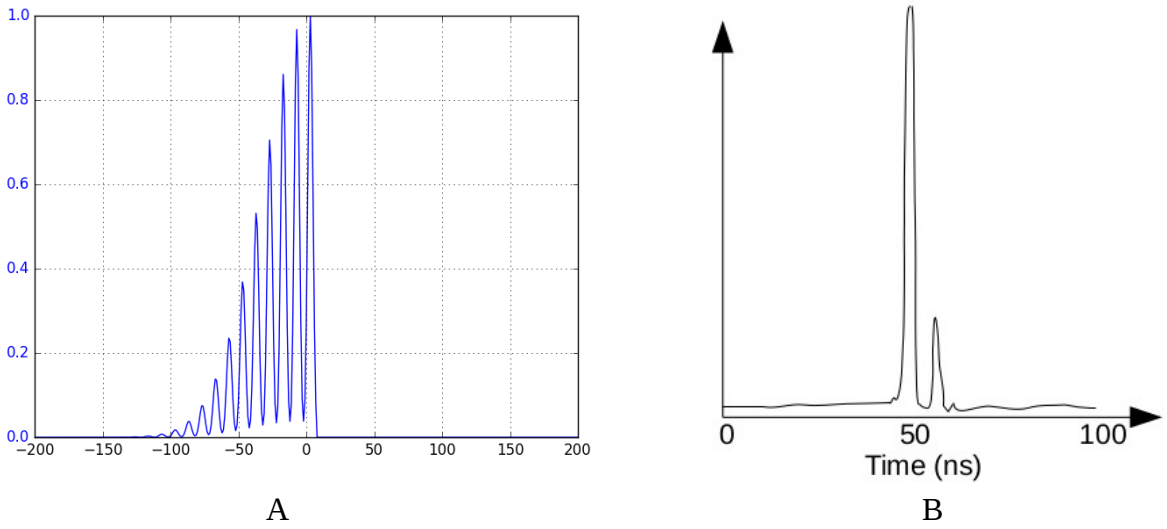

Figure 5.3: Q-switching by Pockel's cell: A-the cut off by Pockel's cell; B-output single pulse detected by diode put after Regen

After the Regen is well seeded, a Pockels cell that works as a Q-switcher in the amplifier will change its voltage and switch the beam out of the Regan. By properly adjusting the Pockels cell, the pulse will be pumped to the maximum energy as shown in figure 5.3-A. A fast diode is put after the Regen to

monitor the quality of the single pulse. For good single pulse, as shown in Figure 5.3-B, the ratio between the main peak and the secondary one should be bigger than 5:1. In addition, the other side peaks should be reduced as much as possible so that most of the pulse power is stored in the main peak. The typical energy of the output pulses after Regen is around 1.8 mJ, or 18 mV with the G-detector.

The next step is to make sure the pulses are compressed to a certain pulse duration, and most of the time it is around 800 fs. To achieve this, the grating distance in the compressor can be changed and the auto-correlator is used to measure the pulse duration. Once the measured pulse duration is around 800 fs for both of the pump pulses, we can send the beams into the hollow fibre chamber for MRG experiment.

5.2 Carry out MRG experiment

Without the multi-pass amplifier, the total pulse energy before the hollow fibre chamber is about 0.3 mJ(most of the time is less than 0.3 mJ), which is good enough to have about 5 Raman orders. Also, if the beam is not well aligned the higher power pulse can damage the front end of the hollow fibre. We should use the low energy beam to do alignment first, and once the 5^{th} anti-Stokes Raman order is generated(a maximum of 7 anti-Stokes is reached for the 0.3 mJ; if the energy goes to 0.27 mJ or even lower, then a 4^{th} anti-Stokes order would be good to turn on the multi-pass), we can power up the beam with the multi-pass amplifier, and run the fully pumped MRG process.

The main purpose of having the 5^{th} anti-Stokes Raman order appearing with the low energy is to make sure that the pump beams are well aligned to go through the hollow fibre. A combination of actions are required together with patience and lots of practice. A detailed description can be found in Turner's thesis[32]. Quite a few things affect the generation of anti-Stokes Raman orders, such as the timing and energy ratio between the two pulses, the single pulse quality, and the seeding quality.

A CCD camera can be put after the hollow fibre to help with the alignment. If the beam is going through properly, the camera will catch a nice circular Gaussian distributed image. Otherwise, the image will have a scattered pattern with lower intensity. The adjustment knobs on both ends of the chamber can help to get the beam through properly. Then, by moving one of the back mirrors in the compressor to time up the two beams, the anti-Stokes Raman order will come up one after another. By balancing among all the factors that affect the Raman orders and with practice, the 5^{th} or even higher

anti-Stokes Raman orders will show up as a victory for the first part of MRG. Thereafter, turning on the second stage of amplifier, the multipass amplifier, pulses with energy of up to 3.0 mJ can be obtained. By fully pumping the MRG process, a rainbow colourful output can be achieved. The highest anti-Stokes order that I have gotten is the 24th with wavelength close to 300 nm. Figure 5.4 shows a colourful image of MRG output beam dispersed by a prism and its spectral measurement with spectrometer.

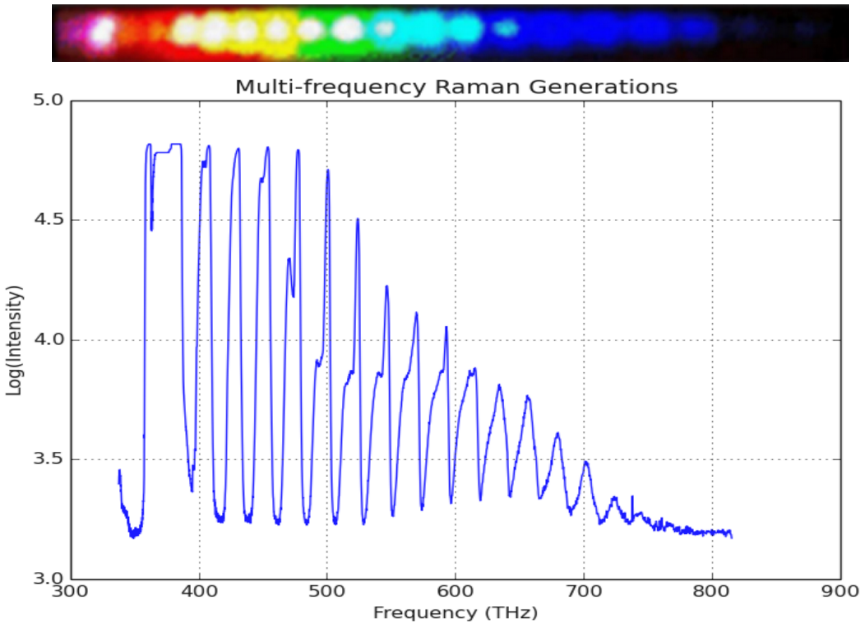

Figure 5.4: The rainbow colourful beam of MRG output and the corresponding spectrum from spectrometer

In Donna's group, we observed an interesting phenomenon that as we change the instantaneous frequency separation between the two pumps. A second peak appears on the red side of each of the Raman orders when the pumps are red-tuned and disappears when they are blue-tuned. The spectrum in Figure 5.4 shows the the result where the red-shifted second peak occurs.

5.3 MRG measurements with spectrometer

Before doing any further study of the red-shifting phenomenon, we will first make sure that MRG process can be done properly in our lab. With the previous steps, we have prepared the two pump beams centred at 786nm and 837nm with total energy of about 2.2 mJ. This energy is lower than the previous 3.0 mJ as we need to make a compromise to have both of the pumps having similar energy. Focusing the beams into the hollow fibre, we can generate a wide spectrum.

As shown in Figure 5.5, more than 22 anti-Stokes Raman orders ranging from 340nm to 740nm are achieved. Note that the plot is used to show all the anti-Stokes Raman orders, while the intensity showing in the figure is not to scale, three measurements of the spectrum for wavelength ranges of 300-450, 450-600, and 600 - 900 nm are used to show the whole spectrum. In fact, the intensity is decreasing as the order of the anti-Stokes going up. There are also Stokes Raman orders, but as the limitation of our spectrometer and the interest of our study, we will not measure them in this thesis. In F. Turner's work, he used a spectrometer with longer wavelength range, and about 8 Stokes orders are detected[32].

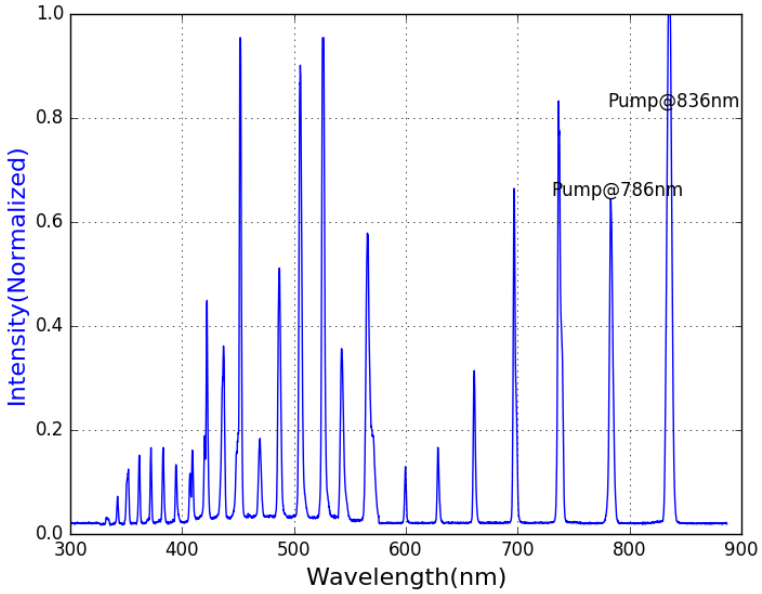

Figure 5.5: Anti-Stokes Raman orders generated from MRG. The intensity is not to scale among the different Raman orders, as three measurements of the spectrum for wavelength ranges of 300-450, 450-600, and 600 - 900 nm are used to show the whole spectrum

MRG does an astonishing work in generating the rainbow colourful spectrum. As can be calculated, with the anti-Stokes alone and if well combined and compressed, a train of pulses of about 2 fs can be generated. Of course, there is still more work that can be done to increase the Raman orders. Since the main purpose of this study is focused on the red-shifted spectrum, we will move on to the production of the novel red-shifted spectrum.

To do that, we can move the back mirror in the compressor by rotating the micrometer. The micrometer has a step resolution of 0.01 mm, and in the experiment, we take measurement with every 5 lines of movement. The 5 lines of rotating will move the mirror backward or forward for 0.05 mm, thus gives

the pulse a 1/3 ps time delay change. Since our pumps are positively or negatively chirped, the time delay between the two pumps will change the instantaneous frequency separation, as shown in Figure 5.6-Left. Knowing the chirp rate of the pumps from FROG calculation is about 2.5 THz/ps. Thus, the 1/3 ps time delay will change the instantaneous frequency separation by 0.83 THz.

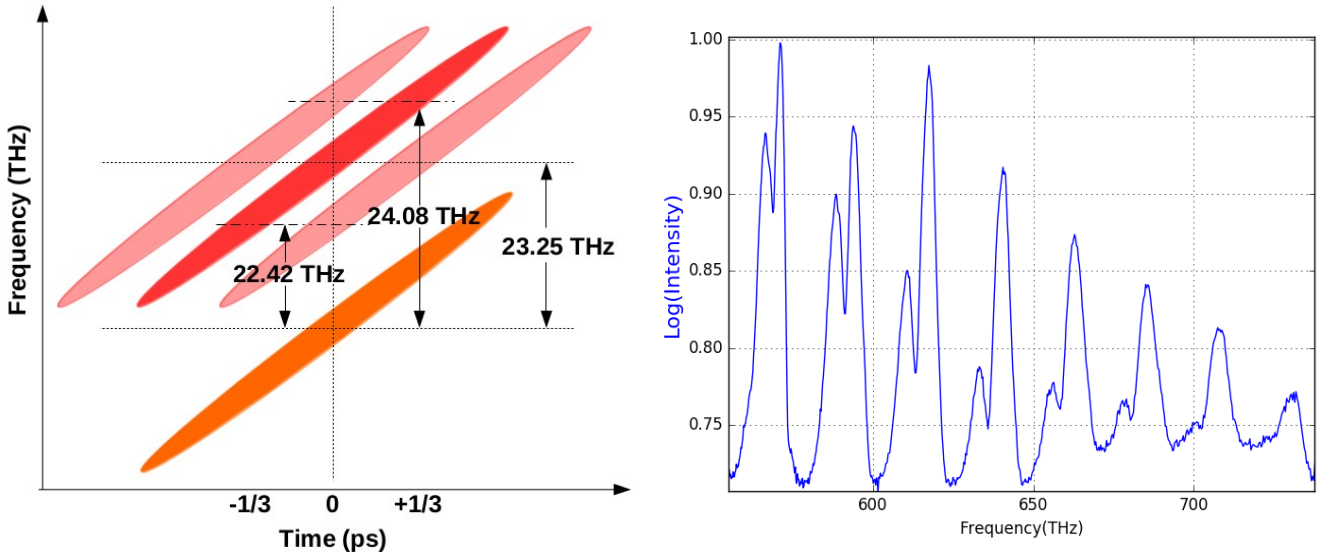

Figure 5.6: Left-Instantaneous frequency separations with different time delays between the pump(red) and the Stokes(orange); Right-Raman spectrum orders with red-shifted shoulders

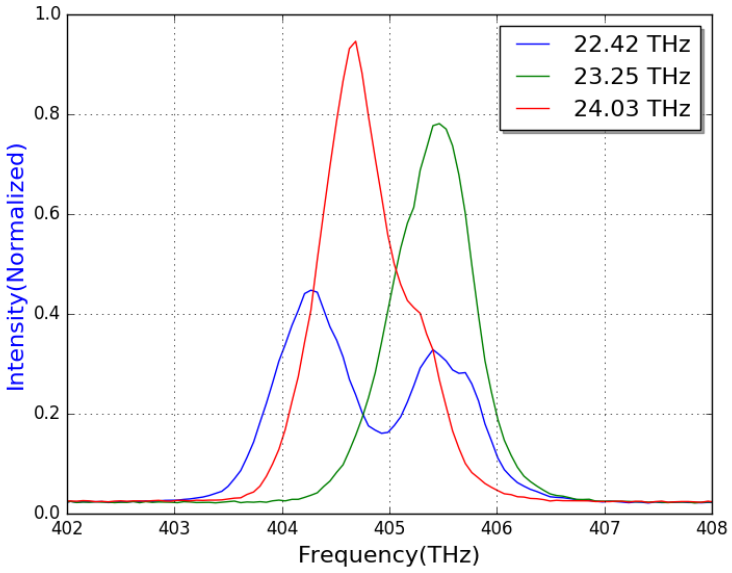

Figure 5.7: Spectral measurement from spectrometer for the first anti-Stokes Raman spectra with different instantaneous frequency separations

In the process of instantaneous frequency separation tuning, we found that the most anti-Stokes Raman orders are achieved when the two pumps are red-tuned, or with smaller instantaneous frequency

separation compared to the 23.25 THz Raman frequency of SF_6. Similar phenomenon was seen by A. V. Sokolov et al., and they suggested that the extra number of Raman orders may be caused by the Stark shifting[147]. Figure 5.6-Right shows the 8-15 anti-Stokes orders with 22.42 THz instantaneous frequency separation. For each of the orders, the right peak is the original anti-Stokes Raman spectrum and there is a second peak showing up on the left side of it, appearing as a double peaked spectrum pattern. Also, as can be seen from the plot, the separation of the two peaks is increasing as the order raises. In Hao's paper, the two-photon Stark shift model is suggested to explain the red-shifted spectrum, and the generalized Rabi frequency Ω' change of each SRS process will add up causing these further separations.[35]

Figure 5.7 shows the first anti-Stokes Raman spectrum with different instantaneous frequencies. As illustrated, the spectrum is switching from a single peaked to a double peaked pattern as we change the time delay, and the separation of the two peaks in 22.42 THz case is about 1.7 THz. The red-shifted spectrum makes the original Raman spectrum bandwidth more than doubled. The widened spectrum might be beneficial as it will help reduce the number of pulses within a profile and hence increase the pulse power. On the other hand, if there is evidence showing that the red-shifted spectrum does no good to our final ultra-short pulses, we should try to get rid of it. To answer this question, we need more information about the spectra. However, the spectrometer is not able to provide extra information.

5.4 Pump and Stokes pulse measurement with FROG

We used the FROG setup to measure the pump pulses. The data was recorded by a CCD camera and a data recording filter was used to suppress background noise and to prevent over saturated data. The recorded data is a 2D array with 720*576 elements, each of the elements represents the intensity of the trace and ranges from 0 to 254. We only record valid traces with maximum number of the 2D array element bigger than 100, and no more than 2 elements equal to 254. Then with the calibration factors, the FROG program can do the calculation and give reconstructed pulses. Figure 5.8 shows the recorded data and the results from FROG calculation for our Stokes pulse with centre-wavelength of 837 nm. The FROG error is about 0.010, which is higher than the 0.005 error that can be achieved with low-noise 128*128 pixel trace data as stated in R. Trebino's book[160]. I would think the high error comes from the noise in the measurement. As shown in the end of Chapter 4, we have large background noise in our system. The FWHM for the Stokes is 840 fs. The pulse duration is similar to what we got from

auto-correlator. However, the FWHM of the spectrum for the Stokes pulse is only 1.85 nm, different from the 3.0 nm as given by the spectrometer.

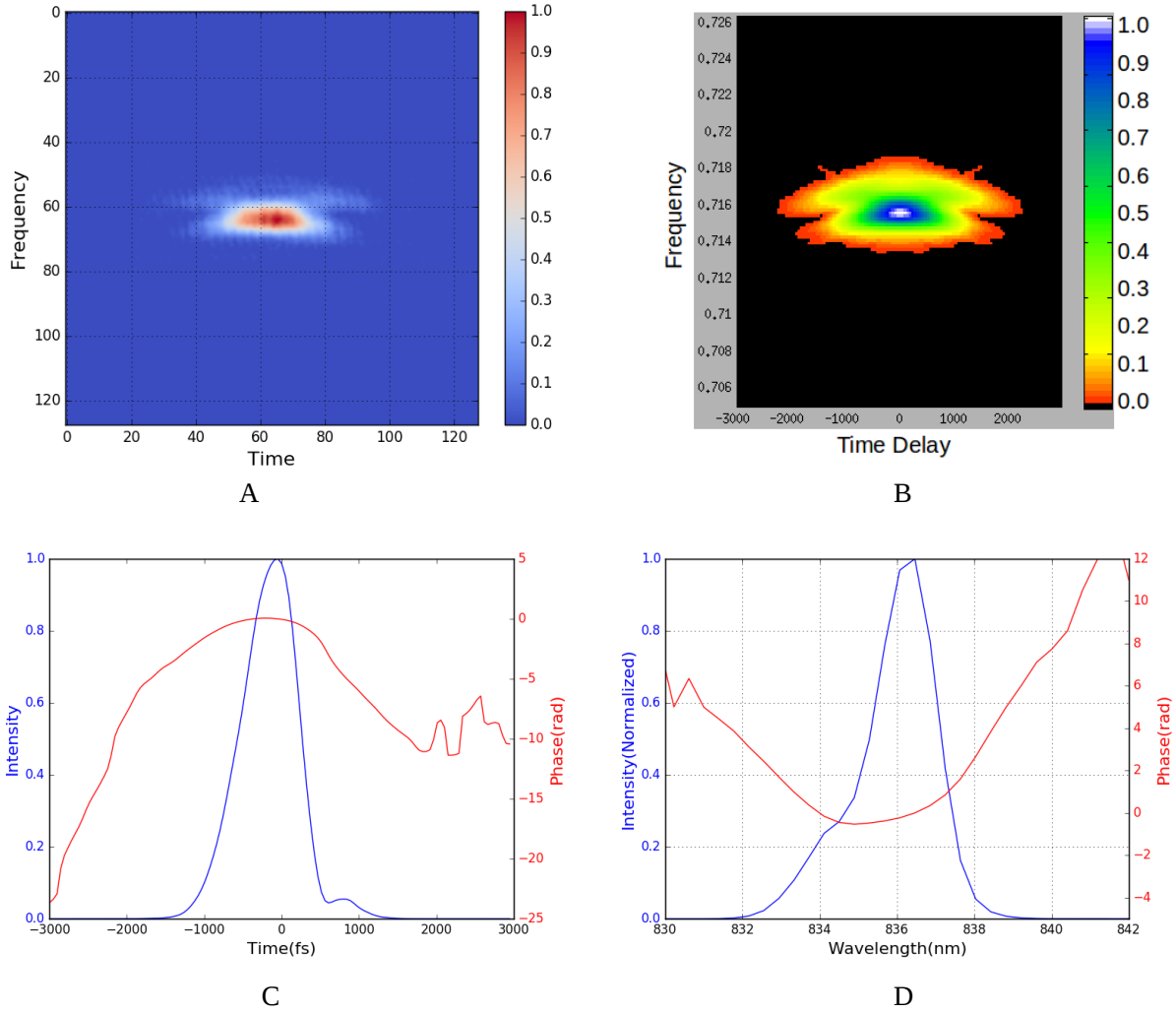

Figure 5.8: Pulse measurement for the 837 nm Stokes pulse with FROG, A-original data(128*128 pixels); B-reconstructed trace(with FROG error of 0.010); C-calculated pulse in time domain; D-calculated pulse in frequency domain, the spectrum

The difference is quite big, but keep in mind that there is also a big difference between the resolutions of the two, 1.5 nm for the spectrometer verses 0.1 nm for the FROG. Thus, if we convolve with the spectrum from the FROG result with the 1.5nm resolution, the modified spectrum then becomes very close to the one from spectrometer, as illustrated in Figure 5.9. As the FROG is working properly for the pump pulses, our next step is to use the device to study the anti-Stokes Raman orders, which follows similar processes as the measurement of the pump pulses. Before the measurement of our destined first anti-Stokes Raman order, it is recommended to check the fluctuation of the pump pulses

as the profile of the pumps plays an important role for MRG experiment. Also in the previous experiments, Hao found that the fluctuation of the *LASER* system is too significant that it washes out the changes caused by the time delay.[166]

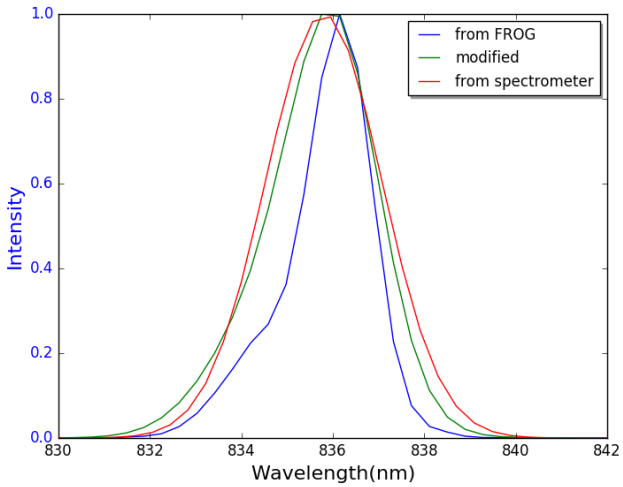

Figure 5.9: Spectrum of the Stokes pulse at 837 nm, comparison between the spectrometer and the FROG, the green line is the result of convolving the FROG spectrum and the 1.5 nm resolution of our spectrometer

With similar process, we can measure the pump pulse centred at 786 nm. As shown in figure 5.10, the pump pulse duration is 800 fs, and the bandwidth is 3 nm. This bandwidth from FROG is similar to what we have from the spectrum as the convolution of 3 nm bandwidth with 1.5 nm resolution will not have a big change to the overall spectrum.

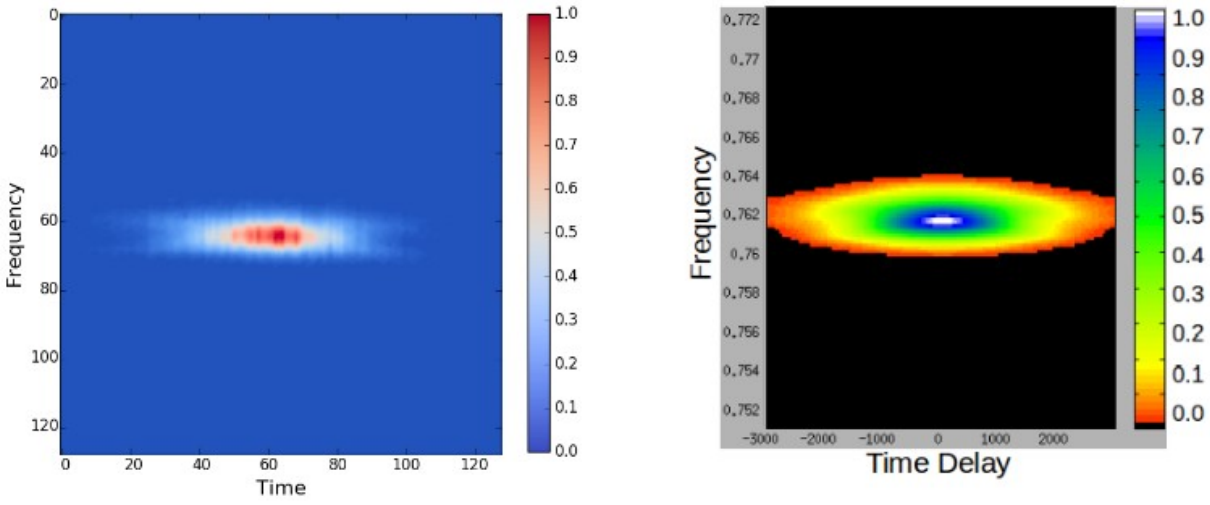

A B

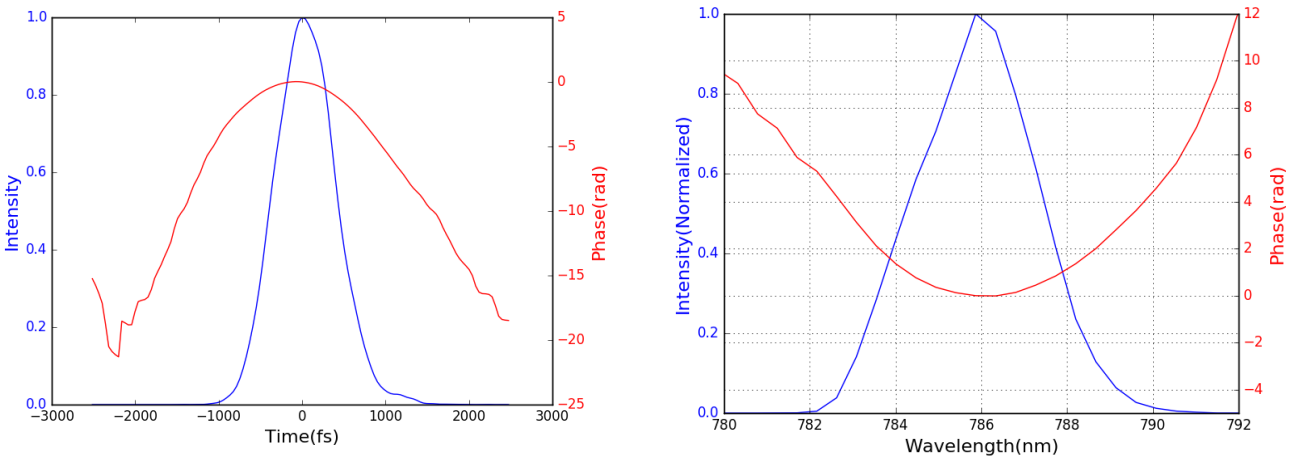

C D

Figure 5.10: Pulse measurement for the 786 nm with FROG, A-original data(128*128 pixels); B-reconstructed trace(with FROG error 0.015); C-calculated pulse in time domain; D-calculated pulse in frequency domain, the spectrum

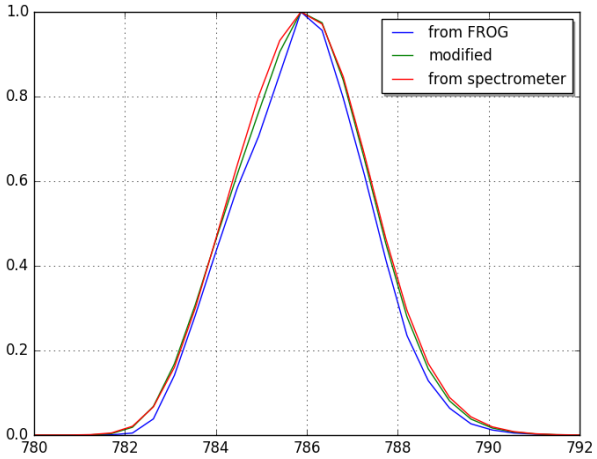

Figure 5.11: Spectrum of the pump pulse at 786 nm, comparison between the spectrometer and the FROG, the green line is the result of convolving the FROG spectrum and the 1.5 nm resolution of our spectrometer

Two comparison sets of measurements were done to show the stability of the pump pulses , with one randomly taken within one hour and the other during several days. As can be seen in Figure 5.12-left, the pulse shape and its instantaneous frequency stay similar within one hour duration, and the fluctuation is relatively small. However, from the right plot, the pulse has a much bigger change in both the pulse profile and the phase with a longer period of time. The one hour duration is chosen since in most cases a set of measurements can be fully accomplished within that duration. It has been noticed

that the *LASER* is much more stable after turning on the system for about 20 minutes, and a set of experiment should be done within 1.5 hours period.

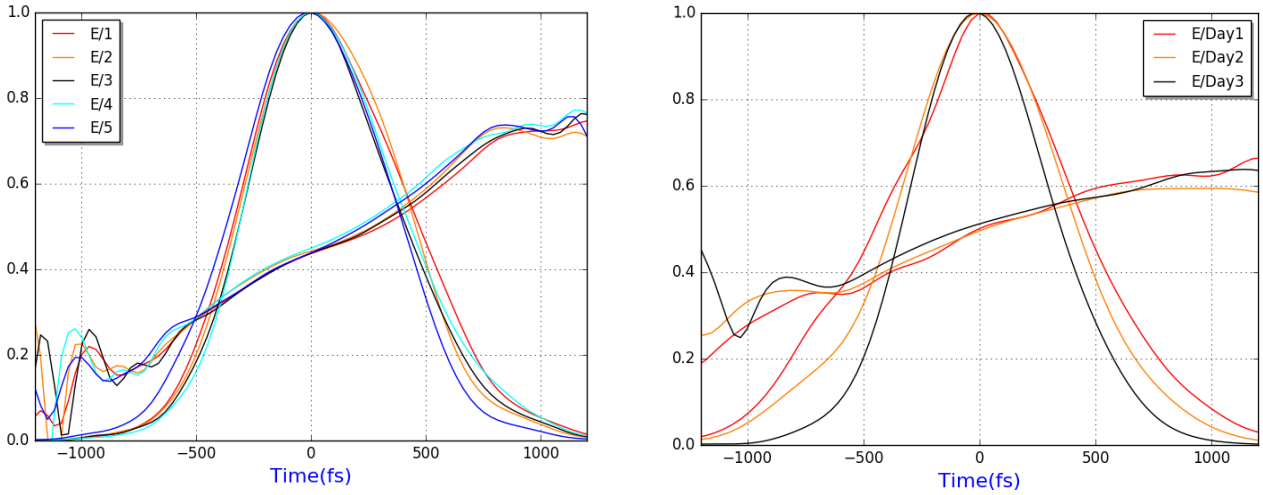

Figure 5.12: Pump pulse and its corresponding instantaneous frequency of different shots, . Left- Measurements randomly taken within one hour; Right- Measurements taken randomly during different days

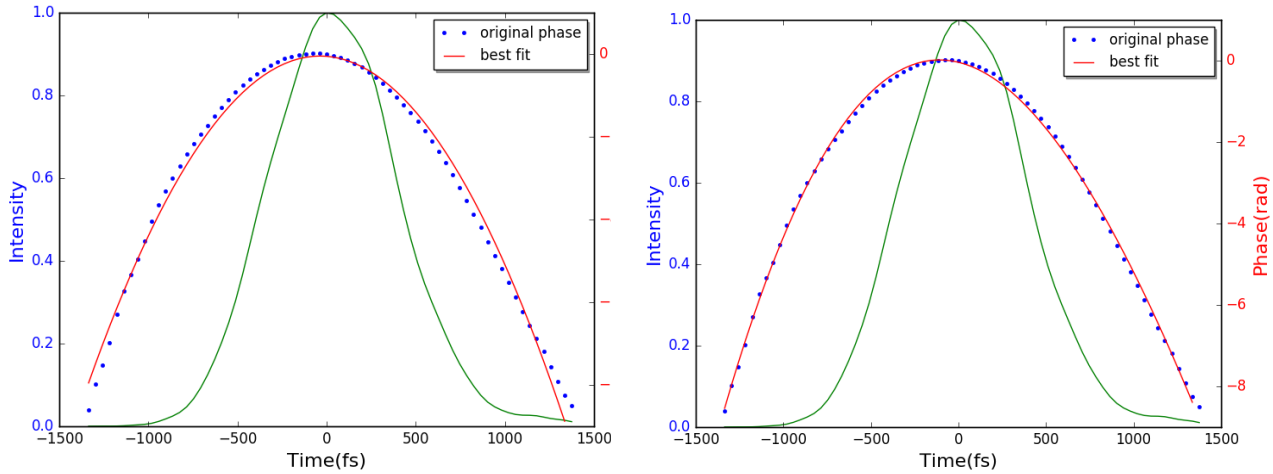

Figure 5.13: Pump pulses phase, green curve is the pulse shape, blue dots are the phase data while the red curve is the best fit. Left- Second order fit for the phase; Right- with both second order and third order fit.

On the other hand, based on the calculated data, the pump pulses seem not just have a linear chirp. To understand how the phase looks like, polynomial fit is applied for the pump pulse, where

$$y = \sum_n p_n x_n^n \quad (5.4\text{-}1)$$

In figure 5.13, a second order and third order poly-fit are done for the phase curve. As shown in the plots, a third order phase matches better to the original data. The extra higher order phase is reasonable

as there are higher orders phase added to the pulse during the preparation of the pulses. Also, the grating-pair compressor supports the existence of higher order phases as it is not able to perfectly compress the pulses to Fourier transform limited pulses.

Table 5.1: The coefficients for the phase curve fit

Fitting order	p_0	p_1	p_2	p_3
Second order	-5.38×10^{-2}	$-3.47\times10^{-4}s^{-1}$	$-4.69\times10^{-6}s^{-2}$	0
Third order	-4.00×10^{-2}	$-1.08\times10^{-3}s^{-1}$	$-4.73\times10^{-6}s^{-2}$	$-6.19\times10^{-10}s^{-3}$

Chapter 6

Experiment Results and Analysis

In this Chapter, the results of MRG experiment, data processing, and data analysis are presented. We started with measuring the first anti-Stokes Raman order by sending the whole beam with all the Raman orders into the FROG setup. It turned out that the signal for the first anti-Stokes Raman order from the BBO crystal not only contains the auto-correlation of the first anti-Stokes order, but also the cross-correlation from the second anti-Stokes and the pump, the third anti-Stokes and the Stokes, etc. To get rid of the extra signals, we then switched to a configuration with a prism-pair to separate the Raman orders and to pick out the first anti-Stokes order for measurement. However, due to the longer travel distance, extra optical devices, and extra dispersion, the measurement for the weak first anti-Stokes Raman order becomes difficult. Finally, a cross-correlation of the first anti-Stokes and the reference beam, the Stokes, is used. The new configuration uses fewer optical devices and can remove the extra signals. Further, the relatively stronger Stokes reference beam makes it possible to measure weaker first anti-Stokes, and up to the third order anti-Stokes can be measured. The FROG results showed that the spectrum becomes two separated peaks with different phases, and the extra red-shifted spectrum turns the first anti-Stokes pulse into an oscillation pattern. In addition, the FROG has poor matching in the low pump intensity cases. Also, other experimental results are presented and discussed, such as measurement of second anti-Stokes Raman order and MRG with negatively chirped pump and Stokes.

To understand the red-shifted spectrum, the FROG setup and algorithm are applied to learn the details of the Raman orders. As suggested by Rick Trebino, the FROG in our lab is constructed by setting up a self-built spectrometer after an auto-correlator. In the following study, we will mainly focus on the measurement and analysis of the first anti-Stokes Raman order. All the following MRG experiments were carried out in a 0.5 m long hollow fiber with diameter of 150 μm and filled with SF_6. The gas pressure was kept constant at 1 atm + 5 PSI. The previous work done by F. C. Turner suggests that the number of MRG orders is maximized around 1 atm gas pressure[32]. An extra 5 PSI is set to ensure that the chamber is well sealed. Besides, as shown in Chapter 5, the pump and Stokes pulses change from day to day, but stay quite the same with a continuing run of experiment. We will provide the measurement of the pump and the Stokes pulses for each of the following experiments. During the pulse preparation of the pump pulse and the Stokes pulse, the auto-correlator and spectrometer are used for the measurement, such that we can easily adjust the pulses to have proper pulse duration and bandwidth. After the pulse preparation, the pulses are measured by the FROG for better and more detailed information.

6.1 Measuring the first anti-Stokes order without beam separation

At the beginning, we re-direct the whole output beam and send it to the FROG setup, as shown in Figure 4.15 in Chapter 4. We thought that each of them would do the auto-correlation and we would be able to measure all of them within one beam by simply turning the BBO crystal to certain angles. Turning the angle of the BBO crystal to have the first anti-Stokes' frequency doubled, we have the signal, record it, and run the FROG algorithm. Table 6.1 shows some of the main characteristics of the pump and the Stokes pulse. The linear approximation chirp rate for the two are similar to each other, with the chirp rate of the pump being slightly higher.

Table 6.1: Characteristics of the pump and the Steokes(please referring to figure C.1 in appendix C for detailed information)

	Center-wavelength	Pulse duration	Bandwidth	Chirp rate (linear approximation)
Pump	778 nm	754 fs	2.8 nm	1.80 THz/ps
Stokes	828 nm	484 fs	3.4 nm	1.60 THz/ps

Figure 6.1 shows the spectra of a set of anti-Stokes with different time delay between the pump and the Stokes, with the pump pulse in advance of the Stokes pulse at 1 ps, 2/3 ps, 1/3 ps, 0 ps, -1/3 ps, and 2/3

ps, which will change the instantaneous frequency separation to be about 25.05 THz, 24.45 THz, 23.85 THz, 23.25 THz, 22.65 THz, and 22.05 THz. As can be seen from the plots, the red-shifted peaks do occur even in the blue-tuned situation. The single peak spectrum only occurs when the pump and Stokes pulses are delayed by 1 ps. If we take the pump duration into consideration, the ~600 fs pump and Stokes pulses would have very little overlapping part. We think that MRG is having pure Raman process at that situation. Comparing the A, B ,C plots in figure 6.2, we can see that the extra part of the spectrum is moving towards the red side. As we keep decreasing the instantaneous frequencies, a new changing pattern appears. As seen from plots D, E, and F, the spectra become double-peaked and the centre frequencies of the two peaks remain in similar positions, where we think the red-shifting effect is taking place. By looking at all the plots, except for B and C we can understand the phenomenon as that the red-shifting effect becomes stronger when the instantaneous frequency separation is decreased. However, what about the cases with the instantaneous frequency separations at 24.45 THz and 23.85 THz, as in B and C, respectively?

While we were dealing with the odd plots, a new problem arised. As we send the whole beam with all the Raman orders and together with the pumps into the FROG for measurement, the cross-correlation between different orders can become an issue. Within the output beam, we have the two pumps, anti-Stokes and Stokes Raman orders. Written in frequencies, we would have components of $\omega_0 \pm j\,\omega_R$, where ω_0 is the frequency of pump 786 nm, ω_R as the Raman frequency, and j can be any integer. The measurement of the first anti-Stokes would have a centre-frequency of $\omega_0+\omega_R$, meaning that the centre-frequency of the signal would be $2(\omega_0+\omega_R)$. However, for the second order anti-Stokes at $\omega_0+2\,\omega_R$ and the pump at ω_0 , the cross-correlation of them would also have a centre-frequency at $2(\omega_0+\omega_R)$. And so does the cross-correlation between the third order with the pump at 837 nm. Though the second and third anti-Stokes order are less intense than the first anti-Stokes, the cross-correlation with the intense pump pulses will still lead to big unwanted signal. In such situation, the FROG traces that we get by sending the whole beam into the BBO crystal might contain a significant amount of unwanted signal, and therefore the traces can not be used to calculate the anti-Stokes pulse.

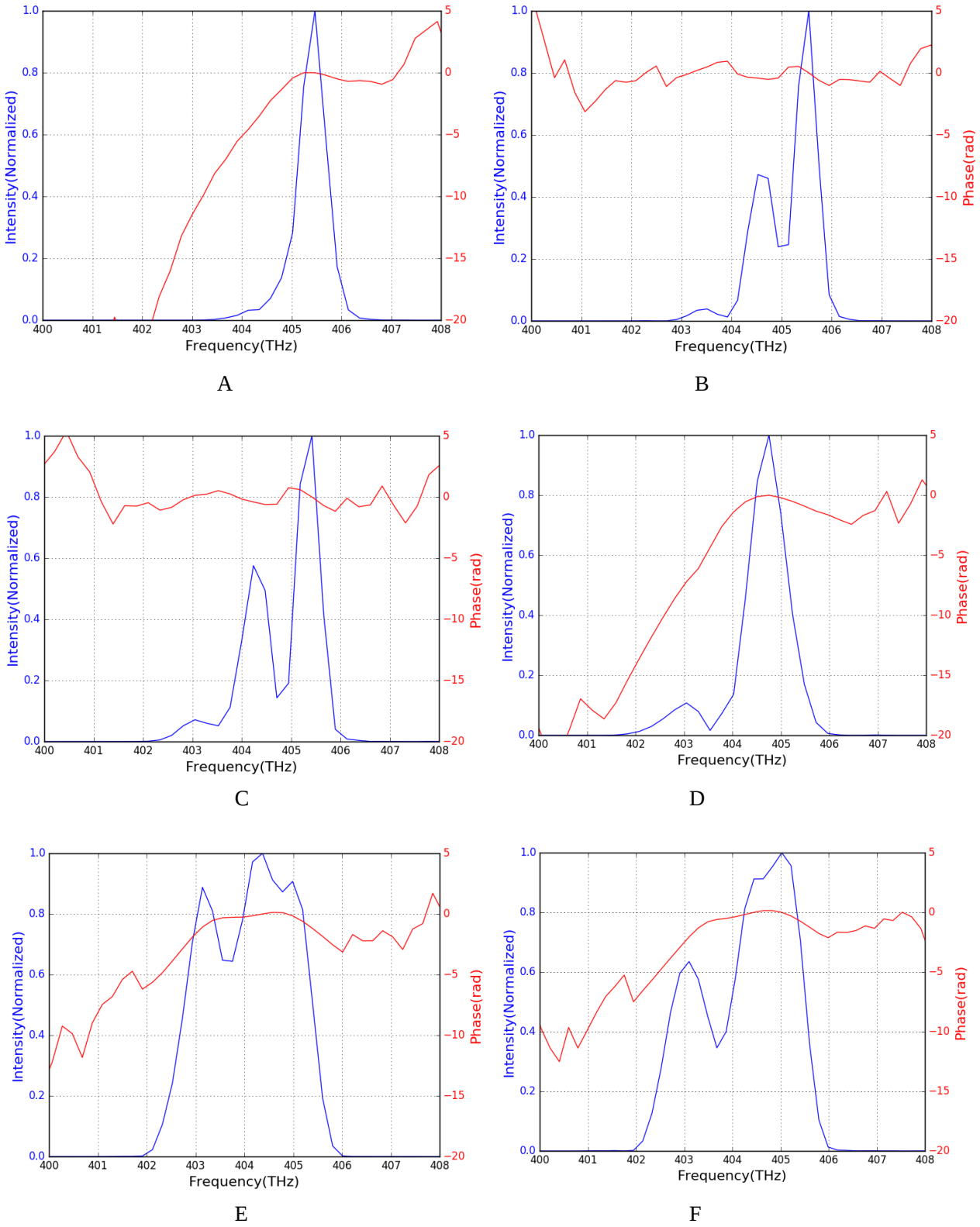

Figure 6.1: FROG reconstructed anti-Stokes Spectra and their phases with different instantaneous frequency separations. A- 25.05 THz; B- 24.45 THz; C- 23.85 THz; D- 23.25 THz; E- 22.65 THz; F- 22.05 THz.

6.2 Measurements with separated orders

When the beam consists of a mixture of different signals, we would not be able to measure the first anti-Stokes pulse. To solve this problem, a new configuration is designed.

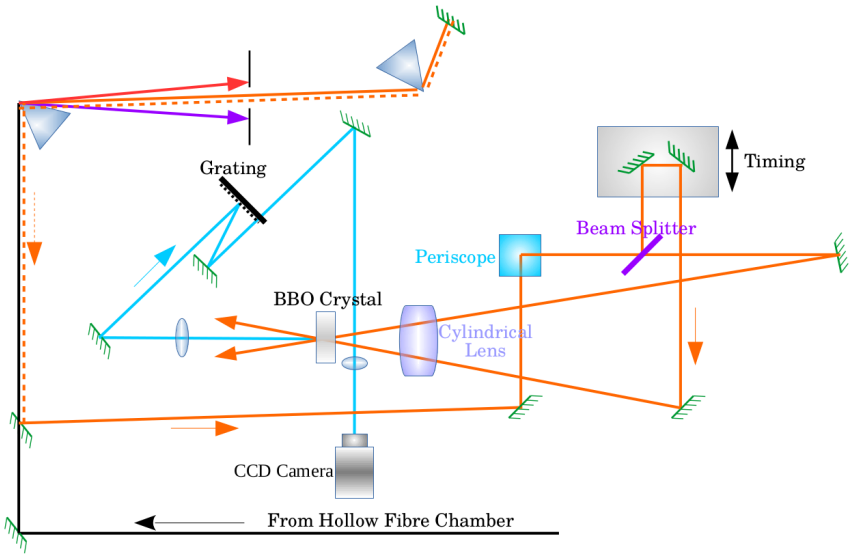

Figure 6.2: Diagram of FROG measuring 1st anti-Stokes Raman order with prism-pair to separate each of the Raman orders

As illustrated in Figure 6.2, instead of sending the whole beam into FROG, we are using a pair of prisms to separate the Raman orders, and a slit is applied to select the specific order while blocking all the others. The slightly lowered returning beam is re-directed to the FROG for measurement. This setup can easily get rid of the problem that different Raman orders get to the BBO crystal at the same time. However, the biggest problem is that the 1st anti-Stokes order is very weak and the ~740 nm wavelength colour is hard to be seen either by bare eyes (with goggles on!) or using the IR-card or the IR-viewer, which makes it challenging to do the alignment. At the meantime, the pair of prisms introduces dispersion and even spatial chirp to the pulses and the long travelling distance would make the alignment even more complicated.

When there is a problem, there is always going to be a solution. Following the setups in Figure 6.2, we need higher power for signal output and we would like to have an easier alignment. Then, comes to the cross-FROG setup as shown in Figure 6.3. We have a bunch of Raman orders in the output from the hollow fiber chamber, and we have the pump beam. Why not just cross-correlate the two beams? Filters available in the lab can be used to filter out the 786 nm pump beam and to keep the beam with only the

Stokes order at 837 nm. The pulse information of the Stokes can be measured from the auto-correlation part. The setup is relatively simple as compared to the previous ones. No prism pairs are needed and less optical devices are used, and the strong Stokes from the pump beam makes it possible to measure Raman orders with very low energy. With this cross-FROG setup, we are able to measure the second anti-Stokes order and even higher Raman orders.

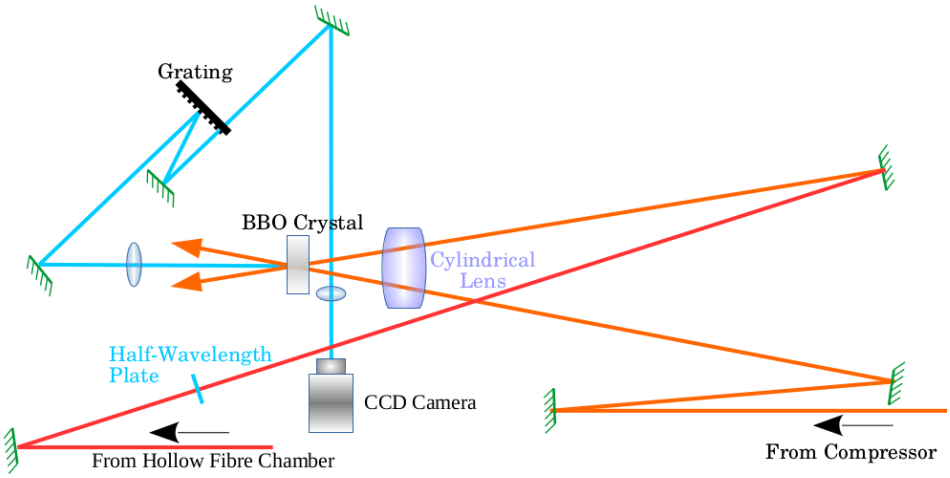

Figure 6.3: Diagram for the Cross-FROG setup for measuring Raman orders

6.2.1 First anti-Stokes with the change of instantaneous frequency separation

With the new configuration of cross-FROG, we can measure the anti-Stokes. The idea is straightforward, we measure the first anti-Stokes order with different instantaneous frequency separations and see what the time domain pulse and frequency domain spectrum look like, respectively. The characteristics of the pump and Stokes pulses are given in table 6.2, the total energy is 2.2 mJ.

Table 6.2: Characteristics of pulses(please referring to figure C.2 in appendix C for detailed information)

	Center-wavelength	Pulse duration	Bandwidth	Chirp rate (linear approximation)
Pump	786 nm	781 fs	2.10 nm	1.18THz/ps
Stokes	836 nm	830 fs	1.75 nm	1.23 THz/ps

Figure 6.4 shows the 1st anti-Stokes order with different instantaneous frequency separations. Three cases are shown here with one instantaneous frequency separation right on the Raman frequency 23.25 THz, and the other two on each side of the Raman frequency. The three cases were chosen as the spectrometer measurement results showed that the red-shifted shoulder occurs and disappears as we red-tuned and blue-tuned the pumps[33]. The spectrum from the FROG calculation has two much thinner

peaks and are more separated from each other. In addition, the red-shifted spectrum appears for the 23.90 THz case, while the spectrum from spectrometer shows no sign of side peak. The differences can be addressed by the fact that the FROG setup has higher resolution.

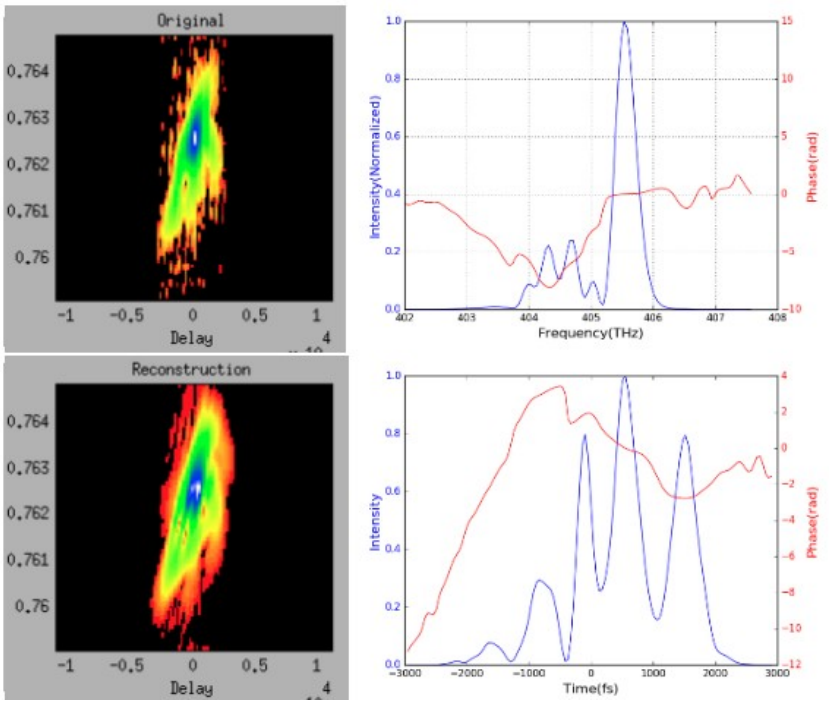

A

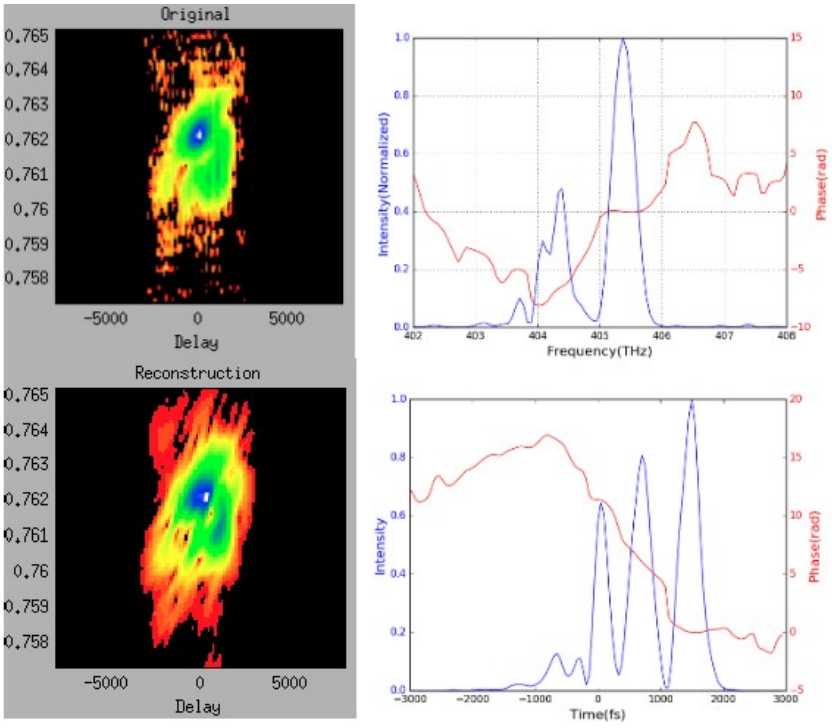

B

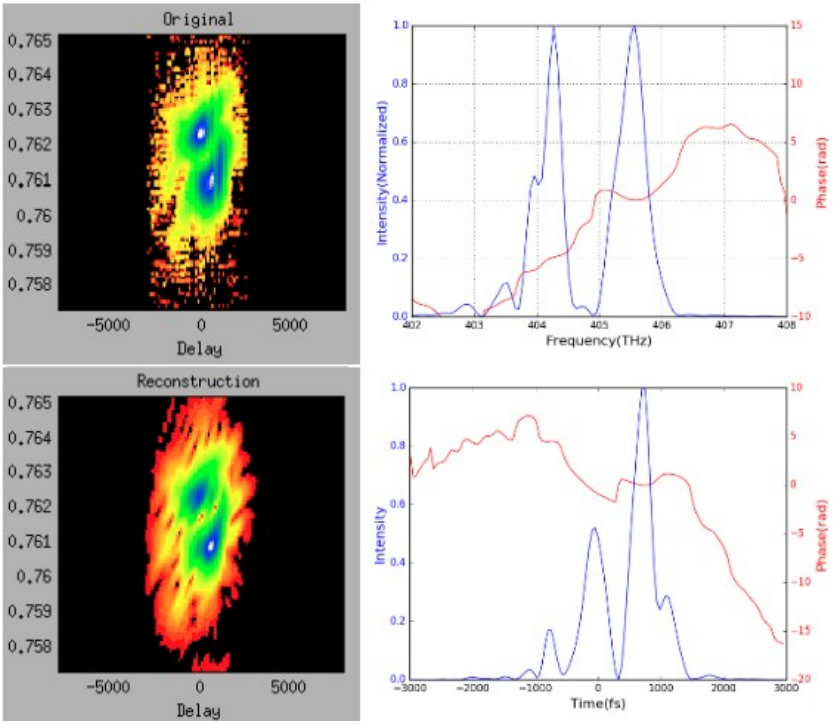

C

Figure 6.4: The first anti-Stokes order calculated by FROG algorithm(FROG errors are 0.014, 0.011, and 0.018 for the A, B, and C, respectively). The instantaneous frequency separations are A-23.90, B-23.25, and C-22.60 THz. For each of the A, B, and C plots, the left-top is the original data from experiment; left-bottom is the reconstructed trace by using the FROG program; right-top is the spectrum; right-bottom is the pulse in time domain.

We checked the variation in the separation of the two peaks in the most separated situation, case C in figure 6.4. We took 11 measurements within the same condition and the results are plotted in figure 6.5. The average peak frequency separation of the FROG result is about 1.35 THz.

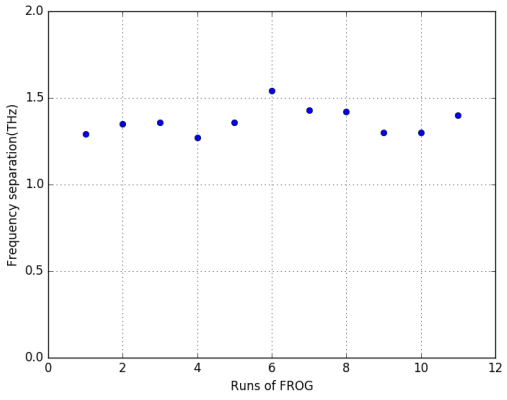

Figure 6.5: The peak separation of the double-peaked spectrum from FROG calculation, in the case of 22.60 THz

For the red-shifted peak in the anti-Stokes Raman order, we have plotted the spectra with different instantaneous frequency separations. As can be seen in figure 6.6, the Raman part is peaked around 405.7 THz, while the red-shifted part is peaked near 404.4 THz. The result indicates that the red-shifted spectrum is not coming from the four waving mixing process. This is because in the four-waving mixing process, the peak will move towards one side as when the instantaneous frequency separation is decreased.

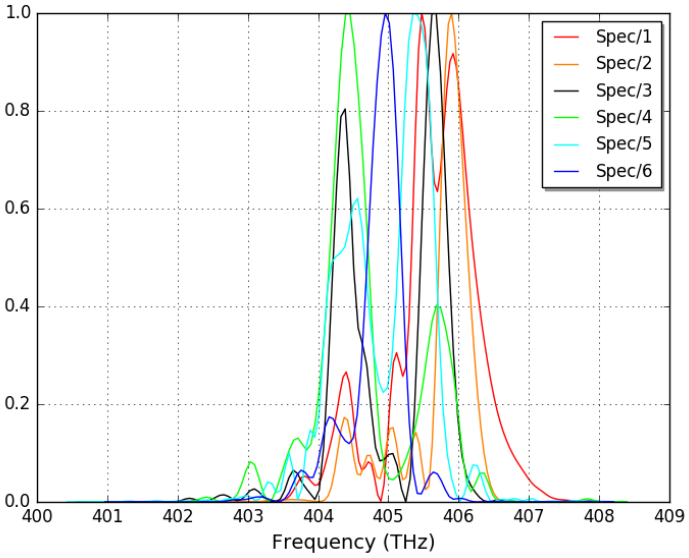

Figure 6.6: Spectra for the first anti-Stokes with different time-delayed pump and Stokes. In the plot, from Spec/1 to Spec/6, the instantaneous frequency separations are 24.55, 23.90, 23.25, 22.60, 21.95, and 21.30 THz.

Also, for the three cases, as shown in figure 6.4, the original Raman part of spectrum stays similar to each other, while the red-shifted spectrum is showing up and growing as we decrease the instantaneous frequency separation. Recalling the equations 2.4-6 and 2.4-7 from Chapter 2, the generalized Rabi frequency is given as $\Omega'^2=\Omega^2+\Delta^2$ with two parts, the Rabi frequency Ω, and detuning Δ. The Rabi frequency is given by $\Omega(t)e^{i\theta}=\frac{\alpha_{12}}{2\hbar}\sum_j V_j(t)V_{j-1}^*(t)$, and thus depends on the amplitude of the overlapped e-fields. In our case, the Rabi frequency is increasing at first and then decreasing along the change of time delay from -1 ps to 1 ps. For the second part, $\Delta=\frac{\partial\theta}{\partial t}+\frac{2\pi(\alpha_{22}-\alpha_{11})I}{\hbar c}+\delta\omega$, the change of instantaneous frequency separation affects the $\frac{\partial\theta}{\partial t}$ term while leaving the other two terms staying the same. For our linearly chirped pumps, the $\frac{\partial\theta}{\partial t}$ term increases linearly as a function of the

time delay. The changes of Rabi frequency and detuning will change the generalized Rabi frequency Ω'. Therefore, by changing the time delays, we get Raman orders with different peak separations.

However, different from the original Raman spectrum, the red-shifted part of spectrum shows an oscillation pattern that is similar to the third order phase effect. We are interested in the mechanism of this third order phase effect, and will discuss it in our simulation part in next chapter.

To better understand the pulses, we plotted out the instantaneous frequency as a function of time throughout the pulse of the anti-Stokes. Figure 6.7 shows the instantaneous frequencies of the anti-Stokes with different time delay between the pump pulse and the Stokes pulse. The B, C, D plots corresponding to the three situations in figure 6.5. In plots C and D, the Raman and red-shifted spectra are much separated from each other and also have amplitudes close to each other. The huge dip in the middle of the instantaneous frequency occurs when the magnitude of the field goes close to zero. If ignoring the middle peak, the slopes of the instantaneous frequency curves are very similar to those of the pump and the Stokes. The differences in plots A, B, and E may come as a result of the less separated spectrum. With this idea in mind, we think both the Raman and the red-shifted spectra have the same phase as the pump (assuming pump and Stokes have the same phase), and we will use this assumption for our pulse setup in the simulations.

In the time domain, the anti-Stokes pulse is no longer a clean single pulse, as the extra part of spectrum turns the pulse into an oscillation pattern. The period of the oscillation is determined by the separation of the spectral peaks. For example, the frequency separation for part C in figure 6.4 is about 1.32 THz. This frequency separation will cause an pulse oscillation of $\frac{1}{1.32\,THz} = 757\,fs$ and the pulse oscillation period from the plot is around 750 fs.

6.2.2 First anti-Stokes Raman order with different pulse energy

As seen from the previous work, the Raman orders are pulse power dependent. Not only the number of orders, but also the details of each order. As far as our research interest concerns, we will only study the effect of pump energy to the first anti-Stokes Raman order.The information for the pump and Stokes pulses are shown in Table 6.3.

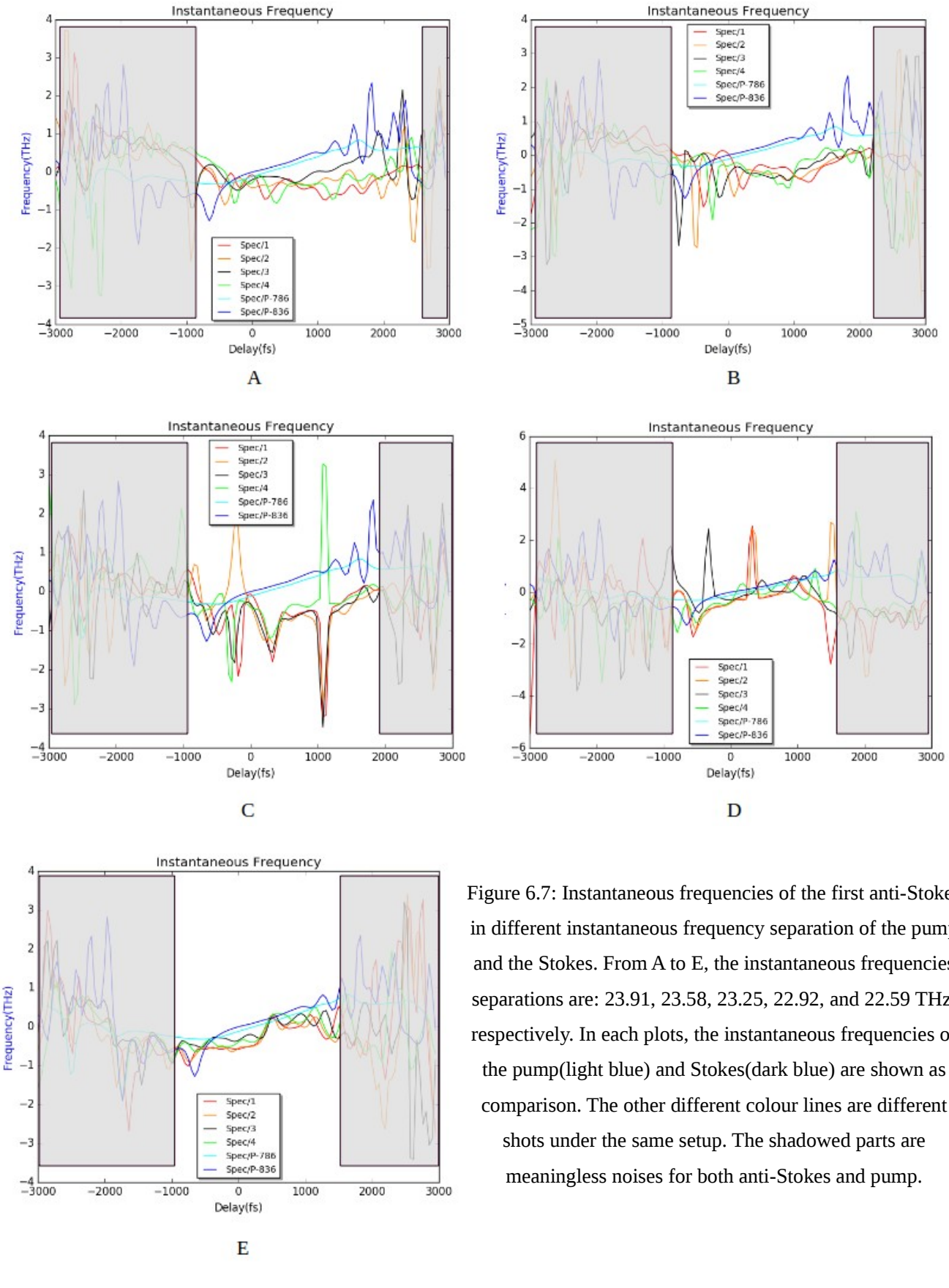

Figure 6.7: Instantaneous frequencies of the first anti-Stokes in different instantaneous frequency separation of the pump and the Stokes. From A to E, the instantaneous frequencies separations are: 23.91, 23.58, 23.25, 22.92, and 22.59 THz, respectively. In each plots, the instantaneous frequencies of the pump(light blue) and Stokes(dark blue) are shown as comparison. The other different colour lines are different shots under the same setup. The shadowed parts are meaningless noises for both anti-Stokes and pump.

Table 6.3: Characteristics of pulses(please referring to figure C.3 in appendix C for detailed information)

	Center-wavelength	Pulse duration	Bandwidth	Chirp rate (linear approximation)
Pump	786.2 nm	902 fs	2.40 nm	1.60 THz/ps
Stokes	836.5 nm	831 fs	4.15 nm	1.50 THz/ps

We use a combination of a wave-plate and a polarizer to change the pump energy. The pump energy can be easily changed by rotating the half waveplate before the polarizer in the beam path. Since the maximum pump energy is 2.2 mJ, we will do an energy scan with 0.5 mJ steps. The instantaneous frequency separation is set to have the maximum red-shifted spectrum for the 2.2 mJ situation and kept the same for all the energy scans. The spectral and temporal profiles of the first anti-Stokes order are shown in Figure 6.8. As shown, the case with total energy of 1.2 mJ does not show a good matching between the FROG and the original trace and the error is more than doubled than the others; thus, little trust should be given to this result from FROG. The inconsistent result in the case of 1.2 mJ may come from the fact that the algorithm of FROG is always assuming a single pulse in its calculation. Thus, it may not work properly with the double-pulse situation, especially when the centre-frequency of the two pulses are close to each other. For the cases of 1.7 mJ and 2.2 mJ, the FROG's reconstructed traces match better with the original traces. From the 11 shots of FROG calculation, the averaged centre-frequency separation of the 1.7 mJ and 2.2 mJ cases are 1.2 THz and 1.72 THz, respectively. Of course, these separations might not be the real separations of the pulses' spectrum, especially for the 1.7 mJ case that adding two smaller separated spectra will have a bigger effect on the final positions of the two peaks, and most of the time, makes them closer.

In Hao's study, he showed that the amount of the red-shifted spectrum depends on the pulses' intensity[170]. As seen from above, the first anti-Stokes scan with pump energy, it is likely that the red-shifted spectrum has a linear dependence on pulse intensity. As can be easily calculated, the energy ratio between the two cases is $\frac{1.7\,mJ}{2.2mJ}=0.773$, while the amount of red-shift is $1.2THz/1.72THz=0.698$. Taking the effect that caused by adding the two spectra, say 10%, then the ratio will be $1.32THz/1.72THz=0.767$.

So far, the results show that the red-shift spectrum is dependent on the pump intensity, or the total pump energy. However, due to the very limited set of data, we can not give a comprehensive conclusion on it. More detailed study is needed to address this problem and we will investigate it more in the double-pulse simulation in the next chapter. On the other hand, the poor matching of the FROG

results in low pump power cases could be a good piece of evidence suggesting that the assumed single-pulse method of FROG does not work well in our cases. To verify this hypothesis, a double-pulse simulation will be built and tested in the next chapter.

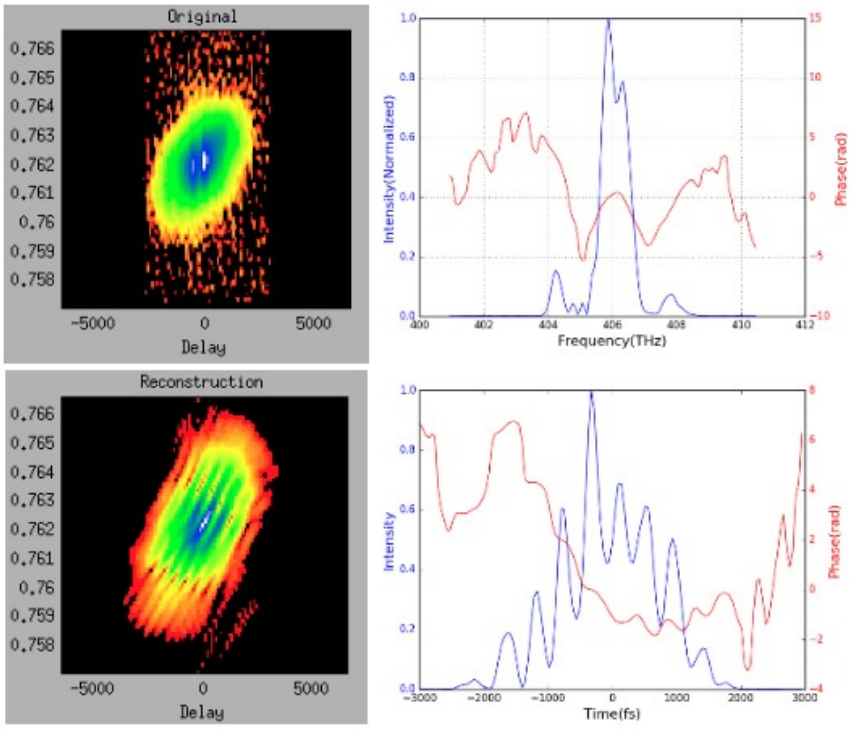

A

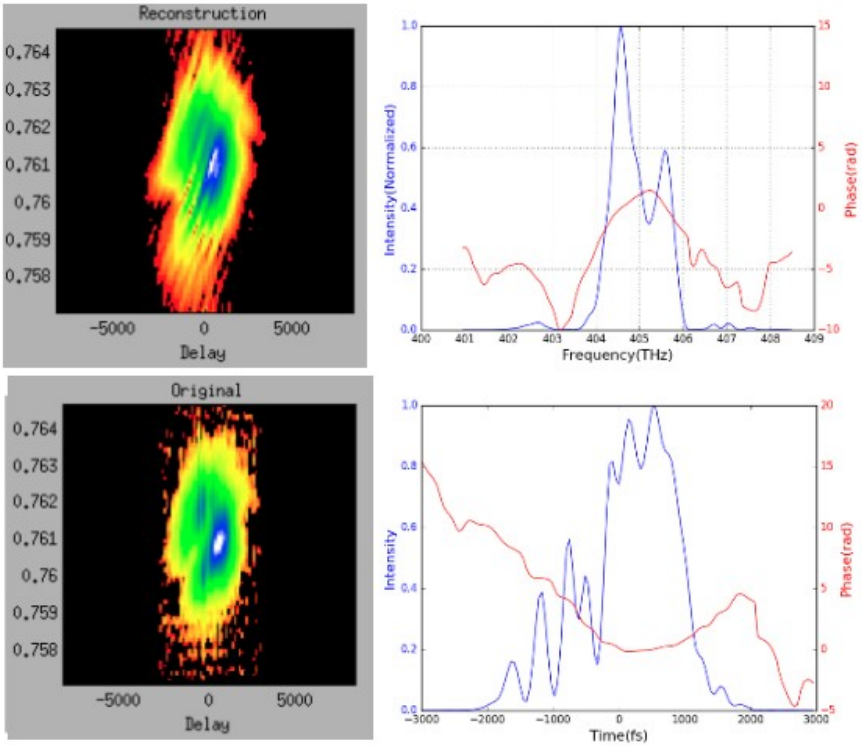

B

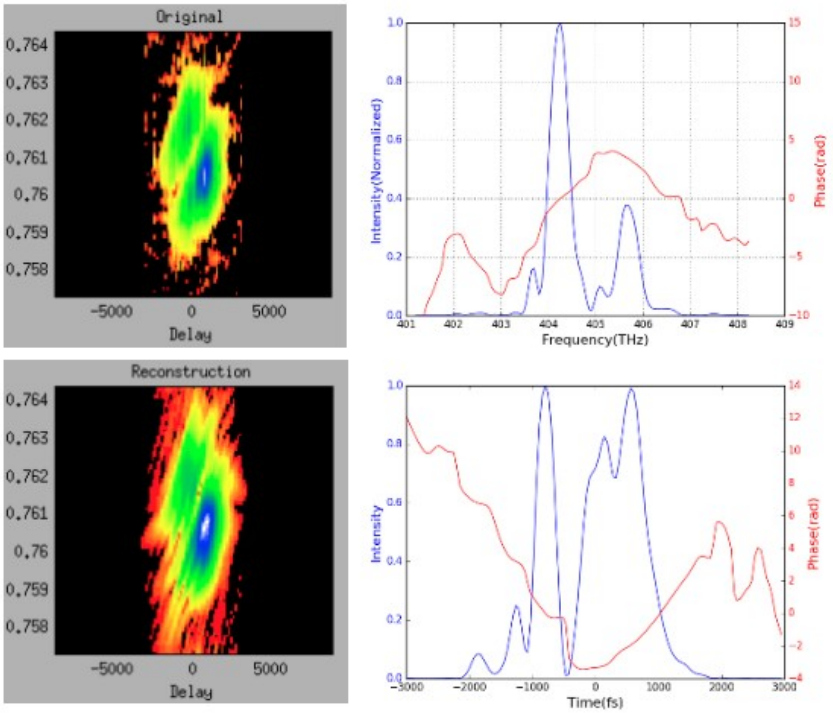

C

Figure 6.8: The first anti-Stokes order calculated by FROG algorithm(128*128 pixels are used for the FROG traces, FROG errors are 0.038, 0.018, and 0.020 for the A, B, and C, respectively). The instantaneous frequency separation is set to have the maximum of red-shifted spectrum. From top to bottom, the energy for each plot is: A-1.2 mJ; B-1.7 mJ; C-2.2 mJ. For each of the A, B, and C plots, the left-top is the original data from experiment; left-bottom is the reconstructed trace by using the FROG program; right-top is the spectrum; right bottom is the pulse in time domain.

6.2.3 Traces of the first and the second anti-Stokes orders

Most of the measurement and analysis work done so far is focused on the first anti-Stokes Raman order. In this section, we will take a look at the second anti-Stokes order. In these sets of experiment, we are using the pump and the Stokes pulses given as below.

Table 6.4: Characteristics of pulses(please referring to figure C.4 in appendix C for detailed information)

	Center-wavelength	Pulse duration	Bandwidth	Chirp rate (linear approximation)
Pump	786 nm	1217 fs	1.32 nm	0.95THz/ps
Stokes	837 nm	1151 fs	1.99 nm	1.00 THz/ps

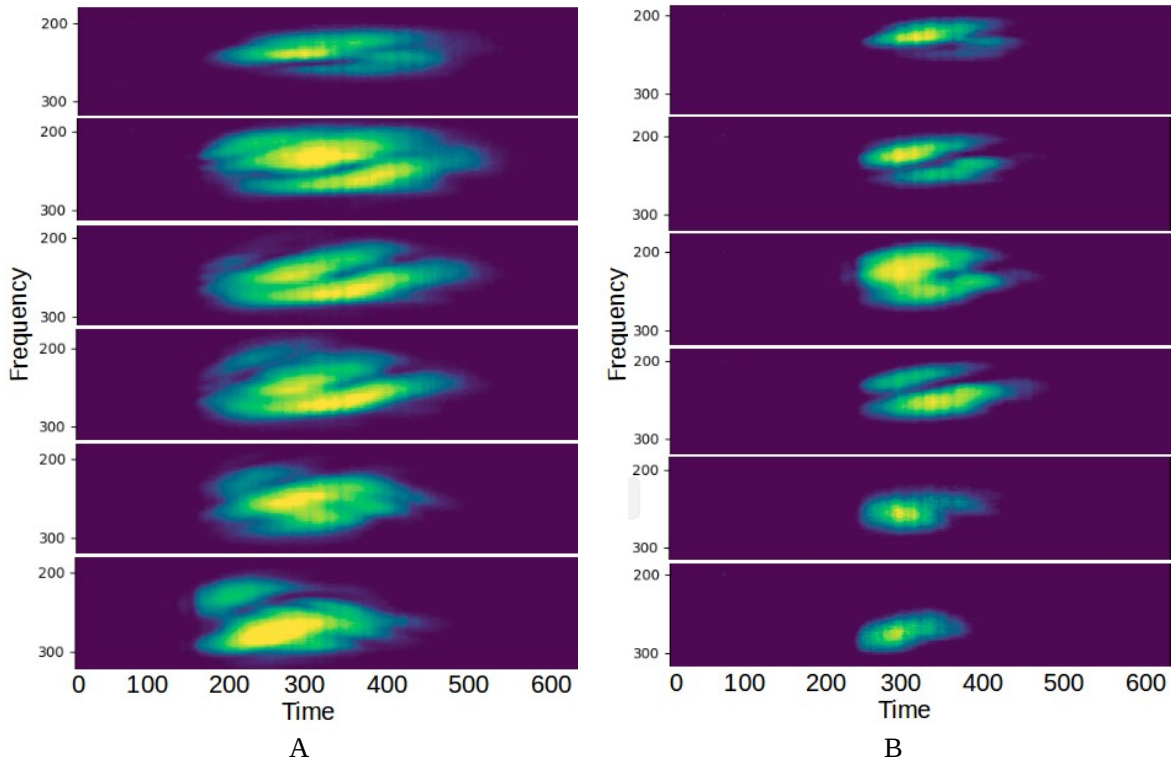

Figure 6.9: Two sets of experiment FROG traces, each set has shots with 6 different instantaneous frequencies, from top to bottom the pump pulse is in advance of the Stokes by -2/3, -1/3, 0, 1/3, 2/3, and 1 ps. A- traces of first anti-Stokes order; B-traces of second anti-Stokes order. In the plots, each pixel stands for 10.3 fs in x-axis, and 0.024 nm in y-axis.

The differences and similarities between the second anti-Stokes order and the first anti-Stokes order can be seen from the FROG traces. In figure 6.9, the side-by-side comparison shows that the traces of the second anti-Stokes order have similar configuration as of the first anti-Stokes. The two-block pattern indicates that the second anti-Stokes order also has a double peaked spectrum. However, the second anti-Stokes order is shortened in time by a factor of about 1.5. That is probably caused by the effect of the intensity dependent process. Given that we have only one set of data for the second anti-Stokes order, future investigation will be needed to validate this possible relationship.

6.2.4 First anti-Stokes measurement with negatively chirped pump and Stokes

During previous study, Z. Cui, etc, carried out a set of experiments with negatively chirped pulses. It showed that the peaks of the anti-Stokes orders remain at the Raman transition frequencies for different instantaneous frequency separations, and that only small red-shifted spectrum appears when the

instantaneous frequency separation is reduced.[33] We tried to replicate the experimental setup used by Z. Cui, with the pump and Stokes pulses given in table 6.5 and table 6.6. In the pulse preparation, with auto-correlator and spectrometer, the pulses were first measured to be around 1 ps with bandwidth of about 4.0 nm for both positively and negatively chirped situation. However, the FROG measurement gave different results. It could be caused by the resolution of our spectrometer or the method we used to calculate the pulse duration in the auto-correlator, since in the later we simply used FWHM/1.414 for the pulse duration. As the chirp rates of the pump pulse and the Stokes pulse affects the red-shifting phenomenon, this set of experiment comparison may not work as we what planned.

Table 6.5: Characteristics of the pulses with positively chirp(please referring to figure C.5 in appendix C for detailed information)

	Center-wavelength	Pulse duration	Bandwidth	Chirp rate (linear approximation)
Pump	786 nm	666 fs	2.67 nm	1.80THz/ps
Stokes	837 nm	643 fs	5.24 nm	2.60 THz/ps

Table 6.6: Characteristics of the pulses with negatively chirp(please referring to figure C.6 in appendix C for detailed information)

	Center-wavelength	Pulse duration	Bandwidth	Chirp rate (linear approximation)
Pump	786 nm	2486 fs	6.33 nm	-1.46THz/ps
Stokes	837 nm	2253 fs	4.68 nm	-1.00 THz/ps

Figure 6.10 shows a comparison between traces from positively chirped and negatively chirped pump and Stokes. The FROG traces give similar results as in Z. Cui's study[33], and in the negatively chirped case, the changes with different instantaneous frequency separations is way smaller compared with the positively chirp cases.

For the frequency axis, unlike its counterpart on the left, the bandwidth stays almost all the same with very little extra spectrum occur. On the horizontal time axis, the pulse's duration has unnoticeable change. For positively chirped situations in figure 6.10-A, the trace moves toward left side as the instantaneous frequency separation decreases. It is probably due to the pump length we used in the two sets of experiment. For the left, the pump and Stokes pulses were under 700 fs, while the right one has duration over 2200 fs. The shorter pulse also limits the time delay that we can apply, as only -1/3, 0, and 1/3 ps can generate measurable first anti-Stokes Raman order.

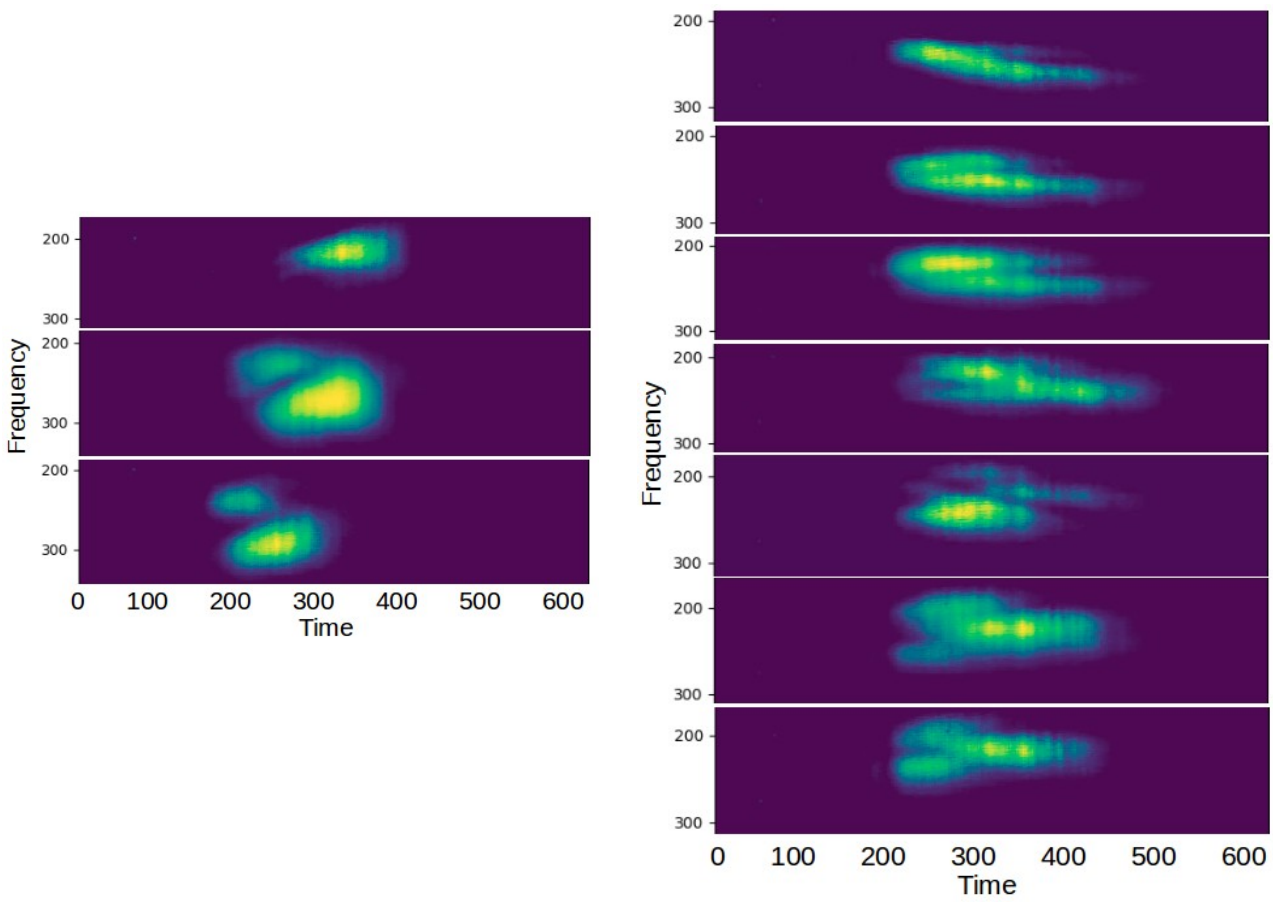

Figure 6.10: Two sets of experiment traces, each set has different instantaneous frequencies, from top to bottom the pump is in advance of the Stokes by -1, -2/3, -1/3, 0, 1/3, 2/3, and 1 ps, while only has -1/3, 0, and 1/3 ps time delays for part A. A- traces of the first anti-Stokes order with positively chirped pump and Stokes ; B- traces of the first anti-Stokes order with negatively chirped pump and Stokes. In the plots, each pixel stands for 10.3 fs in x-axis, and 0.024 nm in y-axis.

Chapter 7

Double-pulse simulation

Using the FROG measurements, good matching to the original traces can be obtained in the widely separated spectrum situations. However, the FROG algorithm has poor reconstructed traces as compared to the original traces for the low intensity cases. To explain the red-shifting phenomenon, a double-pulse model is proposed in this study. In this Chapter, we will show how we came up with the double-pulse model, and how well the model matches with the experiment data. We started from a basic double-pulse model with a simplified pulse setup, and the high degree of matching between the simulation and the raw data motivated us to continue the efforts. Thereafter, we improved our simulations with more precise pulse descriptions, and tested the model from different points of view. An iteration program was written so that better and more efficient simulations are possible. In addition, we collaborated with an AI group to further improve our double-pulse model.

Thanks to the advanced pulse measurement tool, the FROG, we are unveiling the mysteries of the red-shifted spectrum. It becomes clear that the extra part of the spectrum comes from processes that go along with the Raman process. As we have shown in previous chapters, the appearance of the red-shifted spectrum depends on the instantaneous frequency separation of the pump and the Stokes pulses, also, the separation between the red-shifted spectrum and the Raman part is intensity dependent. So far, we have learnt from the FROG results that the phases for the two parts are different from each other, and the pulse has an oscillation pattern instead of a single pulse. Furthermore, the poor matching between the FROG retrieved trace and the recorded trace from the low intensity set of experiments raised concerns about the accuracy of the FROG results in such cases.

7.1 The basic double-pulse model

Looking at the results from FROG calculation, especially when the cases where the two parts of spectra are far away from each other, the first anti-Stokes seems to be a mixing of two pulses. As shown in figure 7.1-A, the cross-correlation FROG trace of the first anti-Stokes pulse almost becomes two well-separated blocks. The FROG retrieved pulses match well with the recorded trace for these well-separated situations with an error of 0.012, and the retrieved spectrum also has two parts separated as in figure 7.1-B.

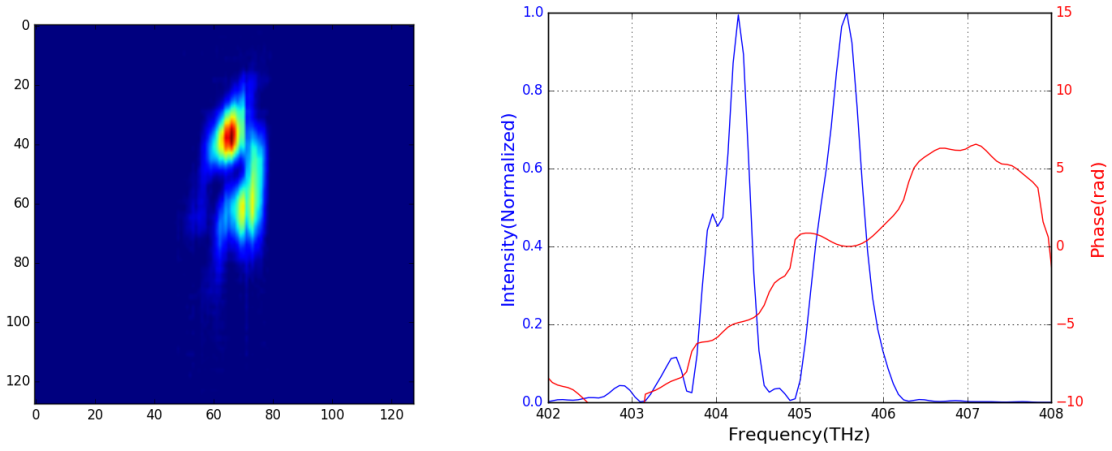

Figure 7.1: Left- Recorded trace(each of pixel on y-axis stands for 0.062 THz, and 126.8 fs for x-axis) and Right-retrieved spectrum for anti-Stokes pulse(with 128*128 pixels, the FROG error is 0.012).

The Raman part of spectrum and its phase match with the cases where only Raman spectrum occurs, and the phase goes with the pump pulse. However, the red-shifted part becomes an oscillation pattern,

possibly indicating an extra of third order phase is added. With the features being seen from the traces and the retrieved pulses, we came up with an idea of double-pulse model for the anti-Stokes pulse. As the red-shifted spectrum occurs, the anti-Stokes pulse becomes a mixing of two pulses, with an extra pulse added to the Raman pulse.

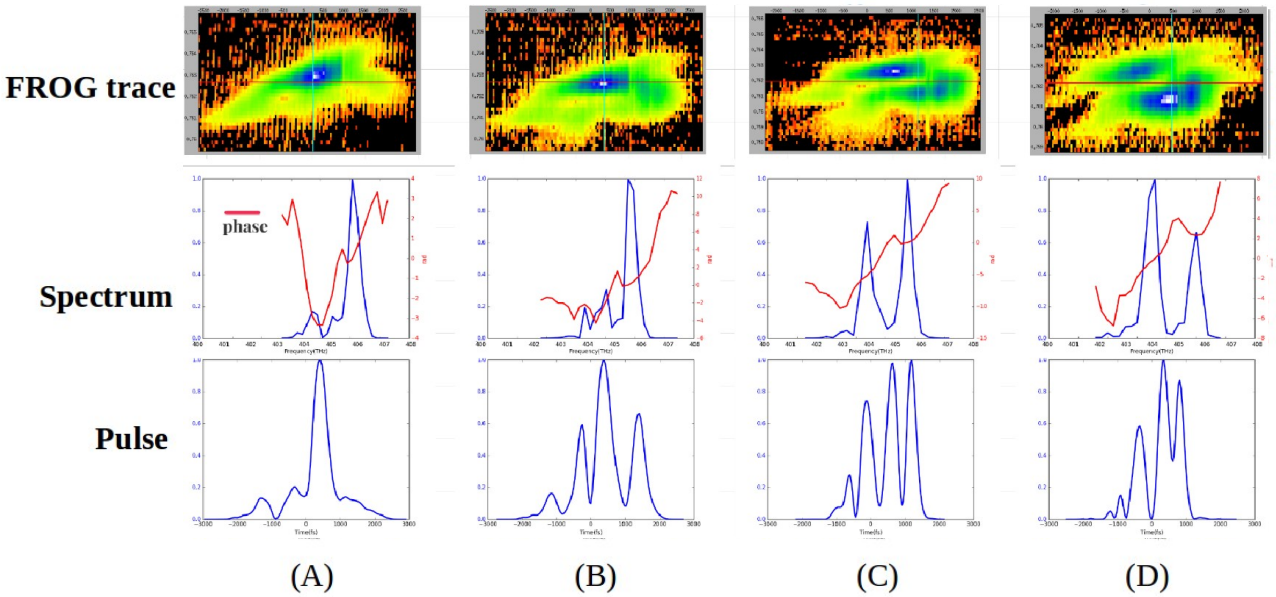

Figure 7.2: FROG traces and calculated results with different instantaneous frequencies. For the FROG traces, x-axis ranges from -2ps to 2ps, y-axis ranges from 750THz to 780 THz. (A) 23.75 THz, (B) 23.25 THz, (C) 22.75 THz, (D) 22.25 THz[171]

With this double-pulse idea in mind, let us take a second look at the experimental results. Figure 7.2 shows a set of data as a comparison. They were measured with the instantaneous frequency separation being the only variant. As shown, little to no red-shifted spectrum shows up when the instantaneous frequency separation is larger than the Raman frequency. The red-shifted spectrum occurs as the instantaneous frequency separation gets smaller, and becomes stronger as the instantaneous frequency separation decreases. Looking at the Raman part of spectrum, we can see that the shapes are similar to each other. We will use an assumption that the shape of the spectrum for both Raman part and red-shifted part stays the same all the time in our double-pulse simulation. For the phases, in (C) and (D), the phase for the red-shifted spectrum becomes a linear line while the phase of the Raman part shows a form of second order phase. As the spectrum in (C) and (D) are well-separated in two parts, we think that the interaction between them is weak and very limited. In fact, in our early simulations, we assumed that the phases are linear for the red-shifted spectrum and quadratic for the Raman spectrum. We also need to pay attention to the time delay between the two pulses, as indicated by the positions of the two blocks of the FROG traces.

In order to test our double-pulse model, we carried out simulations with assumptions that we got from the observation of the data sets and the retrieved pulses. As the name indicates, in our model the Raman pulse $E(\omega,t)$ is an addition of two pulses, which is given as

$$E(\omega,t)=E_1(\omega_1,t_1)+\alpha E_2(\omega_2,t_2) \quad (7.1\text{-}1)$$

where $E_1(\omega_1,t_1)$ and $E_2(\omega_2,t_2)$ are the two pulses with different centre-frequency and time delay. The factor α is the amplitude ratio between the two pulses. In our early simulations, we assumed that the two pulses have Gaussian profiles with pulse duration the same as the pump pulse, and the complete definition of the e-field goes as

$$e(\omega,\tau)=e(T,\omega,A,\phi,\tau)=A\sqrt{e^{-4\ln 2\left(\frac{t-\tau}{T}\right)^2}}\,e^{-j(\omega t+\phi)} \quad (7.1\text{-}2)$$

where T is the time duration, ω is the centre-frequency, A is the amplitude and is set to be 1.0 for normalized pulses, ϕ is the phase, and τ is the time delay.

We used linear phase for the red-shifted spectrum and quadratic phase for the Raman part. The variables are the amplitude ratio, time delay between the two pulses, and centre-frequency separation. Then, we cross-correlate the $E(\omega,t)$ with our reference pulse, the pump pulse $E_0(\omega_0,t)$, to generate the simulated traces as

$$I_{FROG}(\omega,\tau)=\left|\int_{-\infty}^{\infty}E(\omega,t)E_0(t-\tau)e^{-i\omega t}\,dt\right|^2 \quad (7.1\text{-}3)$$

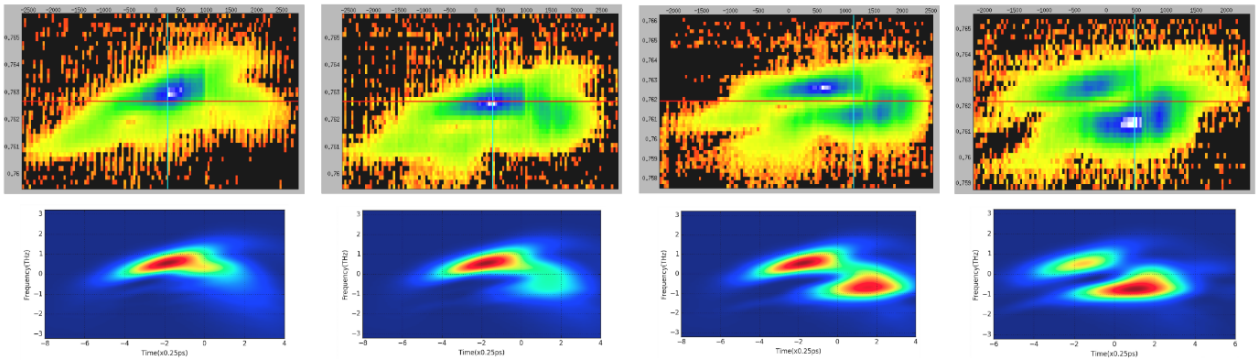

Figure 7.3: Original FROG traces and simulated traces. These simulations were initial done to show that the double-pulse model yields visually similar results as to the original FROG traces. The degree of matching is not calculated for these simulations, but will be calculated in the coming analysis.

As shown in figure 7.3, the simulated traces show high degree of matching to the experiment data. In fact, we are amazed that we can have such a good matching by only changing the three variables under the assumption that the pulses have Gaussian shape and the same pulse duration as the pump.

Table 7.1: Simulation parameters for results in figure 7.3

Instantaneous Frequency separation	23.75 THz	23.25 THz	22.75 THz	22.25 THz
Intensity ratio (α^2)	0.2	0.6	0.9	1.25
Time separation	200 fs	500 fs	700 fs	500 fs
centre-frequency separation	0.8 THz	1.1 THz	1.3 THz	1.5 THz

The simulation is coarse as the assumptions we are using might not be that accurate, and the simulation is done with a manually varying operation method. Thereafter, a more efficient simulation program has been written in Python and can be found in Appendix A. As in table 7.1, the intensity ratio between the two pulses decreases as the instantaneous frequency separation reduces, which is obvious as the red-shifted spectrum occurs and gets stronger. The intensity of the Raman part is reduced but it is there all the time with fairly strong intensity. For the time separation, it is a bit of meaningless for the first number of 200 fs as very little red-shifted spectrum occurs. However, it does seem to have a tendency that the time separation increases at first and then decreases. The centre-frequency separation between the two pulses is getting bigger as the red-shifted spectrum becomes stronger, and we are getting about 0.2 THz increments for a 0.5 THz decreasing rate of the instantaneous frequency separation.

7.2 Improving the double-pulse model

From the observation, the results from the basic double-pulse model is surprisingly good. To determine the degree of similarity, a specific metrics is needed. Therefore, we introduced a new parameter, δ_D , to describe the degree of the matching, which is similar to the error definition in the FROG algorithm.

$$\delta_D = \sqrt{\frac{\sum_{i,j=0}^{N} \left(I_{FROG}[i,j] - I_{DATA}[i,j]\right)^2}{\sum_{i,j=0}^{N} I_{DATA}^2[i,j]}} \quad (7.2\text{-}1)$$

where I_{FROG} is the simulated 2D trace, the I_{DATA} is the FROG trace from experiment, and the sum includes all the pixels of the 2D trace.

We ran the simulation again with this new checking error, however, it turned out that the error δ_D is way too big. With a double check of the data and the simulated trace, it suggests that the "good matching" is only looking good, as they are not matching each other and the error between the two is over 1. By adjusting all the parameters for E_1 and E_2, we finally got the simulated trace not only "looking good", but also with smaller error that is comparable to the error from FROG algorithm. However, the pulse durations for E_1 and E_2 are about 1200 fs, while the pump has a duration around 800 fs. That is quite strange, as shown in Chapter 2, MRG is a $\chi^{(3)}$ process. If it is intensity dependent, we would expect to have a pulse shape that goes as

$$I = I_0^2 * I_{-1} \quad (7.2\text{-}2)$$

where I_0 is the intensity of pump, I_{-1} is for the Stokes, and I as the intensity of the generated anti-Stokes. Hence, the pulse duration would become smaller, for example, if both of the pump and Stokes have Gaussian profile and the same duration T, the duration of the anti-Stokes would be $\frac{T}{\sqrt{3}}$, which is around 460 fs for our cases. However, we have gotten longer duration about 1000fs in simulations. The big mismatch between the theory and the simulation results indicates that something is not right and need to be improved.

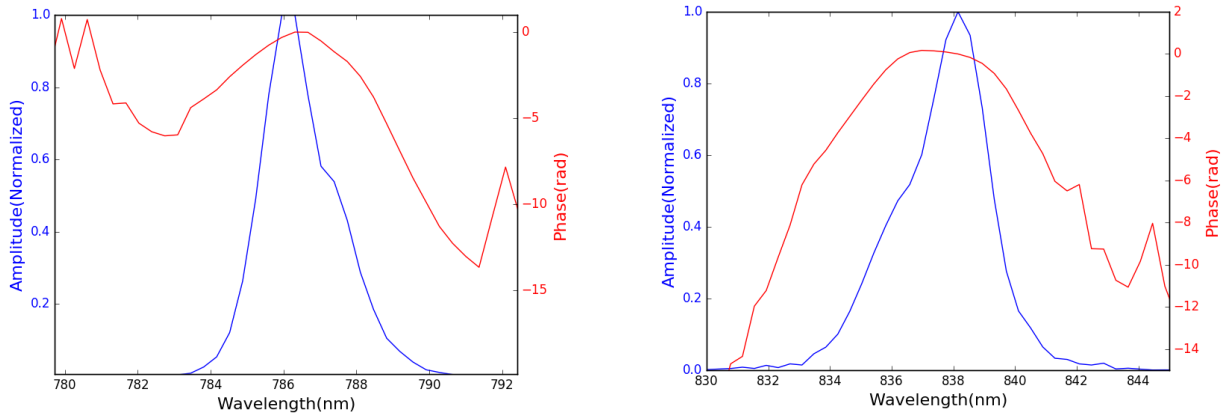

Figure 7.4: Spectra of the pump and the Stokes. Left- pump's spectrum at 786 nm; Right- Stokes' spectrum at 837 nm

So far, we have been building the pulses from the time domain, but it was not successful. What about from the frequency domain? Looking at the spectra in figure 7.2, especially for the last two, the

spectrum has two fairly well separated parts, the Raman and the red-shifted. We would like to find some relation between the Raman and red-shifted spectra in figure 7.1 to the pump and Stokes spectra in figure 7.4.

It was assumed that the spectra of the anti-Stokes orders have the same bandwidth as the pump or the Stokes. However, it turned out the assumption is not right. To start with, let us look at the case where the two parts of the spectrum are well apart. As the three plots of the spectra for the Stokes, pump, and anti-Stokes shown in figure 7.5, the Stokes and the pump have similar bandwidth, but the anti-Stokes is different. The whole spectrum of the anti-Stokes is wider than that of the pump, and if we split it into Raman and red-shifted parts, then, each of the two part is narrower than that of the pump.

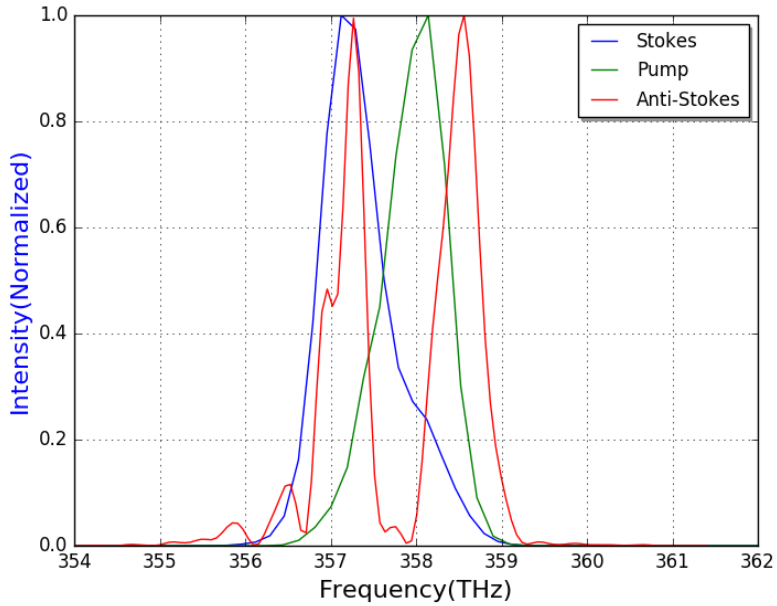

Figure 7.5: Spectrum plot for the Stokes, pump, and anti-Stokes. They are set to overlap each other for better comparison.

Back to MRG, it is a $\chi^{(3)}$ process. The anti-Stokes spectrum might depend on the spectrum's profile. Similar to the intensity dependence in equation 7.2-2, we can have the formula for the spectrum given by

$$S = S_0^2 * S_{-1} \quad (7.2\text{-}3)$$

where S_0 is the spectrum profile of the pump, and S_{-1} as the profile of the Stokes.

We will go with the idea that the each of the two parts of the anti-Stokes spectrum comes from its own process, and both of them are spectrum profile dependent as given in equation 7.2-3. As can be seen

from figure 7.6, the new combined spectrum has a high degree of similarity to the measured spectrum, especially the Raman part. The red-shifted part also has a good match for the main peak, however, no side peaks are observed for the combined spectrum. The good match for the spectrum gives us confidence that we may on the right direction. The next step is to build the pulses from the combined spectrum and check how it behaves in the time domain.

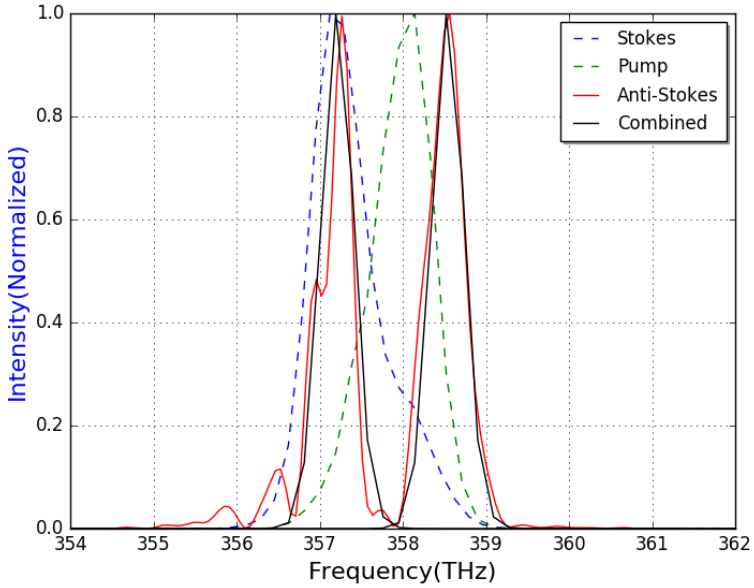

Figure 7.6: New spectrum plot with the anti-Stokes order's spectrum has an intensity dependence on the spectrum profile of the pump and Stokes

The example we showed above is the case where the two parts of the spectrum are very much apart from each other, such that, very limited effect they will have on each other. Despite the lacking of side peaks, we will continue with the pulse setup for now, and will pick up the details later, thus

$$A_{Raman} = \sqrt{S_0^2 * S_{-1}} * e^{i\omega t} \quad (7.2\text{-}4A)$$

$$A_{shifted} = \sqrt{S_0^2 * S_{-1}} * e^{i(\omega - \Delta_f)t} \quad (7.2\text{-}4B)$$

$$A = A_{Raman} + A_{shifted} \quad (7.2\text{-}4C)$$

where A_{Raman} , $A_{shifted}$, and A are the amplitudes for the Raman spectrum, red-shifted spectrum, and total spectrum, respectively. ω is the centre-frequency for Raman part and Δ_f is the frequency separation between the Raman and red-shifted. With the amplitudes given by equation 7.2-4, we can calculate the e-fields for the pulses by using the Fourier transform function, $\mathcal{F}$.

$$E_{Raman} = \mathcal{F}(A_{Raman} * e^{-i\phi}) \quad (7.2\text{-}5A)$$

$$E_{shifted} = \mathcal{F}(A_{shifted} * e^{-i\phi}) \quad (7.2\text{-}5B)$$

where ϕ is the phase of the anti-Stokes, a reasonable form of which would come from the phases of the pump and Stokes, due to the $\chi^{(3)}$ process of MRG,

$$\phi = 2\phi_{pump} - \phi_{Stokes} \quad (7.2\text{-}6)$$

Having the new e-fields from equation 7.2-5, we can form the total e-field simply by inserting them into equation 7.1-1 with some time delay added.

$$E = \alpha_1 E_{Raman}(t) + \alpha_2 E_{shifted}(t+\tau) \quad (7.2\text{-}7)$$

α_1 and α_2 are chosen to have a good match for the spectrum, then, by simply changing the time delay τ, we can get a fairly good match as in figure 7.7 below.

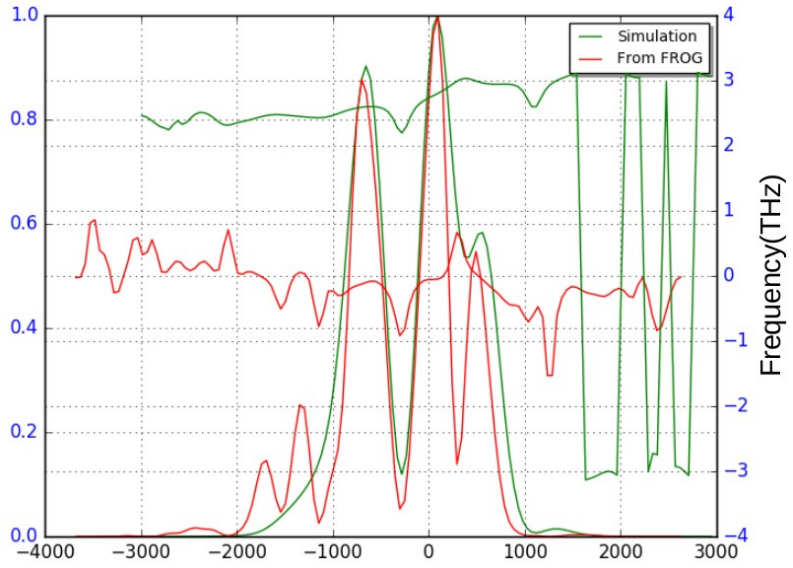

Figure 7.7: Time domain pulses and instantaneous frequency (derivative of phase $\psi(t)$) from the FROG calculation(red lines) and the double-pulse simulation(green lines).

The lack of side peaks in time domain may come as a result of the missing of side peaks in the spectrum. The instantaneous frequency also shows some similarity along the main peaks. Keep in mind that the simulation is done manually and the time delay changing is about 50 fs per step.

In the above simulations, we ignored the side peaks of the red-shifted spectrum in setting up the pulses. A possible reason for the side peaks in the red shifted part may come from the third order phase effect

in the time domain pulse. New simulations are carried out by taking the side peaks into account. From figure 7.8, an extra third order phase is added to $E_{shifted}$, however, unlike what we have expected, we can not get a good match for the red-shifted part. In the time domain, the number of peaks seems to have a better match to the FROG calculation but not in details.

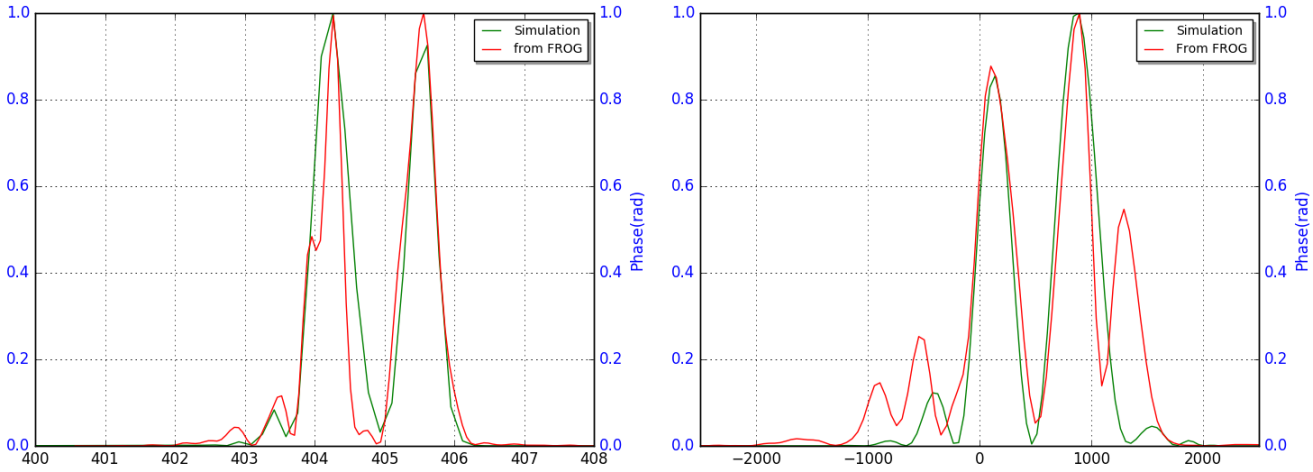

Figure 7.8: Simulation with adding an extra third order phase to the red-shifted spectrum. Left- in frequency domain; Right- in time domain.

To this point, the double pulse model simulation does show us a right direction of the red-shifted phenomenon. As more parameters are being involved in the simulation(such as the time delay, the intensity ratio, the third order phase factor, the centre-frequency separation, etc), a more solid iteration simulation is needed.

7.3 Double-pulse Model iteration

The double-pulse model assumes that the anti-Stokes is a mixing of two pulses and each of the pulses' spectrum is related to the pump pulse and the Stokes pulse, which seems to explain the mysteries of the red-shifted phenomenon in MRG. However, the manually run simulation is too time consuming and limits the process of further refinements on the model. To get the simulation done faster and better, here we introduce an iteration of the simulation. A program written in Python can be found in Appendix A.

The iteration is based on the previous basic double-pulse model, where the first guess comes from an addition of two pulses. At the beginning, we are trying to use the same idea as what the FROG

algorithm did, by replacing the magnitude of the current guess with the square root of the measured FROG trace, goes as

$$E'_{sig}(\omega,\tau)=\frac{E_{sig}(\omega,\tau)}{\left|E_{sig}(\omega,\tau)\right|}\sqrt{I_{DATA}(\omega,\tau)} \quad (7.3\text{-}1)$$

It turned out that this method will quickly wash out the effect of the double-pulse model and go back to the single-pulse FROG calculation. Then, we carried out the iteration by only changing the parameters in the pulse setup. From equations 7.2-4 to 7.2-7, the parameters in the total pulse are: centre-frequency of the Raman spectrum, ω_R ; centre-frequency of the red-shifted, ω_r ; extra third order phase, $\phi^{(3)}$; amplitude ratio between E_{Raman} and $E_{shifted}$, α ; and time delay, τ . Thus the total e-field should be $E(\omega_R,\omega_r,\phi^{(3)},\alpha,\tau)$. For each step of the iteration, we can have a small change of one of the five parameters, and see if the change gives a smaller error, or a better match. Let's use the ω_R as an example. We build the e-fields as $E(\omega_R-\Delta\omega,\omega_r,\phi^{(3)},\alpha,\tau)$, $E(\omega_R,\omega_r,\phi^{(3)},\alpha,\tau)$, and $E(\omega_R+\Delta\omega,\omega_r,\phi^{(3)},\alpha,\tau)$. Then, we can calculate the simulated FROG trace as $I(\omega_R-\Delta\omega,...)$, $I(\omega_R,...)$, and $I(\omega_R+\Delta\omega,...)$. By using equation 7.2-1, we can get the errors $\delta_D(\omega_R-\Delta\omega)$, $\delta_D(\omega_R)$, and $\delta_D(\omega_R+\Delta\omega)$. At the end of this step of iteration, we will figure out which one is the smallest and choose the corresponding frequency as the new centre-frequency for the Raman spectrum. Figure 7.9 shows the trace from experiment, retrieved trace from FROG, and trace from our double-pulse simulation. The FROG result has an error of 0.1(the error from FROG calculation is 0.014, but the definition of our error δ_D is a little different from the FROG. A factor of $\frac{N}{\sqrt{\sum_{i,j} I_{FROG}^2}}$ should be added to the FROG error, where N = 128 is the size of data and I_{FROG} is the normalized FROG trace data. We will use the calibrated error as FROG error in the following discussion.), while the double-pulse model gives an error of 0.07. It is amazing that the double-pulse model can have results with an even smaller error than the FROG algorithm.

The double-pulse simulation works great in the situations where the two parts of the spectrum are far away from each and both have strong intensity. However, for the other cases, the iteration can not get a good match, and run into endless loop. With some test runs, it seems in order to get a good match the initial pulse setup is very critical. For example, the changing of the initial condition of the

instantaneous frequency separation $\Delta\omega$ from 1.4 THz to 1.5 THz would lead the final trace from a very good match to a not even close result. According to the simulation results in figure 7.3, we believe that it may come from the method that we have been using to process the iteration. Work needs to be done to improve the iteration program.

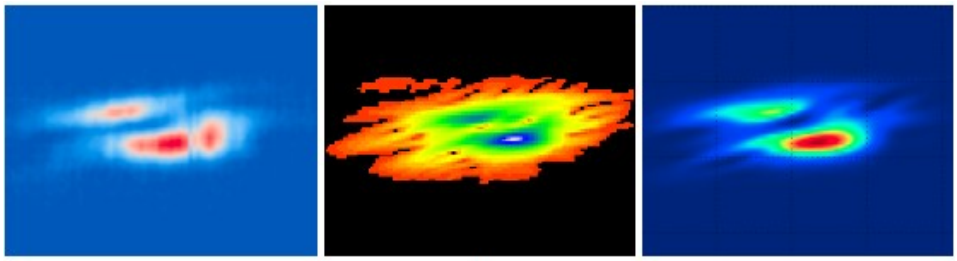

Figure 7.9: Simulation result compared with the original trace and FROG calculation. a-Original trace; b- retrieved trace from FROG algorithm; c- simulated trace from double-pulse model. The FROG algorithm error is 0.1, and the simulation error is 0.07.

7.4 Double-pulse model with phase shift instead of time delay

The double-pulse model simulation can get better results than the FROG algorithm in some situations, showing that the idea of mixing two pulses of the Raman order is on the right track. However, it is hard to give a physical explanation to the hundreds of fs time delay between the two pulses and also the red-shifted part is in advance of the Raman part. The dispersion in our MRG system does introduce time delays, but would not cause such big delays. After a second investigation of the FROG data, we realized that instead of having time delay, there could be a phase shift between the Raman and the red-shifted parts. For the phase-shift idea, the total e-field $E(\omega_R, \omega_r, \phi^{(3)}, \alpha, \tau)$ becomes $E(\omega_R, \omega_r, \phi^{(3)}, \alpha, \psi)$, with ψ as an extra phase added to $E_{shifted}$. Also, from figure 7.2, for the most separated case, the amplitude of the total e-field is close to zero at time zero. Thus, we took the extra phase ψ as π, and carried out the simulation using the modified phase-shift model. Figure 7.10 shows a simulation result with the extra π phase. As shown in figure 7.10, a phase-shift in the double-pulse model can also lead to a good match for the traces.

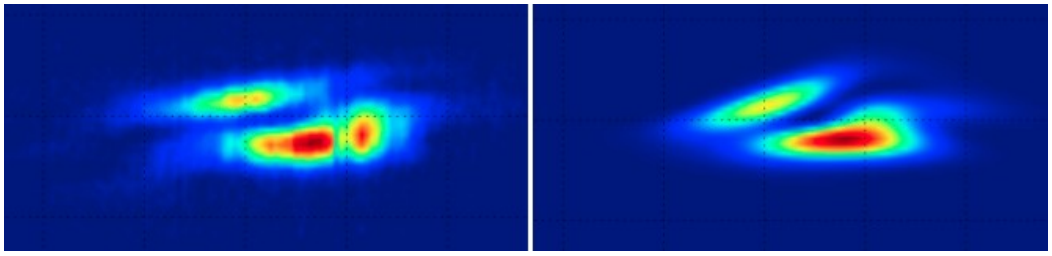

Figure 7.10: Simulation with extra phase added to red-shifted part. left-Original FROG trace; right- simulated trace from double-pulse model. The simulation error is 0.14 while FROG has an error of 0.1

Adding an extra π phase instead of time delay, we have run the simulation for the cases with different instantaneous frequency separations between the pump and Stokes pulses. As shown in figure 7.11, by changing the amplitude ratio between E_{Raman} and $E_{shifted}$ and adjusting the peak frequency separation, we can get simulations that have similar errors as the FROG program gives.

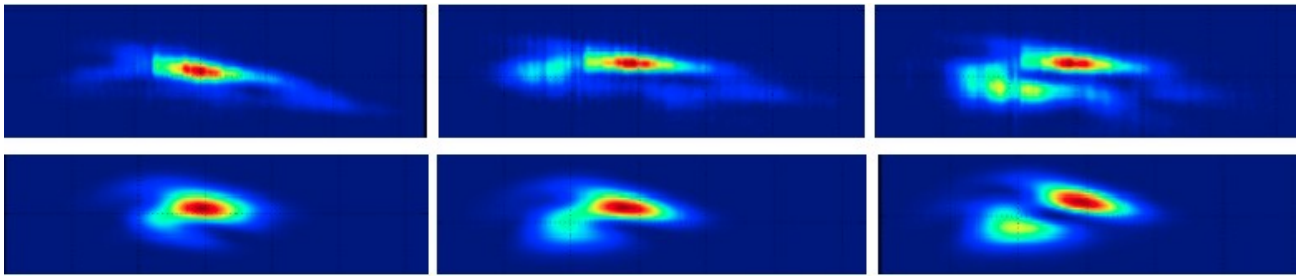

Figure 7.11: Simulation results with extra π phase added to the red-shifted part. Top-Original traces; Bottom-Simulation. From A to C, the instantaneous frequency separation between the pump and Stokes pulses are 23.75 THz, 23.25 THz, and 22.75 THz, respectively. The simulation errors(calibrated errors) for A, B and C are 0.2, 0.16, and 0.18, compared to 0.12, 0.11, and 0.12 from FROG calculation. **For these plots, the time is flipped as compared to the previous plots.**

7.5 Gradient descent method for finding the best matching traces

The iteration program that we have been using in all the previous simulation is initial condition sensitive, and some time the iteration can go endless without converging to a good matching trace. It is time consuming to have find a good result with small error. To make the iteration faster and more stable, we then collaborated with Dr. Kisor Kumar Sahu's group that uses AI technique in data analysis. They suggested to run the program with gradient descent method. At the beginning, the AI group ran the simulation with our first double pulse model, where a time delay was added to the pulses. Then, we

switched to the idea of adding an extra π phase to the red-shifted spectrum. Finally, we made the extra phase also a variable. All the AI group calculation used Gaussian pulses with second order and/or third order phases. The simulation results are getting better along the way with the error getting lower and lower. Figure 7.12 shows an example of the final version of the simulation result from the gradient descent method and its original trace, and table 7.2 gives all the parameters that are used in simulations. The parameters for trace 1 corresponding to the trace in figure 7.12. The error of this simulation is about 0.069, while it is 0.09 from the FROG algorithm.

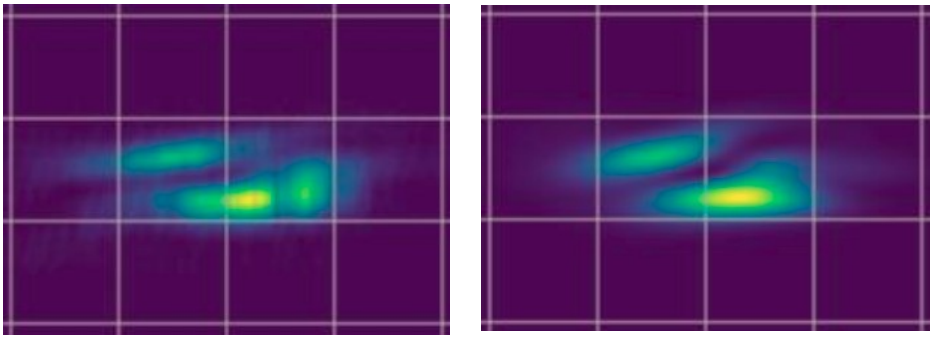

Figure 7.12: Best matching trace with gradient descent method with the extra phase as variable. Left-Original trace; Right-Simulation[iii]. The simulation error is 0.069 compared to 0.09 from FROG calculation

We have run the same simulation for traces from 11 different shots, see results from Dr. Kisor Kumar Sahu's group in appendix D. Among all the 11 shots, 2 of them (trace 3 and trace 7 as shown in appendix D) showed odd third order phases with positive factors. For trace 3, the double-pulse simulation is not working properly as only one block in the original trace. As can be seen in Table 7.2, the frequency separation is negative, meaning the centre-frequency of the red-shifted spectrum is larger than the Raman part. For trace 7, the large error indicates a bad match. Hence, we ignored these two in the following discussion.

Table 7.2: Simulation results for 11 traces (the red-coloured of traces 3 and 7 data outliers)

Trace	Error (Simulation)	Error (FROG)	E_{Raman} duration (fs)	$E_{shifted}$ duration (fs)	Amplitude ratio α	Frequency separation (THz)	Second order phase factor(10^{-6})	Third order phase factor(10^{-9})	Time delay (fs)	Extra phase
1	0.076	0.091	468.0	1081.6	0.912	0.866	-3.40	-1.15	2799.8	2.82
2	0.070	0.089	473.0	1073.1	0.886	0.867	-3.37	-1.27	2798.8	2.83
3	0.073	0.081	509.1	822.9	0.540	-0.147	-0.58	0.58	2617.0	-2.36
4	0.059	0.061	410.6	1032.8	0.664	0.310	-3.67	-1.40	3026.5	2.74
5	0.059	0.061	409.9	1033.8	0.663	0.311	-3.67	-1.40	3026.8	2.74

iii Plots provided by Dr. Kisor Kumar Sahu's group

6	0.091	0.089	573.5	1140.4	1.148	0.800	-3.00	-0.62	2725.9	3.07
7	0.126	0.088	796.2	1338.8	1.146	0.411	-2.98	1.77	3017.8	3.01
8	0.059	0.064	661.0	919.6	1.663	0.770	-3.64	-0.47	2710.6	-3.01
9	0.096	0.091	528.4	960.4	0.995	0.766	-3.40	-1.07	2789.8	-3.08
10	0.093	0.088	512.6	1167.3	0.680	0.553	-3.65	-1.00	2951.5	3.13
11	0.064	0.071	628.2	814.7	1.381	0.728	-3.70	-0.30	2669.2	3.03

Most of the errors for the traces are similar or even smaller than that from the FROG, indicating a good match between our double-pulse model and the original traces. The parameters for the pulses stay similar to each other. The pulse duration for E_{Raman} varies around 500 fs, which goes along with the $\chi^{(3)}$ process of MRG. As in the $\chi^{(3)}$ process, the generated pulse should be $\frac{1}{\sqrt{3}}$ of the pump or in our case, and the Raman order should have a shape that goes as $I_{Raman}=I_{pump}^2*I_{Stokes}$. The pump and Stokes pulses have pulse durations of 830 fs and 781 fs with 1/3 ps time delay between them. Thus, the calculated generated pulse FWHM should be 470 fs, as shown in figure 7.13, which may agree with the $\chi^{(3)}$ process of MRG. The pulse duration for $E_{shifted}$ is about 1000 fs. The second order phase factor keeps close to -3.0×10^{-6} , while the third order phase factor is shifting between -0.3×10^{-9} and -1.2×10^{-9} . The extra phases range from 2.7 to 3.2, and they are around our initial assumption of extra $\pi=3.14$ phase.

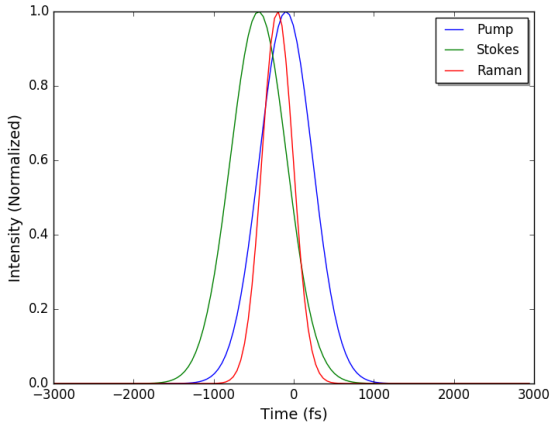

Figure 7.13: Pulse shapes of Intensity dependent $\chi^{(3)}$ process

From table 7.2, traces 4, 5, and 10 have much smaller frequency separation than the rest, and the amplitude ratio between Raman part and red-shifted part are also small, meaning that most of the energy is transferred to the red-shifted part. They are also about 200 to 300 fs later in the overall time

delay compared to the others. This effect is similar to that when we change the time delay between the pump and the Stokes pulses by delaying the pump pulse. As the pulses have fluctuations in time, these data could come from pulses that are closer to each other.

The gradient descent method helps us to run the iteration faster, however, it is still initial condition sensitive. A small change of initial condition may lead to different result. This can be understood as there are more than one local minimum with so many input parameters, and the way the iteration program works can lead to a local minimum rather than an overall minimum in some cases. The AI group is trying to include artificial neural network(ANN) in the iteration program, such that it can find all the local minimums of the simulation, and thus lead to the overall minimum.

7.6 Pulse intensity dependent Rabi frequency

Let us take a look at the instantaneous frequency vs time of the pulses. In figure 7.14-Left, we showed the instantaneous frequencies of the Raman part along with the pump, the Stokes, and the combined one. The combined one is calculated with $2*pump-Stokes$, as we believe that the Raman part comes from the $\chi^{(3)}$ precess of MRG. As shown in the plot, the chirp rate of the Raman part matches with the combined one. In figure 7.14-Right, we plotted the instantaneous frequencies of the Raman part and the red-shifted part. The Raman part is a linear line while the red-shifted part is a quadratic curve, forming a dip in the middle. This dip may come from the intensity dependent Rabi frequency, and we are going to discuss it in the following writing.

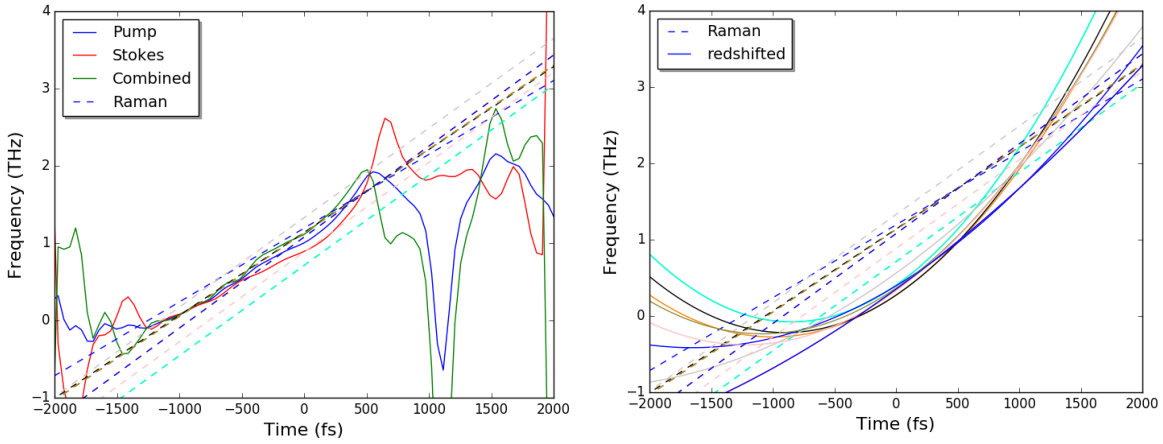

Figure 7.14: Instantaneous frequencies. Left- instantaneous frequency comparison between the Raman part and pumps'; Right- instantaneous frequencies of the Raman part and the red-shifted part.

Recalling Hickman's theory about MRG process discussed in Chapter 2. The equations for the Rabi frequency are,

$$\Omega'^2 = |\Omega|^2 + \Delta^2 \quad \text{(a)}$$

$$\Omega e^{i\theta} = \frac{\alpha_{12}}{2\hbar} \sum_j V_j V_{j-1}^* \quad \text{(b)}$$

$$\Delta = \frac{\partial \theta}{\partial t} + \frac{2\pi(\alpha_{22} - \alpha_{11}) I}{\hbar c} + \delta\omega \quad \text{(c)}$$

As shown in the equations (a,b,c), the generalized Rabi frequency Ω' is related to pulse energy through Ω and Δ. Higher pulse intensity will lead to bigger Rabi frequency and detuning, and thus ends up with larger Ω'. In our transient MRG, we may need to take the pulse profile into consideration, hence equations (a,b,c) becomes time dependent,

$$\Omega'^2(t) = |\Omega|^2(t) + \Delta^2(t) \quad \text{(a1)}$$

$$\Omega(t) e^{i\theta} = \frac{\alpha_{12}}{2\hbar} \sum_j V_j(t) V_{j-1}^*(t) \quad \text{(b1)}$$

$$\Delta(t) = \frac{\partial \theta}{\partial t} + \frac{2\pi(\alpha_{22} - \alpha_{11}) I(t)}{\hbar c} + \delta\omega \quad \text{(c1)}$$

To fully calculate the generalized Rabi frequency, it is required to consider all the anti-Stokes, the pump, and Stokes. However, it will be too much work to figure out all of them. Since two strong pump and Stokes pulses are used in our experiment, it would be appropriate to just use the pump and Stokes as a proper approximation. In our case the durations of them are 781 fs and 830 fs, and with a time delay of 1/3 ps between them, and as shown in figure 7.15-Left, the generalized Rabi frequency has a FWHM of 800 fs.

For the two photon dressed two-level system, the time varying Rabi frequency will have effects on the red-shifted spectrum while leaving the Raman spectrum untouched. As shown in figure 7.15-Right, for a linearly chirped pulse, the instantaneous frequency of the generated Raman spectrum is a straight incline, while the red-shifted spectrum will have a dip in the middle as caused by the varying of Rabi frequency.

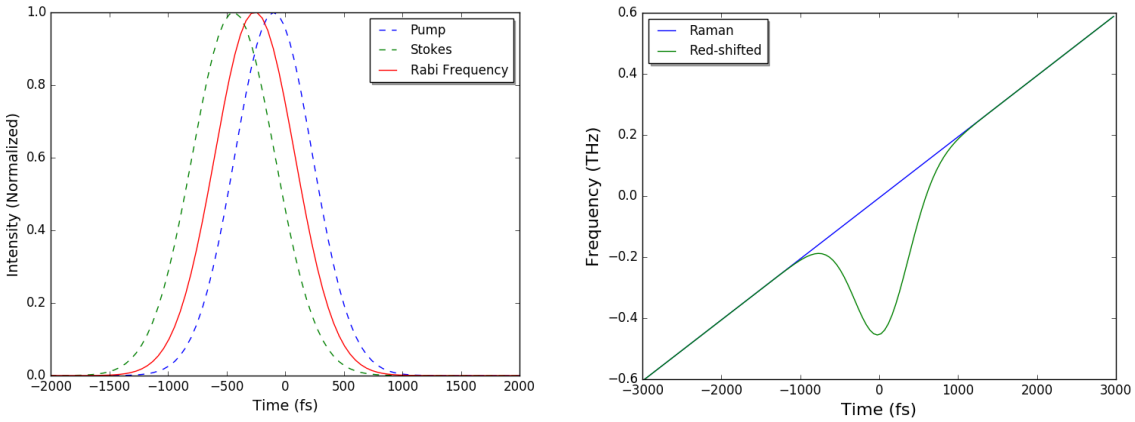

Figure 7.15: Left- Shape of the generalized Rabi frequency with the pulse intensity goes as a 800 fs Gaussian shape; Right- Instantaneous frequency of Raman part and red-shifted part, as caused by the time varying Rabi frequency

In our previous simulations, we have used two different centre-frequencies for E_{Raman} and $E_{shifted}$, they are

$$E(\omega_R, \omega_r, \phi^{(3)}, \alpha, \tau) = E_{Raman}(\omega_R) + \alpha E_{shifted}(\omega_r, \phi^{(3)}, \tau) \quad (7.6\text{-}2)$$

$$E(\omega_R, \omega_r, \phi^{(3)}, \alpha, \psi) = E_{Raman}(\omega_R) + \alpha E_{shifted}(\omega_r, \phi^{(3)}, \psi) \quad (7.6\text{-}3)$$

Now, taking the intensity dependent Rabi frequency into account, the double-pulse model turns into a new form with only one centre-frequency, and no extra time delay or extra phase needed,

$$E(\omega_R, \alpha, \phi) = E_{Raman}(\omega_R) + \alpha E_{shifted}(\omega_R, \phi) \quad (7.6\text{-}4)$$

where ϕ is a phase comes from the integral of the green curve in figure 7.15-Right.

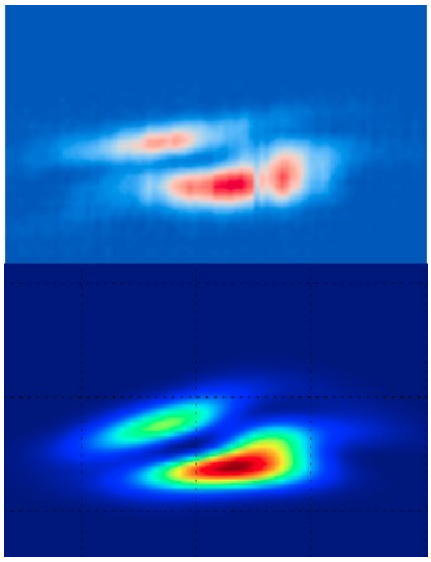

Figure 7.16: Double pulse simulation with intensity dependent Rabi frequency. Top-Original; Bottom-Simulation

Simulation was carried out with double-pulse model using equation 7.6-4 while the assumption of Gaussian shape pulses was still applied. As shown in figure 7.16, the result matches the original trace in high degree with error of 0.08 which is lower than the 0.09 from the FROG iteration.

We then did a check for this new double-pulse model by using the experimental data with different total energies. As can be seen from the model, the only factor that affects the red-shifted part comes from the intensity of the pulses. For the case of different total energies, the amplitude of the pulse varies, and thus will have effects on the amplitude of the frequency dip. As shown in figure 7.17 and table 7.3, by purely adjusting the amplitude factor to 2.0, 4.0, and 5.0, we are able to get high degree of match with the original data for the total energy of 1.2 mJ, 1.7 mJ, and 2.2 mJ, respectively. Especially for the 1.2 mJ, the FROG calculation was not able to give a good matching result, while the double-pulse model shows a consistent output. This suggests that the FROG algorithm does not work well for the red-shifted Raman spectrum. On the contrary, the double-pulse model simulation shows good matching to the original traces. Thus, it strengthened our idea that the time varying Rabi frequency is on the right track for the explanation of the red-shifting phenomenon.

Along the development of the double-pulse model, the simulation results suggest that MRG in transient regime is probably following the two photon dressed states with intensity dependent Rabi frequency. The Stark shifting turns the anti-Stokes order into two parts, the regular Raman part and the red-shifted part. The Raman part follows the $\chi^{(3)}$ MRG precess, while the red-shifted part is generated from the time varying Rabi frequency.

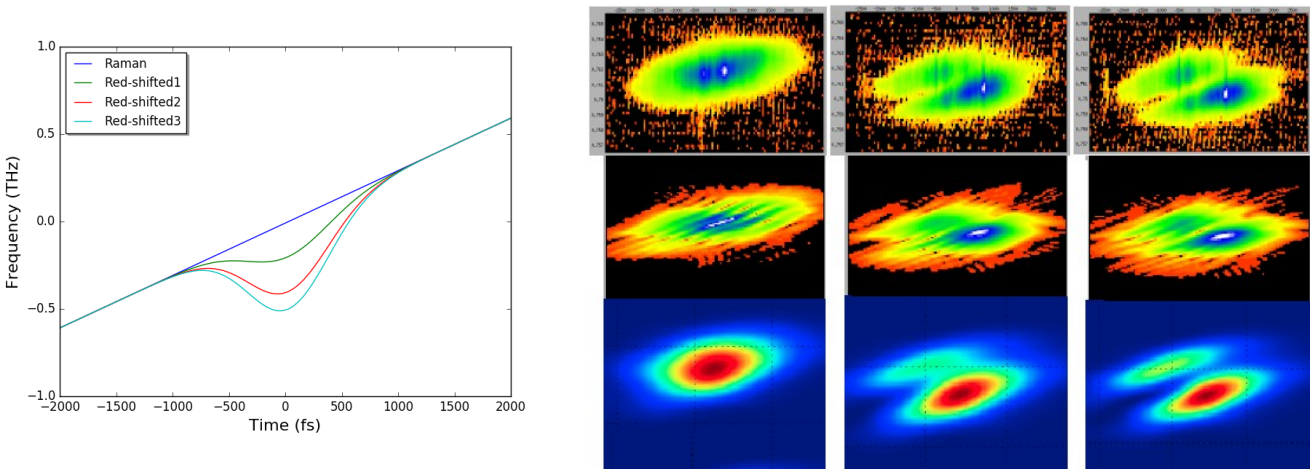

Figure 7.17: Double-pulse model simulation with different total energies. Left- instantaneous frequencies of the red-shifted spectrum with different amplitudes of dip; Right- from top to bottom, comparison among the original traces, FROG reconstructed traces, and the simulation results from DPM. The total energies are 1.2 mJ, 1.7 mJ, and 2.2 mJ from left to right.

Table 7.3: Amplitude factors of the dips in the simulation with different total energies

Total energy	1.2 mJ	1.7 mJ	2.2 mJ
Amplitude factor	2.0	4.0	5.0

7.7 Double-pulse model and FROG algorithm

All through this thesis, FROG algorithms and FROG pulse measurement setups have been used to study the red-shifted spectrum. It turned out that the FROG works well with the measurements of pumps, and also the first anti-Stokes generated under high-energy pumps(total energy of the pumps > 2.0 mJ). However, the FROG algorithm seems not getting good results for the first anti-Stokes with low-energy pumps(total energy of the pumps < 1.2 mJ).

On one hand, from the FROG results with high-energy pumps, we believe that the first anti-Stokes Raman order is a mixing of two pulses, i.e. the Raman pulse and the red-shifted pulse. On the other hand, we think that the two overlapped spectra with different phases in the low-energy situations may make it hard for the FROG algorithm to resolve. Then, a double-pulse model was introduced to describe the first anti-Stokes Raman order. Our simulations with double-pulse model have achieved errors that are similar to or even smaller than that from FROG. In addition, as shown in section 7.6, the double-pulse model describes the Raman pulse better in low-energy pumps situation.

In the simulations, we have been using a Gaussian pulse assumption for both Raman part and red-shifted part. It may seem too good to have errors smaller than FROG with such a simple Gaussian pulse assumption. However, the FROG is using all the data points, including all the noises, and the algorithm is trying to have a reasonable electric field by taking all the data points into account. That is also why the reconstructed traces have jagged edges, for example, as shown in figure 7.17. Let us have a look at the total electric fields from both the double-pulse model simulations and the FROG calculations. In figure 7.18, examples are provided for the comparison between intensity plot of the two. As can be seen from the plots, the pulses from the double-pulse model match with the FROG results for the main peaks, while the fine details are missing. The mismatch of the fine details is reasonable as we are using two Gaussian pulses for the simulations and adding temporal phases to the pulses.

Another interesting part is for the 1.2 mJ low-energy situation, the FROG reconstructed trace is far off from the original trace with error that is significantly higher than that from the high-energy cases, while the double-pulse model gives reasonable result. I searched around for any possible similar problem that

may occur in others FROG measurements, but could not find any. The possible reason that I have been thinking is that in low-energy situations, the frequency separations between the Raman and red-shifted parts are small, meaning there is a big overlapped part between the two. And, according to our intensity dependent Rabi frequency model, the two overlapped spectra are having different phases. The FROG algorithm may have difficulty in separating this overlapped spectrum.

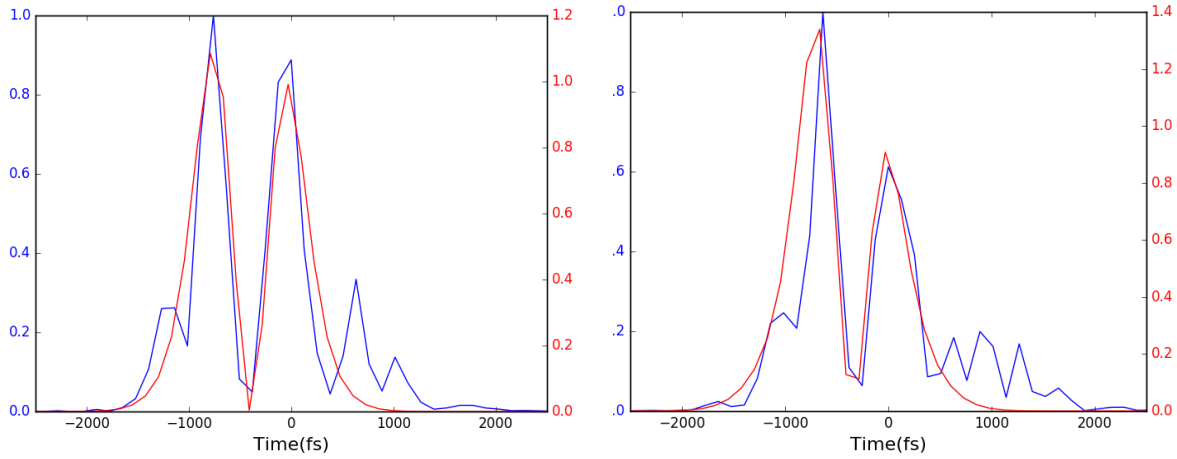

Figure 7.18: Intensity plots of the electric fields from the double-pulse model simulation(red line) and FROG reconstruction(blue line).

Chapter 8

Conclusion and Future Outlook

In this last chapter we will provide a brief overview of the project, and give a summary and conclusion to the whole study. Some possible future work is discussed as the closure of this thesis.

This study was inspired by the pursuit of the GGG, the generation of ultra-short pulses around 1 fs with high-energy by using MRG technique. During MRG experiments, an extraordinary phenomenon with extra red-shifted spectrum occurring on each of the anti-Stokes Raman orders attracted our interest. With the motivation and awareness that the red-shifted spectrum might help us in getting higher energy pulses, we have performed various experiments and developed a new model to study and explain the phenomenon.

8.1 Conclusion of the project

In this study, we have used an advanced and widely used pulse measuring technique, the FROG, as the main tool to measure and analyze the first anti-Stokes Raman order. The higher solution and much more detailed results help us in better understanding the red-shifted spectrum. Depending on the instantaneous frequency separation of the pump and the Stokes, the red-shifted spectrum occurs and disappears. When the red-shifted spectrum occurs, the anti-Stokes pulse turns into an oscillation pattern from a single pulse. In the frequency domain, the spectrum becomes double peaked with different phases for each part. With total pulse energy above 2.2 mJ and an instantaneous frequency separation of 22.75 THz, the anti-Stokes spectrum is split into two well separated parts, the Raman part and red-shifted part.

We carried out MRG experiment with energy scans, and the results show that the separation of the two parts is intensity dependent. The dependence is most likely a linear relationship. The derivatives of the anti-Stokes phases show similar slope to the that of the pump when the spectrum is split into two parts. The extra red-shifted spectrum complicates the pulses, and probably due to the mixing of the spectrum, the FROG algorithm results in poorly matched traces when the total initial energy is low. Looking at the cases where the Raman and red-shifted spectra are well separated, we felt like it might be a mixing of two pulses. A first version of double-pulse model is introduced, where the pulse duration is set to be the same as the pump, and phases for the Raman and red-shifted are set to be quadratic and linear, respectively. The simulation result matches the recorded data in high degree. With the confidence from the basic double-pulse model, we then refined the model by setting up the pulses from the spectrum with the awareness of the $\chi^{(3)}$ process of MRG, and improved the simulation with an iteration program with calculable error. Some simulations from the double-pulse model give traces that match the recorded data even better than the FROG algorithm. The results suggest that MRG in transient

regime is likely following the two photon dressed states with intensity dependent Rabi frequency. The Stark shifting turns the anti-Stokes order into two parts, which are the regular Raman part and the red-shifted part. The Raman part follows the $\chi^{(3)}$ MRG precess, while the red-shifted part is generated from the time varying Rabi frequency.

8.2 Future outlook

The red-shifted spectrum in MRG process is a novel and promising phenomenon, however, very limited work has been done to study it. Based on what we have learnt from the work during this project, future work on the following three aspects are necessary, which include improving the red-shifted experiment, improvement of the double-pulse simulation, and setup for pulse synthesis.

8.2.1 Experiment for the red-shifted spectrum

To obtain further understanding of the red-shifted phenomenon and also of MRG process, the following experiments are recommended.

For the energy scan of the anti-Stokes, it would be better to increase the total pulse power so that we can have much more steps to figure out the relationship between the amount of the red-shift and the initial intensity. So far, it seems that we need to have total pulse energy larger than 2.0 mJ to have a well separated spectrum, and I have been getting 2.2 mJ for most of time. In our lab, it would not be too difficult to get the total energy to 3.5 mJ, but the current devices, such as the grating in the compressor and the mirrors in the multi-pass amplifier, are not efficient and causing large energy loss.

The trace of the second order anti-Stokes is about 1.5 times shorter in time, which may come as a result of the pulse-profile depended process. Therefore, measurement of the third or higher anti-Stokes order might be able to give a much more comprehensive answer. Meanwhile, some data from the second or higher Stokes order might provide details for the red-shifted spectrum, and so as to MRG process.

8.2.2 Improvement of the iteration program

The double-pulse simulation has shown the ability to get good results in many situations, but seems not

work all the time. I would suggest that the problem comes from the way we do the iteration. We need to find a much more solid way to run the iteration. That is why we are working with a computer science team to see if bringing some artificial intelligent(**AI**) techniques can improve the double-pulse simulation. To date, the gradient descent method has been applied. Our next step would be to implement the artificial neural network in the model calculation. The model of using intensity dependent Rabi frequency with Gaussian shape dip in the middle for the red-shifted spectrum seems to work great, but so far we have not applied any iteration to get the best matched trace yet. A solid iteration program for this Gaussian shaped Rabi frequency model may help to unveil the mystery of the red-shifted spectrum.

8.2.3 Pulse synthesis

Though the red-shifted spectrum is not fully understood, the double-pulse model has shown as one of the best models to explain the phenomenon. With the information we have gotten so far, when the red-shifted spectrum occurs, the classical way of using prism-pair, grating-pair, or chirped mirror will not be able to synthesize the Raman orders to a perfect ultra-short pulse. Spatial light modulator might be able to solve the problem.

1 The Horse in motion. "Abe Edgington," owned by Leland Stanford; driven by C. Marvin, trotting at a 2:24 gait over the Palo Alto track, 15th June 1878 / Muybridge.
2 Nico de Jong, Chien T. Chin, Charles T. Lancee, Jerome Borsboom, Frits Mastik, Michel Versluis, Detlef Lohse, and Vance Parker "Brandaris 128: a rotating-mirror digital camera with 128 frames at 25 Mfps", Proc. SPIE 4948, 25th International Congress on High-Speed Photography and Photonics, (1 August 2003)
3 Ehn, A. et al. FRAME: femtosecond videography for atomic and molecular dynamics. Light: Science & Applications 6, e17045–e17045 (2017).
4 Maiman, T. H. Stimulated Optical Radiation in Ruby. Nature 187, 493–494 (1960).
5 McClung, F.J.; Hellwarth, R.W. (1962). "Giant optical pulsations from ruby". Journal of Applied Physics. 33 (3): 828–829.
6 Hargrove L.E. et al. (1964) Locking of He-Ne LASER Modes Induced by Synchronous Intracavity Modulation, Applied Physics Letters 5, pp.4-5
7 Strickland, Donna; Mourou, Gerard (1985). "Compression of amplified chirped optical pulses" (PDF). Optics Communications. Elsevier BV. 56 (3): 219–221.
8 Spence, D. E., Kean, P. N. & Sibbett, W. 60-fsec pulse generation from a self-mode-locked Ti:sapphire LASER . Opt. Lett., OL 16, 42–44 (1991).
9 Perry, M. Crossing the Petawatt threshold. Science and Technology Review (1996).
10 "Press release: NNSA and LLNL announce first successful integrated experiment at NIF". Lawrence Livermore National Laboratory. 6 October 2010.
11 McClung, F. J., and Hellwarth, R. W., “Giant optical pulsations from ruby”, J. Appl. Phys. 33 (3), 828 (1962)
12 Keller, U., "Ultrafast solid-state LASER oscillators: a success story for the last 20 years with no end in sight," Appl Phys B,Vol.100, Issue 1, pp 15šC28,2010.
13 Keller, U., Miller, D., Boyd, G., Chiu, T., Fergosun, J., and Asom, M., "Solid-state low-loss intracavity saturable absorber for Nd:YLF LASER s: an antiresonant semiconductor FabryšCPerot saturable absorber," Optics Letter,Vol. 17, Issue 7,pp. 505-507,1992.
14 Yariv, A., and Yeh, P., "Optical waves in crystals," Wiley-Interscience Publications,1984.
15 Degnan, J. J., “Optimization of passively Q-switched LASER s”, IEEE J. Quantum Electron. 31 (11), 1890 (1995).
16 Ell, R. et al. Generation of 5-fs pulses and octave-spanning spectra directly from a Ti:sapphire LASER . 3.
17 Franken, P. A., Hill, A. E., Peters, C. W. & Weinreich, G. Generation of Optical Harmonics. Phys. Rev. Lett. 7, 118–119 (1961).
18 Stoicheff, B.P. (1963). "Characteristics of stimulated raman radiation generated by coherent light". Physics Letters. Elsevier BV. 7 (3): 186–188.
19 Li, J. et al. Attosecond science based on high harmonic generation from gases and solids. Nature Communications 11, (2020).
20 Corkum, P. B., Plasma perspective on strong field mul-tiphoton ionization, Phys. Rev. Lett. 71 (13) (1993) 1994–1997. doi:10.1103/PhysRevLett.71. 1994
21 Schafer, K. J., Yang, B., DiMauro, L. F. & Kulander, K. C. Above threshold ionization beyond the high harmonic cutoff. Physical Review Letters 70, 1599–1602 (1993).
22 Lewenstein, M., Balcou, P., Ivanov, M. Y., L’Huillier, A., Corkum, P.B., Theory of high-harmonic generation by low-frequency LASER fields, Phys. Rev. A 49 (3) (1994) 2117–2132. doi:10.1103/PhysRevA.49.2117
23 Gaumnitz, T. et al. Streaking of 43-attosecond soft-X-ray pulses generated by a passively CEP-stable mid-infrared driver. Opt. Express, OE 25, 27506–27518 (2017).
24 Nazarkin, A., Korn, G., Wittmann, M. & Elsaesser, T. Generation of Multiple Phase-Locked Stokes and Anti-Stokes Components in an Impulsively Excited Raman Medium. Phys. Rev. Lett. 83, 2560–2563 (1999).
25 Yavuz, D. D., Walker, D. R., Yin, G. Y. & Harris, S. E. Rotational Raman generation with near-unity conversion efficiency. Opt. Lett. 27, 769 (2002).
26 Strickland, D.; Mourou, G. (1985). "Compression of amplified chirped optical pulses" (PDF). Optics Communications. Elsevier BV. 56 (3): 219–221.
27 Turner, F. C. & Strickland, D. Anti-Stokes enhancement of multifrequency Raman generation in a hollow fiber. Opt. Lett., OL 33, 405–407 (2008).
28 Wang, K., Zhi, M., Hua, X., Strohaber, J. & Sokolov, A. V. Coherent broadband light generation with a double-path configuration. Applied Optics 53, 2866 (2014).
29 Zhdanova, A. A., Bahari, A., Shutova, M. & Sokolov, A. V. Synthesis of ultrafast waveforms using coherent Raman sidebands. arXiv:1901.11155 [physics] (2019).
30 Sali, E., Mendham, K. J., Tisch, J. W. G., Halfmann, T. & Marangos, J. P. High-order stimulated Raman scattering in a highly transient regime driven by a pair of ultrashort pulses. Opt Lett 29, 495–497 (2004).
31 Alharbi, M. et al. Raman gas self-organizing into deep nano-trap lattice. Nature Communications 7, ncomms12779 (2016).

32 Turner, F. Multifrequency Raman Generation in the Transient Regime. (2006).
33 Cui, Z. et al. Spectral red-shifting of multi-frequency Raman orders. Optics Communications 288, 118–121 (2013).
34 Yan, H. & Strickland, D. Effect of Two-Photon Stark Shift on the Multi-Frequency Raman Spectra. Applied Sciences 4, 390–401 (2014).
35 Hao, Y., Characterizing Transient Regime Multi-frequency Raman Generation by the Aid of Spectral Phase Interferometry for Direct Electric-field Reconstruction, master thesis in University of Waterloo, 2013.
36 Franken, P.; Hill, A.; Peters, C.; Weinreich, G. (1961). "Generation of Optical Harmonics". Physical Review Letters. 7 (4): 118–119.
37 McClung, F. J. & Hellwarth, R. W. Giant Optical Pulsations from Ruby. Journal of Applied Physics 33, 828–829 (1962).
38 Hargrove L.E. et al. (1964) Locking of He-Ne LASER Modes Induced by Synchronous Intracavity Modulation, Applied Physics Letters 5, pp.4-5
39 Fork, R. L., Greene, B. I. & Shank, C. V. Generation of optical pulses shorter than 0.1 psec by colliding pulse mode locking. Appl. Phys. Lett. 38, 671–672 (1981).
40 Ell, R. et al. Generation of 5-fs pulses and octave-spanning spectra directly from a Ti:sapphire LASER . Opt. Lett., OL 26, 373–375 (2001).
41 Ferray, M. et al. Multiple-harmonic conversion of 1064 nm radiation in rare gases. J. Phys. B: At. Mol. Opt. Phys. 21, L31–L35 (1988).
42 Midorikawa, K. High-Order Harmonic Generation and Attosecond Science. Jpn. J. Appl. Phys. 50, 090001 (2011).
43 Christov, I. P., Murnane, M. M. & Kapteyn, H. C. High-Harmonic Generation of Attosecond Pulses in the “Single-Cycle” Regime. Phys. Rev. Lett. 78, 1251–1254 (1997).
44 Gaumnitz, T. et al. Streaking of 43-attosecond soft-X-ray pulses generated by a passively CEP-stable mid-infrared driver. Opt. Express, OE 25, 27506–27518 (2017).
45 Eckhardt, G. et al. Stimulated Raman Scattering From Organic Liquids. Phys. Rev. Lett. 9, 455–457 (1962).
46 Imasaka, T., Kawasaki, S. & Ishibashi, N. Generation of more than 40 LASER emission lines from the ultraviolet to the visible regions by two-color stimulated raman effect. Appl. Phys. B 49, 389–392 (1989).
47 Yoshikawa, S. & Imasaka, T. A new approach for the generation of ultrashort optical pulses. Optics Communications 96, 94–98 (1993).
48 Kaplan, A. E. Subfemtosecond Pulses in Mode-Locked $2\ensuremath{\pi}$ Solitons of the Cascade Stimulated Raman Scattering. Phys. Rev. Lett. 73, 1243–1246 (1994).
49 Nazarkin, A., Korn, G., Wittmann, M. & Elsaesser, T. Generation of Multiple Phase-Locked Stokes and Anti-Stokes Components in an Impulsively Excited Raman Medium. Phys. Rev. Lett. 83, 2560–2563 (1999).
50 Shverdin, M. Y., Walker, D. R., Yavuz, D. D., Yin, G. Y. & Harris, S. E. Generation of a Single-Cycle Optical Pulse. Phys. Rev. Lett. 94, 033904 (2005).
51 Yoshii, K., Anthony, J. K. & Katsuragawa, M. The simplest rout to generating a train of attosecond pulses. 5.
52 Hänsch, T. W. A proposed sub-femtosecond pulse synthesizer using separate phase-locked laser oscillators. Optics Communications 80, 71–75 (1990).
53 Raman, C. V. (1928). "A new radiation". Indian Journal of Physics. 2: 387–398.
54 Harris and Bertolucci (1989). Symmetry and Spectroscopy. Dover Publications.
55 Hellwarth, R. W. Theory of Stimulated Raman Scattering. Phys. Rev. 130, 1850–1852 (1963).
56 M. Maier, W. Kaiser, J. A. Giordmaine: Phys. Rev. Lett. 17, 1275 (1966)
57 Woodbury, E. J.; Ng, W. K. (November 1962). "Ruby LASER operation in the near IR". Proceedings of the Institute of Radio Engineers. 50 (11): 2367.
58 Woodbury, E. J., Eckhardt, G. M., : US Patent No. 3,371,265 (February 27, 1968)
59 Eckhardt, G. et al. Stimulated Raman Scattering From Organic Liquids. Phys. Rev. Lett. 9, 455–457 (1962).
60 Geller, M., Bortfeld, D. P. & Sooy, W. R. New woodbury-raman LASER materials. Appl. Phys. Lett. 3, 36–40 (1963).
61 Giordmaine, J. A. & Howe, J. A. Intensity-Induced Optical Absorption Cross Section in Phys. Rev. Lett. 11, 207–209 (1963).
62 Minck, R. W., Terhune, R. W. & Rado, W. G. LASER -stimulated raman effect and resonant four-photon interactions in gases h2, d2, and ch4. Appl. Phys. Lett. 3, 181–184 (1963).
63 Eckhardt, G., Bortfeld, D. P. & Geller, M. STIMULATED EMISSION OF Stokes AND ANTI-Stokes RAMAN LINES FROM DIAMOND, CALCITE, AND α-SULFUR SINGLE CRYSTALS. Appl. Phys. Lett. 3, 137–138 (1963).
64 Shen, Y. R. & Bloembergen, N. Theory of Stimulated Brillouin and Raman Scattering. Phys. Rev. 137, A1786–A1805 (1965).
65 Bloembergen, N. The Stimulated Raman Effect. American Journal of Physics 35, 989–1023 (1967).
66 Robert W. Boyd: Nonlinear Optics (Third edition) pp. 497-488
67 C.-S. Wang: Phys. Rev. 182, 482 (1969)
68 G. Eckhardt: IEEE J. QE-2, 1 (1966)
69 N. Bloembergen: Am. J. Phys. 35, 989 (1967)

70 Y.-R. Shen: In Light Scattering in Solids, ed. by M. Cardona, Topics Appl. Phys., Vol. 8 (Springer, New York 1975) pp. 275-328
71 R . L . Carmen, F. Shimizu, C. S. Wang, N. Bloembergen: Phys. Rev. A2, 60 (1970)
72 Wilke, V. & Schmidt, W. Tunable coherent radiation source covering a spectral range from 185 to 880 nm. Appl. Phys. 18, 177–181 (1979).
73 Brink, D. J. & Proch, D. Efficient tunable ultraviolet source based on stimulated Raman scattering of an excimer-pumped dye LASER . Opt. Lett., OL 7, 494–496 (1982).
74 Boyd, R. W. Chapter 6, Rabi Oscillations and Dressed Atomic States, Nonlinear Optics, Third edition.
75 Stark, J. Observation of the Separation of Spectral Lines by an Electric Field. Nature 92, 401–401 (1913).
76 Wu, F. Y., Ezekiel, S., Ducloy, M. & Mollow, B. R. Observation of Amplification in a Strongly Driven Two-Level Atomic System at Optical Frequencies. Phys. Rev. Lett. 38, 1077–1080 (1977).
77 Gruneisen, M. T., MacDonald, K. R. & Boyd, R. W. Induced gain and modified absorption of a weak probe beam in a strongly driven sodium vapor. J. Opt. Soc. Am. B 5, 123 (1988).
78 Gardiner, D.J. (1989). Practical Raman spectroscopy. Springer-Verlag.
79 Maker, P.D.; Terhune, R.W. (1965). "Study of Optical Effects Due to an Induced Polarization Third Order in the Electric Field Strength". Physical Review. 137 (3A): 801–818.
80 Aussenegg, F. R., Lippitsch, M. E., Brandmüller, J. & Nitsch, W. Collinear and noncollinear emission of anti-Stokes and second order Stokes Raman radiation. Optics Communications 37, 59–66 (1981).
81 Grasyuk, A. Z., Losev, L. L., Lutsenko, A. P. & Sazonov, S. N. Raman parametric generation of anti-Stokes radiation under conditions of amplification of an external Stokes signal. Sov. J. Quantum Electron. 20, 529–532 (1990).
82 Losev, L. L., Lutsenko, A. P. & Sazonov, S. N. Efficient parametric generation of higher stimulated Raman scattering components with diffraction-limited divergence. Sov. J. Quantum Electron. 20, 878–879 (1990).
83 Yoshikawa, S.W., Kawasaki, S., Imasaka, T., and Ishibashi, N., Jpn. J. Appl. Phys. Lcn. 30 (1991) 283.
84 Yoshikawa, S. & Imasaka, T. A new approach for the generation of ultrashort optical pulses. Optics Communications 96, 94–98 (1993).
85 McDonald, G. S., Losev, L. L., Shaw, M., Lutsenko, A. P. & New, G. H. C. Ultrabroad-bandwidth multifrequency Raman generation. *Opt. Lett.*, *OL* **19**, 1400–1402 (1994).
86 Turner, F. Multifrequency Raman Generation in the Transient Regime. (2006).
87 Strickland, D. Review of Multi-Frequency Raman Generation. *Chinese Journal of Physics* **52**, 546–568 (2014).
88 Jain, M., Xia, H., Yin, G. Y., Merriam, A. J. & Harris, S. E. Efficient Nonlinear Frequency Conversion with Maximal Atomic Coherence. Phys. Rev. Lett. 77, 4326–4329 (1996).
89 Harris, S. E. & Sokolov, A. V. Broadband spectral generation with refractive index control. Phys. Rev. A 55, R4019–R4022 (1997).
90 Harris, S. E. & Sokolov, A. V. Subfemtosecond Pulse Generation by Molecular Modulation. Phys. Rev. Lett. 81, 2894–2897 (1998).
91 Sokolov, A. V., Yavuz, D. D. & Harris, S. E. Subfemtosecond pulse generation by rotational molecular modulation. Opt. Lett. 24, 557 (1999).
92 Yavuz, D. D., Walker, D. R., Yin, G. Y. & Harris, S. E. Rotational Raman generation with near-unity conversion efficiency. Opt. Lett. 27, 769 (2002).
93 Walker, D. R. et al. Raman self-focusing at maximum coherence. Opt. Lett. 27, 2094 (2002).
94 Sokolov, A. V., Yavuz, D. D., Walker, D. R., Yin, G. Y. & Harris, S. E. Light modulation at molecular frequencies. Phys. Rev. A 63, 051801 (2001).
95 Harris, S. E., Walker, D. R. & Yavuz, D. D. Raman technique for single-cycle pulses. Phys. Rev. A 65, 021801 (2002).
96 Sensarn, S., Goda, S. N., Yin, G. Y. & Harris, S. E. Molecular modulation in a hollow fiber. Opt. Lett. 31, 2837 (2006).
97 Huang, S. W., Chen, W.-J. & Kung, A. H. Vibrational molecular modulation in hydrogen. PHYSICAL REVIEW A 11.
98 Chen, W.-J. et al. Sub-Single-Cycle Optical Pulse Train with Constant Carrier Envelope Phase. Physical review letters 100, 163906 (2008).
99 Hsieh, Z.-M. et al. Controlling the Carrier-Envelope Phase of Raman-Generated Periodic Waveforms. Phys. Rev. Lett. 102, 213902 (2009).
100 Chan, H. et al. Synthesis of attosecond waveforms using Raman-generated frequency combs. in CLEO/QELS: 2010 Laser Science to Photonic Applications 1–2 (2010).
101 Kien, F. L. et al. Subfemtosecond pulse generation with molecular coherence control in stimulated Raman scattering. Phys. Rev. A 60, 1562–1571 (1999).
102 Losev, L. L., Yoshimura, Y., Otsuka, H., Hirakawa, Y. & Imasaka, T. A multipass hydrogen Raman shifter for the generation of broadband multifrequencies. Review of Scientific Instruments 73, 2200–2202 (2002).
103 Yoshii, K., Kiran Anthony, J. & Katsuragawa, M. The simplest route to generating a train of attosecond pulses. Light Sci Appl 2, e58 (2013).

104 Berger, N. K., Levit, B., Bekker, A. & Fischer, B. Compression of periodic optical pulses using temporal fractional Talbot effect. IEEE Photonics Technology Letters 16, 1855–1857 (2004).
105 Yoshii, K., Nakamura, Y., Hagihara, K. & Katsuragawa, M. Generation of a train of ultrashort pulses by simply inserting transparent plates on the optical path. in 2014 Conference on LASER s and Electro-Optics (CLEO) - LASER Science to Photonic Applications 1–2 (2014). doi:10.1364/CLEO_QELS.2014.FTh1D.5.
106 Belenov E. M., Nazarkin A. V., Prokopovich I. P, "Dynamics of an intense femtosecond pulse in a Raman-active medium," Pisma ZhETF, Vol. 55, ISSUE 4 , PAGE 218, 1992.
107 Korn, G., Dühr, O. & Nazarkin, A. Observation of Raman Self-Conversion of fs-Pulse Frequency due to Impulsive Excitation of Molecular Vibrations. PHYSICAL REVIEW LETTERS 81, 4 (1998).
108 Wang, J. K., Siegal, Y., Lü, C., Mazur, E., and Reintjes, J., "Subpicosecond stimulated Raman scattering in highpressure," Journal of the Optical Society of America B, Vol. 11, Issue 6, pp. 1031-1037 , 1994.
109 Krylov, V., Ollikainen, O., Wild, U., Rebane, A., Bespalov, V., and Staselko, D., "Femtosecond stimulated Raman scattering in pressurized gases in the ultraviolet and visible spectral ranges," Journal of the Optical Society of America B, Vol. 15, Issue 12, pp. 2910-2916, 1998.
110 Nazarkin, A., Korn, G., Wittmann, M. & Elsaesser, T. Generation of Multiple Phase-Locked Stokes and Anti-Stokes Components in an Impulsively Excited Raman Medium. Phys. Rev. Lett. 83, 2560–2563 (1999).
111 Wittmann, M., Nazarkin, A. & Korn, G. New regime of fs-pulse stimulated Raman scattering: Appl Phys B 70, S261–S267 (2000).
112 Zhavoronkov, N. & Korn, G. Generation of Single Intense Short Optical Pulses by Ultrafast Molecular Phase Modulation. Phys. Rev. Lett. 88, 203901 (2002).
113 McDonald, G. S., Losev, L. L., Shaw, M., Lutsenko, A. P. & New, G. H. C. Ultrabroad-bandwidth multifrequency Raman generation. Opt. Lett., OL 19, 1400–1402 (1994).
114 McDonald, G. S. Ultrabroad-bandwidth multifrequency Raman soliton pulse trains. Opt. Lett., OL 20, 822–824 (1995).
115 Sali, E., Mendham, K. J., Tisch, J. W. G., Halfmann, T. & Marangos, J. P. High-order stimulated Raman scattering in a highly transient regime driven by a pair of ultrashort pulses. Opt Lett 29, 495–497 (2004).
116 Tani, F., Belli, F., Abdolvand, A., Travers, J. C. & Russell, P. S. J. Generation of three-octave-spanning transient Raman comb in hydrogen-filled hollow-core PCF. Optics Letters 40, 1026 (2015).
117 Losev, L. L., Song, J., Xia, J. F., Strickland, D. & Brukhanov, V. V. Multifrequency parametric infrared Raman generation in $KGd(WO_4)_2$ crystal with biharmonic ultrashort-pulse pumping. *Opt. Lett., OL* **27**, 2100–2102 (2002).
118 Turner, F. C., Trottier, A., Strickland, D. & Losev, L. L. Transient multi-frequency Raman generation in SF6. *Optics Communications* **270**, 419–423 (2007).
119 Turner, F. Multifrequency Raman Generation in the Transient Regime. (2006).
120 Shon, N. H., Le Kien, F., Hakuta, K. & Sokolov, A. V. Two-dimensional model for femtosecond pulse conversion and compression using high-order stimulated Raman scattering in solid hydrogen. Phys. Rev. A 65, 033809 (2002).
121 Grabtchikov, A. S. et al. Observation of Raman conversion for 70-fs pulses in KGd(WO_4)_2 crystal in the regime of impulsive stimulated Raman scattering. Opt. Lett. 28, 926 (2003).
122 Zhi, M., Pestov, D., Wang, X., Murawski, R. & Sokolov, A. Broadband generation produced in Raman-active crystals by two- and three-color femtosecond laser pulses. W15.022 (2006).
123 Zhi, M. & Sokolov, A. V. Broadband coherent light generation in a Raman-active crystal driven by two-color femtosecond LASER pulses. Opt. Lett. 32, 2251 (2007).
124 Zhi, M. & Sokolov, A. V. Broadband generation in a Raman crystal driven by a pair of time-delayed linearly chirped pulses. New J. Phys. 10, 025032 (2008).
125 Zhi, M., Wang, K., Hua, X. & Sokolov, A. V. Pulse-shaper-assisted phase control of a coherent broadband spectrum of Raman sidebands. Opt. Lett. 36, 4032 (2011).
126 Lu, C.-H. et al. Raman-assisted octave-spanning continuum generation in single-crystal diamond for sub-cycle pulse synthesis. in CLEO: 2013 QW3E.4 (OSA, 2013). doi:10.1364/CLEO_QELS.2013.QW3E.4.
127 Wang, K., Zhi, M., Hua, X., Strohaber, J. & Sokolov, A. V. Coherent broadband light generation with a double-path configuration. Applied Optics 53, 2866 (2014).
128 Zhdanova, A. A., Bahari, A., Shutova, M. & Sokolov, A. V. Synthesis of ultrafast waveforms using coherent Raman sidebands. arXiv:1901.11155 [physics] (2019).
129 Bahari, A., Zhdanova, A. A., Shutova, M. & Sokolov, A. V. Synthesis of ultrafast waveforms using coherent Raman sidebands. Phys. Rev. A 102, 013520 (2020).
130 Shutova, M., Shutov, A. D., Zhdanova, A. A., Thompson, J. V. & Sokolov, A. V. Coherent Raman Generation Controlled by Wavefront Shaping. Sci Rep 9, 1565 (2019).
131 Fabry, C; Perot, A (1899). "Theorie et applications d'une nouvelle methode de spectroscopie interferentielle". Ann. Chim. Phys. 16 (7).
132 Birks, T. A., Roberts, P. J., Russell, P. S. J., Atkin, D. M. & Shepherd, T. J. Full 2D photonic band gaps in silica/air structures. Electronics Letters 31, 1941–1943 (1995).

133 Benabid, F. Stimulated Raman Scattering in Hydrogen-Filled Hollow-Core Photonic Crystal Fiber. Science 298, 399–402 (2002).
134 Benabid, F., Bouwmans, G., Knight, J. C., Russell, P. S. J. & Couny, F. Ultrahigh Efficiency LASER Wavelength Conversion in a Gas-Filled Hollow Core Photonic Crystal Fiber by Pure Stimulated Rotational Raman Scattering in Molecular Hydrogen. Phys. Rev. Lett. 93, 123903 (2004).
135 Trabold, B. M., Abdolvand, A., Euser, T. G. & Russell, P. S. J. Efficient anti-Stokes generation via intermodal stimulated Raman scattering in gas-filled hollow-core PCF. Optics Express 21, 29711 (2013).
136 Couny, F., Benabid, F., Roberts, P. J., Light, P. S. & Raymer, M. G. Generation and Photonic Guidance of Multi-Octave Optical-Frequency Combs. Science 318, 1118–1121 (2007).
137 J. von Neumann, E.P. Wigner (1929). "Über merkwürdige diskrete Eigenwerte". 30 (Phys. Z. ed.): 465–467.
138 Benoît, A. et al. Over-five octaves wide Raman combs in high-power picosecond-LASER pumped H_2-filled inhibited coupling Kagome fiber. Opt. Express 23, 14002 (2015).
139 Eimerl, D., Hargrove, R. S. & Paisner, J. A. Efficient Frequency Conversion by Stimulated Raman Scattering. Phys. Rev. Lett. 46, 651–654 (1981).
140 Hickman, A. P., Paisner, J. A. & Bischel, W. K. Theory of multiwave propagation and frequency conversion in a Raman medium. Phys. Rev. A 33, 1788–1797 (1986).
141 Hickman, A. P. & Bischel, W. K. Theory of Stokes and anti-Stokes generation by Raman frequency conversion in the transient limit. Phys. Rev. A 37, 2516–2523 (1988).
142 Losev, L. L. & Lutsenko, A. P. Parametric Raman LASER with a discrete output spectrum equal in width to the pump frequency. Quantum Electronics 23, 919–926 (1993).
143 McDonald, G. S., Losev, L. L., Shaw, M., Lutsenko, A. P. & New, G. H. C. Ultrabroad-bandwidth multifrequency Raman generation. Opt. Lett., OL 19, 1400–1402 (1994).
144 Losev, L. L. & Lutsenko, A. P. Ultrabroadband parametric stimulated Raman scattering in a highly transient regime. Optics Communications 132, 489–493 (1996).
145 Syed, K. S., McDonald, G. S. & New, G. H. C. Transverse effects in ultrabroadband multifrequency Raman generation. 10.
146 Sali, E. et al. Behavior of high-order stimulated Raman scattering in a highly transient regime. Phys. Rev. A 72, 013813 (2005).
147 Turner, F. C. & Strickland, D. Anti-Stokes enhancement of multifrequency Raman generation in a hollow fiber. *Opt. Lett., OL* **33**, 405–407 (2008).
148 Yan, H. & Strickland, D. Effect of Two-Photon Stark Shift on the Multi-Frequency Raman Spectra. *Applied Sciences* **4**, 390–401 (2014).
149 Sokolov, A.V.; Walker, D.R.; Yavuz, D.D.; Yin, G.Y.; Harris, S.E. Raman generation by phased and antiphased molecular states. Phys. Rev. Lett. 2000, 85, 562–565.
150 Sali, E.; Kinsler, P.; New, G.H.C.; Mendham, K.J.; Halfmann, T.; Tisch, J.W.G.; Marangos, J.P.Behavior of high-order stimulated Raman scattering in a highly transient regime. Phys. Rev. A2005, 72, 013813.
151 Alharbi, M. et al. Raman gas self-organizing into deep nano-trap lattice. Nature Communications 7, ncomms12779 (2016).
152 Trebinoand, R. Kane, D. J. Characterization of Arbitrary Femtosecond Pulses Using Frequency-Resolved Optical Gating. J. Opt. Soc. Am. A **10**, 1101 (1993).
153 Peatross, J. & Rundquist, A. Temporal decorrelation of short LASER pulses. J. Opt. Soc. Am. B 15, 216 (1998).
154 Diels, J.-C. M., Fontaine, J. J., McMichael, I. C. & Simoni, F. Control and measurement of ultrashort pulse shapes (in amplitude and phase) with femtosecond accuracy. Appl. Opt. 24, 1270 (1985).
155 Stark, H., ed. Image Recovery: Theroy and Application. 1987, Academic Press: Orlando.
156 Richman, B. A., DeLong, K. W. & Trebino, R. Temporal characterization of the Stanford mid-IR FEL micropulses by “FROG”. Nuclear Instruments and Methods in Physics Research Section A: Accelerators, Spectrometers, Detectors and Associated Equipment 358, 268–271 (1995).
157 Clement, T. S., Kane, D. J. & Taylor, A. J. Single-shot measurement of the amplitude and phase of ultrashort LASER pulses in the violet. Opt. Lett. 20, 70 (1995).
158 Sweetser, J. N., Fittinghoff, D. N. & Trebino, R. Transient-grating frequency-resolved optical gating. Opt. Lett. 22, 519 (1997).
159 DeLong, K. W., Trebino, R., Hunter, J. & White, W. E. Frequency-resolved optical gating with the use of second-harmonic generation. J. Opt. Soc. Am. B 11, 2206 (1994).
160 Tsang, T., Krumbügel, M. A., DeLong, K. W., Fittinghoff, D. N. & Trebino, R. Frequency-resolved optical-gating measurements of ultrashort pulses using surface third-harmonic generation. Opt. Lett. 21, 1381 (1996).
161 Fienup, J. R., Phase retrieval algorithms: a comparison, Appl. Opt., vol 21, pp. 2758-2769, 1982.
162 J. R. Fienup, C. C. Wackerman, "Phase-retrieval stagnation problems and solutions", J. Opt. Soc. Amer. A, vol.3, 1986.

163 K. W. DeLong, R. Trebino, "Improved Ultrashort Pulse-retrieval Algorithm for frequency resolved optical gating", JOSA A, vol.11. 1994.
164 Trebino, R., Frequency-Resolved Optical Gating: The Measurement of Ultrashort LASER Pulses, Chapter 10 Practical Issues, Marginals, Error Checks, and Error Correction
165 Zhang, Z., Deslauriers, A. M. & Strickland, D. Dual-wavelength chirped-pulse amplification system. Optics Letters 25, 581 (2000).
166 Herzberg, G., Molecular spectra and molecular structure, Vol. 2 (Van Nostrand Reinhold, New York, 1979)
167 R. Fork, O. Martinez and J. Gordon, "Negative dispersion using pairs of prisms," Optics Letters, Vol. 9, Issue 5, pp. 150-152, 1984.
168 E. Treacy, "Optical pulse compression with diffraction gratings," IEEE Journal of Quantum Electronics, Vol. 5, no. 9, pp. 454 - 458,1969
169 Trebino, R. et al. Frequency-resolved optical gating: the state of the art. in The 15th Annual Meeting of the IEEE LASER s and Electro-Optics Society vol. 1 223–224 vol.1 (2002).
170 Yan, H. Characterizing Transient Regime Multi-frequency Raman Generation by the Aid of Spectral Phase Interferometry for Direct Electric-field Reconstruction. (2013).
171 Xu, Z., Rahnama, A., Strickland, D., “Temporal and Spectral Measurement of Red-shifted Spectrum in Multi-frequency Raman Generation”, Photonics North, IEEE, 2018

Appendix A

Code written in Python

A1. Data recording program

##This program is written by Zujun Xu, 2018, for the purpose of data recording. Only tested with Python 2.7, works similar as the labview program in the lab, though, command-line only

```
import numpy as np
import cv2
import matplotlib.pyplot as plt

def gaus_fit(data):     #Gaussian fit for the auto-correlation intensity curve, still need to be improved
    x = np.arange(data.size)
    a = np.sum(x*data)/np.sum(data)
    sigma = np.sqrt(np.abs(np.sum((x-a)**2*data)/np.sum(data)))
    fit = lambda t : data.max()*np.exp(-(t-a)**2/(2*sigma**2))
    FWHM = 2*np.sqrt(2*np.log(2))*sigma
    return fit, FWHM

i = 0
#cap = cv2.VideoCapture('E:/Trace/1.mpg')
cap = cv2.VideoCapture(0)
next_step = input('Choose one of the following operations:\n 1:background saving\n 2:calibration for time \n 3:calibration for spectrum \n 4:data recording(FROG) \n 5:video view \n 6:auto-correlation\n PLEASE REMEMBER TO SAVE BACKGROUND FIRST!\n')
if next_step == 1:
    while(True):
        ret,frame = cap.read()
        gray = cv2.cvtColor(frame, cv2.COLOR_BGR2GRAY)
        #cv2.imshow('Camera0',gray)
        if np.amax(gray)>0:
            np.savetxt('background0.txt',gray,fmt='%03d')   #original background
            a = np.sum(gray,axis=0)
            np.savetxt('background1.txt',a,fmt='%03d')  #time axis background
            b = np.sum(gray,axis=1)
            np.savetxt('background2.txt',b,fmt='%03d')  #spectral axis background
            plt.plot(a)
            break
        if cv2.waitKey(1) & 0xFF == ord('q'):
            break

elif next_step == 2:
    bg = np.loadtxt('background1.txt')
    while(True):
```

```
        ret, frame = cap.read()
        gray = cv2.cvtColor(frame, cv2.COLOR_BGR2GRAY)
        M = np.amax(gray)   #maximum pixel intensity
        cv2.imshow('Camera1',gray)
        if M>100 and M<255:          #use this intensity number to get rid of captures with too low or over
saturated ones
            i = i+1
            a = np.sum(gray,axis=0)#-bg  #with background deduction
            plt.plot(a)
            print np.argmax(a)
        if i>10:
            break
        if cv2.waitKey(1) & 0xFF == ord('q'):
            break

elif next_step == 3:
    bg = np.loadtxt('background2.txt')
    while(True):
        ret, frame = cap.read()
        gray = cv2.cvtColor(frame, cv2.COLOR_BGR2GRAY)
        M = np.amax(gray)   #maximum intensity
        cv2.imshow('Camera2',gray)
        if M>100 and M<255:
            i = i+1
            a = np.sum(gray,axis=1)#-bg  #with background deduction
            plt.plot(a)
            print np.argmax(a)
        if i>10:
            break
        if cv2.waitKey(1) & 0xFF == ord('q'):
            break

elif next_step == 4:
    delay_time = input('Please input time delay for this set data!\n')
    bg = np.loadtxt('background0.txt')
    while(True):
        ret, frame = cap.read()
        gray = cv2.cvtColor(frame, cv2.COLOR_BGR2GRAY)
        M = np.amax(gray)   #maximum intensity
        cv2.imshow('Camera3',gray)
        if M>100 and M<255:
            i = i+1
            #gray0 = np.array(gray)-np.array(bg)
            #np.savetxt('%d-%d.txt' %(delay_time, i),gray0,fmt='%03d')
            np.savetxt('%d-BG%d.txt' %(delay_time, i),gray,fmt='%03d')
        if i>50:
            break
```

```
        if cv2.waitKey(1) & 0xFF == ord('q'):
            break

elif next_step == 5:
    bg = np.loadtxt('background0.txt')
    while(True):
        ret, frame = cap.read()
        gray = cv2.cvtColor(frame, cv2.COLOR_BGR2GRAY)
        cv2.imshow('Camera4',gray)
        #print np.amax(gray)
        if cv2.waitKey(1) & 0xFF == ord('q'):
            break

elif next_step == 6:
    calibration_factor = input('please provide calibration factor using fs/pix: \n')
    bg = np.loadtxt('background1.txt')
    while(True):
        ret, frame = cap.read()
        gray = cv2.cvtColor(frame, cv2.COLOR_BGR2GRAY)
        M = np.amax(gray)   #maximum intensity
        cv2.imshow('Camera5',gray)
        if M>100 and M<255:
            i = i+1
            a = np.sum(gray,axis=0)#-bg  #with background deduction
            fit,FWHM = gaus_fit(a)
            plt.plot(a)
            print 'Pulse Duration: ', int(FWHM*calibration_factor/np.sqrt(2.0))
        if i>10:
            break
        if cv2.waitKey(1) & 0xFF == ord('q'):
            break

plt.show()
#when everything done, release the capture
cap.release()
cv2.destroyAllWindows()
```

A2. Show and plot the raw data

##This program is used to show and plot the recorded data so we can have a look at it before further analysis. The main reason for it is the recorded data might be just noise, too weak, or over saturated;.

```
import glob
import numpy as np
from pylab import *
import matplotlib.pyplot as plt
```

```
def showtrace(path):              #define the load and plot funtion
    files = glob.glob(path)
    filenumber = len(files)
    j = 0
    for file in files:
        f = np.loadtxt(file)
        plt.imshow(f)
        savefig(file+"%d.png" %j)
        j = j+1
        print j
        plt.close()

path0 = 'rawfile/'
path = path0+'*.frg'
showtrace(path)
```

A3. Preparing data for the FROG program

##This simple program is used to add the text headlines for the data, as the raw data does not have the calibration factors, the centre-frequency, or the dimensions.

```
import numpy as np
from pylab import *

cw = input('Please input the center wavelength, in nm.\n')      #418 nm for Stokes pump, 393 nm for pump, and 381.5 nm for the first antiStokes

f1 = open('raw_data.txt','r')          #read the raw data that recorded by the CCD camera
f2 = open('b.frg','w')
a = np.loadtxt('raw_data.txt')
a = a.T

f2.write('%s\t %s\t 22.85\t 0.051\t %s\n'%(len(a), len(a[0]), cw))      #add the headlines that contains the horizontal length, vertical length, time calibration factor, spectrum calibration factor, and the centre-frequency

for k in f1:
    f2.write(k)

f1.close()
f2.close()
```

A4. Plotting pulses

##A simple plotting program to show the pulses and its phases, also a curve fitting is added to fit the phase to gain further understanding of the phases. It can be modified to deal with a bunch of files with one single run.

```
import numpy as np
import matplotlib.pyplot as plt

a = np.loadtxt('b.bin.Ek.dat')
b = a[:]        #choose part of data, as most of the far out data is noise
d = b.T

f = open('E.dat','w')
np.savetxt(f,b,fmt='%f')          #save the data for future use
f.close()

h = np.polyfit(d[0],d[2],8)       #fit the phase
g = np.poly1d(h)                  #the formula for the fit curve
x_new = d[0]
y_new = g(x_new)

fig, ax1 = plt.subplots()         #plot with subplots
ax1.plot(d[0], d[1], 'b')         #show the intensity
#ax1.plot(d[0], np.sqrt(d[1]), 'b')        #show the amplitude
ax1.set_xlabel('Time Delay(fs)',fontsize=16)
ax1.set_ylabel('Intensity', fontsize=16,color='b')
## Make the y-axis label and tick labels match the line colour.
for tl in ax1.get_yticklabels():
    tl.set_color('b')

ax2 = ax1.twinx()
ax2.plot(d[0], d[2], 'r')#, x_new, y_new, 'y')
ax2.set_ylabel('Phase(rad)',fontsize=16, color='r')
for tl in ax2.get_yticklabels():
    tl.set_color('r')

plt.title("Pulse and phase")
plt.xlim(-4000,4000)

plt.show()
```

A5. Spectrum plotting

##This program is for spectrum plotting, similar to the previous pulse plotting, but this one is a multi-file plotting program that deals with a bunch of pulses at one run.

```
import numpy as np
import matplotlib.pyplot as plt
import glob
from pylab import *
```

```
color_sequence = ['#FF0000', '#FF8000', '#000000', '#00FF00', '#00FFFF',
                  '#0000FF', '#9B30FF', '#EE82EE', '#CDC1C5', '#008080',
                  '#8E8E38', '#FFC1C1', '#CD5B45', '#D2691E', '#FFD700',
                  '#98FB98', '#FFFF00', '#00BFFF', '#837FFF', '#DA70D6']     #introducing colour sequence

def ReadFile(path):              #define the loading data function
    a = np.loadtxt(path)
    b = a[:]
    d = b.T
    return d

path0 = 'Spec/*'                 #showing file direction
files = sorted(glob.glob(path0))

N = len(files)
i = 0
c = 299792458.0                  #speed of light, m/s

for i in range(0,N):
    path1 = files[i]+'/b.bin.Speck.dat'
    d = ReadFile(path1)
    n = len(d[0])

    fig, ax1 = plt.subplots()
    e = d[0]                                #with wavelength in nm
    #e = [c/(a*1000.0) for a in e]          #with frequency in THz
    ax1.plot(e, np.sqrt(d[1]), 'b')         #plot the amplitude
    #ax1.set_xlabel('Frequency(THz)',fontsize=16)
    #ax1.set_ylabel('Intensity(Normalized)',fontsize=16, color='b')
    ax1.set_xlabel('Wavelength(nm)',fontsize=16)
    ax1.set_ylabel('Amplitude(Normalized)',fontsize=16, color='b')
    for tl in ax1.get_yticklabels():
        tl.set_color('b')

    ax2 = ax1.twinx()
    ax2.plot(e, d[2], 'r')                  #plot the phases
    ax2.set_ylabel('Phase(rad)',fontsize=16, color='r')
    #plt.xlim(355,361)
    #plt.xlim(830,842)
    plt.ylim(-8,5)
    for tl in ax2.get_yticklabels():
        tl.set_color('r')

    savefig("%d.png" %i)
    plt.close()

plt.show()
```

A6. Instantaneous Frequency calculation and plotting

```
##This program is for calculation of the instantaneous frequency and plotting
import numpy as np
import matplotlib.pyplot as plt
from sympy import *
import glob

#w0 = 358.17            #centre wavelength of the 837nm pump, in THz
#w0 = 381.42            #the 786nm
w0 = 404.67             #first anti-Stokes


def ReadFile(path):
    a = np.loadtxt(path)
    b = a[:]
    d = b.T
    return d

path0 = 'Spec/*'
files = sorted(glob.glob(path0))
c = 299792458.0         #speed of light, m/s
N = len(files)
i = 0

for i in range(0,N):
    path1 = files[i]+'/b.bin.Ek.dat'
    d = ReadFile(path1)
    n = len(d[0])
    e = d[0]
    x = (d[0][n-1] - d[0][0])/n
    y = np.gradient(d[2],x)
    plt.plot(d[0],d[1],cmap='coolwarm')#,label=files[i])  #cmap, a new way to define colour sequence
    plt.plot(d[0],y*100,cmap='coolwarm',label=files[i])

plt.xlim(-2500,2500)
plt.xlabel('Time(fs)')
plt.ylabel('Frequency(THz)', color='b')
plt.title('Instantaneous Frequency')
legend = plt.legend(loc='best', shadow=True, fontsize=16)

plt.show()
```

A7. Double-pulse model simulation

##This program is created and edited by Zujun Xu, 2018, for the generation of FROG-trace with given pulse

```
import numpy as np
import matplotlib.pylab as plt
from matplotlib import cm
from pylab import *

#################
# define functions #
#################
## for generate Gaussian pulses
def gaussian_pulse(T,f,A,phase,tau):
    w0 = f*2*np.pi        #central angular frequency of pulse
    E0 = A*np.sqrt(np.exp(-4.0*np.log(2.0)/np.log(np.e)*((t-tau)/T)**2))*np.exp(-1j*w0*t)
    E = E0*np.exp(1j*phase)
    return E0,E

## calculate correlation of two functions. f(t)*f(t-tau), without sum/integral
def correlation(e,td):        #shift one pulse by time delay tau
    E_delay = e*1.0
    if td<=0:
        E_delay[0:N+td] = e[-td:]
        E_delay[N+td:] = [0]*(-td)
    else:
        E_delay[0:td] = [0]*(td)
        E_delay[td:] = e[0:N-td]
    return  E_delay,e*E_delay

def xcorr(e0,e,td):           #shift pulse by time delay tau
    E_delay = e*1.0
    if td<=0:
        E_delay[0:N+td] = e0[-td:]
        E_delay[N+td:] = [0]*(-td)
    else:
        E_delay[0:td] = [0]*(td)
        E_delay[td:] = e0[0:N-td]
    return  E_delay,e*E_delay

## generate FROG trace with given pulse
def FROG_generator(e,E,TD):
    FROG = np.zeros((TD,N),dtype=float)
    for td in range(-TD/2,TD/2):
        #E_delay, E_corre = correlation(e,td)
        E_delay, E_corre = xcorr(e,E,td)
```

```
            temp0 = np.fft.fftshift(np.fft.fft(E_corre,5*N))
            temp0 = temp0[2*N+20:3*N+20]
            FROG[(td+TD/2)-1] = abs(temp0)**2
        return FROG

## plot out FROG trace
def FROG_trace_plot(FROG):
        fig,ax = plt.subplots()
        plt.imshow(FROG.T, extent=[-0.128*dt*4,0.128*dt*4,-
64000*df/5,64000*df/5])#,vmax=abs(FROG).max(), vmin=-abs(FROG).max())
        #plt.ylim(-1,1)
        plt.xlim(-10,10)
        ax.set_ylabel('Frequency(THz)')
        ax.set_xlabel('Time(x0.25ps)')
        #plt.title("FROG trace")
        #plt.show()
        plt.grid(True)
        savefig("%d.png" %i)
        plt.close()

## plot out pulse with phase
def pulse_phase_plot(E,phase,t):
        t = t-T0/2
        fig, ax1 = plt.subplots()
        ax1.plot(t, E*np.conj(E), 'b')
        ax1.set_xlabel('Time Delay(fs)')
        ax1.set_ylabel('Intensity', color='b')
        #Make the y-axis label and tick labels match the line color.
        for tl in ax1.get_yticklabels():
            tl.set_color('b')
        ax2 = ax1.twinx()
        ax2.plot(t, phase,'r')
        ax2.set_ylabel('Phase(rad)', color='r')
        for tl in ax2.get_yticklabels():
            tl.set_color('r')
        plt.title("E-field and phase")
        #plt.xlim(0,1000)
        #plt.ylim(0,20)

## get frequency domain phase
def spectrum_phase(E0,E,f):
        N0 = int(f/df)
        #print N0
        S = np.fft.fftshift(np.fft.fft(E,N))##np.fft.fftshift
        S0 = np.fft.fftshift(np.fft.fft(E0,N))
        ph0_f = np.angle(S0)#[N0-10:N0+10])
        #ph0_f = [mt.atan2(k.imag,k.real) for k in S0[N_min:N_max]]
```

```
    ph0_f = np.unwrap(ph0_f)
    ph0_f = ph0_f
    ph_f = np.angle(S)#[N0-10:N0+50])
    #ph_f = [mt.atan2(k.imag,k.real) for k in S[N_min:N_max]]
    ph_f = np.unwrap(ph_f)
    freq1 = freq#[N0-50:N0+50]
    return S0,S,ph0_f,ph_f,freq1

## get time domain phase
def pulse_phase(E0,E):
    ph0_t = np.angle(E0)
    #ph0_t = [mt.atan2(k.imag,k.real) for k in E0]
    ph0_t = np.unwrap(ph0_t)
    ph_t = np.angle(E)
    #ph_t = [mt.atan2(k.imag,k.real) for k in E]
    ph_t = np.unwrap(ph_t)
    return ph_t-ph0_t

## plot out spectrum and phase
def spectum_phase_plot(S,freq,phase):
    fig, ax1 = plt.subplots()
    ax1.plot(freq, S*np.conj(S)/max(S*np.conj(S)), 'b')
    ax1.set_xlabel('Frequency(THz)')
    ax1.set_ylabel('Intensity', color='b')
    #Make the y-axis label and tick labels match the line colour.
    for tl in ax1.get_yticklabels():
        tl.set_color('b')
    ax2 = ax1.twinx()
    ax2.plot(freq, phase,'r')
    ax2.set_ylabel('Phase(rad)',color='r')
    for tl in ax2.get_yticklabels():
        tl.set_color('r')
    plt.title("Spctrum and phase")
    #plt.xlim(0,1000)
    #plt.ylim(-100,10)

## FROGs with different time delay
def FROGs_T(delay):
    A1 = 1.0            #-
    A2 = 2.0            #+
    f1 = 0.6/1000           #Raman order
    f2 = (-0.30)/1000#shoulder
    f = (f1+f2)/2.0
    tau1 = T0/2         #pulse peak time
    tau2 = T0/2+i

    phase1 = (a2*(t-tau1)**2+a3*(t-tau1)**3)            #zero phase at pulse peak
```

```
    phase2 = (a2*(t-tau2)**2+a3*(t-tau2)**3)

    E10,E1 = gaussian_pulse(T1,f1,A1,phase1,tau1)      #generate Gaussian pulse E-field
    E20,E2 = gaussian_pulse(T2,f2,A2,phase2,tau2)
    E = E1+E2
    E0 = np.sqrt(E*np.conj(E))
    ph_t = pulse_phase(E0,E)
    S0,S,ph0,ph,freq0 = spectrum_phase(E0,E,f)
    #pulse_phase_plot(E,ph,t)
    S10,S1,ph10,ph1,freq1 = spectrum_phase(E10,E1,f1)
    S20,S2,ph20,ph2,freq2 = spectrum_phase(E20,E2,f2)
    FROG = FROG_generator(e,E,TD)
    FROG_trace_plot(FROG)

##########################################
# define a few constants fft python random phase #
##########################################
c = 300        #nm/fs
e0 = np.loadtxt('b.bin.Ek.dat')
e0 = e0.T
e1 = np.sqrt(e0[1])
e1_ph = e0[2]
e = np.array(e1)*np.exp(1j*(np.array(e1_ph)))

N = len(e0[0])          #steps
N_max = np.max(e0[0])
N_min = np.min(e0[0])
t = e0[0]-N_min
T0 = N_max-N_min
dt = T0/(N-1)
df = 1.0/T0
TD = 2*N    #time delay for FROG-trace generation
freq = np.arange(0,1/dt,df)*1000
T1 = 1200                    #pulse duration in fs, FWHM
T2 = 800

##########################################
# define phase factors for different phase orders #
##########################################
a1 = 0
a2 = 2.50*10**-6      #second order phase factor 1.50*10**-6
#a2 = 0
a3 = 2.50*10**(-9)
#a3=0
a4 = 0

#############
```

```
# FROG trace #
##############
for i in range (0,1000,50):
    FROGs_T(i)

#plt.plot(S1*np.conj(S1))
#plt.plot()
#pulse_phase_plot(E1,phase1,t)
#spectum_phase_plot(S1,freq1,ph1)
#spectum_phase_plot(S,freq,ph-ph0)          ##For program testing and checking
#FROG = FROG_generator(e,E,TD)
#FROG_trace_plot(FROG)
#plt.xlabel('Time(fs)')
#plt.ylabel('Frequency(THz)', color='b')
#plt.title('Instantaneous Frequency')
#plt.ylim(399,410)
#plt.show()
```

A8. Double-pulse semi-iteration

##This program is created and edited by Zujun Xu, 2019, for the generation of FROG-trace with given pulses. Double-pulse simulations iteration.

```
import numpy as np
import matplotlib.pylab as plt
from pylab import *
import sys
#sys.setrecursionlimit(10000)

#################
# define functions #
#################
def gaussian_pulse(T,f,A,phase,tau)          #As in previous program

def xcorr(e0,e,td)                           #As in previous program

## calculate the different of trace A and trace B
def array_diff(A,B):
    A = A/np.max(A)
    B = B/np.max(B)
    return np.sum(np.square(A-B))/np.sum(np.square(B))

def FROG_generator(e,E,TD)                   #As previous

def FROG_trace_plot(FROG)                    #As previous

## calculate FROG traces with different time delays
```

```
def FROGs(T1,i0,A,f0,a,a2,a3):
    phase1 = a2*(t-tau1)+a3*(t-tau1)**2    #zero phase at pulse peak
    phase1 = integral(phase1)
    phase2 = a2*(t-tau1)#a2*(t-tau1)+a*(np.exp(-4.0*np.log(2.0)/np.log(np.e)*((t-tau1)/Tp)**2))-
0.0000#+np.exp(-4.0*np.log(2.0)/np.log(np.e)*((t-tau1+0)/850.0)**2))
    phase2 = a*(np.exp(-4.0*np.log(2.0)/np.log(np.e)*((t-tau1)/Tp)**2))#-0.0005
    phase2 = integral(phase2)
    E1 = gaussian_pulse(T1,f0,A,phase1,tau1)  #generate Gaussian pulse E-field
    E2 = gaussian_pulse(T1,f0,1.0,phase2,tau1)
    E = E1+E2
    FROG = FROG_generator(e,E,TD)
    delta = array_diff(FROG, original_trace)
    return delta
    #FROG_trace_plot(FROG)

def best_T1():                          #find the best time delay
    global T1
    delta0 = FROGs(T1,i0,A,f0,a,a2,a3)
    delta1 = FROGs(T1+delta_T,i0,A,f0,a,a2,a3)
    delta2 = FROGs(T1-delta_T,i0,A,f0,a,a2,a3)

    #print delta0, delta1, delta2
    if delta0>delta1:
        T1 = T1+delta_T
        best_T1()
        #print T1,"aa"
    elif delta0>delta2:
        T1 = T1-delta_T
        best_T1()
        #print T1,"bb"
    else:
        T1 = T1
        #return T1,T2,i0,i1,A,f0,f,a,a2
        #print T1,"cc"

def best_A():                       #find the best amplitude ratio
    global  A
    delta0 = FROGs(T1,i0,A,f0,a,a2,a3)
    delta1 = FROGs(T1,i0,A+delta_A,f0,a,a2,a3)
    delta2 = FROGs(T1,i0,A-delta_A,f0,a,a2,a3)
    #print A
    if delta0>delta1:
        A = A+delta_A
        best_A()
    elif delta0>delta2:
        A = A-delta_A
        best_A()
```

```
    else:
        A = A
        #return T1,T2,i0,i1,A,f0,f,a,a2

def best_f0():                  #find the best centre-frequency
    global f0
    delta0 = FROGs(T1,i0,A,f0,a,a2,a3)
    delta1 = FROGs(T1,i0,A,f0+delta_f,a,a2,a3)
    delta2 = FROGs(T1,i0,A,f0-delta_f,a,a2,a3)
    if delta0>delta1:
        f0 = f0+delta_f
        best_f0()
    elif delta0>delta2:
        f0 = f0-delta_f
        best_f0()
    else:
        f0 = f0
        #return T1,T2,i0,i1,A,f0,f,a,a2

def best_a():                   #find the best intensity dependent factor
    global a
    delta0 = FROGs(T1,i0,A,f0,a,a2,a3)
    delta1 = FROGs(T1,i0,A,f0,a+delta_a,a2,a3)
    delta2 = FROGs(T1,i0,A,f0,a-delta_a,a2,a3)
    if np.abs(a)>10:
        a = a
    elif delta0>delta1:
        a = a+delta_a
        best_a()
    elif delta0>delta2:
        a = a-delta_a
        best_a()
    else:
        a = a
        #return T1,T2,i0,i1,A,f0,f,a,a2

def best_a2():                  #find the best second order phase factor
    global a2
    delta0 = FROGs(T1,i0,A,f0,a,a2,a3)
    delta1 = FROGs(T1,i0,A,f0,a,a2+delta_a2,a3)
    delta2 = FROGs(T1,i0,A,f0,a,a2-delta_a2,a3)
    if delta0>delta1:
        a2 = a2+delta_a2
        best_a2()
    elif delta0>delta2:
        a2 = a2-delta_a2
        best_a2()
```

```
    else:
        a2 = a2
        #return T1,T2,i0,i1,A,f0,f,a,a2

def best_a3():                  #find the best third order phase factor
    global a3
    delta0 = FROGs(T1,i0,A,f0,a,a2,a3)
    delta1 = FROGs(T1,i0,A,f0,a,a2,a3+delta_a3)
    delta2 = FROGs(T1,i0,A,f0,a,a2,a3-delta_a3)
    if delta0>delta1:
        a3 = a3+delta_a3
        best_a3()
    elif delta0>delta2:
        a3 = a3-delta_a3
        best_a3()
    else:
        a3 = a3

def integral(a):
    z = a
    y = a*1.0
    n = len(a)
    #print n
    for i in range (0,n):
        z[i] = np.trapz(y[0:i],dx=dt)
    return z

def rotate_array(a,i):
    b = a*1.0
    N = len(a)
    b[0:i] = 0
    b[i:] = a[0:N-i]
    return  b

def minimize_delta():
    i = 0
    while i<20:
        delta = FROGs(T1,i0,A,f0,a,a2,a3)
        best_f0()
        best_a()
        best_a2()
        best_a3()
        #best_T1()
        best_A()
        i+=1
        print delta
    print T1,'\n',A,'\n',a,'\n',a2,'\n', f0,'\n',a3
```

```
    #print delta
    phase1 = a2*(t-tau1)#+a3*(t-tau1)**2 #zero phase at pulse peak
    phase1 = integral(phase1)
    phase2 = a2*(t-tau1)#a*(np.exp(-4.0*np.log(2.0)/np.log(np.e)*((t-tau1)/Tp)**2))
    phase2 = integral(phase2)
    E1 = gaussian_pulse(T1,f0,A,phase1,tau1)  #generate Gaussian pulse E-field
    E2 = gaussian_pulse(T1,f0,1.0,phase2,tau1)
    E = E1+E2
    FROG = FROG_generator(e,E,TD)
    FROG_trace_plot(FROG)

######################
# define a few constants #
######################
c = 300                         #define with unit of nm/fs
e0 = np.loadtxt('pump.dat')     #load the reference pulse, pump @837 nm
e0 = e0.T
e1 = np.sqrt(e0[1])
e1_ph = e0[2]
#print e1_ph
e = np.array(e1)*np.exp(1j*(np.array(e1_ph)))       #reforming E-field

g0 = np.loadtxt('E.dat')        #load the reference pulse, pump @837 nm
g0 = g0.T
g1 = np.sqrt(g0[1])
g1_ph = g0[2]
g = np.array(g1)*np.exp(1j*(np.array(g1_ph)))

original_trace = np.loadtxt('trace.frg')
original_trace = original_trace[::-1]
original_trace = original_trace.T

N = len(e0[0])          #timesteps
N_max = np.max(e0[0])
N_min = np.min(e0[0])

t = e0[0]-N_min
T0 = N_max-N_min  #totoal time duration
dt = T0/(N-1)
#print dt
df = 1.0/T0       #frequency steps
TD = N            #time delay for FROG-trace generation
freq = np.arange(0,1/dt+df,df)*1000

##################
# initial parameters #
##################
```

```
T1 = 1600.0        #Gaussian pulse duration in fs, FWHM
A = 1.0            #-
a = 0.009          #intensity dependent factor
a2 = -2.0*10**-6#second order phase factor 1.50*10**-6#
f0 = 2.00/1000.0 #Raman order
a3 = 5.0*10**-9

Tp = 800.0
i0 = 1000.0
tau1 = T0/2+i0          #pulse peak time

############################
#parameter changing amount #
############################
delta_T = 1.0           # for time in fs
delta_A = 0.01
delta_f = 0.01/1000.0
delta_a = 0.0001
delta_a2 = 1.0*10**-8
delta_a3 = 1.0*10**-11

############################
# FROG trace main program#
############################
minimize_delta()
```

Appendix B

Oscillator maintenance

For the daily use and maintenance. First of all, hold the power button for a few seconds to open the LASER , wait a minute or so for the system to warm-up, the system will stay in the standby mode P1. Then, press P2 button to switch to the working mode. The power will build up all the way to 4.00 W while the green LASER light growing brighter and stronger. After the power reaches 4.00 W, press the reach-out button ‘Starter’ at the back of the fs oscillator box. If the system is in good condition, the output beam should be an ultrashort pulse with a similar spectrum as shown in figure 2.

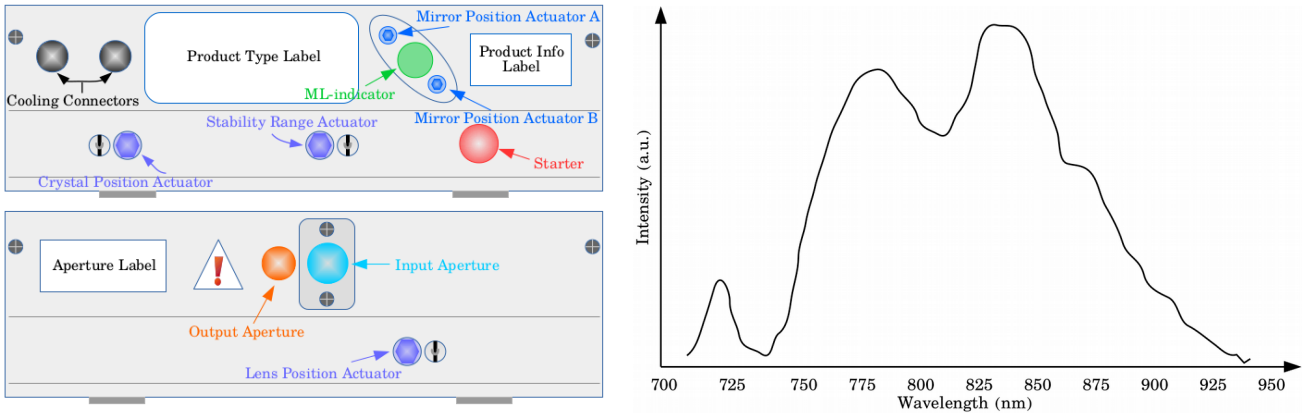

Figure 2: Left-Oscillator conceptional drawing (UP-front view, DOWN-back view); Right-Spectrum of the FemtoLASER s Scientific Pro oscillator

If not showing a stable or strong spectrum, push the ‘Starter’ a few times before going through further alignment. If the spectrum pattern is there but not stable or too weak, meaning the alignment is a little bit off. Then, use the Allen key to slightly twist the Stability Range Actuator till it reaches a strong and nice spectrum. If, unfortunately, the system is too much off. Then a more complicated alignment process is needed.

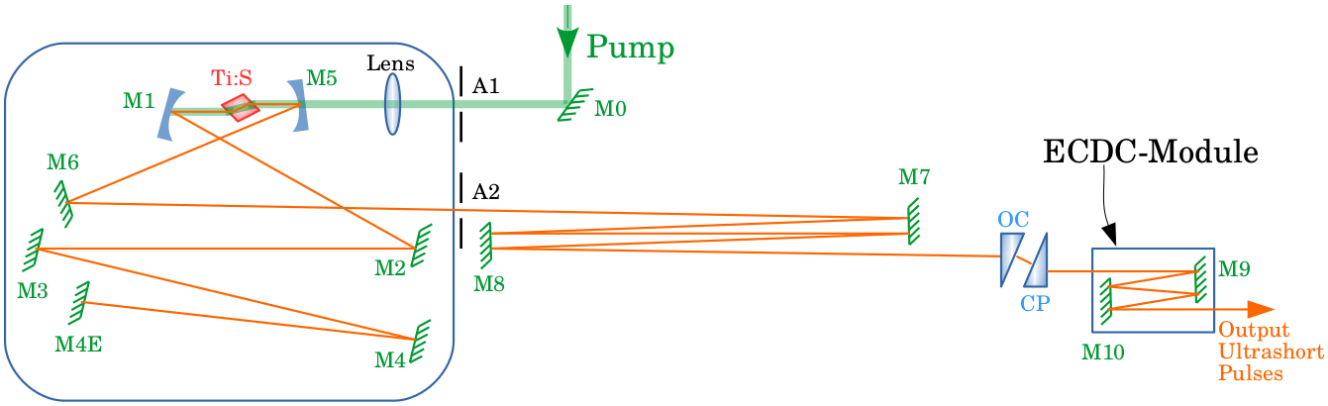

Figure 3: Diagram for the FemtoLASER s Scientific Pro Oscillator

When the Oscillator is too much off, most of the cases, the problem comes from the ‘OC’ and ‘CP’ part as shown in Figure 3. To get it back to normal working condition, place a power meter after the ‘CP’ to measure the output beam. Then do the alignment as following,

1: Use an Allen key to turn the Stability Range Actuator(**SRA**) on the front of the oscillator to get a maximum output power.

2: Slightly rotate one of the knobs on ‘OC’ holder to maximize the power, and then go back to slowly rotate the SRA till the power meter reaches a maximum number. Repeat the process till the power can not go higher. Try the other knobs on ‘OC’ with the same process. Once the power reaches higher than 670 mW, the oscillator should be working. The higher power, the better, while a 725 mW power might be the best.

3: If the 2ed step can not get a good power, slightly rotate the front side ‘Crystal Position Actuator’ or the back side ‘Lens Position Actuator’, till a maximum number is reached. Then goes back to step 2.

4: (Try not to do this step)If still not getting a high number, carefully rotate the ‘Mirror Position Actuator’ on the front side. The two actuator are very sensitive, rotate as slowly as possible, too much movement might make the situation worse. Then, go back to step 2.

5: Once a good power output is reached, rotate the SRA in the clockwise direction till the power number gets back to around 350 mW.

6: Press the ‘Starter’ to get the oscillator mode-locked. Some small rotate of the SRA might needed to get the oscillator working at the best condition.

Most of time, carefully following these steps will bring the oscillator back to work. A 700 mW plus power is suggested when doing the alignment as higher power alignment will keep the oscillator working well for a few months. However, if the oscillator is out of condition, for example, no output beam at all, then, the user’s manual gives more details in setting up the oscillator.

Appendix C

Pump pulse and Stokes pulse

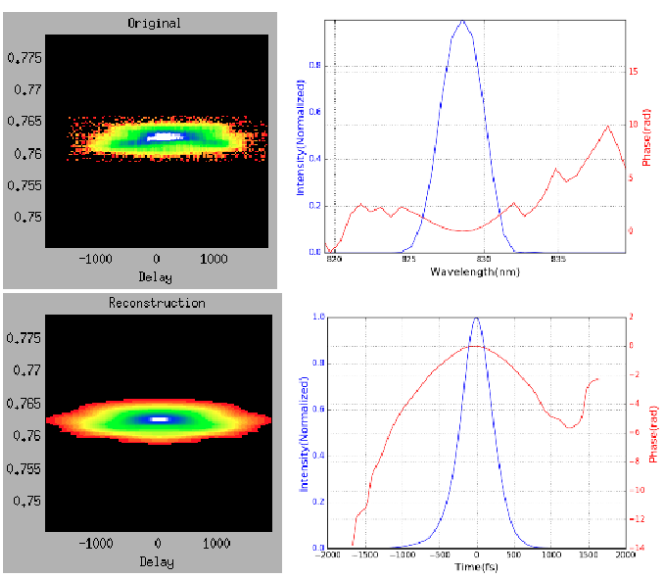

A1

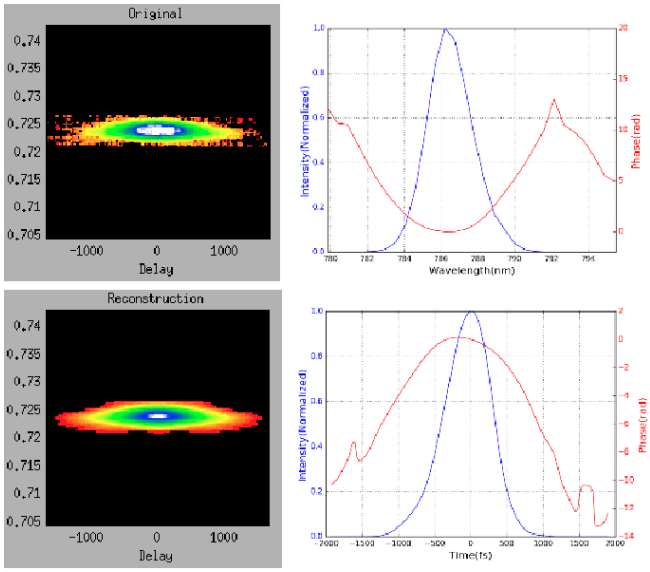

A2

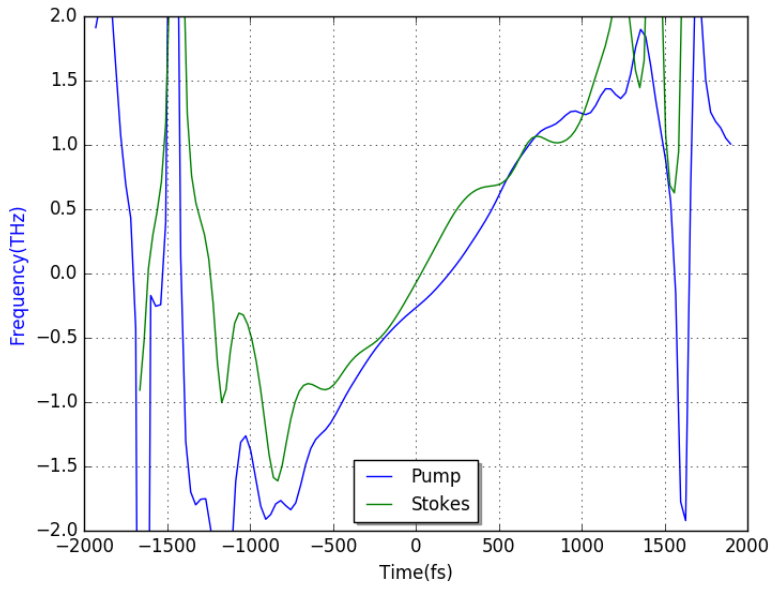

A3

Figure C.1: Pump pulse and Stokes pulse measurement from FROG. A1 is for the Stokes pulse centred at 828 nm; A2 is for the pump pulse with center-wavelength of 778 nm; A3 is the instantaneous frequency of the pump and Stokes pulses. For A1 and A2, the left-top is the original data from experiment; left-bottom is the reconstructed trace by using the FROG program; right-top is the spectrum; right bottom is the pulse in time domain.

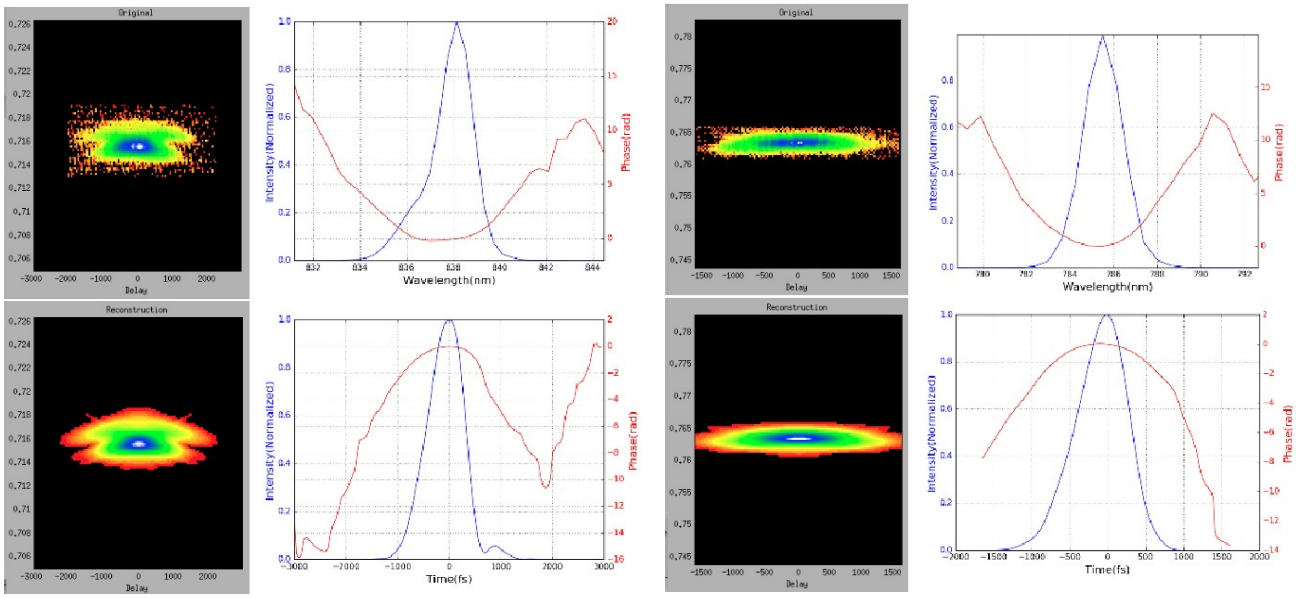

A1 A2

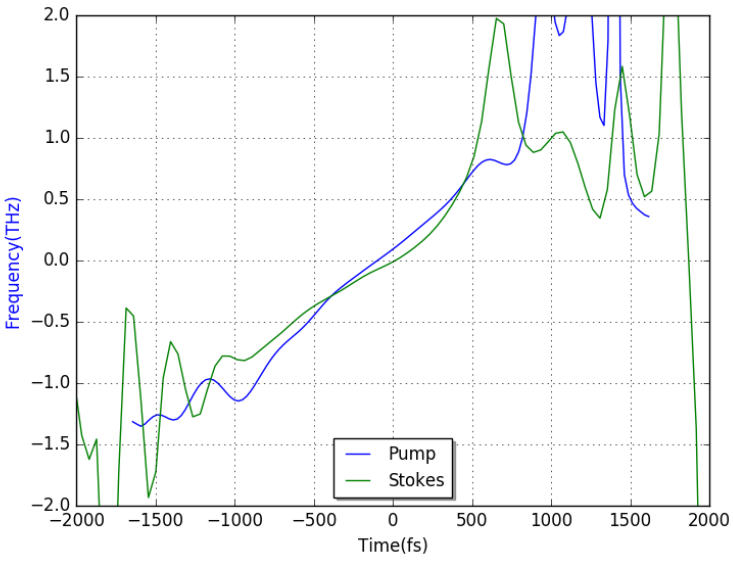

A3

Figure C.2: Pump pulse and Stokes pulse measurement from FROG. A1 is for the Stokes pulse centred at 837 nm; A2 is for the pump pulse with center-wavelength of 786 nm; A3 is the instantaneous frequency of the pump and Stokes pulses. For A1 and A2, the left-top is the original data from experiment; left-bottom is the reconstructed trace by using the FROG program; right-top is the spectrum; right bottom is the pulse in time domain.

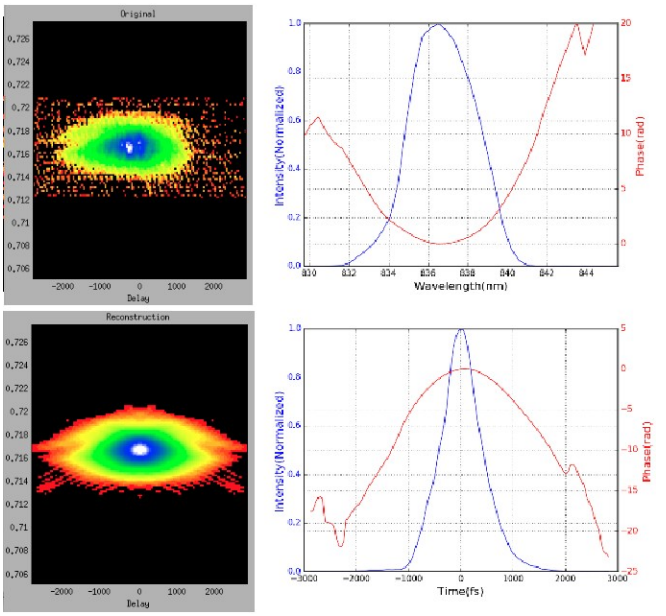

A1

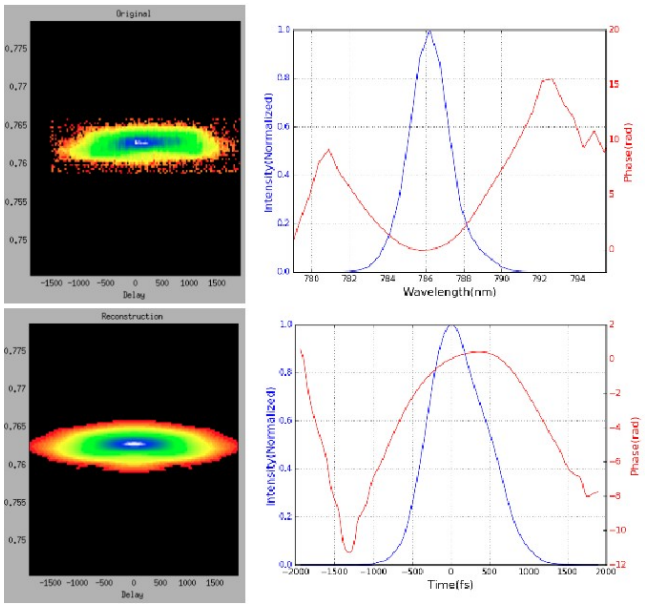

A2

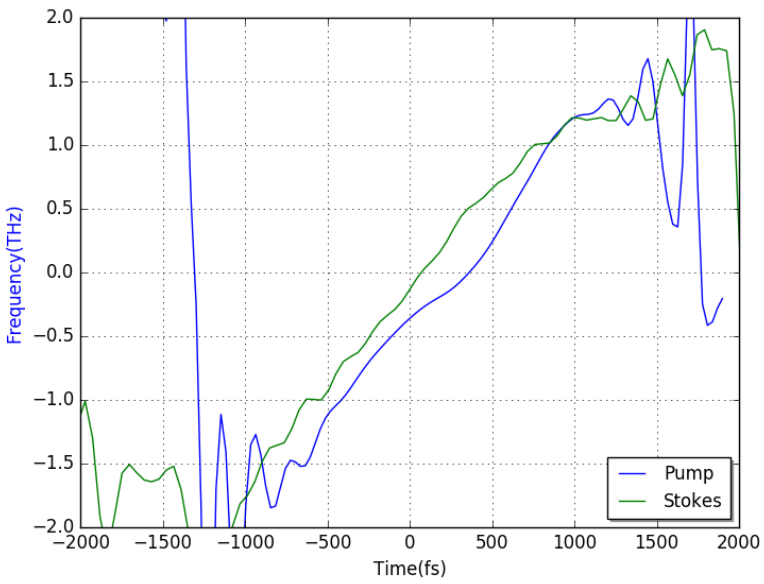

A3

Figure C.3: Pump pulse and Stokes pulse measurement from FROG. A1 is for the Stokes pulse centred at 837 nm; A2 is for the pump pulse with center-wavelength of 786 nm; A3 is the instantaneous frequency of the pump and Stokes pulses. For A1 and A2, the left-top is the original data from experiment; left-bottom is the reconstructed trace by using the FROG program; right-top is the spectrum; right bottom is the pulse in time domain.

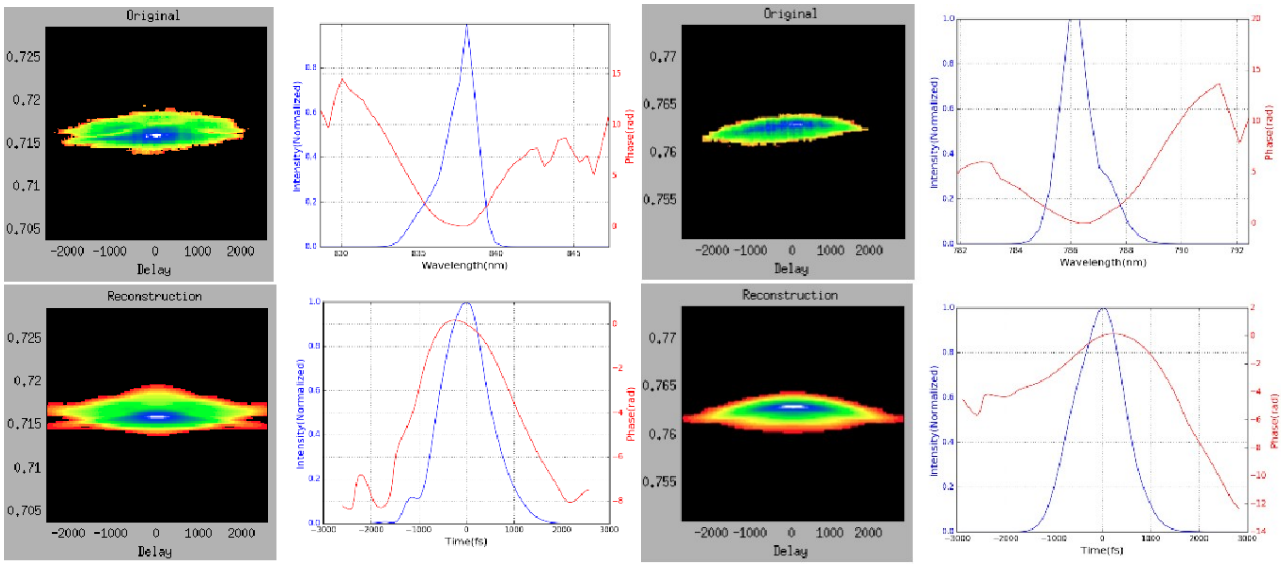

A1 A2

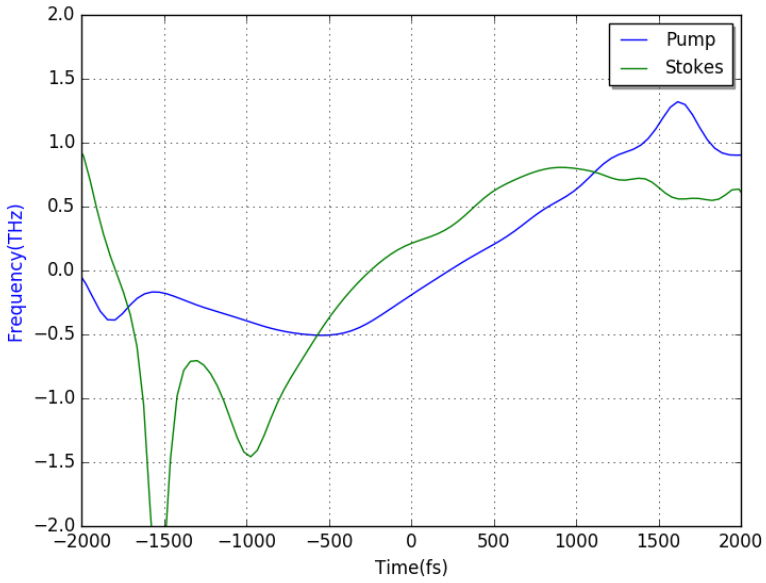

A3

Figure C.4: Pump pulse and Stokes pulse measurement from FROG. A1 is for the Stokes pulse centred at 837 nm; A2 is for the pump pulse with center-wavelength of 786 nm; A3 is the instantaneous frequency of the pump and Stokes pulses. For A1 and A2, the left-top is the original data from experiment; left-bottom is the reconstructed trace by using the FROG program; right-top is the spectrum; right bottom is the pulse in time domain.

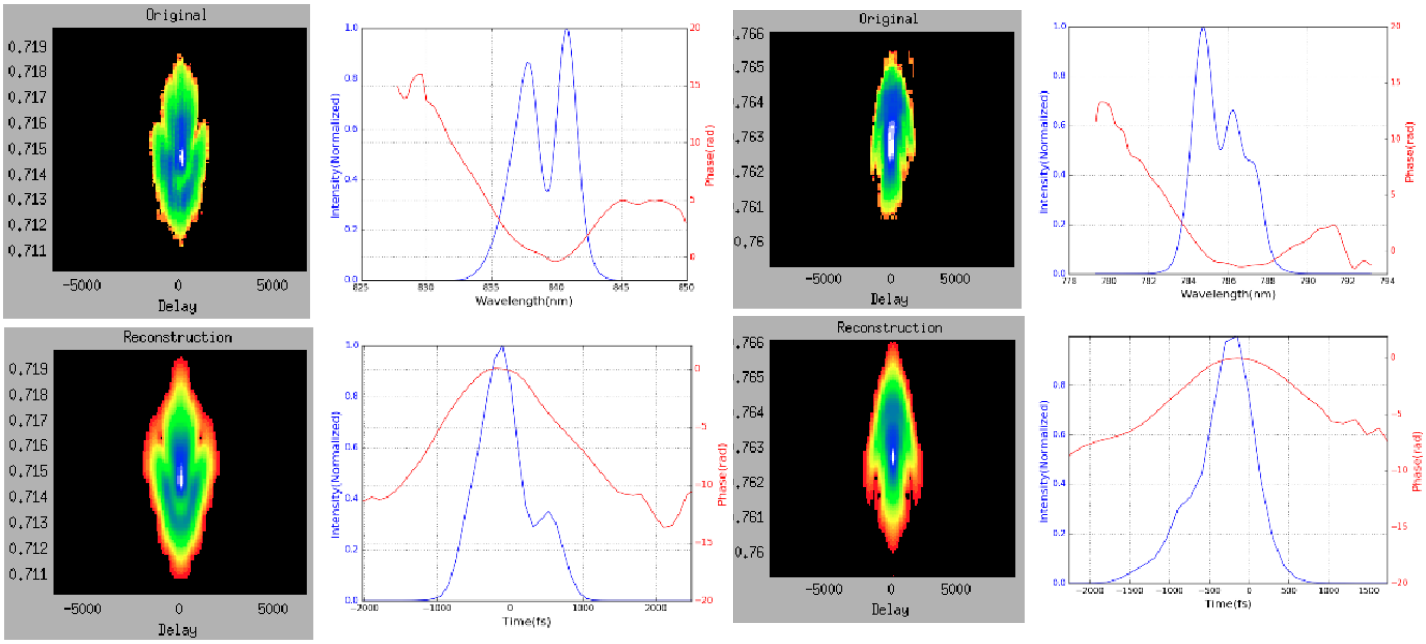

A1 A2

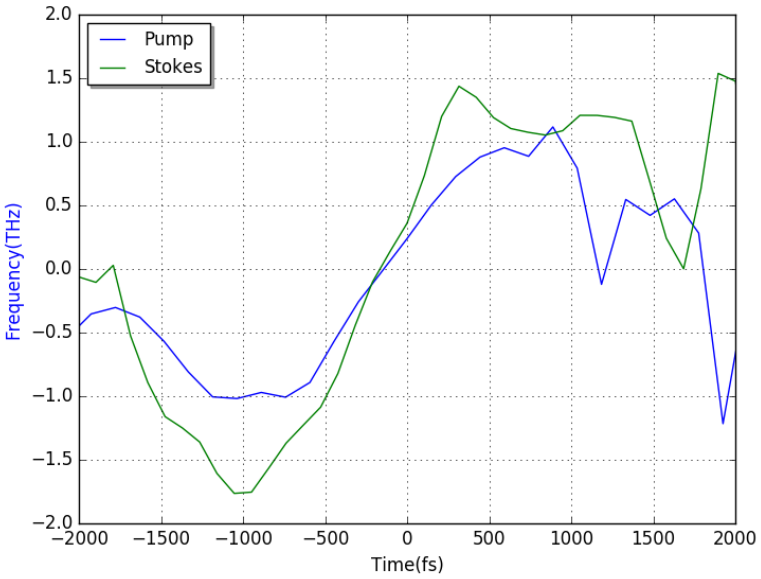

A3

Figure C.5: Pump pulse and Stokes pulse measurement from FROG. A1 is for the Stokes pulse centred at 837 nm; A2 is for the pump pulse with center-wavelength of 786 nm; A3 is the instantaneous frequency of the pump and Stokes pulses. For A1 and A2, the left-top is the original data from experiment; left-bottom is the reconstructed trace by using the FROG program; right-top is the spectrum; right bottom is the pulse in time domain.

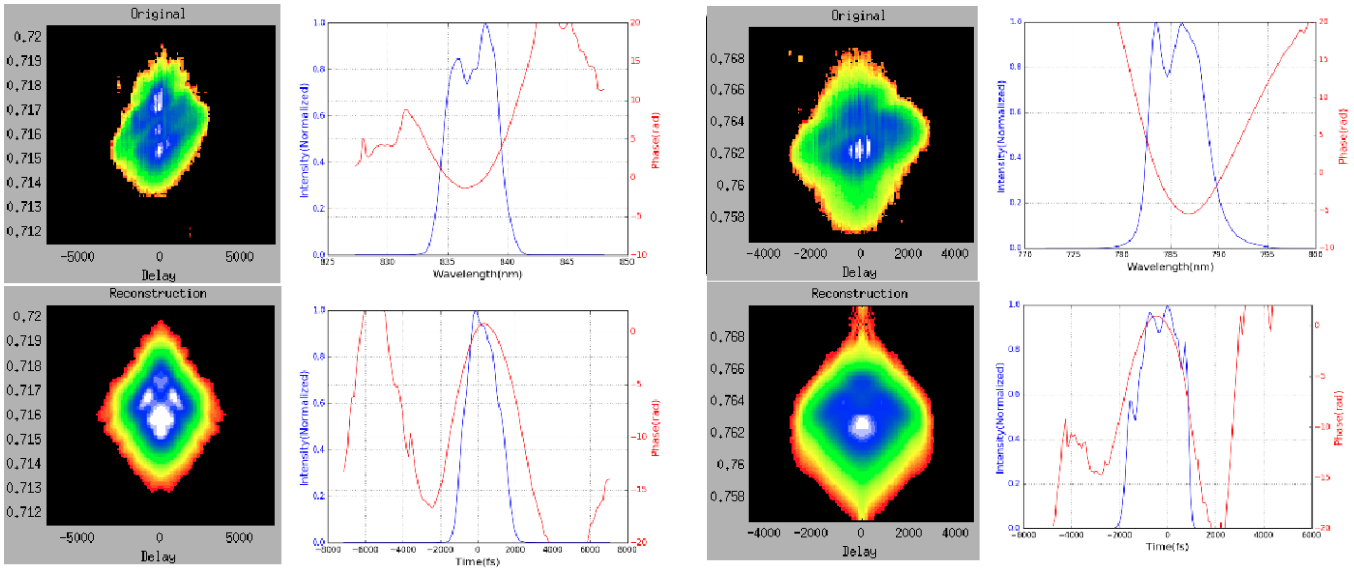

A1

A2

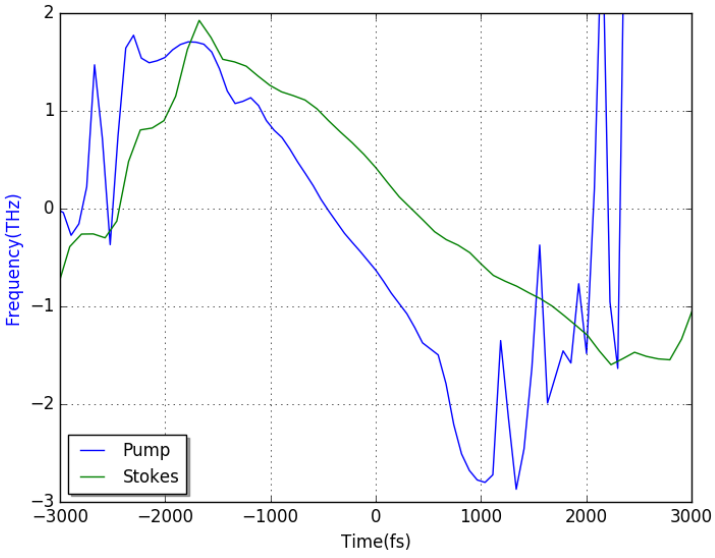

A3

Figure C.6: Pump pulse and Stokes pulse measurement from FROG. A1 is for the Stokes pulse centred at 837 nm; A2 is for the pump pulse with center-wavelength of 786 nm; A3 is the instantaneous frequency of the pump and Stokes pulses. For A1 and A2, the left-top is the original data from experiment; left-bottom is the reconstructed trace by using the FROG program; right-top is the spectrum; right bottom is the pulse in time domain.

Appendix D

Best matching traces with gradient descent method

by Dr. Kisor Kumar Sahu's group (use with permission)

In the following simulations, the reconstructed electric field is a combination of two Gaussian shape pulses,

$$E = E_1(T_1, f_1, A_1, \phi_{1,}\tau) + E_2(T_2, f_2, A_2, \phi_{2,}\tau) \quad \text{(D-1)}$$

where $T_{1/2}$ are time duration of the Gaussian pulses, $f_{1/2}$ are the center-frequencies, $A_{1/2}$ are the amplitude factors, $\phi_{1/2}$ are the phases, and τ is an overall time delay. For the phases, the Raman part only has second order phase while the red-shifted part has both second order and third order phase, and an extra constant phase.

$$\phi_1 = \alpha_2(t-\tau)^2 \quad \text{(D-2)}$$

$$\phi_2 = \alpha_2(t-\tau)^2 + \alpha_3(t-\tau)^3 + \psi \quad \text{(D-3)}$$

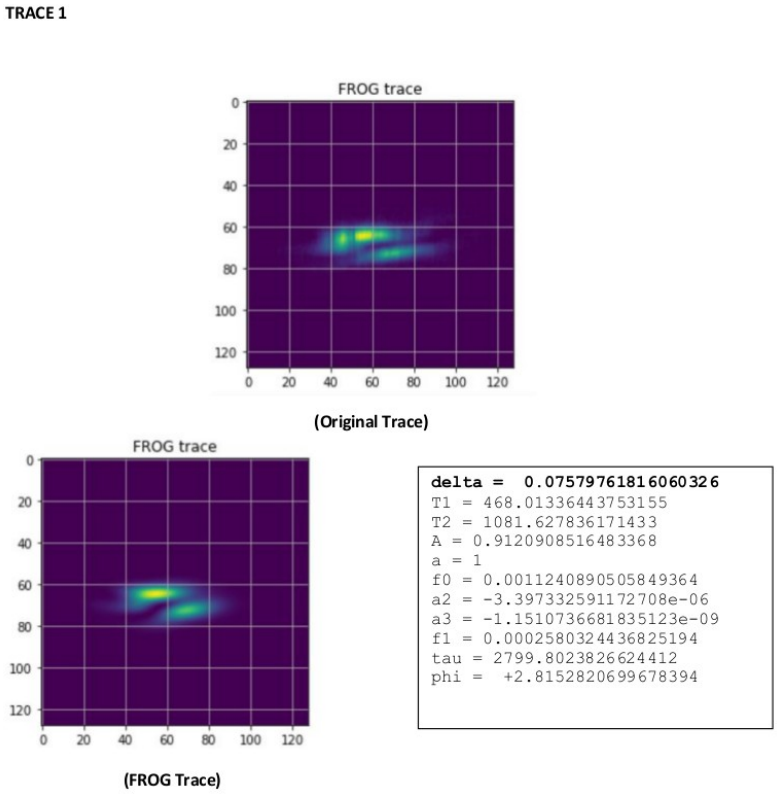

(1)

TRACE 2

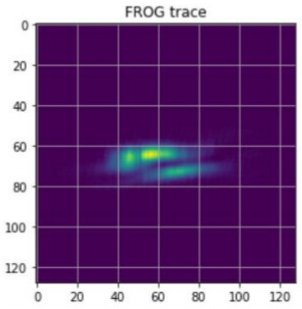

(Original Trace)

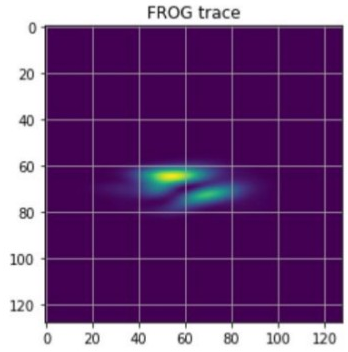

(FROG Trace)

```
delta =  0.06965830405740844
T1 = 473.02331522508587
T2 = 1073.0848087748218
A = 0.8856527072662574
a = 1
f0 = 0.001123362840465577
a2 = -3.370235770941672e-06
a3 = -1.2737059193637148e-09
f1 = 0.000256482066790027
tau = 2798.8011002720905
phi =  +2.829052256347886
```

(2)

TRACE 3

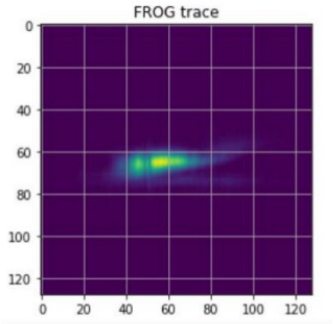

(Original Trace)

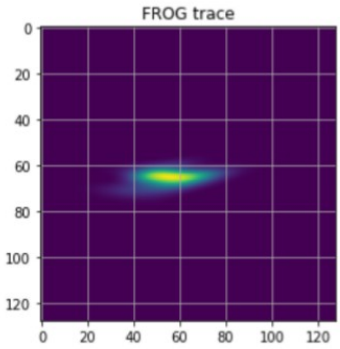

(FROG Trace)

```
delta =  0.07254961459378684
T1 = 509.1375865207681
T2 = 822.8557352019651
A = 0.5396514542702597
a = 1
f0 = 7.946489765218844e-05
a2 = -5.810277733038661e-07
a3 = 5.815609294937908e-10
f1 = 0.0002262142881839372
tau = 2617.0111005518106
phi =  -2.360396520600938
```

(3)

TRACE 4

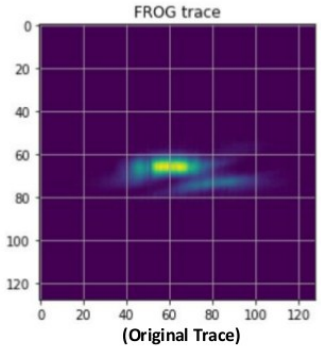

(Original Trace)

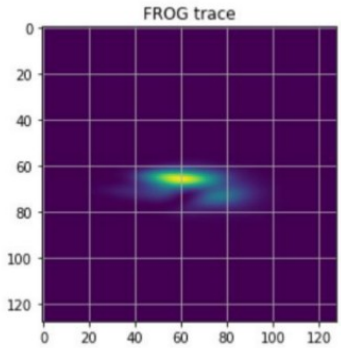

(FROG Trace)

delta = 0.058856174803190456
T1 = 410.646076434209
T2 = 1032.7593921577948
A = 0.6642422917436082
a = 1
f0 = 0.0007413895863495356
a2 = -3.6654937645816873e-06
a3 = -1.3977803408472281e-09
f1 = 0.00043176484687512304
tau = 3026.546006539186
phi = 2.73885533183277

(4)

TRACE 5

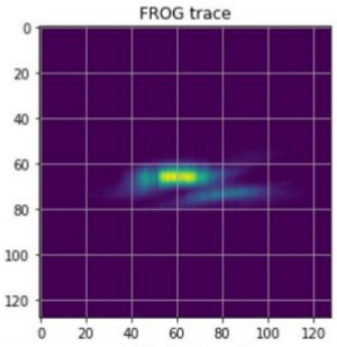

(Original Trace)

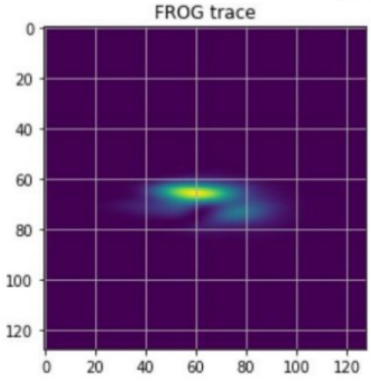

(FROG Trace)

delta = 0.05886600880047471
T1 = 409.8618252979511
T2 = 1033.7644909397734
A = 0.6637511492003063
a = 1
f0 = 0.00074442200223546
a2 = -3.668880893215602e-06
a3 = -1.3980195753752486e-09
f1 = 0.0004326941032077173
tau = 3026.856175096695
phi = 2.7394596366334145

(5)

TRACE 6

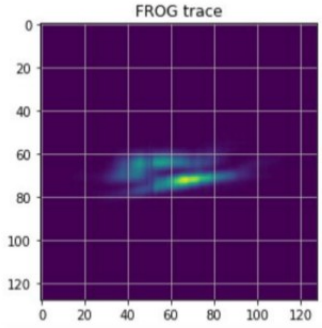

(Original Trace)

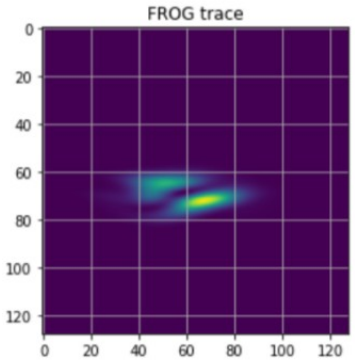

(FROG Trace)

```
delta =  0.09145191438676177
T1 = 573.4849681105591
T2 = 1140.4219515809743
A = 1.1478425874897864
a = 1
f0 = 0.0011554061711149014
a2 = -2.9927487927335984e-06
a3 = -6.145796795117294e-10
f1 = 0.000354980619984249
tau = 2725.8622231118075
phi =  3.071364830240233
```

(6)

TRACE 7

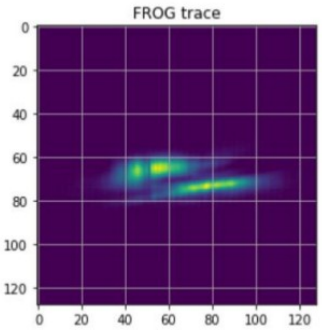

(Original Trace)

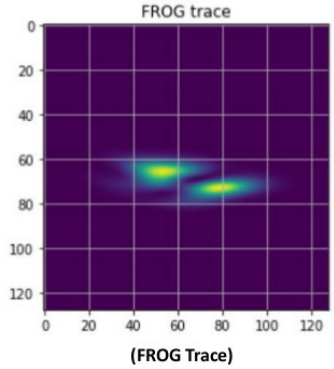

(FROG Trace)

```
delta =  0.1263569302383617
T1 = 796.1540734869375
T2 = 1338.8460065455963
A = 1.1455982220324152
a = 1
f0 = 0.001039337190536355
a2 = -2.9812025989400743e-06
a3 = 1.7749326157145826e-10
f1 = 0.0006283361250743467
tau = 3017.771775197688
phi =  3.0052144809460124
```

(7)

TRACE 8

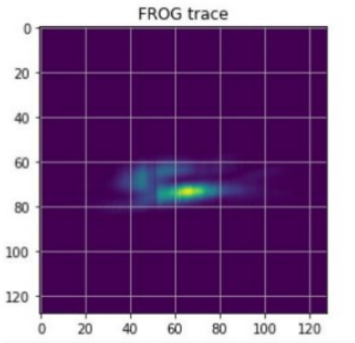

(Original Trace)

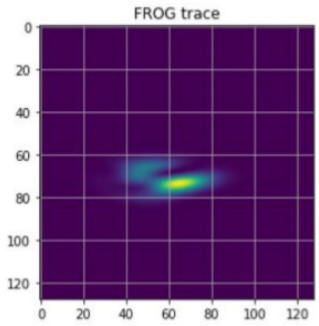

(FROG Trace)

```
delta =  0.05883519127211731
T1 = 660.9589544981898
T2 = 919.5835692777335
A = 1.6634558680337337
a = 1
f0 = 0.0013191192689807846
a2 = -3.6393199251247224e-06
a3 = -4.6483135880981577e-10
f1 = 0.0005495880636196685
tau = 2710.638983776011
phi =  -3.007012258150894
```

(8)

TRACE 9

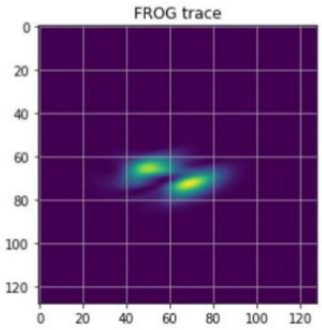

(Original Trace)

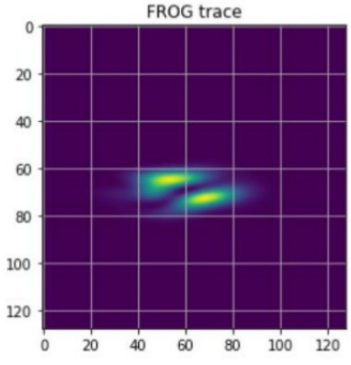

(FROG Trace)

```
delta =  0.0956125211611112
T1 = 528.4235135428202
T2 = 960.3796510682632
A = 0.99527187205328
a = 1
f0 = 0.0011053021347232365
a2 = -3.3975179997025603e-06
a3 = -1.0692774674680475e-09
f1 = 0.00033891494145412543
tau = 2789.7659665198353
phi =  -3.080565432119071
```

(9)

TRACE 10

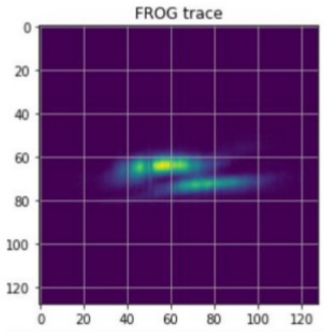

(Original Trace)

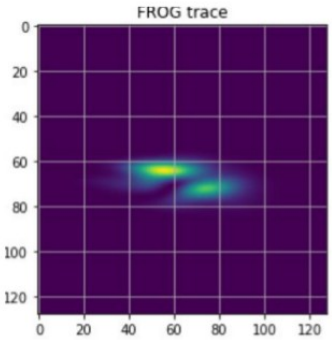

(FROG Trace)

delta = 0.09292265397432713
T1 = 512.6436014436026
T2 = 1167.3478436525113
A = 0.6796264476719411
a = 1
f0 = 0.000882320648505951
a2 = -3.6480519581069683e-06
a3 = -9.950115249751099e-10
f1 = 0.00032916836804063715
tau = 2951.525461207706
phi = 3.1299912497244353

(10)

TRACE 11

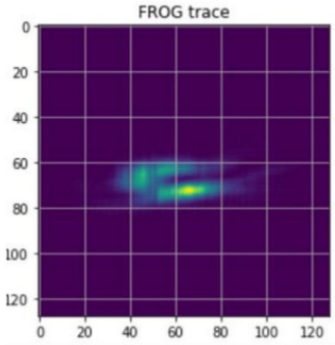

(Original Trace)

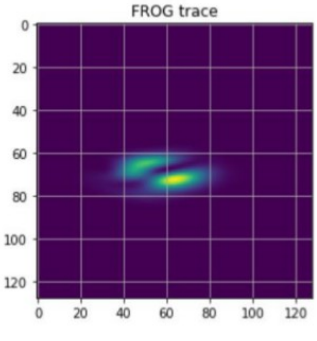

(FROG Trace)

delta = 0.06399064797675894
T1 = 628.1868361457925
T2 = 814.6636770590093
A = 1.3805350538268453
a = 1
f0 = 0.0010739668437121383
a2 = -3.6952894571248897e-06
a3 = -2.9623560770680614e-10
f1 = 0.00034590921390117275
tau = 2669.1596637972953 \phi = 3.032718081037862

(11)